2015

The peritectic phase transition and continuous casting practice

Suk-Chun Moon
University of Wollongong, scmm87@uowmail.edu.au

UNIVERSITY OF WOLLONGONG

The Peritectic Phase Transition and Continuous Casting Practice

A thesis submitted in fulfilment of the requirements for the award of the degree

DOCTOR OF PHILOSOPHY

from

UNIVERSITY OF WOLLONGONG

by

SUK-CHUN MOON, B.Sc., M.Eng.

Faculty of Engineering and Information Sciences

March 2015

Certification

I, Suk-Chun Moon, declare that this thesis, submitted in fulfilment of the requirements for the award of Doctor of Philosophy, in the Faculty of Engineering and Information Sciences, University of Wollongong, is wholly my own work unless otherwise referenced or acknowledged. The document has not been submitted for qualifications at any other academic institution.

Suk-Chun Moon

Wollongong, March 2015

Declaration

Large scale experiments using a mould simulator and Submerged Split-Chill Contraction (SSCC) tests can only be conducted by teams of highly experienced individuals. Differential Scanning Calorimetry (DSC) measurements were conducted on specialized equipment by a DSC specialist. I designed the experiments and interpreted the result as shown below.

Experiment with the mould simulator (Chapter 5)

- My role:

  Planning experiments, mould texture design, measuring thickness profiles of solidified shells and interpretation of result

- Role of participants:

  Mr. Hee-Tae Jeong from CEM R&DE Project Department in POSCO has done the detailed design of the sandblasted and longitudinal grooved texture moulds. Dr. Eun-Yi Ko and Dr. Sang-Woon Moon from POSCO Research Laboratory were involved in the discussions of establishing test conditions, arrangement of tests and supervising tests. Mr. Yong-Mok Shin (Foreman) and his team from POSCO Research Laboratory prepared the melts, set-up and controlled the mould simulator and fabricated the solidified shells.

Dip test (Chapter 5) and SSCC test (Chapter 6)

- My role:

  Planning experiments, selecting steel grades, defining test conditions and interpretation of the result in collaboration with Prof. Christian Bernhard, Dr. Robert Pierer and their team from the Institute of Ferrous Metallurgy, University of Leoben

- Role of participants:

  Dr. Robert Pierer and his team were involved in discussions for the establishing of test conditions, dummy-test body preparation, melt preparation, setting-up and control of the testing facility, supervising tests and assistance in the interpretation of data.

DSC measurement (Chapter 6)

- My role:

  Selecting steel grades and sample arrangement

- Role of participants:

  Mr. Peter Presoly from the Institute of Ferrous Metallurgy, University of Leoben conducted the DSC experiments and assisted in the interpretation of the data.

Abstract

The thin solidifying shell in the meniscus region of a continuous caster deforms due to severe contraction in steels of near-peritectic composition, thereby exacerbating the risks of cracking and in the extreme, breakouts. The main purpose of the present study was to contribute to an improved understanding of the fundamentals underpinning the solidification behaviour of selected steels of industrial importance and to relate these fundamentals to industrial practice. A further aim was to explore the potential of countermeasures aimed at avoiding or at least minimizing surface defects that originate as a result of the occurrence of the peritectic phase transition.

Several experimental techniques were employed to simulate various aspects of solidification events that occur in the meniscus region of an operating continuous caster. *In-situ* observations of solidification in addition to subsequent solid-state phase transformations were made by employing a concentric solidification technique in a high-temperature laser-scanning confocal microscope (HTLSCM) in real time and at temperature. It is possible by this technique to effectively simulate early solidification events occurring in an operating continuous caster and the solidification behaviour of a series of steel of near-peritectic composition and of industrial importance have been assessed and compared. Differential scanning calorimetry (DSC) was employed to determine the exact phase relationships in the selected steels as a function of temperature as an aid to the interpretation of the outcomes of the solidification studies. A potential countermeasure that can be taken in industrial practice to counteract uneven solidification is to texture the mould surface. In order to explore and evaluate the effect of different mould surface textures on reducing the unevenness of the solidifying, a simple dip-test was developed, followed by more sophisticated experiments and analyses in a continuous casting mould simulator. In parallel to the texture studies in the mould-simulator certain aspects of the interaction between mould, strand and mould-flux have also been assessed. The stresses encountered in and development of these stresses in the course of solidification, were assessed by the use of a submerged split-chill contraction (SSCC) technique. In an attempt to relate the fundamental studies to operational practice, an in-plant study of off-corner crack formation was conducted.

The solidification studies conducted in a high-temperature laser-scanning microscope revealed that the velocity of the liquid/delta-ferrite interface decreases with the extent of segregation occurring in the early stages of solidification. An increase in alloy content of steels and/or an increase in cooling rate exacerbate segregation during solidification. It is understood that the migration of the interface requires the diffusion of large amounts of solute across the interface, implying that the delay in shell growth in the very early stage of solidification in mould might be attributed to this segregation. This is an important observation since it means that the initial rate of

solidification in industrial practice is a strong function of steel composition, but that the influence of alloying elements on the rate of solidification can be quantified through experimental simulation studies. The rate of the solid-state delta-ferrite to austenite phase transformation in the presence of liquid phase is significantly higher in hypo-peritectic steels than in the other steels investigated, even at low cooling rates. The higher undercooling of these steels before nucleation of austenite initiates has been attributed to the pre-existence of a higher fraction of primary solidified delta-ferrite in the steels of hypo-peritectic composition. However, it is not the fraction of pre-existing delta-ferrite as such that causes the deeper undercooling, but rather the higher solute concentration gradients that develop in the delta-ferrite phase in these steels that leads to an increased rate of the subsequent delta-ferrite to austenite phase transformation.

In order to illustrate the ill-effects of uneven solidification in a thin-slab caster in industrial practice, the case of off-corner cracking of titanium bearing steels close to peritectic composition was selected for further study. This in-plant study revealed that off-corner cracks can occur as a result of excessive growth of austenite grains caused by the peritectic phase transition and/or by the precipitation of fine TiN precipitates at grain boundaries.

Experiments conducted by the simple dip-test have shown that textured surfaces with 2 mm interval grooves provided the best mould surface to produce even solidification. These grooves also provided the most extensive shell growth through the improved contact between shell and textures mould surface. This observation is attributed to the effect of grooves on the dispersion of deformation sites in the thin shell. In mould simulator experiment, with the application of mild cooling mould flux the growth of shell in hypo-peritectic steel became much evener. Also with mild cooling much thicker shell grew through more intimate contact between shell and mould. The mould simulator experiments revealed that the use of a ‘mild cooling mould flux’ provided conditions conducive to high shell growth rates and even shell formation in casting hypo-peritectic steel. This observation is also attributed to the intimate contact between shell and mould as a result of the reduced heat extraction rate achieved with the ‘mild cooling mould flux’.

In industrial practice it is difficult to predict the solidification behaviour of a specific steel design. The experiments conducted by DSC techniques provided convincing evidence that the susceptibility to the ill-effects of the peritectic phase transition of a given steel cannot be predicted by currently available thermodynamic software or by the calculation of the carbon equivalent alone. It is necessary to determine the absolute values of the phase boundaries as a function of temperature. It was shown that DSC technique is a tool for the identification of steels that will be subject to undergoing the peritectic transformation during continuous casting. It was found that in the case of at least one steel, DSC measurements proved it to be of hypo-peritectic composition whereas thermodynamic software predicted it to be of hyper-peritectic composition.

It was possible to measure the stress developing in the course of solidification in each of the steels investigated by the use of the SSCC test. It was also found that the effect of a reduction in heat transfer by the use of a zirconium oxide coating in the SSCC test on decreasing the contraction forces is more pronounced in the case of hypo-peritectic steels.

In summary: An attempt was made to explore practical measures (or the directions towards improvement) aimed at minimizing defects resulting from solidification events in high-speed continuous casting processes such as uneven shell formation, depressions, cracks and even breakouts. Specific attention was paid to the high stresses that result from the massive-type of phase transformation occurring in the meniscus region. The present study confirmed that it is necessary to gain a comprehensive understanding of the factors, fundamental and operational, that impact on solidification in order to predict the solidification behaviour of steels that fall within the peritectic composition range. Steel composition, casting speed and cooling rate play dominant roles. Two distinct occurrences close to the liquid/solid interface in a solidifying steel shell in a continuous casting mould were identified as of paramount importance: A massive type of delta-ferrite to gamma-austenite transformation with planar liquid/solid interface morphology in the very initial stages of solidification in the meniscus region, which is caused by solute elements build-up in the liquid ahead of the growing solid/interface (partitioning) and a diffusionally driven delta-ferrite to gamma-austenite transformation upon further solidification in the region of dendritic growth as a result of smoothed concentration gradients. Hot-spots need to be avoided at all cost and the development of a thin shell of even thickness in the region below the meniscus is a pre-requisite to preventing casting defects.

Acknowledgements

I should like to acknowledge the extensive support from a large number of people who inspired me in various ways while I have been involved in this doctoral study in a challenging period of my life. I can truly say that the interactions with these individuals have had a significant impact on my life and I appreciate this opportunity to acknowledge their support and contributions to my study and achievement of this milestone.

First of all, I wish to express my sincere gratitude to Prof. Rian Dippenaar who has been supervising this study by providing endless support. Also many thanks for being a kind advisor, providing support in my personal life and often being a delightful companion ever since 2002 when I met him and conducted a master's thesis with him.

My special thanks are due to Dr. Geon Shin and Dr. Sang-Hyeon Lee who afforded me the opportunity to work in the CEM R&DE Project Department in POSCO, South Korea where I was able to gain very high levels of professional credentials, but most importantly for the privilege I have had to work happily with the most impressive, competent and delightful colleagues and companions I have ever had. Also I deeply appreciate the establishment of research projects between POSCO and University of Wollongong which became a connecting chain to this study.

I deeply appreciate the unconditional support provided me by Dr. Mark Reid, especially with the experimental aspects of my work and for also many fruitful discussions. I have the highest regard for his exceptional experimental skills and insight into fundamentals, which helped not only me, but many others in conducting experiments correctly and efficiently.

I wish to extend a special word of thanks to Prof. Christian Bernhard from University of Leoben for participating in the meaningful interaction between POSCO, The University of Wollongong and The University of Leoben. I fully acknowledge his permission to use some of the research done in collaboration with him in my thesis. I also thanks to Dr. Robert Pierer, Mr. Peter Presoly and their talented team for conducting the SSCC and DSC experiments.

I am most grateful to Mr. In-Jae Lee for the limitless encouragement to me, warm concern over my family and most importantly, for providing the opportunity to study abroad in 2002, which later served as a momentum for my family and I to immigrate to this beautiful Australia.

I am much indebted to Dr. Seong-Yeon Kim who was my last team leader in POSCO, for dealing with great delicacy with the difficult personal situations I was confronted with and assisting me in the most sympathetic way when I had to make the difficult decision to leave POSCO. I also

thank to him for participating in our never-ending in-depth discussions with respect to the many interesting behavior of steels.

My thanks are extended to Drs. Stefan Griesser and Salar Niknafs for exchanging valuable ideas in the earlier part of my PhD studies.

I am thankful to my junior colleague Hee-Seon for the arrangement of experimental materials for the HTLSCM experiment and to Dr. Eun-Yi Ko, Dr. Sang-Woon Moon and Mr. Hee-Tae Jeong for the arrangements of the mould simulator experiment.

I am mostly grateful to Mr. and Mrs. Lee (Young-Seob and Naru) for providing intimate friendship and love for my family and most especially for their warm care on my family in my absence, which enabled me to concentrate on my work without any worry.

I should acknowledge the Australian Postgraduate Award from Australian Government and the University Postgraduate Award from The University of Wollongong, which provided financial support for my studies.

Finally, my deepest and most sincere thanks to my darling wife, Kwang-Young, my sons Joon-Young and Soo-Young for their generous love, patience, encouragement and support, and also to my parents, parents-in-law, brothers and sisters for their endless concern and support for me and my family over such a long distance.

Contents

List of Figures

List of Tables

Introduction

Steel is said to be God's gift. Due to its wide application, steel is one of the most common materials in the world with more than 1.3 billion tonnes produced annually. Since the introduction of continuous casting technology in the 1950s, it has replaced ingot casting processes in the steel industry and has evolved to achieve improved productivity, quality, yield and cost efficiency.

Improvements in productivity of processes up- and down-stream from the continuous casting process necessitated increased productivity improvements in the continuous casting process, which in part at least, has been achieved by increasing the casting speed. The advent of thin-slab casting technology increased the flexibility of the production route of steel strip, resulting in the development of various new variants of thin-slab and hot-rolling processes. Most of these processes incorporate much higher casting speeds as a key ingredient to achieve higher efficiencies.

A particularly serious quality problem that has been encountered in most of new developments, but exacerbated at high-casting speeds, is slab surface cracking. These cracks are retained on the surface even after hot-rolling and the slab has to be scrapped when the cracks are long and deep enough to be retained even at scarfing while there is no choice but downgrading in thin-slab and hot-rolling processes due to the unavailability of scarfing. Moreover, operational failures such as breakouts are often the result from these quality issues and corrective measures taken to counteract quality problems frequently lead to unstable process operations. It is therefore vitally important to more fully understand the interrelationship between the fundamental causes of quality problems, remedial action that can be taken and the sensitivity of operational parameters controlling remedial action.

The surface quality of continuously cast slabs is a strong function of events occurring during the early stages of solidification in the meniscus region of the mould. Moreover, the subsequent micro-structural evolution in certain steels, of which many advanced steels are examples, is complicated by the occurrence of a peritectic phase transition. Steels that undergo the peritectic transition are the most difficult to produce with respect to surface quality, especially at high casting speeds [2-6], most probably because of the peritectic phase transition, which occurs in the meniscus region [7-11] when the shell is extremely thin. The volume contraction associated with the peritectic phase transition results in the detachment of the solidified shell from the mould, which in turn leads to a decrease in heat flux, resulting in hot spots, which significantly increases the risk of surface cracking or breakouts. These risks are higher in the thin slab casting process than in conventional casting process. Therefore, the operational window for variations in important operational parameters in the continuous casting process becomes quite narrow in producing peritectic steels.

Transverse crack along the oscillation mark

Longitudinal facial crack

Breakout

Example of surface cracks on a slab and breakout in steel of near-peritectic composition in thin slab casting process (Pictures were taken in the Gwangyang Works of POSCO, South Korea)

Driven by the diversification of steel products, the demand for production of steels close to peritectic composition range such as HSLA (High Strength Low Alloy) and AHSS (Advanced High Strength Steel) grades has have been increasing. The ever increasing demands on the mechanical properties of steel products and cost reduction in alloy designs are the main reasons why these steels are designed close to the peritectic composition range. For example, the automotive industry is increasingly utilizing advanced high-strength steels, primarily to reduce the mass of motor vehicles. However, many of these steels fall within the peritectic composition range, which are notoriously difficult to cast by continuous casting techniques. The casting problems of steels close to the peritectic composition are exacerbated at high casting speeds and they are therefore of specific concern in the development of high-casting speed technologies, such as thin-slab and hot-rolling processes. High casting speeds in turn, are required to achieve high production rates to attain economics of production as a consequence there is a premium on the development of new technologies designed for stable production techniques of steel of near-peritectic composition. Improved technology will broaden the operational windows for important operational parameters and will also relieve the limitation in composition designs as a result of the difficulties encountered in the production of these steels.

Through many fundamental studies, it is now well established that many of the quality problems encountered in the casting of steel of near-peritectic composition originate in the early stages of solidification when the solidifying shell is very thin. Hence, it is fundamentally important to go one step further and obtain detailed knowledge of the initial solidification behaviour of steels of near-peritectic composition in industrial practice. Such knowledge is required to ensure operational stability and slab surface quality especially in the new high-speed continuous casting processes. The present study was designed against this background with the following specific aims:

- To assess the initial solidification behaviour of a series of selected steels by simulating experimentally the early solidification events occurring in the meniscus region of an

operational caster

- To assess the crack susceptibility of this series of steels
- To explore techniques by which the undesirable influence of uneven solidification can be reduced
- To simulate the interaction between mould, strand and mould flux

In an attempt to achieve these aims, the present project design was as follows:

- In order to contribute to a better understanding of the root cause of surface defects, which occur as a result of uneven solidification, a concentric solidification technique was employed in a high-temperature laser-scanning confocal microscope to simulate experimentally the events occurring in the early stages of solidification in an operational continuous caster (HTLSCM)
- In these studies, a series of steels of industrial importance was selected, but to enable a credible interpretation of the results it was necessary to determine the exact phase compositions as a function of temperature. This was done by conducting differential scanning calorimetry (DSC)
- In an attempt to correlate the experimental simulation with operational practice, an in-plant study of off-corner crack formation was conducted
- The crack susceptibility of the selected series of steels was assessed by conducting a submerged split-chill contraction (SSCC) test
- In order to explore techniques by which uneven solidification can be reduced, the effect of mould surface texturing was studied. This was done by initially conducting a simple dip-test followed by more sophisticated mould simulator tests. The interaction between mould, strand and mould flux was studied concurrently with the mould texture studies in the mould simulator.

Chapter 1. Literature Review of Peritectic Solidification in Steel

1.1 Sequence of Peritectic Solidification

The peritectic transition in steel, where liquid+δ→γ, is an extremely complex and challenging phase transformation to study either experimentally or mathematically. Kerr *et al.* [12] have defined the peritectic transition into two separate components: the peritectic reaction (δ-ferrite + liquid → γ-austenite), followed by the peritectic phase transformations (δ-ferrite → γ-austenite and liquid → γ-austenite) as shown in Fig.1.1. The peritectic reaction occurs under conditions where all three phases (liquid, δ-ferrite and γ-austenite) are in contact, and the liquid and δ-ferrite phases react to form γ-austenite. This reaction is rapid, so that a film of γ-austenite quickly separates the liquid and δ-ferrite phases. From this point onward, further formation of γ-austenite from the liquid and from the delta-ferrite phase is defined as the peritectic transformations.

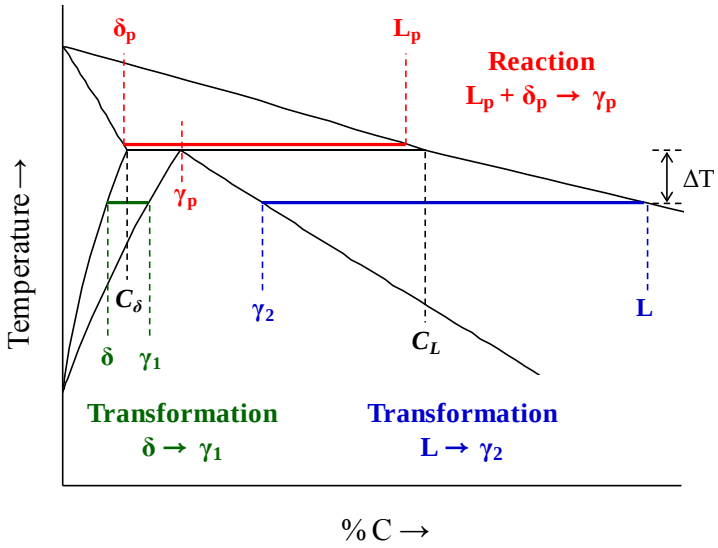

Fig.1.1 Peritectic reaction and subsequent phase transformations

In the past, studies of the peritectic phase transition have been hampered by our inability to conduct high resolution metallography at the high temperatures pertaining to the peritectic phase transition and the subsequent decomposition of γ-austenite. Through the use of recently developed high-temperature laser-scanning confocal microscopy (HTLSCM) originally developed by Emi and his colleagues, it has now become possible to observe *in-situ* and at high resolution, events

occurring at high temperature [13]. Shibata *et al.* [1] used this new experimental technique to provide the first *in-situ* experimental evidence that the peritectic reaction initiates and propagates at high speed by the growth of a thin γ-austenite layer along the liquid/δ-ferrite interface as shown in Fig.1.2. Once the reaction is completed and the liquid/δ-ferrite interface is covered by γ-austenite, the peritectic transformations start. This sequence of events has been confirmed by the experiments by Phelan *et al.* [14] as shown in Fig.1.3. In addition to their own new information, Shibata *et al.* [1] also summarized much of the earlier work on the mechanism and rate of the peritectic transition in steel.

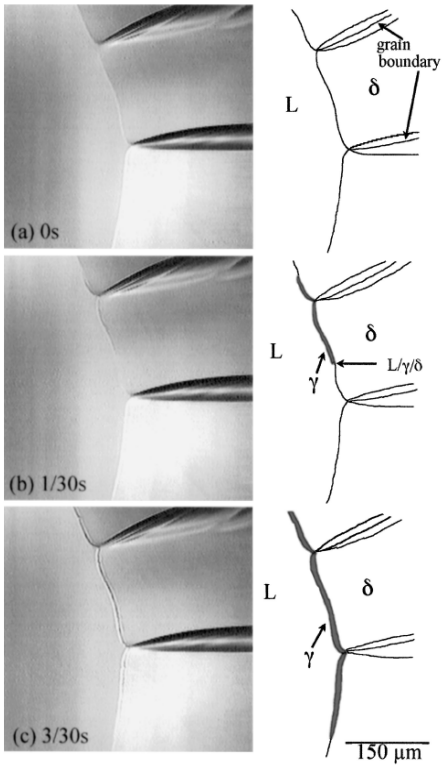

Fig.1.2 Peritectic reaction occurs at liquid/solid interface [1]

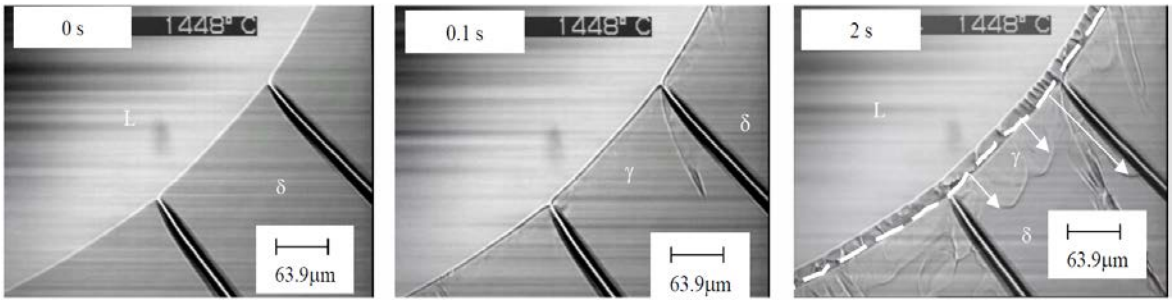

Fig.1.3 Peritectic reaction and transformations in a Fe-0.18wt%C alloy. Cooling rate 10 °C/min. The superimposed broken line in the frame at t = 2s, corresponds to the position of the liquid/δ interface at t = 0 [14]

Stefanescu [15] further interpreted and summarized the sequence of events as shown in Fig.1.4 : during the peritectic reaction δ-ferrite, γ-austenite and liquid are in contact and a thin film of γ-austenite grows along the liquid/δ-ferrite interface, driven by liquid super-saturation. Solute rejected by γ-austenite will diffuse through the liquid to δ-ferrite phase contributing to its dissolution. The γ-austenite phase will also thicken in the direction perpendicular to its growth, by direct growth into the liquid and at the expense of δ-ferrite phase by solid state diffusion. Once the reaction is completed and all the liquid/δ-ferrite interfaces are covered by γ-austenite, the peritectic transformation starts. The liquid and primary δ-ferrite phases are isolated by the γ-austenite film. The δ-ferrite to γ-austenite transformation takes place by long-range solid-state diffusion through the peritectic (γ-austenite) phase. The γ-austenite phase grows by direct solidification in the liquid. The *in-situ* observations of Phelan *et al.* [14], shown in Fig.1.3, illustrate the growth of γ-austenite into δ-ferrite and into liquid respectively.

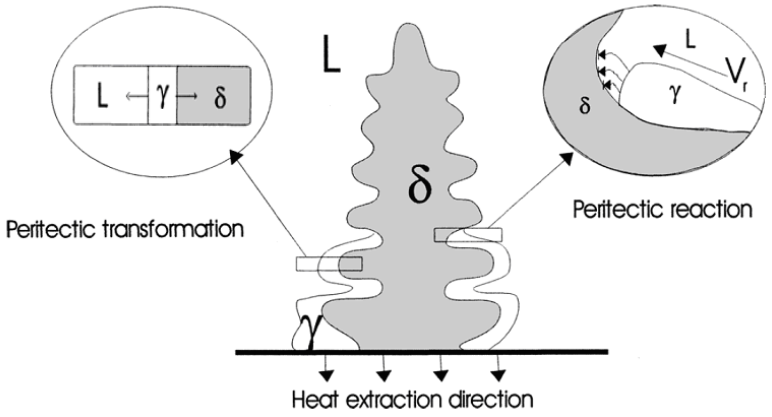

Fig.1.4 Mechanism of peritectic solidification [15]

It is important to note that a concentration gradient is established across the thin γ-austenite layer that separates the δ-ferrite phase from the liquid since local equilibrium is maintained at the respective interfaces. With reference to Fig.1.1, the concentration at the δ-ferrite/γ-austenite interface is γ_1, whereas the concentration of γ-austenite at the liquid/γ-austenite interface is γ_2 at an under-cooling of ΔT. Stefanescu [15] proposed that in practice, this growth of the γ-austenite layer occurs along δ-ferrite dendrites (peritectic reaction) and subsequently the newly formed γ-austenite layer grows into the liquid (normal solidification) and back into δ-ferrite by the δ-ferrite to γ-austenite phase transformation as shown in Fig.1.4.

1.2 Mechanism and Kinetics of Peritectic Reaction

The peritectic reaction can be described as the solidification of γ along the liquid/δ interface and is to be clearly distinguished from the subsequent peritectic transformation. At the peritectic temperature, δ reacts with the liquid to form γ, which starts to grow laterally on the surface of δ. The lateral growth of γ is determined by the thermodynamic equilibrium at the triple-point, defined as the point where the liquid, δ and γ are in contact.

Being based on the classical diffusion model, Bosze and Trivedi [16] derived the lateral growth rate of a γ-plate growing on the surface of δ during a peritectic reaction as given by:

$$v = \frac{9D^L}{8\pi R^\gamma} \times \left(\frac{\Omega}{\Omega'}\right)^2 \tag{1.1}$$

where D^L is the diffusion coefficient of carbon in the liquid, R^γ is the tip radius of the growing plate and is equal to half of the thickness of the laterally growing γ shell and Ω and Ω' are defined as:

$$\Omega = (x_C^{L/\gamma} - x_C^{L/\delta})/(x_C^{L/\gamma} - x_C^{\gamma/L}) \tag{1.2}$$

$$\Omega' = 1 - (2\Omega/\pi) - (\Omega^2/2\pi) \tag{1.3}$$

where $x_C^{L/\gamma}$ and $x_C^{L/\delta}$ are the concentration of carbon in the liquid in equilibrium with γ and δ respectively, $x_C^{\gamma/L}$ is the concentration of carbon in γ in equilibrium with the liquid.

Further Nassar *et al.* [17] derived a theoretical model for the growth rate of a plate-shaped participate by extending Bosze and Trivedi's model [16] with the surface tension coefficient between δ-ferrite and γ-austenite:

$$v = \frac{27 \cdot D^L \cdot R \cdot T(k_{Fe}^{\gamma/L} - k_C^{\gamma/L})(x_C^{L/\gamma} - x_C^{L/\delta})}{128 \cdot \pi \cdot \sigma^{\delta/\gamma} \cdot V_m^L} \times \left(\frac{\Omega}{\Omega'}\right)^3 \tag{1.4}$$

where R is the gas constant, $k_{Fe}^{\gamma/L}$ and $k_C^{\gamma/L}$ are the partition coefficients of iron and carbon respectively at the liquid/γ interface, $\sigma^{\delta/\gamma}$ is the surface tension coefficient between δ and γ , V_m^L is the molar volume of the liquid. Thus, the lateral growth rate of γ during the peritectic reaction is

strongly dependent on Ω, which is a function of the shape of the phase diagram below peritectic temperature, T_p. The lateral growth rate and Ω are calculated as functions of undercooling from the peritectic temperature, ΔT_p, for the Fe-C binary system with a chosen value for the diffusivity of carbon in the liquid $D^L = 2\times10^{-8}\text{m}^2/\text{s}$, and the rapid increase in the lateral velocity with the increase in undercooling can be seen in Fig.1.5 [17].

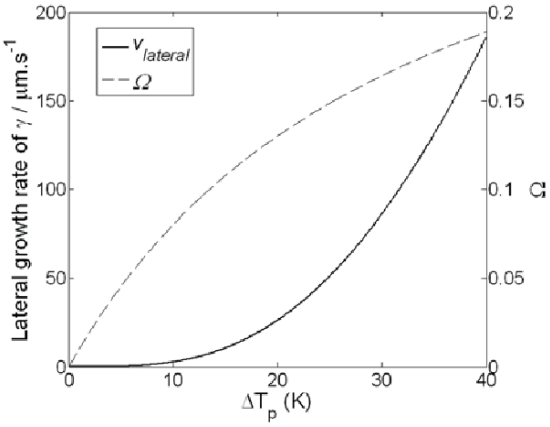

Fig.1.5 Lateral growth rate of γ and Ω as a function of ΔT_p during the peritectic reaction in the Fe-C system [17]

Griesser [18] in his recent work using HTLSCM proved that under conditions close to chemical and thermal equilibrium, i.e., under very small undercooling, the growth of the austenite platelet during the peritectic reaction can be explained by diffusion-controlled mechanisms. In addition, Griesser [8] confirmed earlier experimental observations by Phelan *et al.* [19] that remelting of delta-ferrite occurs at the growing austenite platelet tip, as originally proposed by Hillert [20]. The peritectic reaction is strongly dependant on the solute diffusivity in the solid phases.

In directional solidification experiments using an Fe-0.42wt%C alloy and utilizing using HTLSCM, Shibata *et al*. [1] observed that the lateral growth rate of γ varied between 1.5 and 4.0mm/s at an undercooling of 10-15 °C, which is two orders of magnitude higher than the calculated values and they argued that these very high growth rates of the austenite platelet along the liquid/delta-ferrite interface cannot be explained by diffusion control.

Chalmers [21] suggested that in the absence of solute diffusion control, the maximum rate of growth is a function of the temperature gradient, the thermal conductivity and density of the solid and that this maximum growth rate can be described by following equation:

$$V_{\max} = \frac{K_S G_S}{\rho L} \tag{1.5}$$

where K_S is the thermal conductivity of δ-ferrite, G_S the thermal gradient in the solid (K/m), ρ

the density of δ-ferrite and *L* is the latent heat of fusion. Using the Bosze and Trivedi [16] model, Phelan *et al.* [19] calculated growth rates ranging from 19 to 855 μm/s for thermal gradients between 1 and 45 °C/mm as shown in Fig.1.6 (indicated as No-remelting). However, their experimentally observed growth rates varied from 0.4×10^3 to 12.5×10^3 μm/s while Shibata *et al.* [1] observed growth rates that varied from 1.5×10^3 to 4.0×10^3 μm/s. It therefore follows that the experimentally observed growth rates cannot be explained by the Bosze and Trivedi analysis.

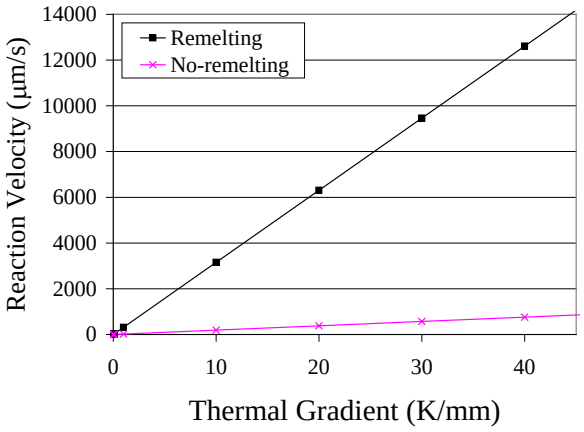

Fig.1.6 Calculated rates of progression of an γ-austenite platelet along the liquid/δ-ferrite interface. The curve *No-remelting* refers to predictions by the Bosze and Trivedi [16] model, that assumes the growth of a macroscopically planar growth front is diffusion controlled. The curve *Remelting* refers to a model where remelting of δ-ferrite ahead of the advancing γ-austenite tip is taken into consideration [19]

Hillert [20] originally proposed that the progression of an γ-austenite platelet is accompanied by the remelting of δ-ferrite ahead of the growing interface and it seems that this remelting of δ-ferrite plays a crucial role in determining the kinetics of the peritectic reaction. Phelan *et al.* [19] proposed that partial melting of δ-ferrite immediately ahead of the growing γ-austenite will absorb a component of the latent heat of fusion liberated by the formation of γ-austenite. The latent heat liberated by the peritectic reaction therefore becomes the difference between the latent heat liberated by the formation of the γ-austenite platelet and that absorbed by the remelting of δ-ferrite ahead of the growing interface. If it is assumed that an equal volume of δ-ferrite remelts during the formation of γ-austenite, the heat that has to be removed for the peritectic reaction to proceed (i.e. for the γ-austenite platelet to progress along the liquid/δ-ferrite interface) is 12 kJ/kg ($L_\gamma - L_\delta$). The velocities of the growing γ-austenite tip as a function of thermal gradient calculated by Eq.1.5 under these conditions are shown in Fig.1.6 and it is evident that the calculated values agree well with the experimentally determined growth rates which varied between 0.4×10^3 to 12.5×10^3 μm/s. Although it is interesting that this model, based on thermal diffusion can explain the experimental results, the problem is that the rate of the progression of an γ-austenite platelet will be controlled by the slowest step and since thermal diffusion is much faster than the diffusion of carbon iron, it is

necessary to determine how and why thermal diffusion can control the growth rate of the γ-austenite platelet.

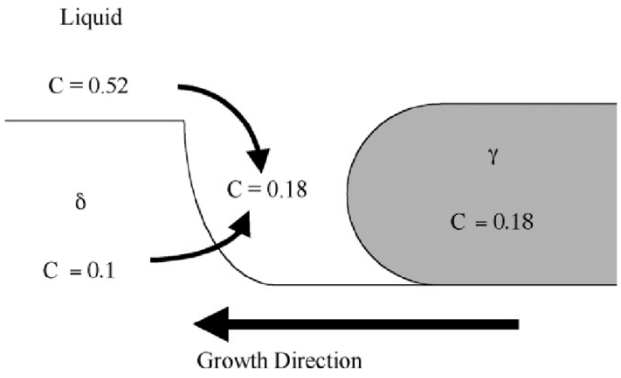

Fig.1.7 Model of peritectic reaction proposed by Phelan *et al.* [19]

Phelan *et al.* [19] considered the situation in the immediate vicinity of a growing γ-austenite tip on the liquid/δ-ferrite interface as shown in Fig.1.7. Under equilibrium condition, the carbon contents of the three phases in contact at the peritectic temperature are: 0.1 wt%C in δ-ferrite, 0.18 wt%C in γ-austenite and 0.52 wt%C in the liquid. With reference to Fig.1.7, they proposed the following sequence of events: Some δ-ferrite remelts ahead of the advancing γ-austenite plate as a result of the heat of fusion released by the formation of γ-austenite. This remelted δ-ferrite (of composition 0.1 wt%C) mixes with liquid (of composition 0.52 wt%C) to form a region of composition 0.18 wt%C immediately ahead of the advancing γ-austenite tip. The γ-austenite therefore grows into a liquid of exactly the same composition and hence the γ-austenite progresses without the need for carbon to diffuse in either γ-austenite or δ-ferrite. The reaction is therefore controlled by thermal diffusion, thus accounting for the rapid growth velocities and the strong influence of the thermal gradient at the advancing interface on the growth rate of the γ-austenite tip.

On the other hand, Nassar *et al.* [17] interpreted the lateral growth of γ in terms of strain energy dissipation. In their interpretation, the lateral growth of γ is strongly dependent on surface tension at the liquid/δ, liquid/γ and δ/γ interfaces, denoted by $\sigma_{L/\delta}$, $\sigma_{L/\gamma}$ and $\sigma_{\delta/\gamma}$ respectively. A force balance at the triple point gives that $\sigma_{\delta/\gamma}$ is equal and opposite in direction to the resultant of $\sigma_{L/\delta}$ and $\sigma_{L/\gamma}$, which is illustrated in the schematic drawing of the triple point in Fig.1.8(a). Nevertheless, it was observed by *in-situ* imaging of laterally growing γ during the peritectic reaction in Fe-Ni binary alloys [22] that the tip of the growing γ is strongly pointed towards the direction of growth, indicating that $\sigma_{\delta/\gamma}$ is larger than $\sigma_{L/\delta}$ and $\sigma_{L/\gamma}$, as illustrated in Fig.1.8(b). It is proposed that high surface tension at the δ/γ interface is caused by elastic strain between δ and γ. The surface tension between δ and γ is thus given by $\sigma^{\delta/\gamma} = \sigma_{eq}^{\delta/\gamma} + \sigma_{\varepsilon}^{\delta/\gamma}$, where $\sigma_{eq}^{\delta/\gamma}$ is the equilibrium surface

tension at the solid-solid δ/γ interface, and $\sigma_{\varepsilon}^{\delta/\gamma}$ is the contribution of the elastic strain to the total surface tension. However this interpretation of Nassar *et al*. [17] has not been proven experimentally and is still in the subject of some arguments.

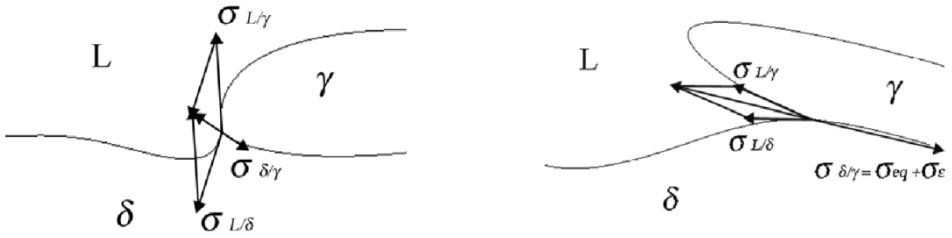

(a) in the case of no δ/γ interface strain

(b) in the case of δ/γ interface strain as observed by Arai *et al.* [22]

Fig.1.8 Surface tension vectors at the triple point during the peritectic reaction [17]

1.3 Peritectic Transformation

After γ covers the surface of δ and separates it from the liquid, the γ-layer begins to thicken and grows simultaneously into δ and into the liquid. This type of growth is referred to as the peritectic transformation (Kerr *et al.* [12]). Peritectic transformations were thought to be controlled by diffusion of solute atoms from the liquid towards δ through the γ-layer. Fredriksson and Nylén [23] derived an expression for the growth rate of γ during the peritectic transformation:

$$\frac{\partial d_{\gamma}}{\partial t} = \frac{\partial d_{\gamma/\delta}}{\partial t} + \frac{\partial d_{L/\gamma}}{\partial t} = \frac{D^{\gamma}}{d_{\gamma}} \cdot \left(\frac{x^{\gamma/L} - x^{\gamma/\delta}}{x^{\gamma/\delta} - x^{\delta/\gamma}} \right) + \frac{D^{\gamma}}{d_{\gamma}} \cdot \left(\frac{x^{\gamma/L} - x^{\gamma/\delta}}{x^{L/\gamma} - x^{\gamma/L}} \right) \tag{1.6}$$

where d_{γ} is the γ-layer thickness, $\partial d_{\gamma/\delta} / \partial t$ and $\partial d_{L/\gamma} / \partial t$ are the growth rates of the γ-layer towards δ and the liquid respectively. D^{γ} is the diffusion coefficient of solute atoms in γ. The terms in parentheses in Eq.1.6 are strongly dependent on the shape of the phase diagram. In the Fe-C binary system, $(x^{\gamma/L} - x^{\gamma/\delta})/(x^{\gamma/\delta} - x^{\delta/\gamma})$ increases rapidly as the undercooling below T_p increases, resulting in higher growth rates. Nassar *et al.* [17] calculated numerically from Eq.1.6, the rate of thickening of γ during the peritectic transformation in the Fe-C system. In order to compare the calculation values with the growth rates observed by Shibata *et al.* [1] during directional solidification experiments on Fe-0.42wt%C, the undercooling was chosen to be 5 °C

and the cooling rate to be $\partial T/\partial t$ = 1 °C/min. The calculated growth rate is in good agreement with the observed growth rates as seen in Fig.1.9, indicating diffusion-controlled growth. Lee *et al.* [24] used a phase field model to study the peritectic transition; their modeling domain consisted of a one-dimensional diffusion couple, both isothermal and with continuous cooling, and a two-dimensional model of the peritectic reaction, taking into account diffusion in all phases. A finding common to all these studies is that during the peritectic transformation, the growth of the δ/γ interface proceeds at a much higher rate than that of the liquid/γ interface.

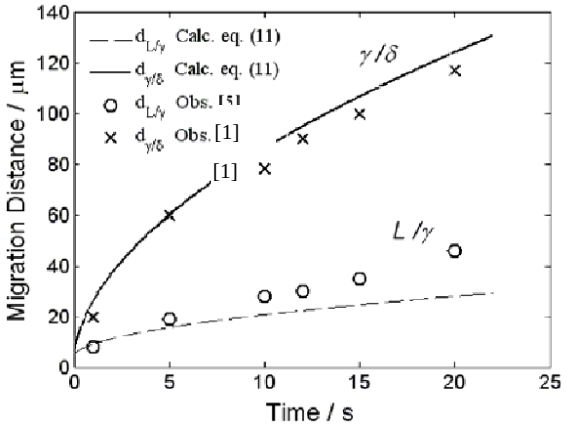

Fig.1.9 Calculated migration distances compared with migration distances observed on Fe-0.42wt%C (The initial γ thickness was assumed to be 10 μm and the diffusion coefficient of carbon in γ is estimated to be in the order of 10^{-9} m^2/s) [17]

The effect of cooling rate on the kinetics of peritectic transformation of 0.18 wt%C steel was analyzed by Phelan *et al.* [14] using HTLSCM and phase field modelling. The predicted interface velocities for a cooling rate of 10 °C/min are shown in Fig.1.10 (a) and the velocities for the solid/solid interface were lower than that of the liquid/solid interface. Judging from the shape of the phase diagram in the Fe-C system, the small compositional gap across the solid/solid phase boundaries, compared to the gap across the liquid/solid phase boundary, results in the solid/solid interface propagating at a higher rate than the liquid/solid interface and equivalent transformation behaviour would therefore be expected. The rationale for this statement is that less solute diffusion is required for the δ-to-γ transformation than for the L to γ transformation and therefore, it is easier for the solid/solid interface to propagate.

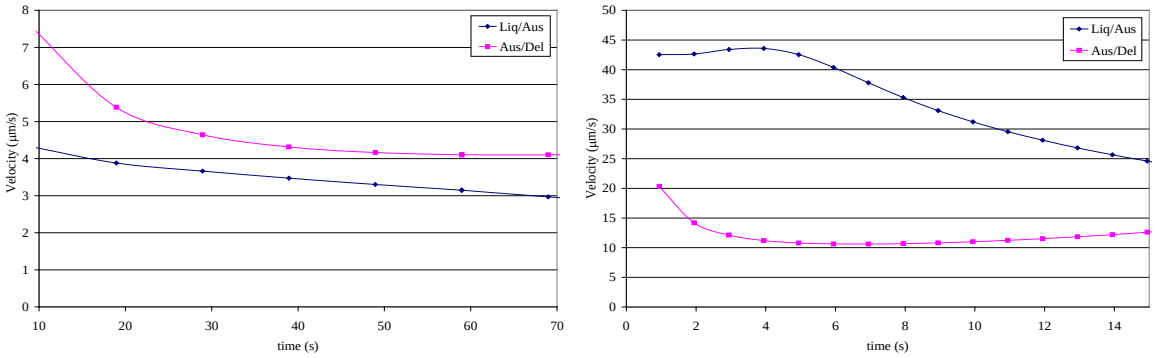

(a) cooling rate = 10 °C/min (b) cooling rate = 100 °C/min

Fig.1.10 Simulated interface velocities of the peritectic transformation in an Fe-0.18wt%C alloy [14]

An increase in the cooling rate is expected, quite naturally, to result in an increase in the transformation kinetics as shown in Fig.1.10 (b). The most interesting feature is that the liquid/γ interface has a higher growth velocity than the δ/γ interface in contrast to the calculations at lower cooling rates. These simulations are in agreement with the *in-situ* observation made in their study. In order to explain the experimentally observed interface velocity inversion, they assessed the solute profiles that develop as a function of cooling rate. In Fig.1.11, solute profiles are presented for two cooling rates, 10 °C/min ((a) and (c)) and 100 °C/min ((b) and (d)). Graphs (a) and (b) are taken at the time of nucleation of γ-austenite, and graphs (c) and (d) are taken when the peritectic reaction is complete and growth is by the peritectic transformation, and hence, a substantial volume of γ-austenite separates the liquid and δ-ferrite phases.

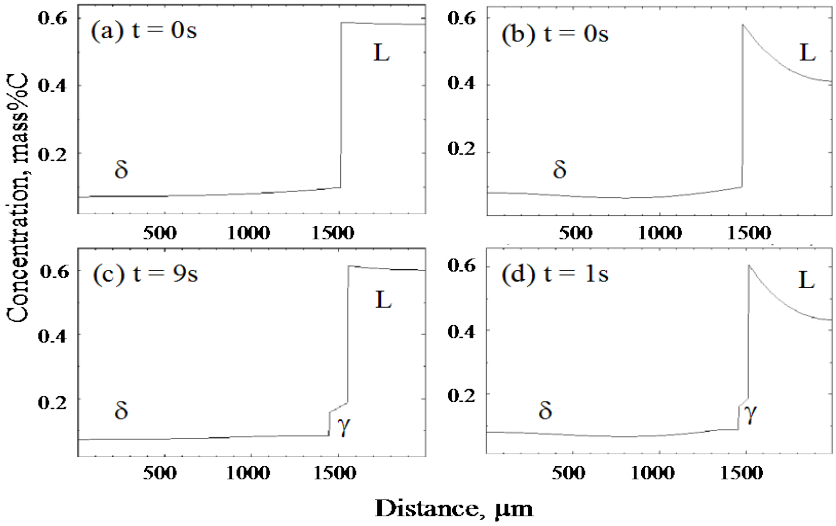

Fig.1.11 Comparison of simulation solute profiles for cooling rates of (a) and (c) 10 °C/min and (b) and (d) 100 °C/min, in an Fe-0.18wt%C alloy, under a temperature gradient G = 200 °C/cm; t = 0 refers to the initiation of the peritectic phase transition [14]

The solute profile in the liquid phase that develops under a cooling rate of 10 °C/min is flatter than the profile that develops at a cooling rate of 100 °C/min. This can be explained by the fact that while the concentration limits across the liquid/γ interface are fixed by the phase diagram, the time available for the diffusion of solute into the liquid is not. Therefore, at a low cooling rate, there is more time for diffusion of solute, leading to a more uniform carbon distribution in the liquid phase, compared to the higher cooling rate. The flux of carbon from the γ-austenite to the liquid phase is determined by the diffusion coefficient of the carbon in the liquid and the concentration gradient in the liquid, per Fick's Law. If the development of solute gradients is ignored in a modelling exercise, as is the case under the assumption of complete mixing in the liquid phase in other previous studies, this increased flux of carbon into the liquid, and hence the subsequent increase in the liquid/γ growth rate, is not taken into account. Hence, the phase-field model predictions, verified by experimental observation that at lower cooling rates the δ/γ interface grows faster, while at higher cooling rates, the liquid/γ interface grows faster, are attributed to an enhanced solute flux into the liquid at higher cooling rates due to the presence of a steep solute concentration gradient in the liquid.

In some experiments, the velocity of δ/γ interface was extremely high. The growth rate of γ into delta-ferrite at a cooling rate of 10 °C/min are several millimetres per second [17] and is akin to a massive-type of transformation. Shibata *et al*. [1] also observed growth rates of the same magnitude in directional solidification experiments in an Fe-0.14wt%C alloy and in some experiments in an Fe-0.42wt%C alloy. These very high growth rates cannot be explained by diffusion and this interesting massive-type of transformation will be discussed in more detail in the next section.

1.4 Massive Transformation

Since growth involve thermally activated jumping of atoms across the interface between two phases, a massive transformation can be defined as a diffusionless civilian transformation and it is characterized by its own C shape curve on TTT or CCT diagrams as shown in Fig.1.12 [25]. The migration of the interfaces is very similar to the migration of grain boundaries during recrystallization of single-phase material. However, in the case of the massive transformation the driving force is orders of magnitude greater than for recrystallization, which explains why the transformation is so rapid.

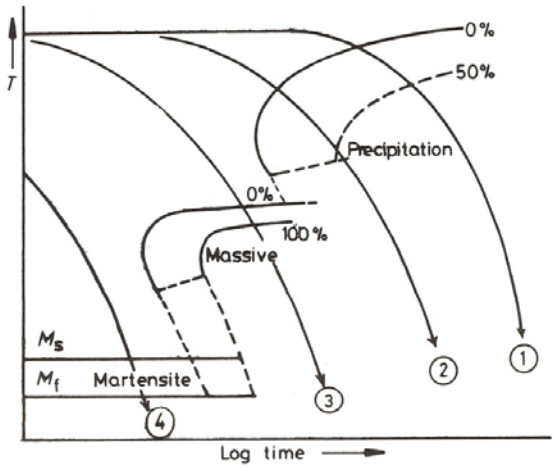

Fig.1.12 A possible CCT diagram for systems showing a massive transformation. Slow cooling ① produces equiaxed morphology. Widmanstatten morphologies result from faster cooing ②. Moderately rapid quenching ③ produces the massive transformation, while the highest quench rate ④ leads to a martensitic transformation [25]

The massive transformation is often described as a kind of composition-invariant nucleation-and growth formation of a solid phase from another solid phase [26]. If the parent phase by cooling is brought into the one-phase field of the new phase, no long-range diffusion will be required and the transformation could turn composition-invariant. The thermodynamic conditions for a composition-invariant transformation may even be fulfilled when the parent phase is cooled below T_0 where T_0 is defined as the temperature at which the two phases have the same Gibbs free energy. This will not have a strong effect on nucleation, which will still be concentrated to the grain boundaries, but the growth rate will increase dramatically. It would be expected that the resulting morphology would develop into larger, more blocky shapes because their growth would not be retarded by the build-up of a composition gradient in front of the migrating interface.

The γ-austenite to α-ferrite transformation in iron and its alloys can also occur massively provided the γ phase is cooled rapidly enough to avoid transformation near equilibrium, but slow enough to avoid the formation of martensite. The effect of cooling rate on the temperature at which transformation starts in pure iron is shown in Fig.1.13.

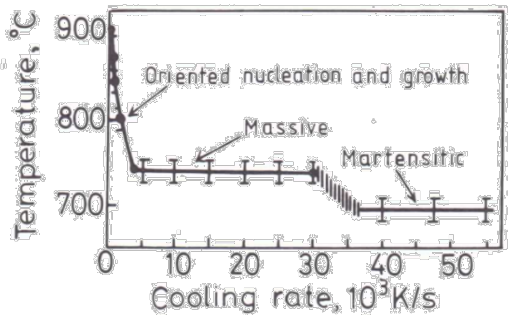

Fig.1.13 The effect of cooling rate on the transformation temperature of pure iron [25]

Aaronson [27] referred to massive transformation as a mechanism of migration of the interface described as ‘atomic jump across the interface’ or ‘nearly random jumping of individual atoms’. An atom on the parent grain side only needs to adjust its position slightly in order to be part of the transition zone. That should cause simultaneous adjustments of the neighbouring atoms, and adjustments could spread all through the transition zone and eventually make an atom on the other side adjust its position slightly to fit into the growing grain. Such a process could hardly be regarded as diffusional. With this possibility in mind, it may not seem wise to include the term diffusional in a general definition of the massive transformation.

Yasuda *et al.* [28] showed in time-resolved in situ observations using synchrotron radiation X-rays that γ nucleation did not occur at the peritectic temperature. The δ phase was easily undercooled in the single γ phase region and then the massive transformation from the δ phase to the γ phase occurred. They proposed that the selection of the massive transformation is related to difficulties of γ nucleation and explained the observation with regard to the interfacial energy between phases. The interfacial energy between the δ and γ phase, between the L and δ phases and between the L and γ phases are 0.7 J/m^2, 0.2 J/m^2 and 0.3 J/m^2 respectively. The relatively high interfacial energy between the δ and γ phases implied that the δ phase was not a preferred γ nucleation site.

Yasuda *et al.* [28] established the solidification sequence in Fe-0.18 wt%C alloys on the basis of their observations using synchrotron radiation X-rays. Fig.1.14 shows a schematic illustration of a massive transformation from a mould (bottom). First, the peritectic solidification, in which the γ phase is produced in the mushy region of L + δ, is considered. When the temperature of the δ phase in contact with the mould reaches a temperature slightly below the peritectic temperature, the γ phase nucleates and follows δ dendrite growth. The volume change due to the δ/γ transformation can be compensated for by melt flow from the top to the bottom of the dendrites. Tensile stresses may be induced in the surface region because melt flow does not completely compensate for the volume change. Next, the massive transformation, which was observed in situ, is considered. The γ phase does not nucleate when the temperature of the δ phase reaches the peritectic temperature ($t = t_2$). The γ phase only nucleates at $t = t_3$ and rapidly grows toward the tips of the δ dendrites. When the δ/γ interface reaches the isothermal plane of the peritectic temperature ($t = t_4$), the peritectic solidification begins. Since the massive transformation ($t_3 < t < t_4$) occurs in the solid δ phase, the volume change caused by the δ/γ transformation is not compensated for by melt flow in the mushy region. A larger strain is therefore induced in the surface region of the solidifying shell.

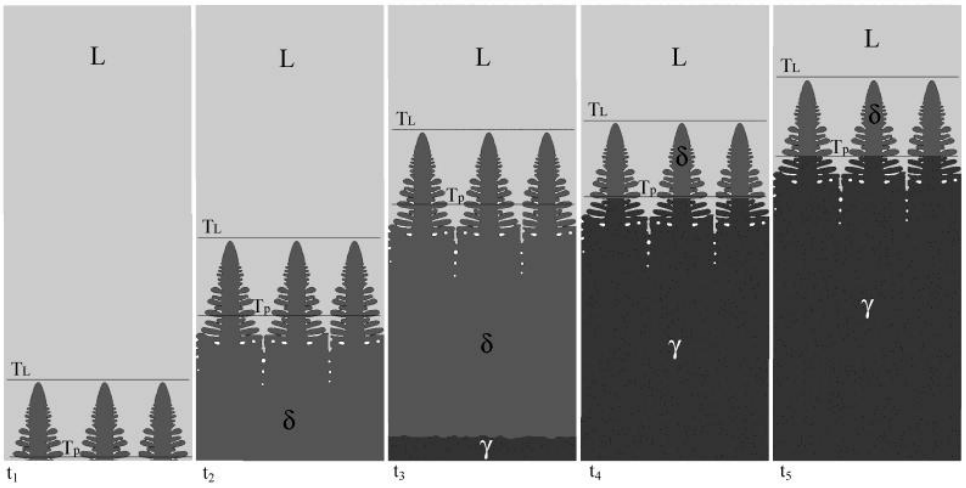

Fig.1.14 Development of solidifying shell and the massive transformation (Fe-0.18wt%C). T_L and T_P are the liquidus temperature (δ) and the peritectic temperature, respectively [28]

Griesser *et al.* [29] in their recent study found a strong correlation between the magnitude of diffusion fields developed at the liquid/solid interface prior to γ nucleation and the resulting constrained nucleation of γ phase. In their experiments, they showed that the higher the fraction of primary solidified δ, the higher the solute concentration gradients in δ due to partitioning and insufficient back-diffusion of solute elements during solidification. These concentration gradients result in the diffusion of carbon from the liquid, through the liquid/δ interface (γ nucleation site) into δ and the higher the magnitude of this flux, the higher the undercooling before nucleation initiates. An increase in the fraction of primary solidified δ with the concomitant increase in magnitude of the carbon diffusion flux, leads to increased nucleation undercooling (ΔT_P), which in turn, leads to an increased rate of the subsequent peritectic phase transition (δ to γ) due to the higher thermodynamic driving force for the formation of γ below the equilibrium peritectic temperature. They also argued and provided convincing experimental proof that constrained nucleation of γ does neither result from the amount of primary phase present, nor from the pertaining concentration gradient, but is the result of the diffusional solute flux through the γ nuclei, thus increasing the Gibbs free energy barrier to nucleation. When nucleation is sufficiently constrained by diffusional suppression, the alloy can be undercooled to a temperature below that where the parent and product phases have the same free energy at the same composition (allotropic phase boundary) and a massive transformation can then occur.

The occurrence of high nucleation undercooling in peritectic systems of steel and the often accompanied massive transformation of δ to γ has frequently been reported [1, 11, 22, 28, 30, 31], but a satisfactory explanation for these nucleation constrains has been lacking until these recent findings of Griesser *et al.* [29] have for intents and purposes resolved the issue.

1.5 Significance of the Peritectic Transition in Industrial Practice

It is generally accepted that the surface quality of continuously cast steel slabs is a strong function of events occurring during the early stages of solidification in the meniscus region of the mould. Brimacombe and Sorimachi [32] provided a comprehensive classification of the origins of cracks in the continuous caster and McPherson and McLean [2] followed by Wolf [3], summarized much of the work relating to transverse cracking. Peritectic steels are the most difficult to produce with respect to surface quality [6-9], most probably because of the volume change that accompanies the delta to gamma phase transition [9, 10]. Ludlow *et al.* [6], using a technique introduced by Hiebler, Bernhard and Xia [9, 10] confirmed that the maximum crack susceptibility is encountered between 0.10wt% and 0.14wt% carbon equivalent.

Surface cracking of continuously-cast steel slabs is a particularly serious problem and these surface cracks are still present after hot rolling. If the cracks are not too severe, it is possible to scarf the surface by conventional processes, but this is an expensive operation. In thin-slab casting and direct rolling processes, because scarfing becomes impossible, if the cracks are often too deep, the slab has to be scrapped. The impact of surface cracks is therefore more severe in thin-slab continuous casting compared to conventional slab casting and the problems are furthermore exacerbated at high casting speeds, such as in the newly developed continuous cast-rolling processes.

It is well known that the peritectic phase transition occurs in the meniscus region of the mould and because many advanced steel grades are designed to be in peritectic composition range, it is important to consider the impact of this phase transition on the integrity of slabs. It is widely accepted that the volume contraction associated with peritectic transition results in the detachment of the solidified shell from the mould and this incurs a decrease in heat flux leading to hot spots, which significantly increases the risk of breakouts or surface cracking. These risks are higher in the thin-slab casting process than in conventional casting process and the risks seem to increase as the casting speed increases as indicated before. The causes of slab quality problems frequently leads to operational failures such as breakouts and unfortunately, measures taken to eliminate quality problems often lead to operational instabilities. So, operational stability and slab surface quality are largely determined by the events occurring in the meniscus region of the continuous casting mould and hence, detailed knowledge of the events occurring in the early stages of solidification is of the essence.

Chapter 2. Experiments of Peritectic Solidification using High-Temperature Laser-Scanning Confocal Microscopy

2.1 Purpose of Study

Whereas new insights have been gained through careful experimentation and convincing models have been developed, important questions about the mechanism and kinetics of the peritectic phase transition remain unanswered. There is still considerable disagreement as to the mechanism responsible for the very high rates at which the γ-austenite layer progresses along the pre-existing liquid/δ-ferrite interface; the liquid to γ-austenite phase transformation is not fully understood and the very high rates of the δ-ferrite to γ-austenite phase transformation sometimes encountered in hypo-peritectic Fe-C alloys, have not been satisfactorily explained. In an attempt to overcome some of the experimental difficulties encountered by Shibata *et al.* [1], a new experimental technique was developed and employed by Reid *et al.* referred as concentric solidification [33], in order to improve *in-situ* observations of solidification and high temperature phase transformations in a HTLSCM. This technique was employed in one part of the present study with the following objectives.

- To gain fundamental understanding of the solidification behaviour of selected peritectic grade steels
- To contribute to a better understanding of the root cause of surface defects, which occur as a result of uneven solidification under high-speed continuous casting conditions
- To clarify the effect of cooling rate on the kinetics of the peritectic transitions in the selected steel grades
- To relate the fundamental studies to industrial practice and to identify potential countermeasures to avoid the surface defects originating from casting steels of near-peritectic composition

2.2 Experiments

2.2.1 Steel Types Investigated

Tab.2.1 shows the composition of the steels that have been studied in the present investigation. The steel grades were selected from considerations of industrial importance as well as research interest. Steel C and G, which are used for dual phase steel applications contain higher manganese contents and are designed to avoid hypo-peritectic range. The composition of steel E, which is used for shipbuilding material was designed for having higher strength and toughness through TMCP processing without losing weldability. Steel A and G were prepared in a laboratory vacuum induction furnace and supplied by POSCO. The others were taken from slabs produced in Gwangyang Works, POSCO. They were cut from 5mm below the slab surface in order to avoid contamination from the surface.

Tab.2.1 Specimen composition analysis (in wt%)

Steel	Description	C	Mn	Si	Al	Ti	N	Nb
A	Pure Fe-C	0.050	< 0.01	< 0.005	0.016	<0.003	0.0015	0
B	Plain Carbon	0.051	0.305	0.016	0.029	0	0.0109	0
C	Dual Phase	0.051	1.507	0.512	0.032	0.002	0.0086	0
D	SAE1010	0.101	0.484	0.01	0.022	0	0.0049	0
E	TMCP	0.08	1.599	0.278	0.025	0.012	0.0029	0.018
F	Medium C	0.182	0.352	0.03	0.023	0.002	0.0094	0
G	Dual Phase	0.085	2.820	1.013	0.027	0.0158	0.0159	0.020
H	High Carbon	0.439	0.693	0.191	0.018	0.001	0.0071	0

2.2.2 Thermodynamic Calculation

In order to understand the high temperature properties of the specimens, equilibrium Fe-C phase diagrams were calculated by Thermo-Calc software [34] (with the thermodynamic database, TCFE4 [35]). Fig.2.1 shows the results of these calculations with and the pertinent chemical compositions of each steel in parenthesis in mass percent. Other minor elements of the specimens were neglected because they have little effect on the shape of phase diagram. From this calculation, specimens were classified into 3 categories according to carbon content: non-peritectic low-carbon steel, hypo-peritectic steel and hypo-peritectic steel.

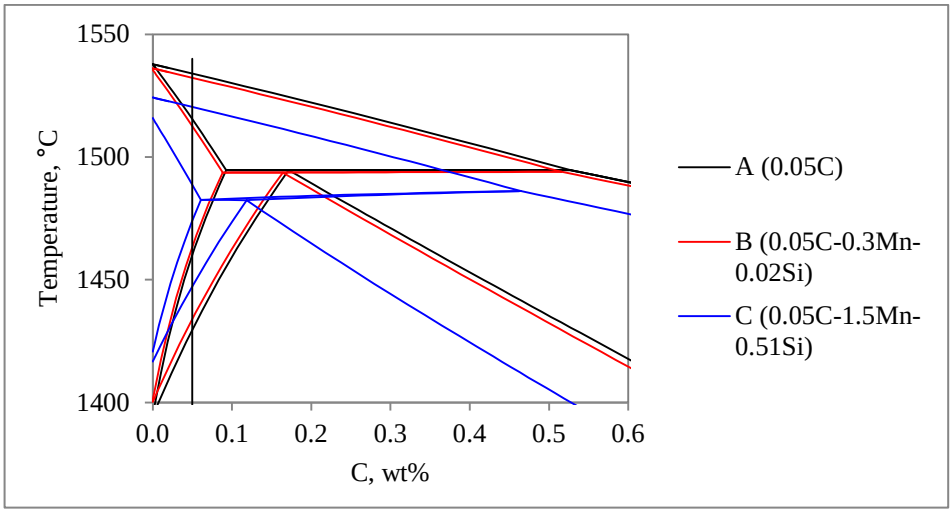

(a) Low carbon (non-peritectic) ; Steel A, B and C

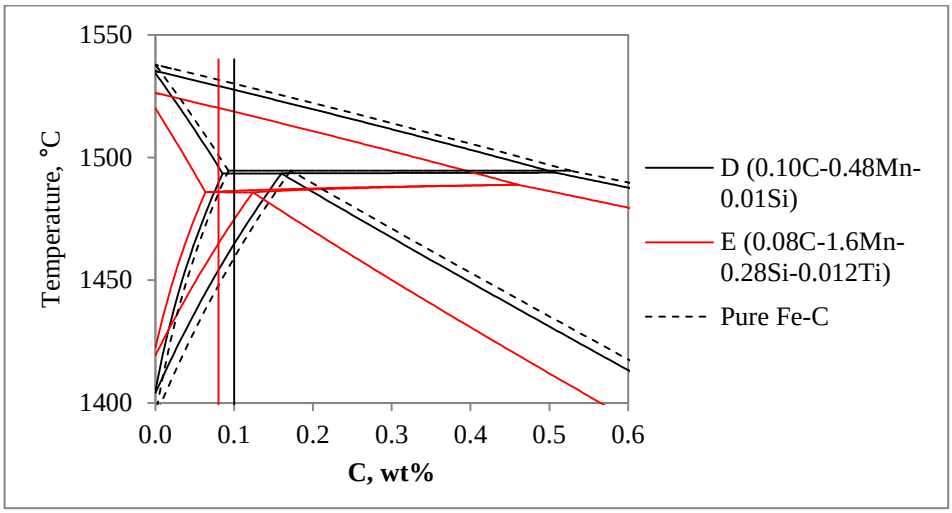

(b) Hypo-peritectic : Steel D and E

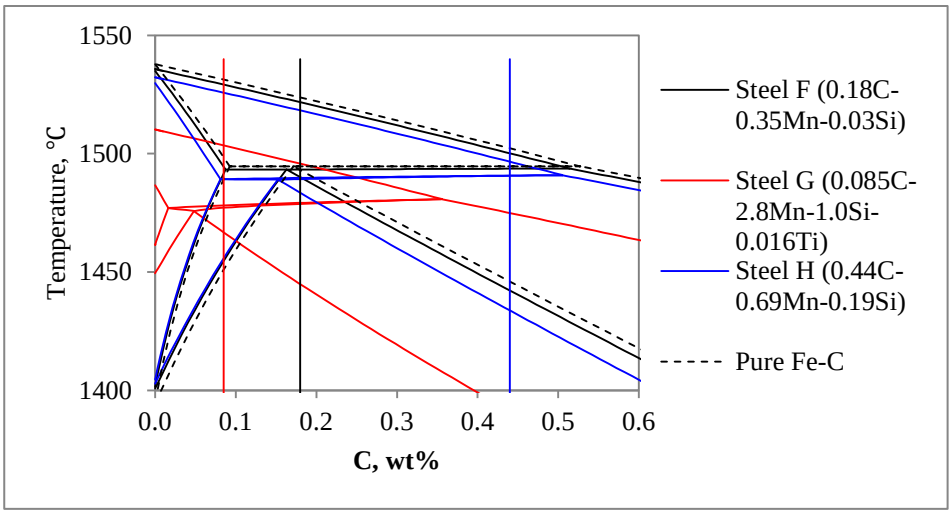

(c) Hyper-peritectic : Steel F, G and H

Fig.2.1 Equilibrium Fe-C phase diagrams (vertical line indicates carbon content of each steel)

2.2.3 Experimental Procedure

A recently developed, new experimental technique enables high-resolution *in-situ* observation of phase transitions at elevated temperatures. This so-called HTLSCM was developed by Emi and his colleagues and has been used to study a variety of phenomena including solidification, δ-ferrite to γ-austenite transformations, and γ-austenite decomposition [1, 36-38]. Shibata *et al.* [1] used this technique to provide the first reported *in-situ* observations of the peritectic reaction and subsequent phase transformations.

Fig.2.2 and Fig.2.3 show a picture of HTLSCM and a schematic diagram of the infrared furnace of the HTLSCM with a sample holder. Samples are placed in a gold-plated ellipsoidal infrared heating furnace in an ultra-high-purity inert atmosphere. A 1.5 kW-halogen lamp located at one focal point of the cavity heats by radiation the specimen located at the other focal point. A quartz plate separates the specimen and lamp chambers so that the atmosphere of the specimen chamber can be controlled and to prevent oxidation, while the lamp is air cooled. The temperature, measured by thermocouples incorporated in the crucible holder and controlled by pre-programmed pattern, is displayed on a monitor and simultaneously recorded with the image on a computer at a rate of 30 frames per second. Specimens are held in an alumina crucible in a round holder constructed from a polymeric end piece, alumina 2-bore tube with an outer silica support tube and a platinum holder welded to a B-type thermocouple wire. Magnifications up to 1350 times at a resolution of 0.2 μm can be obtained, using a He-Ne laser with a wavelength of 632.8 nm. In the system used, a laser beam 0.5 μm in diameter is reflected and scanned by an acoustic optical deflector in the horizontal direction at a rate of 15.7 kHz and a galvano-mirror in the vertical direction at 60 Hz.

Fig.2.2 Picture of the HTLSCM

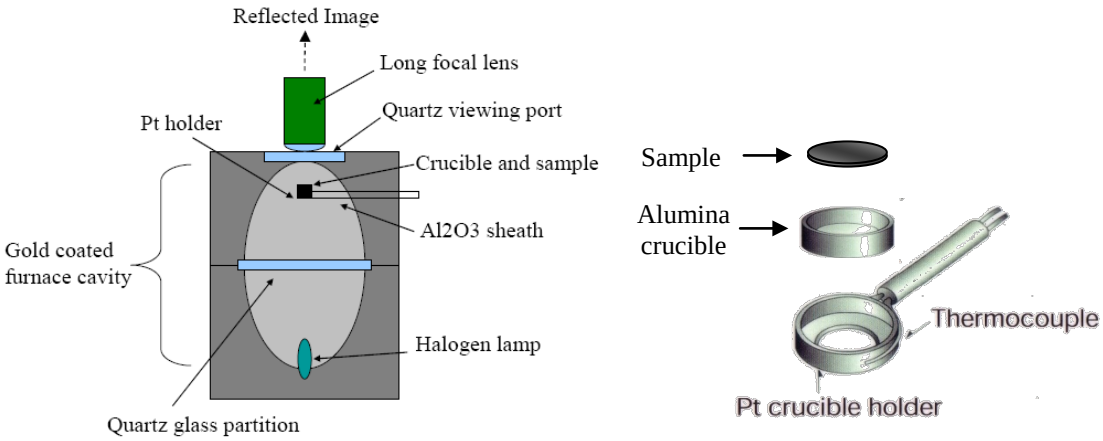

Fig.2.3 Schematic diagram of the infrared furnace of the HTLSCM and a sample holder

Shibata *et al.* [1] found it difficult to control the progress of the peritectic reaction in the specific experimental arrangements they used and their study had been impeded by the inherent difficulty of imposing a temperature gradient on the growth front in the confocal microscope. They also found it difficult to maintain a large area in focus. Although the shallow depth of focus in the confocal system is one of the unique features because sharp images can be obtained, it can unfortunately also be the Achilles heel of the technique. The limitation on the focal depth is of special importance when studying molten metal pools which, due to the high surface tensions typical of these systems, leads to the formation of a pronounced meniscus. In an attempt to overcome these impediments, Reid *et al.* [33] developed a new experimental technique that they refer to as concentric solidification. By employing this concentric solidification (also called melt-pool) technique, *in-situ* observation of solidification and high temperature phase transformations in the HTLSCM has been improved. The experimental arrangement in the concentric solidification technique is shown in Fig.2.4. Because a radial temperature gradient develops in a specimen situated in the microscope, a liquid pool can be generated in the centre of a cylindrical specimen 10mm diameter and about 0.25mmthick while the outer rim remains solid. This arrangement provides an elegant way of studying the progression of solidification as well as the peritectic reaction.

Once the sample is exposed to the melting temperature in the furnace, it begins to melt from the centre toward the edge due to the thermal gradient. In this study, when the liquid pool reaches 6mm in diameter, the temperature is held for 3 minutes in order to stabilize the liquid pool and then the solidification experiment begins by imposing a fixed cooling rate. Cooling rates of 5, 20 and 50 °C/min were employed for varying experimental condition in all steels investigated.

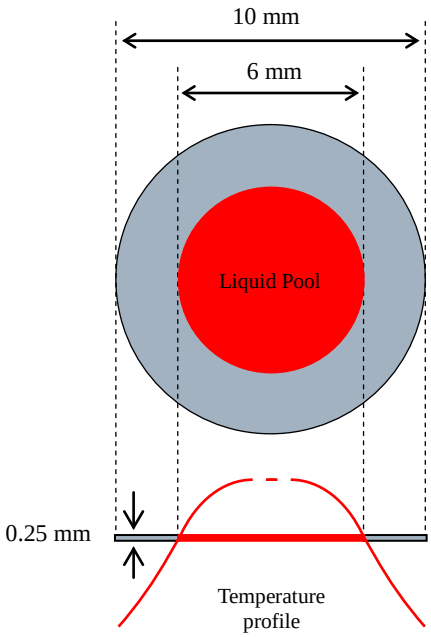

Fig.2.4 Geometry of sample for concentric solidification using HTLSCM

It is important to understand the temperature distribution across the sample. Griesser [18] measured the diameter of the focused radiation from the heat source (focal point diameter) using thermographic paper in the same experimental set up as shown in Fig.2.5. The focal point radius on the same plane with the metallic sample in the crucible was found to be about 1 mm. Additionally Griesser also carried out concentric solidification experiments using a Fe-0.0036C alloy as shown in Fig.2.6. It should be noted that the liquid/solid interface velocity decreases for a liquid pool radius smaller than 1 mm (focal point radius) and this proved the existence of focused radiation in the centre of sample.

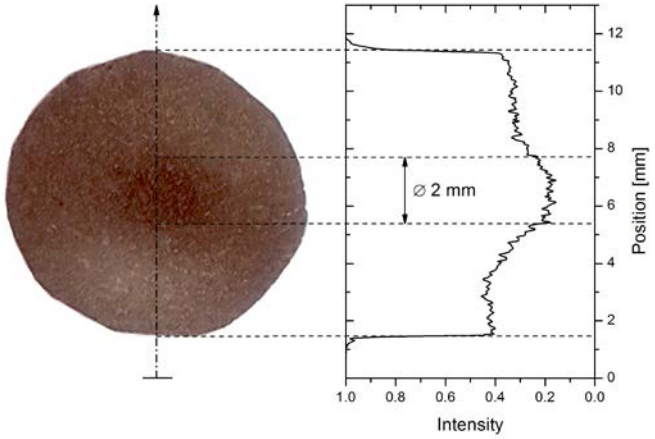

Fig.2.5 Focal point diameter measured on thermographic paper [18]

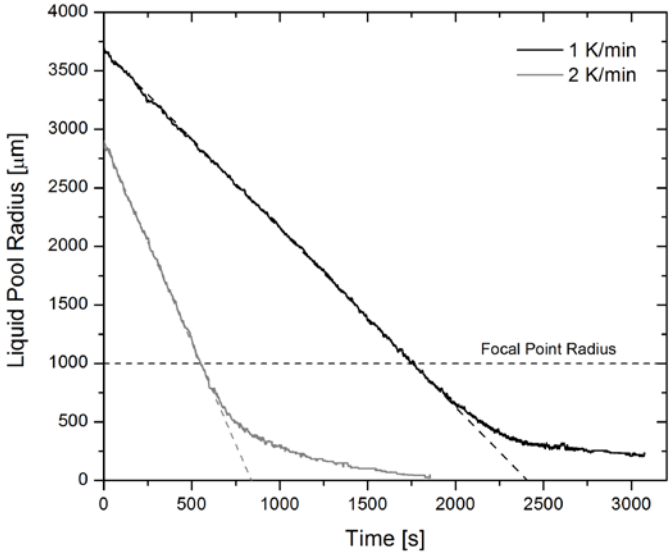

Fig.2.6 Solidification of a Fe-0.0036C alloy at two different cooling rates [18]

From these experimental results, the temperature profile across the sample at the moment of completing final solidification can be derived. This calculation is based only on the step-by-step progression of the liquid/solid interface and the calculated temperature difference between the current interface and the position of the previous interface at given cooling rate and distance moved. Fig.2.7 shows the calculated temperature profile and thermal gradient across the sample at a cooling rate of 2 °C/min. It indicates that the thermal gradient in the main body of the sample is 9.8 °C/mm while the thermal gradient near the centre of the sample is 139.7 °C/mm due to the focused radiation in the crucible.

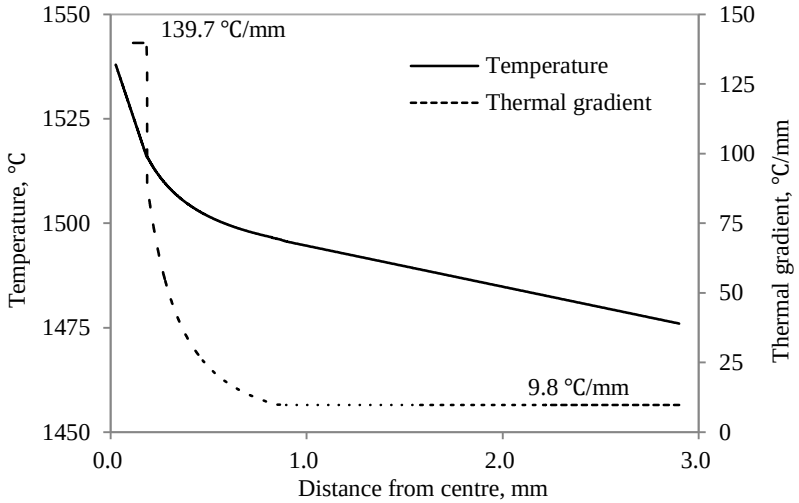

Fig.2.7 Temperature profile and thermal gradient across the Fe-0.0036C alloy at a cooling rate of 2 °C/min at the moment of completing final solidification. Calculated using Fig.2.6

In their earlier study, Phelan *et al.* [19] measured the temperature distribution using pure metallic iron particles distributed across an empty alumina crucible as shown in Fig.2.8 in the same experimental set up. The problem with this analysis is that the thermal conductivity of a metallic specimen is not taken into account because the pure iron particles were isolated from each other. Therefore, it is more reasonable to regard the profile measured by Phelan as the imposed thermal profile on the sample from heat source rather than the temperature distribution in the disk sample itself. It is instructive to compare the temperature distribution calculated from Griesser's result to the measurements of Phelan as shown in Fig.2.9. Although the existence of focal point is not clear in Phelan's measurement, it is evident that in the absence of thermal conduction, the slope becomes much steeper compared to the calculation from Griesser's observation. It is therefore concluded that the steep thermal gradient shown in the imposed thermal profile results in a much lower thermal gradient in the actual metallic sample because of the radial conduction of heat in the radial direction.

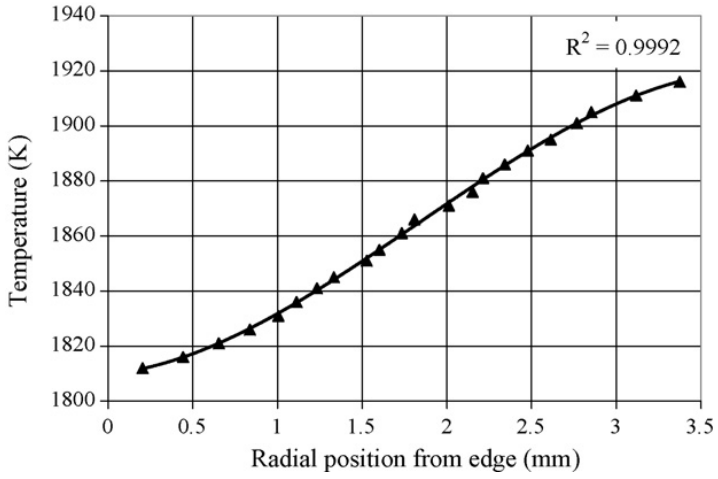

Fig.2.8 Temperature distribution across a 10mm crucible [19]

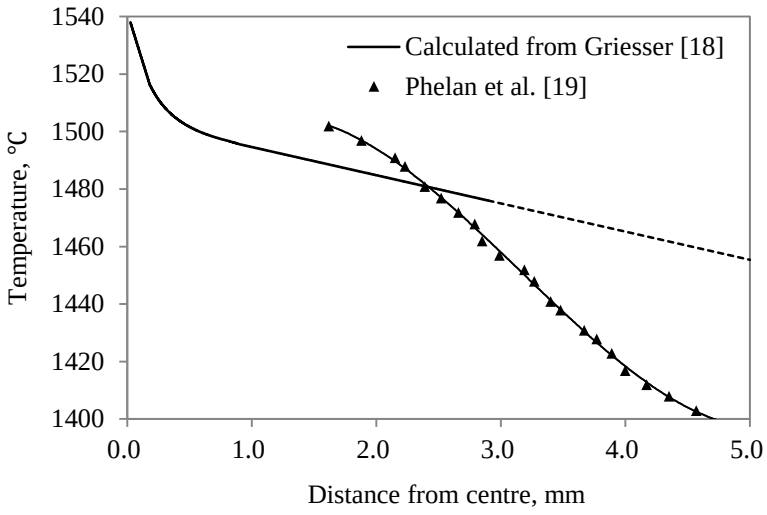

Fig.2.9 Comparison of temperature distribution measured by Phelan [19] and Calculation from Griesser's observation [18]

2.3 Results

2.3.1 Progression of the Liquid/δ-ferrite Interface

During the solidification of steel that will undergo the peritectic reaction, δ-ferrite forms first. A detailed understanding of the progression of the liquid/δ-ferrite interface is fundamentally important since it is the rate at which this initial solidification front progresses that will determine the thickness of the solidifying shell in the meniscus region of a continuous caster. It is also essential to better understand the morphology of the development of this liquid/δ-ferrite interface during these initial stages of solidification. For example, it is important to know if the interface progresses as a planar interface or whether dendrites form and moreover, if the morphology of the progressing interface is a function of steel composition and cooling rate. By using the concentric solidification technique in the HTLSCM outlined earlier, the progression of the liquid/δ-ferrite interface can be tracked. The experimental arrangement when using the concentric solidification was shown in Fig.2.4 and the image is recorded at a rate of 30 frames per second. Hence, the movement of an interface observed can be analysed frame by frame. Typically, a melt-pool 6 mm diameter is established before cooling is activated.

Extracts from videos of the *in-situ* observations in the HTLSCM are shown in Fig.2.10 for all the steels under investigation. The progression of the liquid/δ-ferrite interface is shown as a function of time at three different cooling rates. The interface and pool morphologies are shown at a time when essentially all the δ-ferrite has formed and hence, just before the occurrence of the δ→γ transformation. In the case of Steel H (0.44C-0.69Mn-0.19Si) no δ→γ transformation was observed. In all cases an increase in the cooling rate resulted in an increased tendency towards instability of the liquid/solid interface.

In the case of Steel A (0.05C) and Steel B (0.05C-0.3Mn-0.02Si) with cooling rates of 5 °C/min and 20 °C/min respectively, no δ→γ transformation occurred until the liquid pool disappeared. On the other hand, in the case of Steel A at cooling rate 50 °C/min and the case of Steel C (0.05C-1.5Mn-0.51Si) at cooling rates of 5 °C/min and higher, the δ→γ transformation occurred when the liquid pool was still present.

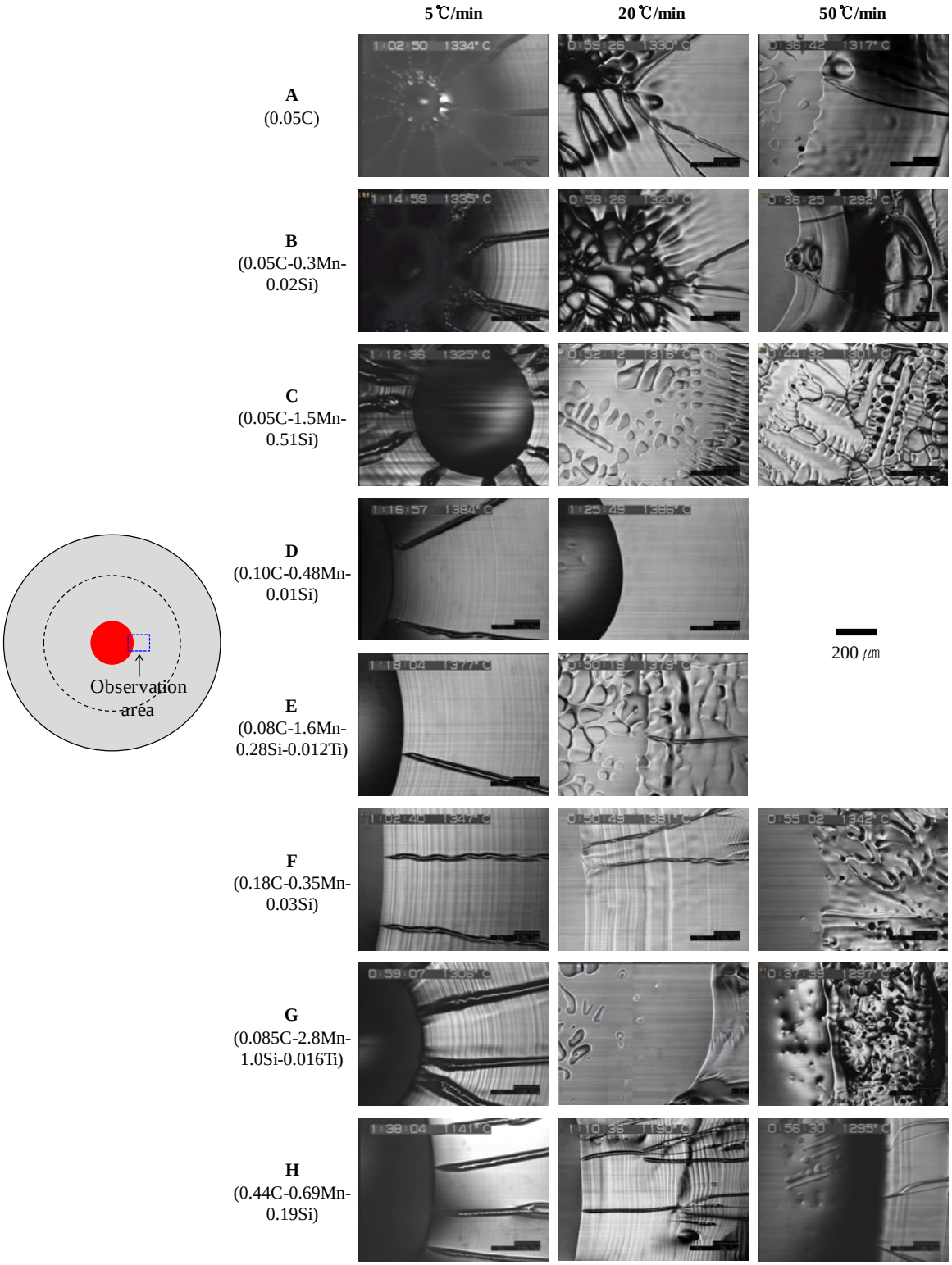

Fig.2.10 Interface & pool morphology before occurrence of the δ→γ transformation

Under most of the experimental conditions at higher cooling rates, the progressing liquid/solid interface becomes unstable with time as a result of the transition from planar to cellular morphology. Also dendrites were formed in the liquid ahead of the growing liquid/solid interface as clearly shown in the case of Steel C (0.05C-1.5Mn-0.51Si), Steel E (0.08C-1.6Mn-0.28Si-0.012Ti) and Steel G (0.085C-2.8Mn-1.0Si-0.016Ti) at cooling rates 20 °C/min and 50 °C/min respectively. This phenomenon is attributed to the decreased temperature gradient near the centre of the melt-pool which is a characteristic of the specific experimental arrangement and it is also might be related to steel composition which determines heat transfer across the sample especially when the liquid enrichment due to segregation is severe. With the emergence of dendrites, the liquid/solid interface became unstable and the interface movement appeared to be slightly retarded but in the end the overall solidification was accelerated by the sudden consumption of the remaining liquid between the dendrites. Steels displaying stable morphology even at higher cooling rates such as Steel D (0.10C-0.48Mn), Steel F (0.18C-0.35Mn) and Steel H (0.44C-0.69Mn) had lower manganese content.

Fig.2.11 shows the position of the liquid/solid interface as a function of time for the steels under consideration. It follows that the steel grade as well as the cooling rate have a marked effect on the rate of solidification. The solidification rate increases in all steel grades as the cooling rate is increased, but it is also evident that the solidification rate becomes lower with an increase of carbon as clearly shown from the comparison among plain carbon steels (B, F, and H) and it becomes lower again with the relatively higher alloyed steels (C, E and G).

In all cases, as the interface progress the velocity was reduced with time. When reaching at the position of 2500 μm, i.e., 500 μm from centre, the progression was suddenly retarded as shown for Steel A, Steel B, and Steel C at 5 °C/min and Steel A and Steel B at 20 °C/min. These results are attributed to the existence of focused radiation of heating in the sample as previously shown in Fig.2.6.

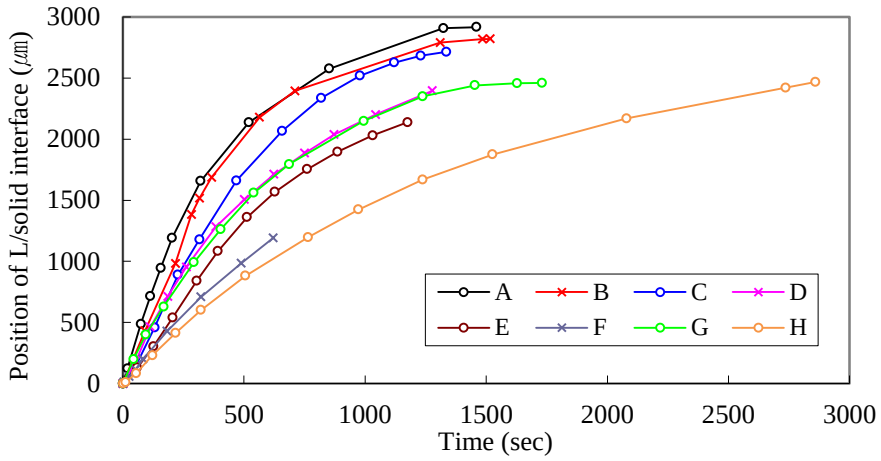

(a) Cooling rate = 5 °C/min

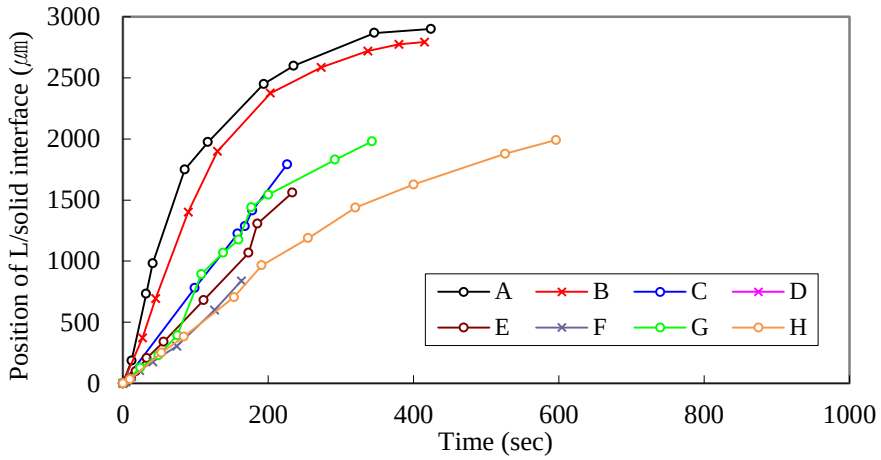

(b) Cooling rate = 20 °C/min

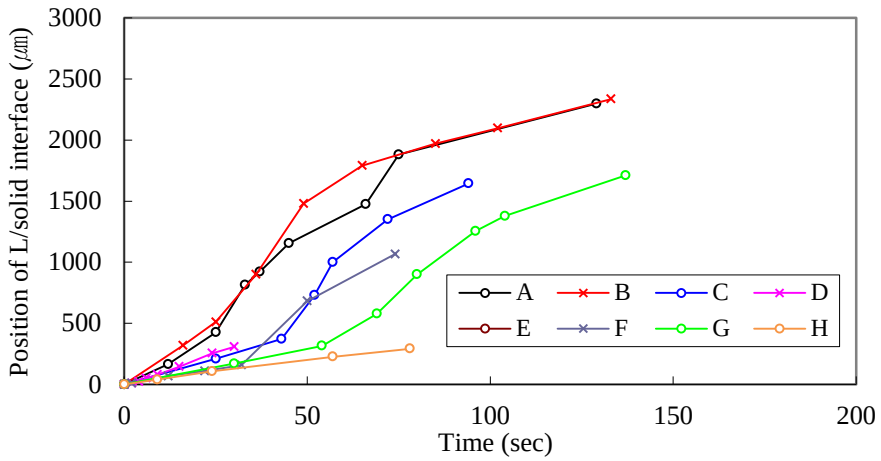

(c) Cooling rate = 50 °C/min

Fig.2.11 Liquid/δ interface movement during cooling from the melt (position '0' means solidification beginning at initial pool radius = 3.0 mm)

2.3.2 Peritectic Reaction

It is now well-established that the peritectic reaction occurs by the growth of a thin γ-austenite layer along the liquid/δ-ferrite interface. Once this film of γ-austenite has formed, γ-austenite grows into the liquid as well as back into the δ-ferrite. This sequence of events is shown in Fig.2.12 for Steel F (0.18C-0.35Mn-0.03Si), confirming the accepted mechanism.

It was not always possible to observe the peritectic reaction *in-situ*, because of both the practical difficulty of obtaining good focus at the liquid/solid interface and the thinner γ-austenite layer at higher reaction velocities. The very shallow depth of focus is one of the unique characteristics of HTLSCM, but it is unfortunately also the Achilles' heel of the technique because if the different phases at the interface are not at the exact same level as is often the case for a liquid/solid interface, both phases cannot be kept in focus. Griesser [18] showed experimentally that a higher reaction velocity resulted in a thinner γ-austenite platelet during the peritectic reaction. For example, for a reaction velocity of 600 μm/s, the corresponding tip radius is well below 1 μm. As a result, for higher reaction velocities, the tip of the γ-austenite platelet could be detected only at high magnification as a small distortion at the liquid/ferrite interface compared to the same position on previous frames. While the relatively low magnification employed in this study is appropriate for studying the overall kinetics of δ→γ transformation, it is difficult to detect the occurrence of the peritectic reaction at low magnification.

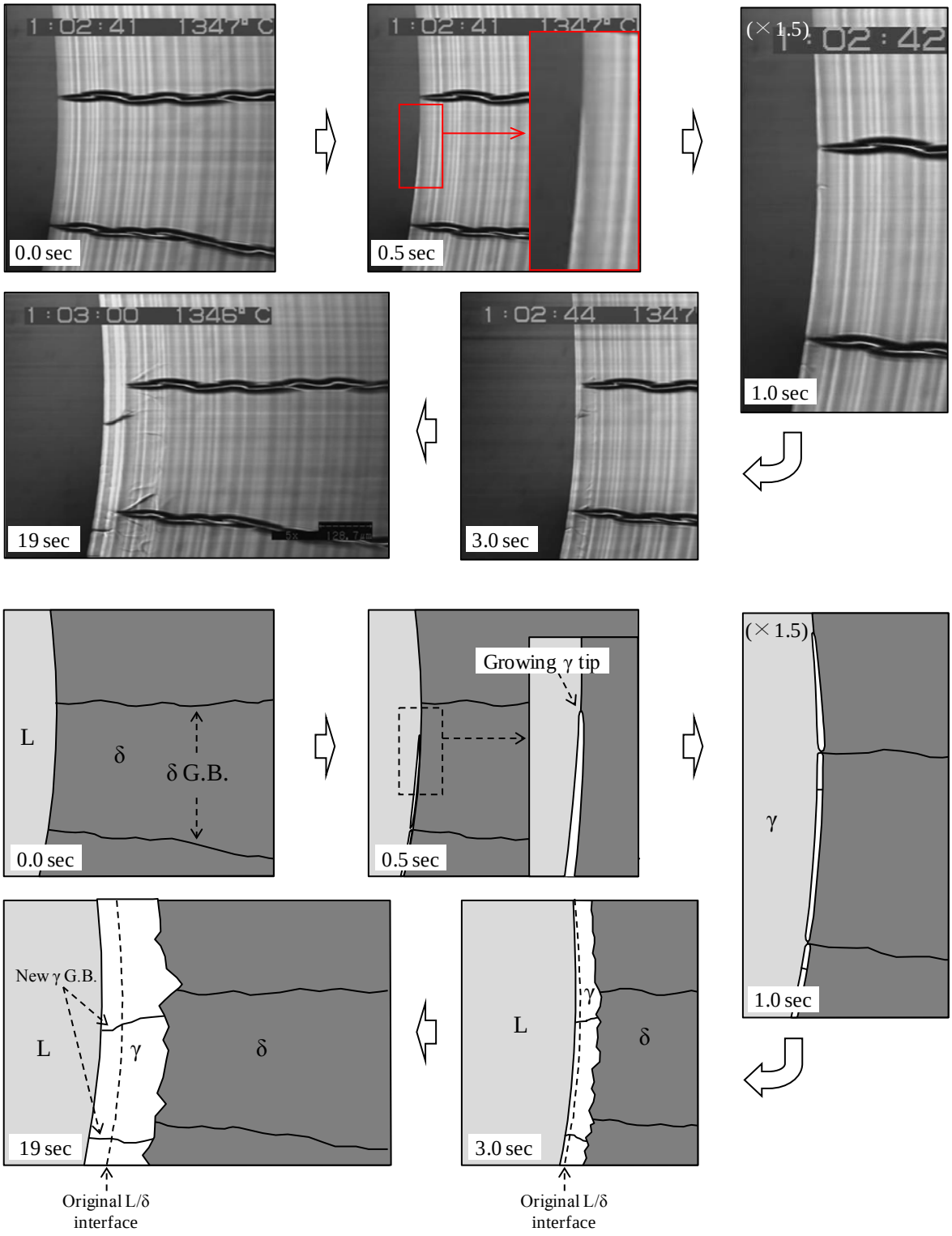

Fig.2.12 The peritectic reaction in Steel F (0.18C-0.35Mn-0.03Si) at a cooling rate of 5 °C/min and at an elapsed time of 0.5 sec indicated in the second video frame. The subsequent progression of the liquid/γ and δ/γ interfaces relative to the original δ/γ interface are also clearly illustrated in the frames marked 3.0 sec and 19 sec, respectively (The temperature readings are those of a control thermocouple and do not indicate the temperature of the specimen)

2.3.3 The L→γ and δ→γ Transformations

Fig.2.13 to Fig.2.18 show several examples of the L→γ and δ→γ and transformations. The morphology of the phase transformation in Steel A (0.05C) at a cooling rate of 5 °C/min is shown in Fig.2.13. The δ→γ transformation occurred following complete solidification of liquid into δ-ferrite. It is evident that the morphology of interface is planar and it takes more than 2.5 seconds for a δ-ferrite grain to transform to γ-austenite in the observed frame. At a rate of 20 °C/min, the same steel is fully transformed within 0.2 seconds also following complete solidification as shown in Fig.2.14. At a rate of 50 °C/min in Steel B (0.05C-0.3Mn-0.02Si), the δ→γ transformation and the L→γ transformation were observed as shown in Fig.2.15. The δ→γ transformation occurred very rapidly within 0.1 seconds. It should be noted that the interface progresses toward the outside of the sample and this observation implies that the γ-austenite nucleated at the liquid/δ-ferrite interface.

In the case of Steel D (0.10C-0.48Mn-0.01Si), the δ→γ transformation was very rapid even at the relatively low cooling rate of 5 °C/min and the transformation was completed within 0.1 seconds as shown in Fig.2.16. In this steel, the L→γ transformation was also observed but the velocity of the liquid/γ interface was much lower than that of δ/γ interface.

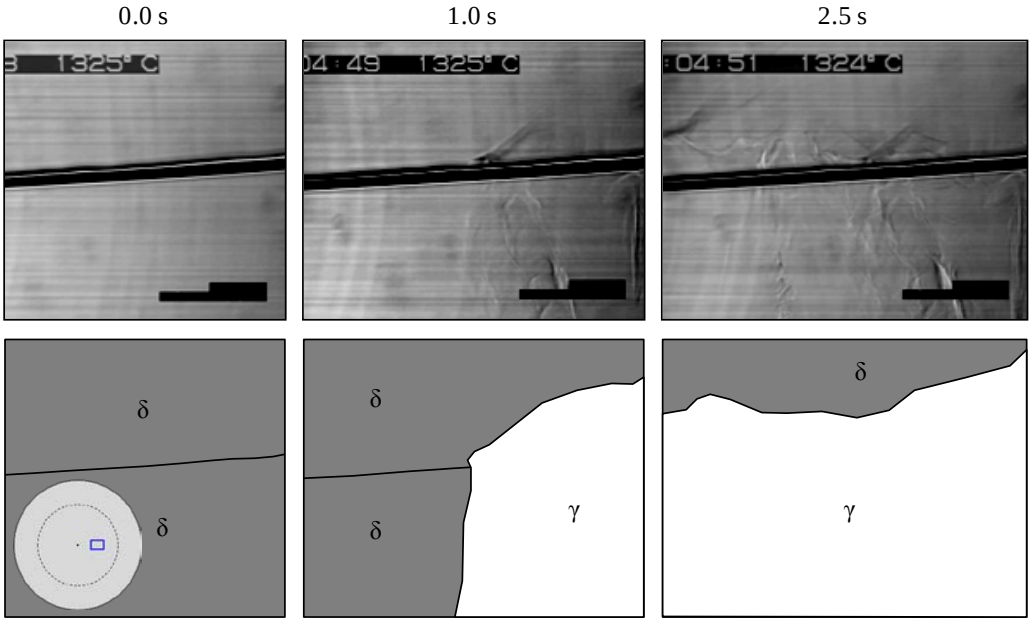

Fig.2.13 δ→γ transformation of Steel A (0.05C) at 5 °C/min

It is interesting to compare the transformations in Steel B at a cooling rate of 50 °C/min with Steel D at a cooling rate of 5 °C/min although the cooling rate was different. There was a big difference in the velocities of liquid/γ interface between Steel B and Steel D, however the δ→γ

transformations in both steels were completed very rapidly at similar velocities. It is also clear that the morphology of δ/γ interface is planar in Steel B while it is acicular in Steel D. The acicular morphology of δ/γ interface in Steel D is confirmed again at an even lower cooling rate of 2 °C/min as shown in Fig.2.17.

In the case of Steel G (0.085C-2.8Mn-1.0Si-0.016Ti), the transformation was completed within just 0.10 seconds at a cooling rate of 20 °C/min in the area under observation as shown in Fig.2.18.

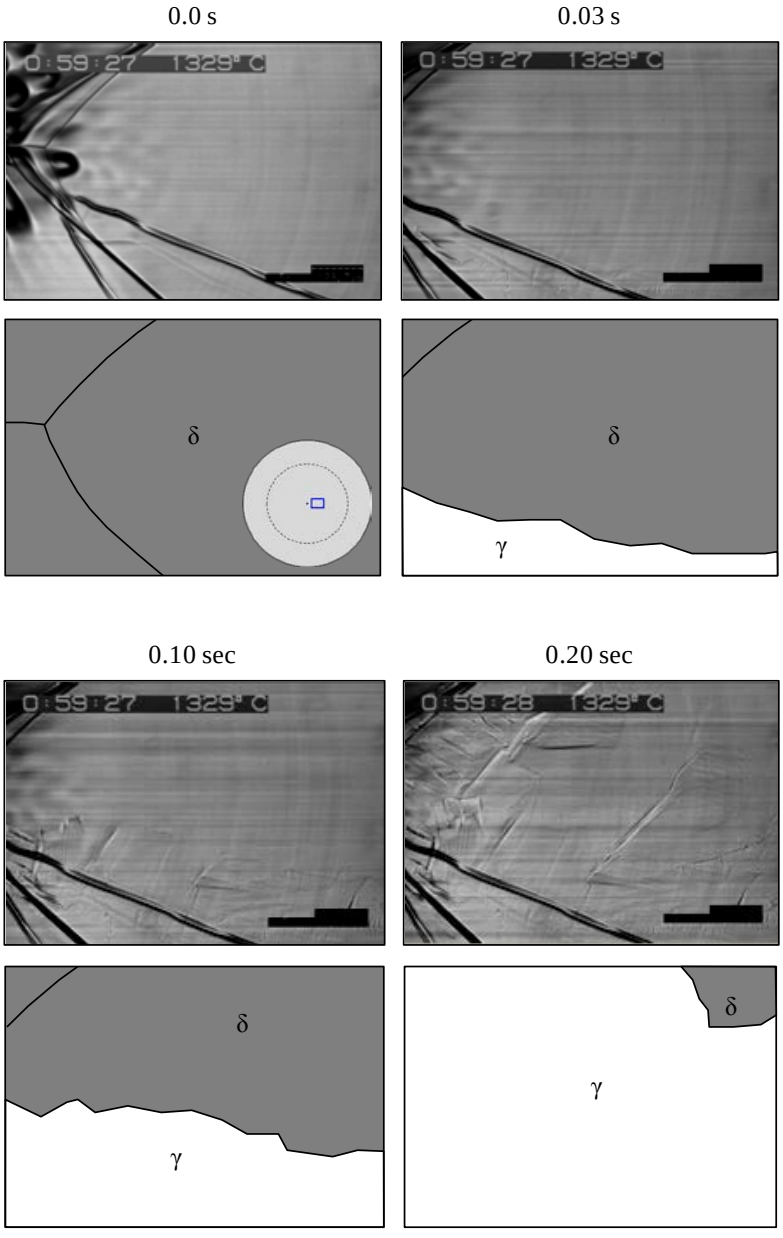

Fig.2.14 δ→γ transformation of Steel A (0.05C) at 20 °C/min

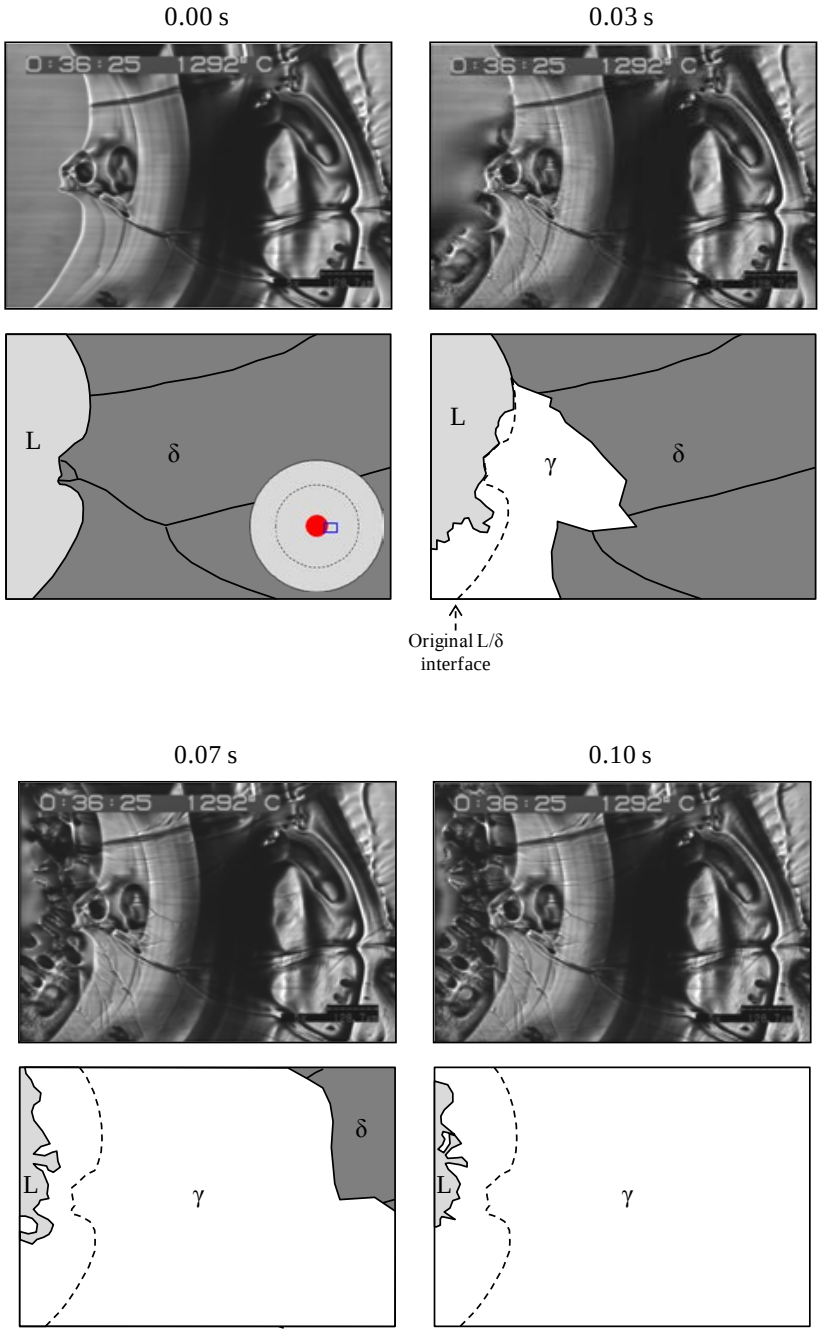

Fig.2.15 δ→γ transformation of Steel B (0.05C-0.3Mn-0.02Si) at 50 °C/min

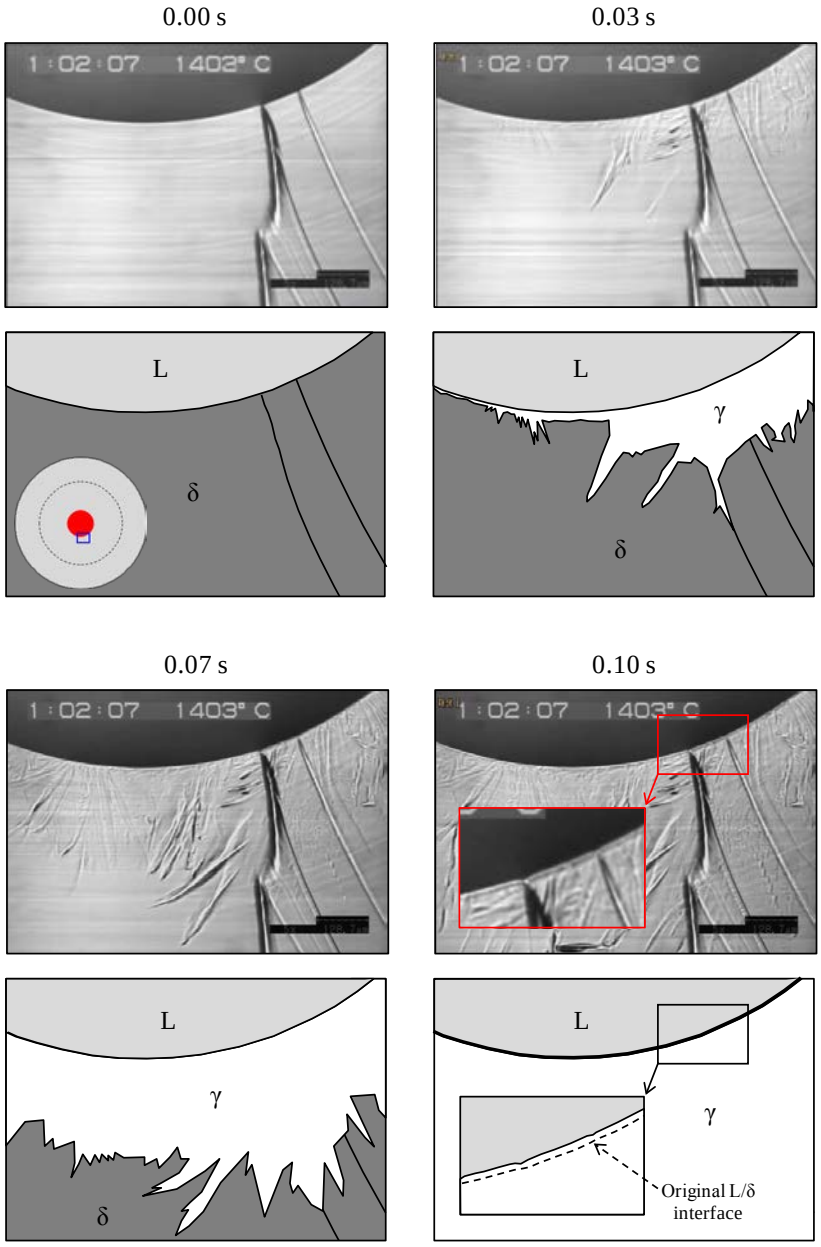

Fig.2.16 δ→γ transformation of Steel D (0.10C-0.48Mn-0.01Si) at 5 °C/min

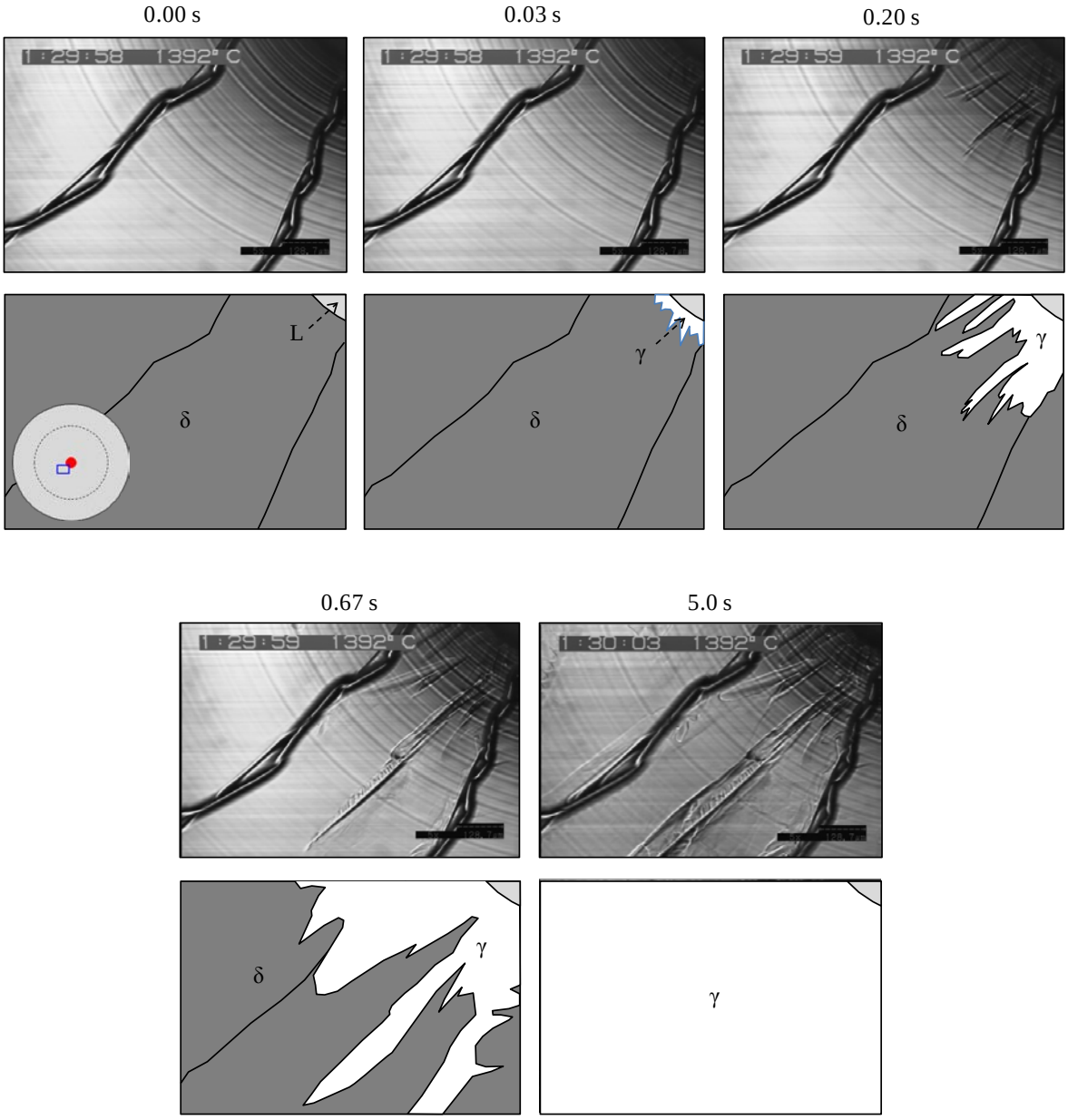

Fig.2.17 δ→γ transformation of Steel D (0.10C-0.48Mn-0.01Si) at 2 °C/min

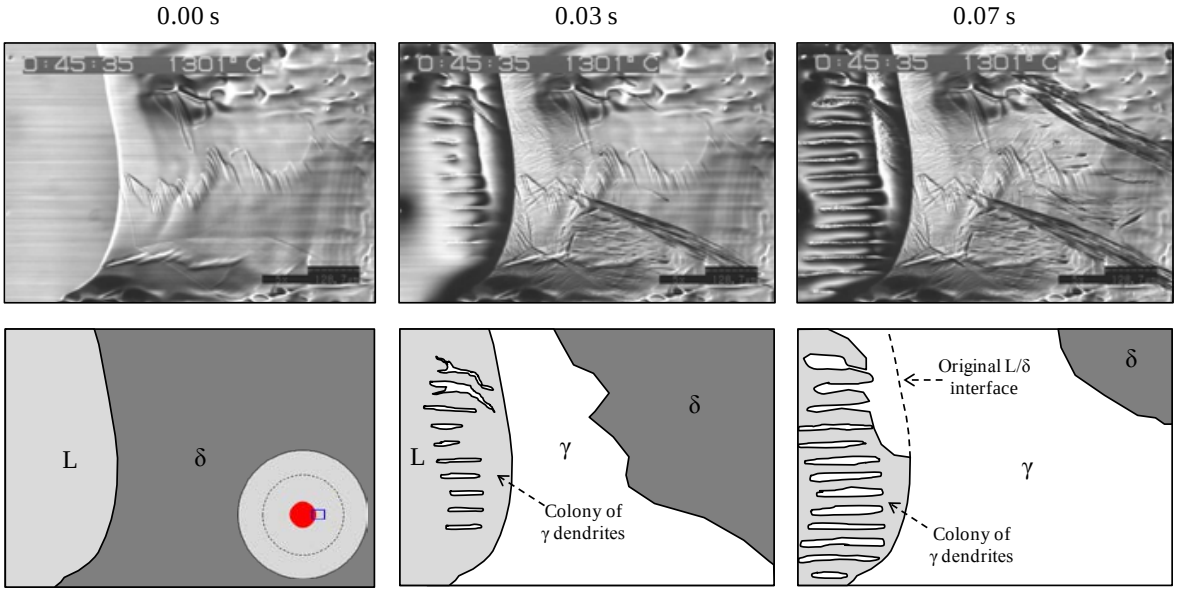

Fig.2.18 δ→γ transformation of Steel G (0.085C-2.8Mn-1.0Si-0.016Ti) at 20 °C/min

In order to establish a relationship between cooling rate and the rate of transformation of δ-ferrite to γ-austenite, frame by frame analysis was conducted on the video recordings and the findings are summarized in Fig.2.19. In interpreting these results, it is important to bear in mind that two-dimensional observations are being made of a three-dimensional phenomenon and therefore care has to be taken. Moreover, a very small area is under observation and in some instances the rate of progression of the interface is very high so that a clear pattern has not emerged. Also, at a cooling rate 50 °C/min, most of steels exhibited unstable liquid/δ interface movement - such as Steel G in Fig.2.10 for example - leaving hampered images behind and making it difficult to observe the δ/γ interface movement at later stages (That is the reason of the note 'Not clear' in Fig.2.19). However, it is quite evident that at a cooling rate of 20 °C/min and higher, the rate of transformation is very high. On the other hand, Steel D and Steel E, which are in the hypo-peritectic range according to equilibrium calculations, are showing very rapid transformation velocities even at a cooling rate of 5 °C/min.

It is also worth noting that in some instances, the δ→γ phase transformation initiated at the liquid/solid interface, but in other cases, it initiated within the solid. Since the δ→γ phase transformation occurs following the peritectic reaction in peritectic steels, the observation of the existence or not, of a liquid pool prior to the δ→γ transformation will be helpful in understanding the origins of γ nucleation. The direction of transformation and the existence of liquid pool just before the occurrence of the δ→γ phase transformation are summarized in Table.2.2. The direction of the arrows indicates the direction in the observed video frame positioned as shown in Fig.2.20.

It is interesting to note that all peritectic steels as clearly shown in Steel D and Steel F at all

cooling rates the δ/γ interface proceeded to right hand side which means γ phase nucleated at liquid/δ interface. On the other hand, in low-carbon steels at a cooling rate of 5°C/min the δ/γ interface proceeded to left hand side and at a cooling rate of 20 °C/min and higher it proceeded to right hand side regardless if there is liquid pool or not.

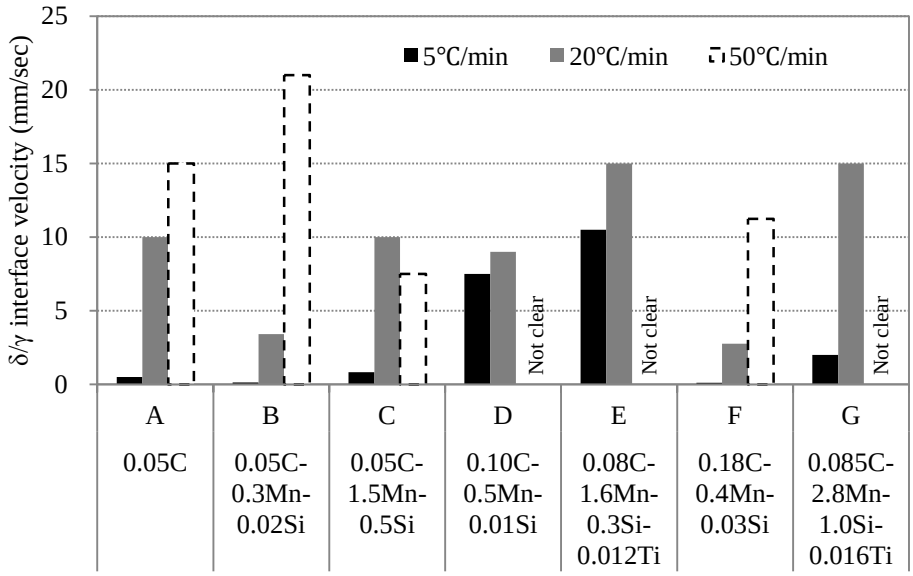

Fig.2.19 δ/γ interface velocity at different cooling rates

Tab.2.2 The direction of δ/γ interface movement. O and X in parenthesis indicates whether a liquid pool existed at the time the δ→γ transformation occurs. O = Liquid pool present, X = No liquid pool

Cooling rate	Low carbon			Hypo-peritectic		Hyper-peritectic	
	Steel A	Steel B	Steel C	Steel D	Steel E	Steel F	Steel G
5 °C/min	↖ (X)	← (X)	↖ (O)	→ (O)	↗ (O)	→ (O)	not clear (O)
20 °C/min	↗ (X)	↑ (X)	→ (O)	→ (O)	↗ (O)	→ (O)	↗ (O)
50 °C/min	not clear (O)	→ (O)	→ (X)	-	-	→ (O)	not clear (O)

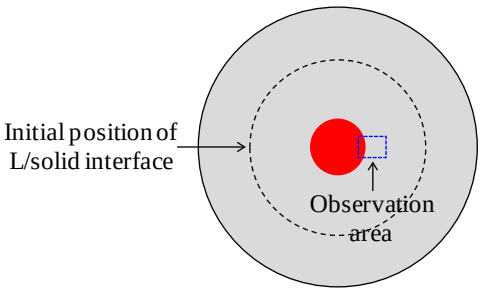

Fig.2.20 Observation area of the specimen. In the case where a liquid pool did not exist at the time of occurrence of the peritectic transformation, the same area of specimen was observed, i.e. the right hand side of the specimen as shown in the figure

2.4 Discussions

2.4.1 Initial Solidification and Partitioning

Under certain experimental conditions, most notably at higher cooling rates, the progressing of the liquid/solid interface becomes unstable with time as a result of the transition from planar to cellular morphology. In some cases the emergence of dendrites ahead of the growing interface inhibits the advance of the solid and under these circumstances an evaluation of the average interface velocity is not meaningful. Hence, a better comparison between the behaviour of the different steels can be made by measuring the initial interface velocity (i.e. interface movement in the absence of obstructions). A summary of the initial velocity of the liquid/δ interface at different cooling rates, is shown in Fig.2.21 for the steel grades under investigation. The initial velocity of the liquid/δ interface increases as the cooling rate increases in all steels. Moreover, it is clear that the initial velocity decreases as the overall solute element content of a steel increases. It is pertinent to explore this observation in more detail. It is assumed that local equilibrium is always maintained at the liquid/solid interface, i.e., the respective solute concentrations at the interface can be obtained from the equilibrium phase diagram. For example, the carbon concentrations in the liquid and solid are represented by $C_{Liquidus}$ and $C_{Solidus}$ respectively in Fig.2.22(a). By comparing the low-carbon steel, Steel B (0.05C-0.3Mn-0.02Si) and the high-carbon steel, Steel H (0.44C-0.7Mn-0.2Si) it is apparent that the difference in carbon concentration between the liquid and solid, ($C_{Liquidus}$-$C_{Solidus}$) is much larger in Steel H than in Steel B and it follows then that the initial velocity of the interface in Steel H will be significantly reduced because the migration of the interface requires the diffusion of large amounts of solute across the interface. As a consequence, the initial velocity of the liquid/δ interface can be expressed as a function of ($C_{Liquidus}$-$C_{Solidus}$) at the liquidus temperature of a given steel grade as shown in Fig.2.22(b). It transpires that there is clear reciprocal relationship between ($C_{Liquidus}$-$C_{Solidus}$) and initial liquid/δ interface velocity.

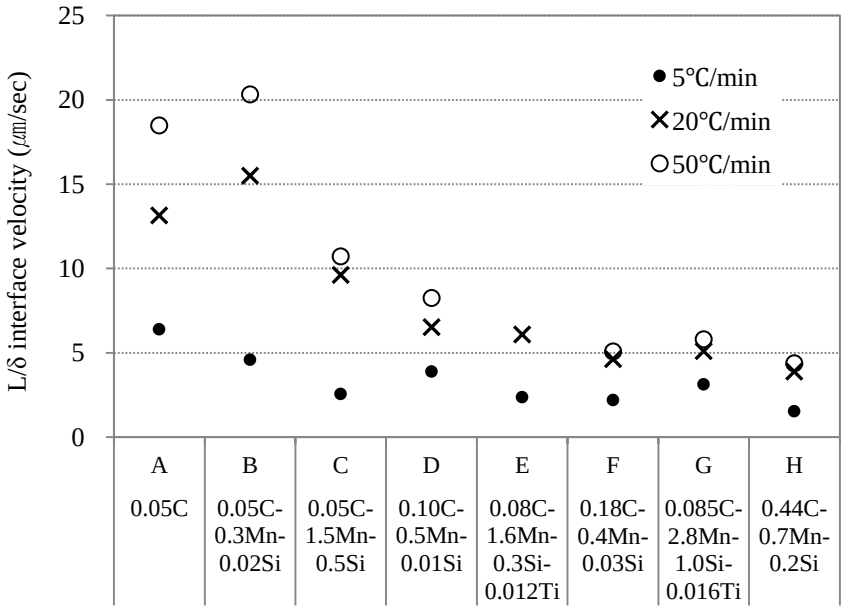

Fig.2.21 Initial velocity of the liquid/δ interface during cooling at different cooling rates

It is also instructive to evaluate the distance progressed by the liquid/δ interface per unit temperature drop as shown in Fig.2.23. It follows that the progression of the liquid/δ interface per unit temperature becomes lower as the cooling rate increases in all the steel grades. This observation needs further clarification. It is possibly due to the fact that the increased cooling rate will limit the time for the rejected solutes from solidified δ-ferrite to diffuse into the liquid and this in turn results in the decreased travel distance of solutes under a given set of circumstances. More solute elements will build up in the liquid ahead of the liquid/solid interface at increased cooling rates thereby enriching the liquid in solute, which in turn will retard the interface movement by way of increasing the value of ($C_{Liquidus}$-$C_{Solidus}$) as indicated in Fig.2.22(a).

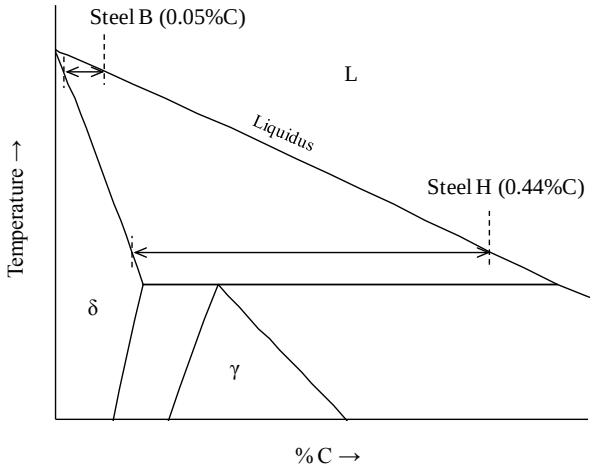

(a) Schematic derivation of the difference in carbon concentrations of the solid and liquid phases respectively from the Fe-C equilibrium phase diagram. The length of arrow indicates the difference in carbon concentration ($C_{Liquidus}$-$C_{Solidus}$) in two different steels.

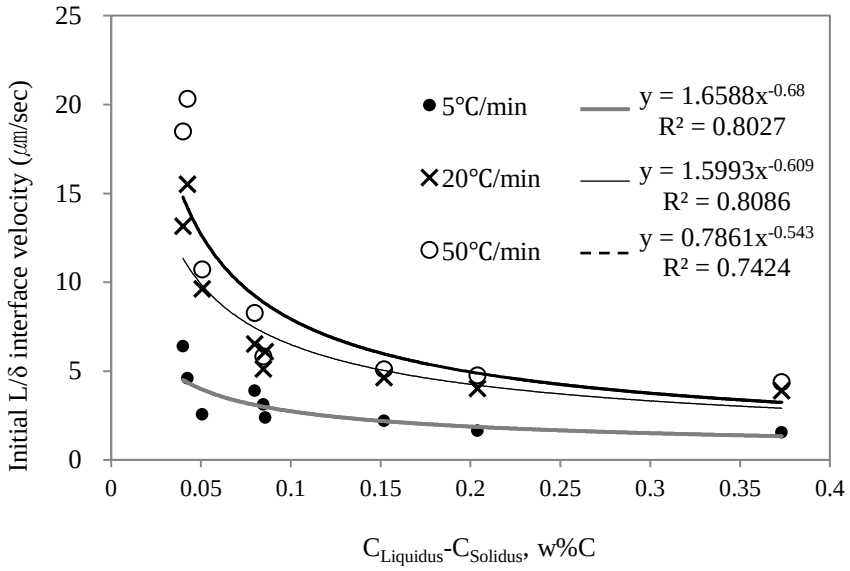

(b) Initial liquid/δ interface velocity vs. $C_{Liquidus}$-$C_{Solidus}$

Fig.2.22 Interface velocity as function of ($C_{Liquidus}$-$C_{Solidus}$) at the liquidus temperature of a given steel

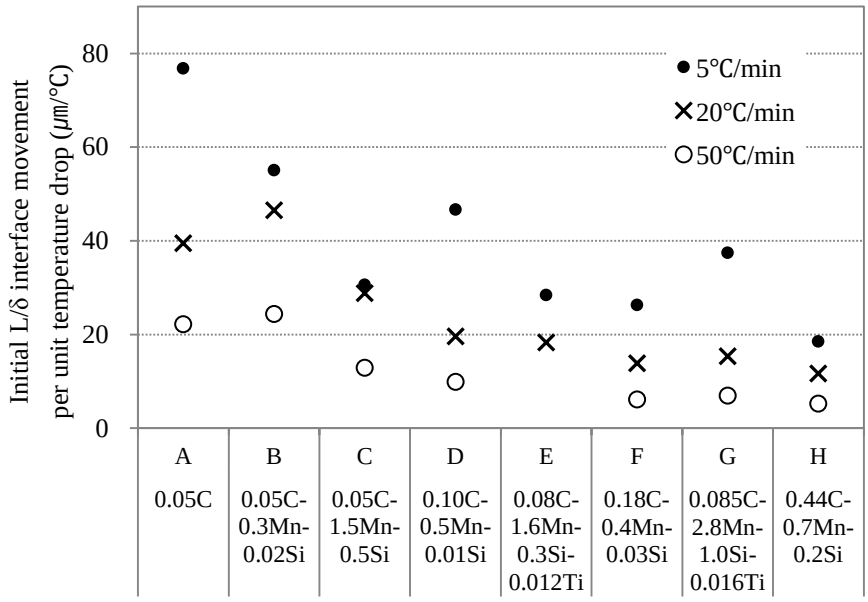

Fig.2.23 Initial growth of the liquid/δ interface during cooling shown as the distance progressed per unit temperature drop

The solid phase fraction that forms under equilibrium conditions can be calculated using the lever rule while non-equilibrium solidification can be assessed by the use of the Scheil model [39]. In this model, no diffusion of solutes in solid is allowed while perfect mixing of solutes in the liquid is assumed. According to this analysis, Steel A (0.05C) which is classified as non-peritectic low-carbon steel can indeed display peritectic solidification. Following solidification, the remaining liquid is significantly enriched in alloying elements. The differences between the equilibrium composition and the average composition of the solid established by the Scheil model are shown in Fig.2.24(a). The dashed line in the figure indicates the average composition of the solid. The mass fraction of solid phase as a function of temperature is shown in Fig.2.24(b), showing that the peritectic reaction can indeed occur in an Fe-0.05 wt%C alloy as a result of carbon segregation. From an industrial continuous casting practice, it can be assumed that the actual conditions during continuous casting will be somewhere between equilibrium and the Scheil model, but possibly closer to the Scheil model condition and as a result, low-carbon steels with equivalent carbon content close to the lower peritectic limit, will frequently display peritectic behaviour.

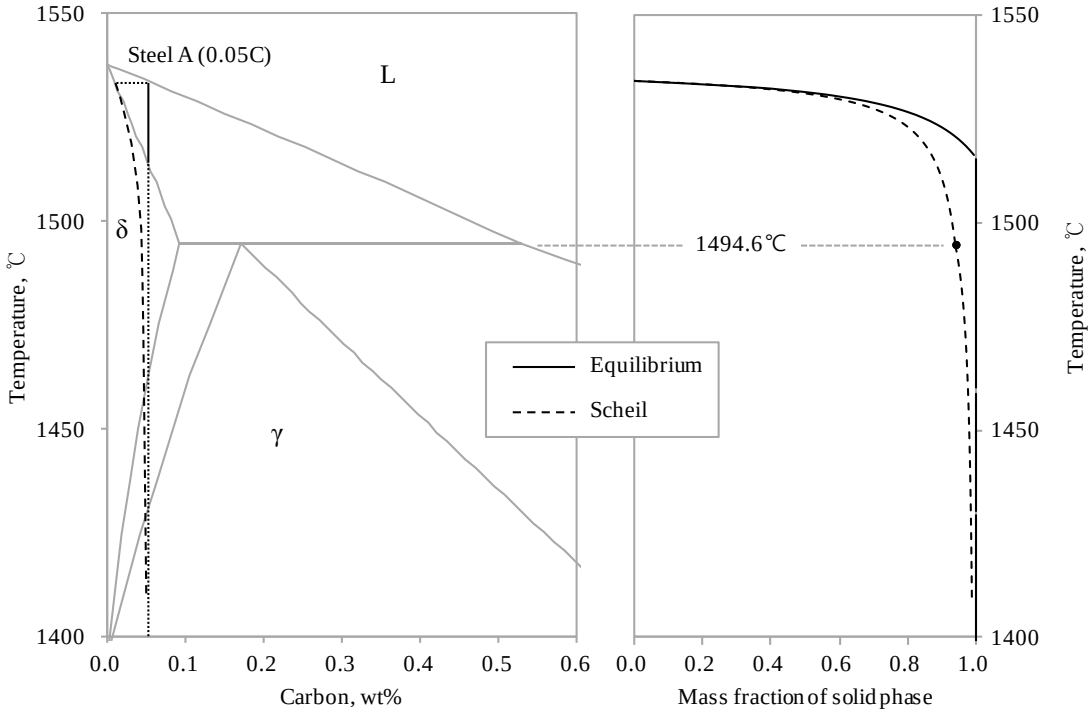

(a) Equilibrium Fe-C phase diagram

(b) Calculated solid phase fraction (from Thermo-Calc)

Fig.2.24 Comparison of equilibrium solidification and non-equilibrium solidification (Scheil model) with reference to the Fe-C phase diagram for Steel A (0.05C). The dashed line in (a) shows the average composition of solid phase calculated by the Scheil model.

2.4.2 Analysis of Peritectic Transition Pertinent to the Concentric Solidification Experiments

As was seen previously, it was not always possible to observe the peritectic reaction *in-situ*, because of both the practical difficulty of obtaining good focus at the liquid/solid interface and the very thin γ-austenite layer that propagate along the liquid/delta-ferrite interface at high reaction velocities. This issue is actually not very important in the present discussion since the focus has not been on a study of the peritectic reaction as such, but rather on the subsequent phase transitions, δ→γ and L→γ. The peritectic reaction in Steel F (0.18C-0.35Mn-0.03Si) is shown in Fig.2.12 at a cooling rate of 5 °C/min in the time frame at 0.5sec indicated in the second video frame. The subsequent progression of the liquid/γ and δ/γ interfaces relative to the original liquid/δ interface is also illustrated in the frames marked 3.0 sec and 19 sec. This observation is in very good agreement with the results of Phelan *et al.* [14] for a similar steel as shown in Fig.1.3. On the other hand, it is interesting to note that the δ grain boundaries doesn't provide preferential site for the growth of γ

phase as shown in the time frames marked 3.0 sec and 19 sec.

The δ→γ transformation was not observed in Steel H (0.44C-0.69Mn-0.19Si) at any cooling rate. This might be an important observation since there is a possibility that the peritectic transition does not occur in a steel of this composition due to the fact that the steel composition falls outside of peritectic range, although the Thermo-Calc calculation showed that this steel will undergo a peritectic reaction. However, the steel composition is very close to upper limit as shown in Fig.2.1(c) and small inaccuracies of the thermodynamic data in the database used can account for the difference in observation and calculation. It is worth mentioning in this regard that Presoly *et al.* [40] has shown by sophisticated thermal analysis that steels that will ostensibly be subject to peritectic transformation as calculated by Thermo-Calc, might not be because of incorrect thermodynamic data.

Phelan *et al.* [14] have shown experimentally that there is an inversion of the relative rates of transformation of the liquid/γ and δ/γ interfaces as a function of cooling rate. This phenomenon was further investigated in the current study. For example, Fig.2.25 shows the rates of progression of these two interfaces at two different cooling rates in Steel F. At a cooling rate of 5 °C/min, the δ/γ interface progresses at a higher rate than the liquid/γ interface while the opposite is true at a cooling rate of 20 °C/min, confirming the findings of Phelan *et al*.

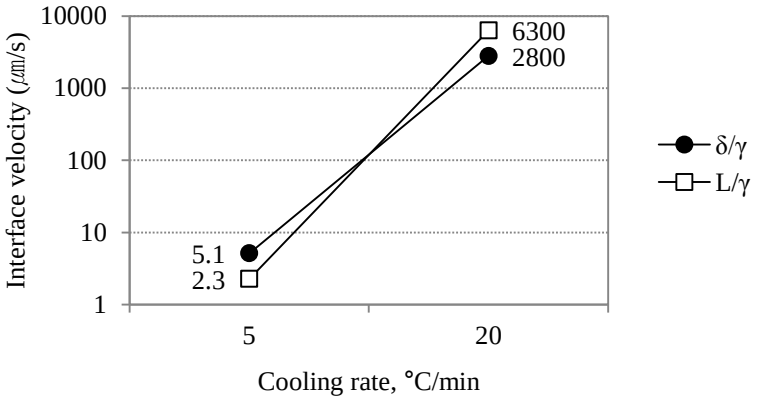

Fig.2.25 Comparison of liquid/γ interface velocity and the δ/γ interface velocity at different cooling rate for Steel F (0.18C-0.35Mn-0.03Si)

Whereas Phelan *et al.* [14] used a phase field model to predict the solute distribution in the vicinity of a progressing interface, in the present study, DICTRA (DIffusion Controlled TRAnsformation) software (version 24) [41] incorporating Thermo-Calc [34] (with the thermodynamic database, TCFE4 [35]) has been employed to simulate the progress of the liquid/solid interfaces. The mobility database MOB2 [42] was used in the DICTRA calculations and the assumption was made that solute diffusion occurs in both solid and liquid. Fig.2.26 shows such an analysis for the case of Steel G (0.085C-2.8Mn-1.0Si-0.016Ti) at different cooling rates.

It follows from Fig.2.26 that the solute concentration gradient in the liquid phase is much steeper at a high cooling rate than at the lower cooling rate. When cooling at a high rate, there is an increased build-up of solute in the liquid ahead of the liquid/solid interface and hence, this higher concentration gradient provides an additional chemical driving force for the progression of the interface and the liquid/γ interface therefore progresses at a higher rate than the δ/γ interface. These results, both the experimental findings and simulations are in excellent agreement with those of Phelan *et al*. [14].

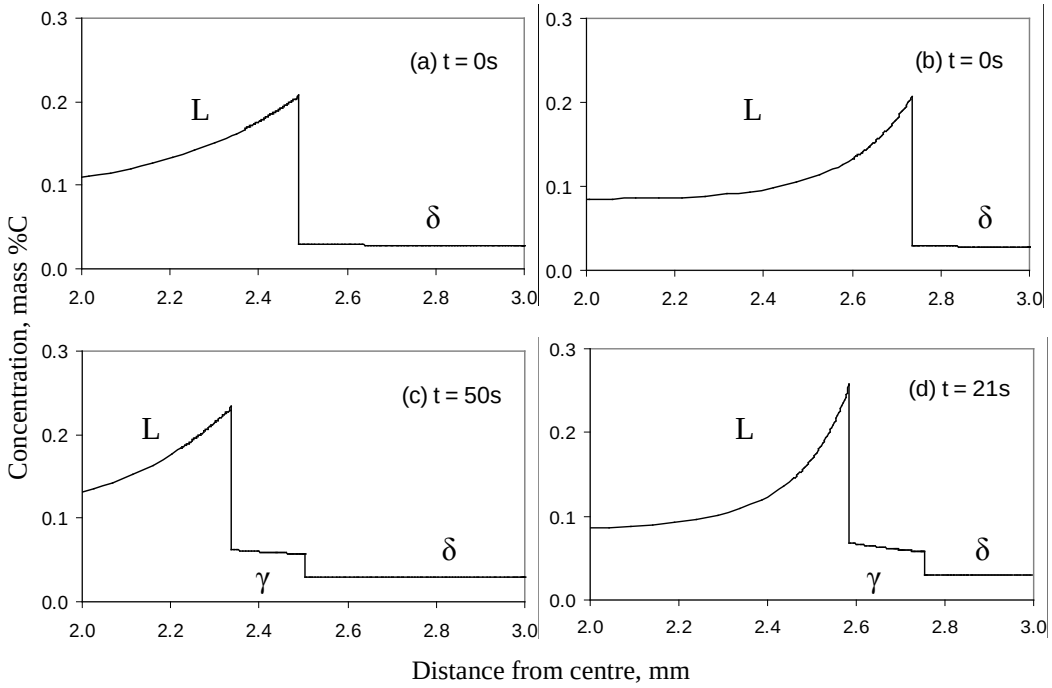

Fig.2.26 Comparison of simulated solute profiles for cooling rates of 5 °C/min (a) and (c) ; 20 °C/min (b) and (d) for in Steel G (0.085C-2.8Mn-1.0Si-0.016Ti). t = 0s refers to the initiation of the peritectic phase transition

At the relatively low cooling rate of 5 °C/min, unlike other steels, Steel D (0.10C-0.48Mn-0.01Si) showed a very high δ/γ interface velocity of 7.5 mm/s, i.e., a massive-type of transformation, as shown in Fig.2.16. This observation is very important because the production of steels with compositions close to that of Steel D is extremely difficult in industrial practice. For instance, the incidence of surface defects peaks at a carbon composition around 0.1 % in addition to the heat transfer rate being a minimum for steels of compositions close to that of Steel D [5]. By contrast, Steel F (0.18C-0.35Mn-0.03Si), which is supposedly very close to the peritectic composition, exhibited a quite low δ/γ interface velocity of 5.1 μm/s at same cooling rate. The implication is that the interface migration in this instance is diffusion controlled (see also Fig.2.19). It is therefore of great interest to further investigate the details of the peritectic transition of these two peritectic steels.

Griesser *et al.* [29] found a strong correlation between the magnitude of diffusion fields and the resulting constrained nucleation of a new phase. In their experiments they showed that the higher the fraction of primary solidified δ, the higher the solute concentration gradients in δ due to partitioning and insufficient back-diffusion of solute elements into the solid during solidification. These concentration gradients result in the diffusion of carbon from the liquid, through the liquid/δ interface (the γ nucleation site) into δ. The higher the magnitude of this flux, the higher the undercooling before nucleation initiates. An increase in the fraction of primary solidified δ with the concomitant increase in magnitude of the carbon diffusion flux, leads to increased nucleation undercooling, which in turn, leads to an increased rate of the subsequent peritectic phase transition (δ to γ) due to the higher thermodynamic driving force for the formation of γ below the equilibrium peritectic temperature.

By capitalizing on this new information, the behaviour of Steels D and F have been re-assessed, but it is firstly necessary to refer to pertinent calculations and calibrations. In order to estimate the temperature at the moving liquid/δ interface, Griesser [18] compared and calibrated the experimentally measured solid fraction at a given temperature to the value calculated by the lever-rule. The calibration is necessary because the application of the lever-rule to non-equilibrium conditions leads to a higher calculated temperature compared to the real temperature at the interface. In order to establish the real interface temperature throughout the duration of the experiment, the temperature trend from the initial solidification is extended, represented by the dashed line in the temperature-time plot in Fig.2.27. In the present study, this methodology has been applied to determine the actual peritectic temperature, i.e., the interface temperature at transformation. The peritectic temperature (T_P) calculated in this way, as well as the solid fraction, calculated from the interface migration distance until transformation, are presented in Tab.2.3.

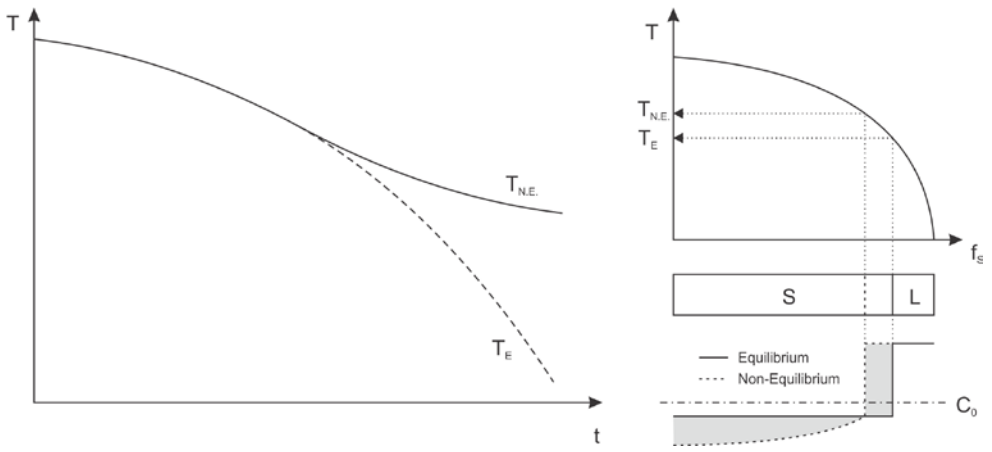

Fig.2.27 Construction of the interface temperature vs. time curve for the concentric solidification experiment [18]

Tab.2.3 Summary of the measurements and calibrations

-	Initial pool radius (μm)	Pool radius at transformation (μm)	Solid fraction at transformation	T_{PE} (°C)	T_P (°C)	ΔT_P (°C)
Steel D	3.00×10^3	0.60×10^3	0.985	1493.5	1458	35.5
Steel F	3.00×10^3	1.81×10^3	0.864	1493.2	1482	11.2

In the present study, the solid fraction of Steel D in the sample prior to peritectic transition is higher than Steel F as shown in the Tab.2.3. The undercooling (the difference between the peritectic temperature and the temperature at which the transformation occurs) is 35.5 °C for Steel D and 11.2 °C for Steel F. These findings can now be compared to those of Griesser *et al.* [29], in order to assess the mechanism of the massive transformation under conditions where there is a high fraction of solid prior to transformation and resulting undercooling. Fig.2.28 shows Griesser's calculated concentration gradients of carbon in δ-ferrite using experimentally measured peritectic temperatures for pure Fe-0.10wt%C and pure Fe-0.18wt%C alloys, which have very similar composition to the industrially produced alloys that are the subject of the present investigation. The concentration gradient of δ at the liquid/δ interface in the Fe-0.10wt%C alloy is 84 $wt\%m^{-1}$, which is more than twice that in the Fe-0.18wt%C alloy.

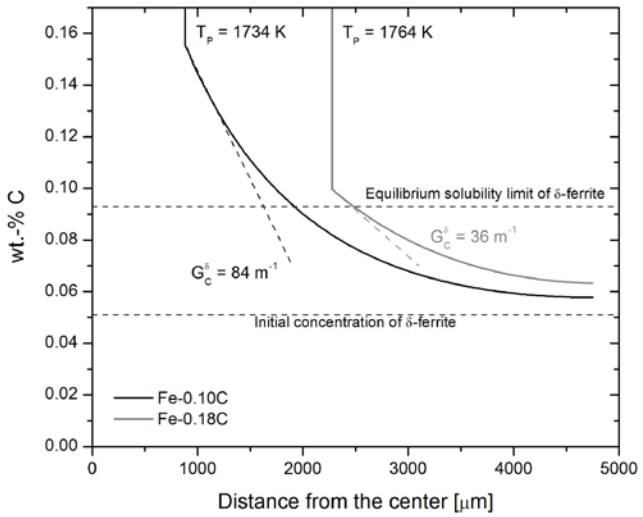

Fig.2.28 Concentration gradients of carbon in δ-ferrite for pure Fe-0.10wt%C and Fe-0.18wt%C alloys at the experimentally measured peritectic temperatures [18]

From a theoretical point of view, a massive (diffusionless) phase transformation can occur when the temperature is below the so-called T_0-temperature, where T_0 is defined as the temperature at which the Gibbs free energy of the two respective phases is the same. Fig.2.29 shows an example

of the calculation of T_0 with reference to the Fe-C phase diagram for a low-carbon steel. This figure indicates that if such steel is rapidly cooled to below T_0 it can transform to γ-austenite by a massive-type of morphology, in agreement with the experimental findings.

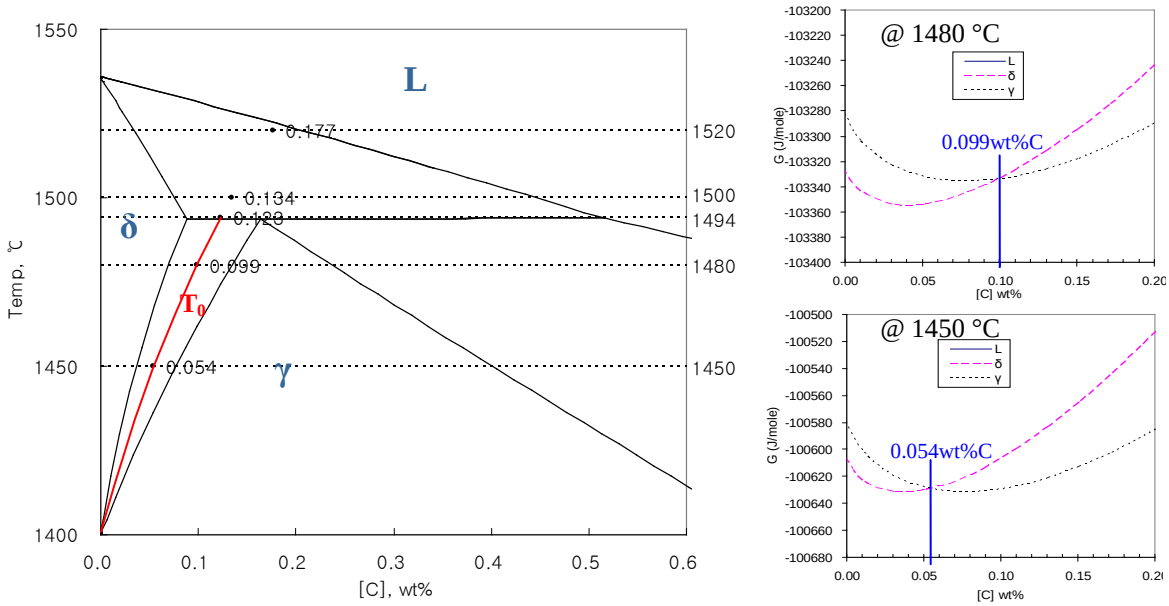

(a) Calculated T_0

(b) Gibbs free energy of the two respective phases

Fig.2.29 Calculation of T_0 with reference to the Fe-C phase diagram for a low-carbon steel

In order to better understand the nature of δ→γ transformation during concentric solidification and in particular nucleation of the γ phase as well as the direction of δ/γ interface progression and the kinetics of the transformation, a schematic diagram illustrating the situation just before the peritectic transition occurs is shown in Fig.2.30. In this diagram, the temperature profile and the concentration profile across the concentric sample and a superimposed corresponding temperature-concentration profile are plotted onto the phase diagram. It is assumed that no diffusion will occur in the solid and the γ-phase will not nucleate before a given amount of undercooling. Therefore, the two end points of the concentration profile curve shown in the lower right hand side of the diagram can be determined by the initial concentration at the position of the initial liquid/δ interface and the undercooling (ΔT_P) from the equilibrium peritectic temperature. The temperature as a function of carbon concentration in the sample can be obtained from the temperature and concentration profiles. This temperature-composition relationship in the sample is superimposed on the phase diagram as shown in the upper right hand side of the diagram as a bold dashed line.

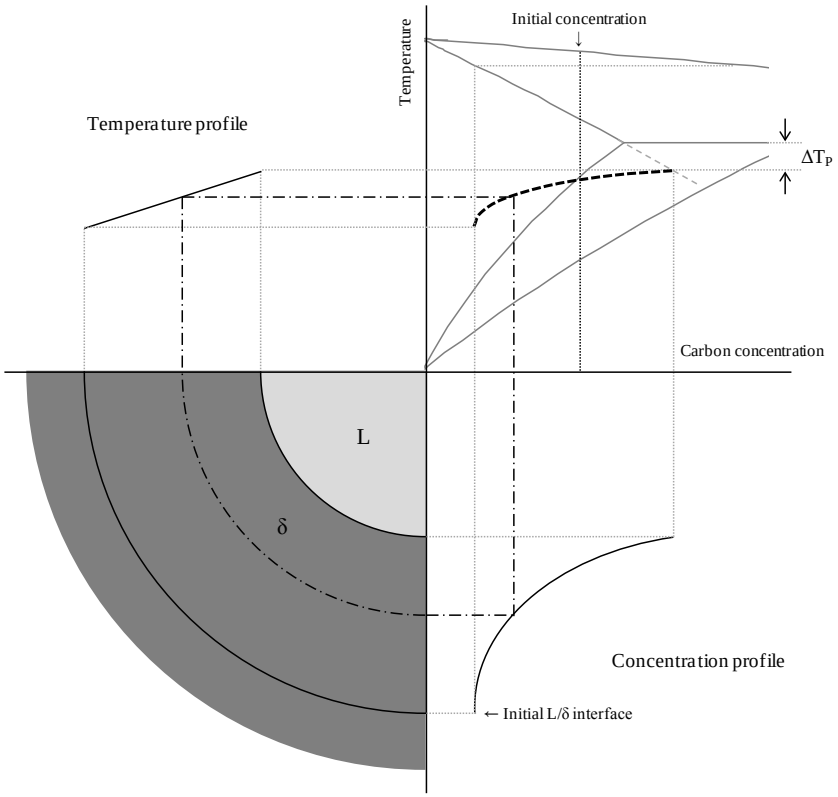

Fig.2.30 Schematic diagram explaining the situation prior to transformation considering the temperature profile and the concentration profile in the solid. The bold dashed line superimposed on the phase diagram indicates the temperature profile of the sample as a function of carbon concentration.

By using the experimentally determined data shown in Tab.2.3, as input into such diagram, it becomes easy to compare and to better understand the different manifestations of the peritectic transition in the different steels under investigation. In this comparison, the temperature profile across the sample was obtained by using a thermal gradient of 9.8 °C/mm, which was obtained from Griesser [18]'s calculations shown in Fig.2.7.

Fig.2.31 and Fig.2.32 show the diagrams for Steel D and Steel F respectively. The kinetics of the peritectic transformation depends on the undercooling below the equilibrium peritectic temperature and the concentration gradients in the parent phases prior to the peritectic transition. Griesser *et al.* [29] have shown that the formation of concentration gradients in the δ-ferrite and the resulting diffusion field across the liquid/ferrite interface cause a barrier to the nucleation of γ-austenite by increasing its free energy. Once nucleation of γ-austenite has occurred at a certain undercooling below the equilibrium peritectic temperature, the thermodynamic driving forces for the transformation of δ-ferrite into γ-austenite lead to increased kinetics of the peritectic reaction and transformation. Having this fact in mind, the behaviour of Steel D as opposed to Steel F can be explained.

In the case of Steel D, the fraction solid at the peritectic temperature is equal to 0.985, leading to

the formation of a steep concentration gradient of carbon in δ-ferrite during the primary solidification of δ-ferrite and a resulting undercooling (ΔT_P) below the equilibrium peritectic temperature of 35.5 °C. From Fig.2.31 it appears that when the nucleation of γ-austenite is constrained to a temperature of about 10 °C below the equilibrium peritectic temperature, the liquid/ferrite interface crosses the allotropic phase boundary (T_0-line) between δ-ferrite and γ-austenite. According to the principles of thermodynamics, massive transformation becomes possible when the free energy of the system can be reduced by the transformation of one phase into another, i.e. when the temperature of the liquid/δ-ferrite interface is below the T_0-temperature of the corresponding composition. A greater difference between the interface temperature and the corresponding T_0-temperature (ΔT_0) results in a higher driving force for a massive transformation of δ-ferrite into γ-austenite.

In the case of the Steel F, the smaller fraction of solid, 0.864, at the peritectic temperature compared to Steel D leads to the formation of a lower concentration gradient of carbon in δ-ferrite, resulting in an undercooling (ΔT_P) of only 11.2 °C. The much lower difference between the interface temperature (barely below the T_0-line as shown in Fig.2.32) and the corresponding T_0-temperature compared to Steel D results in a much lower driving force for a massive transformation to occur. Therefore, the transformation occurs in a diffusion controlled manner as previously shown in Fig.2.12.

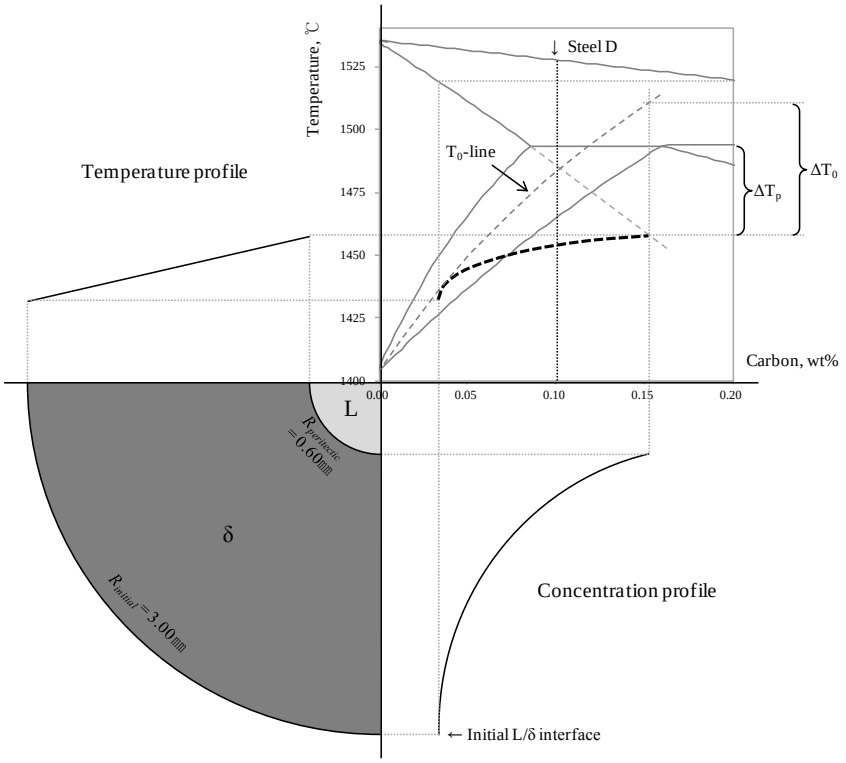

Fig.2.31 The situation prior to peritectic transition in Steel D (0.10C-0.48Mn-0.01Si) at a cooling rate of 5 °C/min considering experimentally determined values

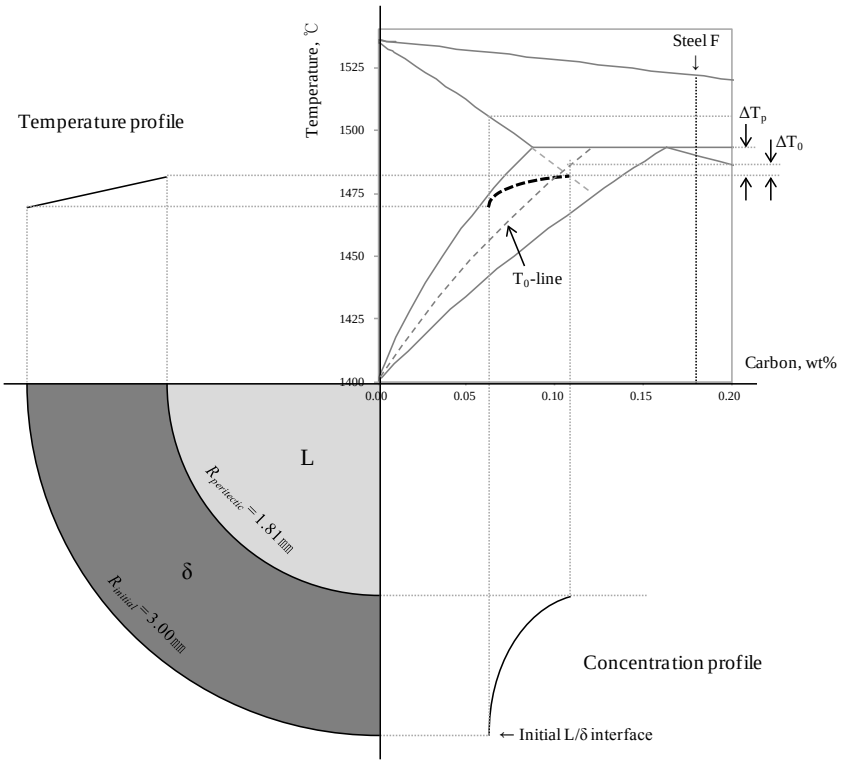

Fig.2.32 The situation prior to peritectic transition in Steel F (0.18C-0.35Mn-0.03Si) at a cooling rate of 5 °C/min considering experimentally determined values

Shibata *et al.* [1] as well as Phelan *et al.* [14] found experimentally by direct observation that the δ→γ transformation can occur at very high rates. The experimental observations made in the course of the present investigation and summarised in Fig.2.19, confirm their conclusions. It is instructive to consider in this context, earlier findings of Niknafs [43]. In studying only the solid-state δ→γ transformation in a 0.05 wt%C steel, he found that the transformation occurs by diffusional growth at cooling rates below about 50 °C/min, but when the cooling rate exceeds this value, the transformation occurs by a massive-type of reaction. The progress of the δ→γ transformation in this 0.05 wt%C steel is shown in Fig.2.33. In the present study, it was consistently found that the δ→γ phase transformation nucleated at the liquid/solid interface and progressed by a massive-type of morphology, even at cooling rates lower than those reported by Niknafs, for example 5 °C/min in Steel D. This observation provides convincing experimental evidence that the cooling rate required to induce a massive δ→γ transformation in the presence of liquid, will not be higher than that required in the solid state transformation in the absence of liquid. The occurrence of the δ→γ transformation at the liquid/solid interface triggers the transformation of the remaining solid and in this way a massive transformation can occur on a large scale.

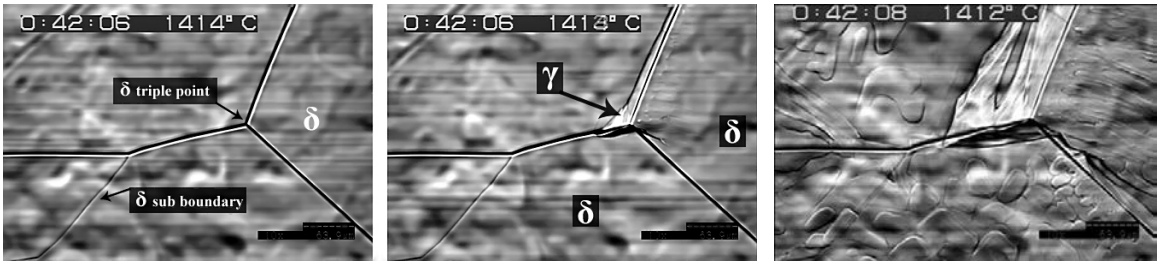

Fig.2.33 Massive-type of phase transformation of δ-ferrite to γ-austenite [43]

The δ→γ transformation that occurs in the presence of a liquid pool usually initiates at the liquid/δ interface and grows in the direction parallel to the direction of heat flow as shown in Tab.2.2. In other words, the γ-austenite nucleates at the liquid/δ interface, which is hotter than the outer region of the specimen and will grow from the high to the low temperature and the reason why this is occurring has been explained above. However, this behaviour was not observed in Steel C and it is pertinent to investigate into more detail this, ostensibly strange behaviour of Steel C. On cooling Steel C at a rate of 5 °C/min, the liquid/δ interface progressed up to 2.71 mm further than in Steel D before the δ→γ transformation occurred. In accordance with the theoretical arguments with respect to nucleation advanced above, the high solid fraction in this steel and the resulting steep concentration gradient in the solid at the liquid/δ interface were supposed to result in a massive transformation, nucleating at the liquid/δ interface as shown in Fig.2.34. However, the γ phase nucleated at a position 2.3 mm from the centre of the specimen at a grain boundary far away

from the liquid/δ interface and progressed slowly toward the centre of the sample as well as towards the outer edge of the sample as can be seen Fig.2.35. The reasons for this interesting observation are further explored below.

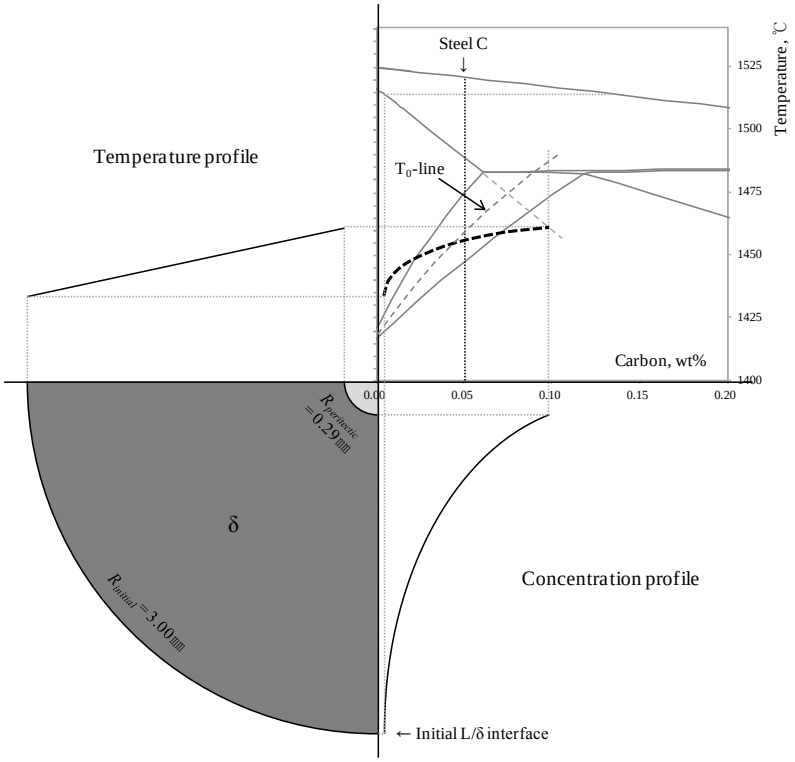

Fig.2.34 The situation prior to the δ→γ transformation in Steel C (0.05C-1.5Mn-0.51Si) at a cooling rate of 5 °C/min showing experimentally determined values

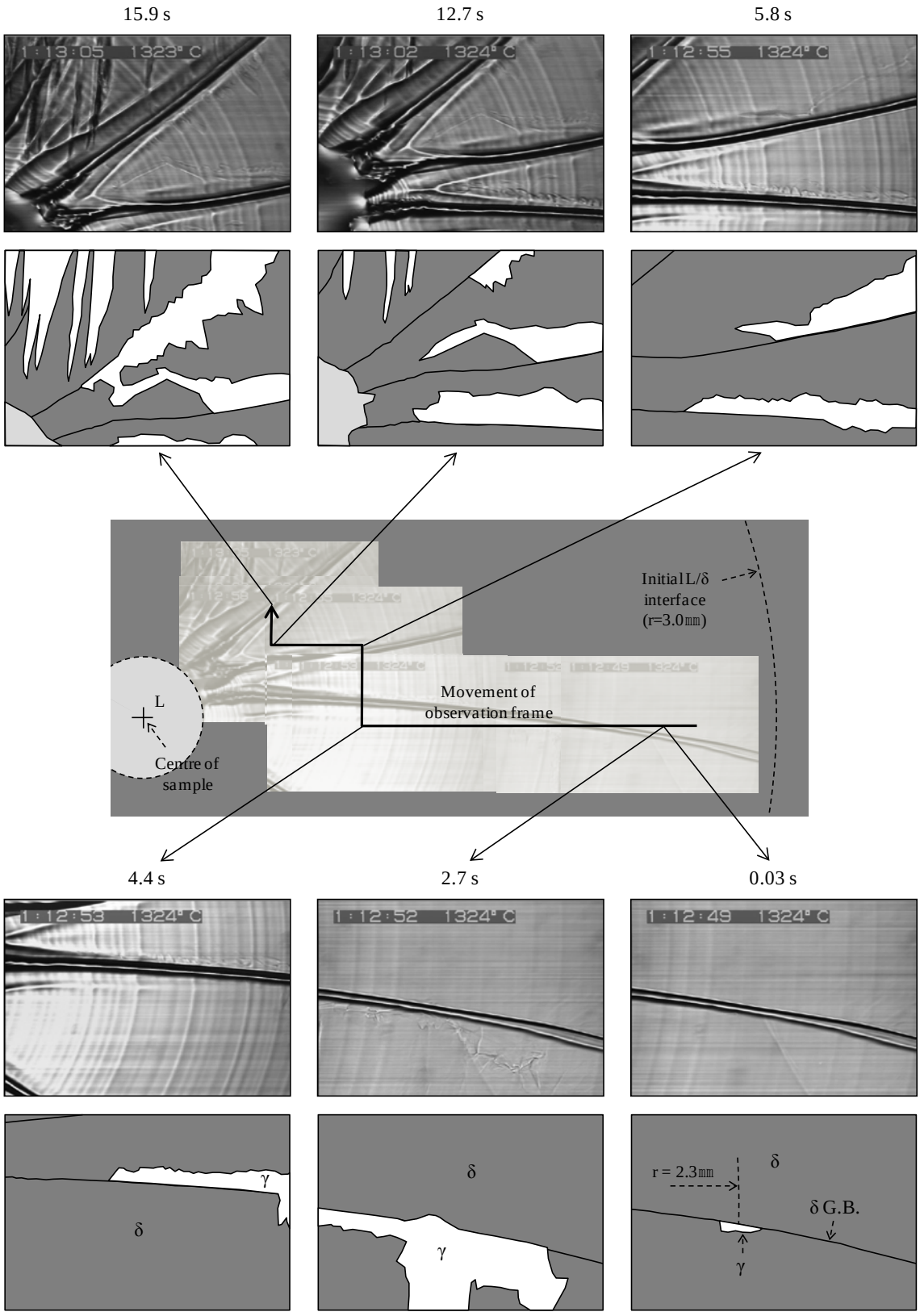

Fig.2.35 Nucleation and growth of γ phase in Steel C (0.05C-1.5Mn-0.51Si) at a cooling rate of 5 °C/min. The γ phase nucleated at a position 2.3 mm from the centre of the specimen and progressed slowly toward the centre of the sample as well as towards the outer edge of the sample.

It will be recalled that two important assumptions were made when the diagram shown in Fig. 2.34 was derived. The first assumption was that the temperature profile is based on a temperature gradient of 9.8 °C/mm, which as shown in Fig.2.7, was the temperature gradient in the bulk of the specimen far away from the centre and determined at a cooling rate of 2 °C/min. The second assumption was that there is no back-diffusion in the solid. These two assumptions need to be revisited with respect to the experimental conditions that Steel C was subjected to. Because the liquid/solid interface progressed by 2.71 mm towards the centre of sample prior to δ→γ transformation (i.e. to within 0.3 mm from the centre) the temperature gradient at the liquid/solid interface is expected to be much higher as shown in Fig. 2.7. The assumption that no back-diffusion occurred in the solid is probably also in error since it is expected the high diffusivity of carbon at the high temperatures under consideration will lead to at least some back-diffusion. Such back-diffusion will smooth the and hence, lower the concentration gradient in the δ phase at the liquid/solid interface. Fig.2.36 shows a re-drawn diagram for Steel C in which these considerations have been taken into account. The temperature as a function of carbon concentration superimposed on the phase diagram (a bold dashed line), has very different shape compared to that shown in Fig.2.34. Although the liquid/solid interface is undercooled below the equilibrium peritectic temperature, the difference between the interface temperature and T_0 is not very high. Also, the position where the γ-phase nucleated r = 2.3 mm is close to T_0-line as indicated by the broken line. Because the γ-phase nucleated in the solid, the driving force for the growth of γ-phase should be higher than it had nucleated at the liquid/solid interface. In the absence of a high driving force for γ-phase nucleation, grain boundaries can act as a preferred nucleation sites as shown in Fig.2.35 and the rate of progression in transformation will be lower.

It is important to realize that the diagrams of the type shown above are intended as a schematic illustration of the phenomena occurring during solidification and as a convenient way of analysing qualitatively, rather than quantitatively, the factors influencing the δ→γ transformation, the kinetics of the massive-type of transformation and the direction of interface migration. However, the strength of this approach is that the situation in the early stages of solidification in the mould of a continuous caster can be simply modelled using this diagram subject to certain assumptions as shown above since there is great similarity between a concentric solidification experiment and the conditions with respect to solidification in the meniscus area of the mould in terms of the direction of heat flow and the development of thermal gradients although the magnitude of the respective values are quite different.

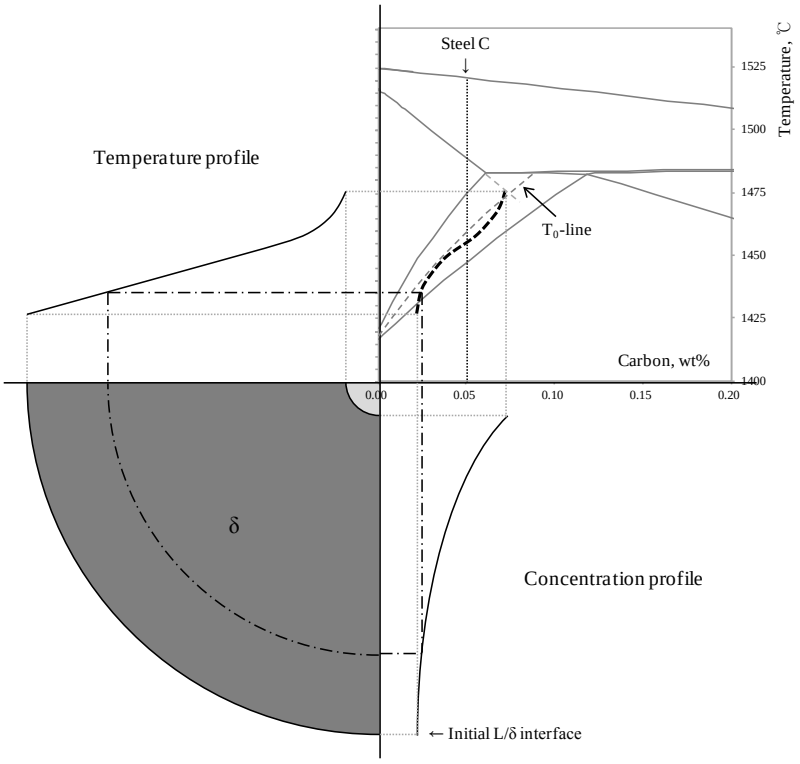

Fig.2.36 The situation prior to δ→γ transformation in Steel C (0.05C-1.5Mn-0.51Si) at a cooling rate of 5 °C/min considering modified temperature profile and concentration profile

2.4.3 Discussion of Items Relating to Practical Issues in the Continuous Casting Process

If a phase transition was to occur by massive means in an operational continuous caster, it has serious implications for it means that the very thin solidifying shell is likely to detach from the mould very suddenly, thereby exacerbating the risks of crack formation and in the extreme, breakouts. It is therefore important to consider the theoretical framework as well as practical aspects of the occurrence of a massive phase transformation in the meniscus region of a continuous caster.

Fig.2.37 shows a solidification microstructure of low-carbon steel from a 90mm thin slab caster. It is evident that a chill zone has developed up to less than 1mm from surface and then a dendritic zone extends towards the centre of the slab. A planar liquid/solid interface is expected to form in the very early stages of solidification in this chill zone due to the very high thermal gradient, resulting in solute elements build-up in the liquid ahead of the growing interface. Recalling the observation that the liquid/solid interface velocity decreases with the increase of the difference in solute concentration between the liquidus and solidus ($C_{Liquidus}$-$C_{Solidus}$) at the liquidus temperature

(in Fig.2.22(b)), it is not difficult to expect the delay of solidification due to the presence of this enriched liquid layer. The delay in solidification will increase the distance at which planar growth will occur causing an increased risk of distortion of the thin solidifying shell due to the stress resulting from the phase transformation.

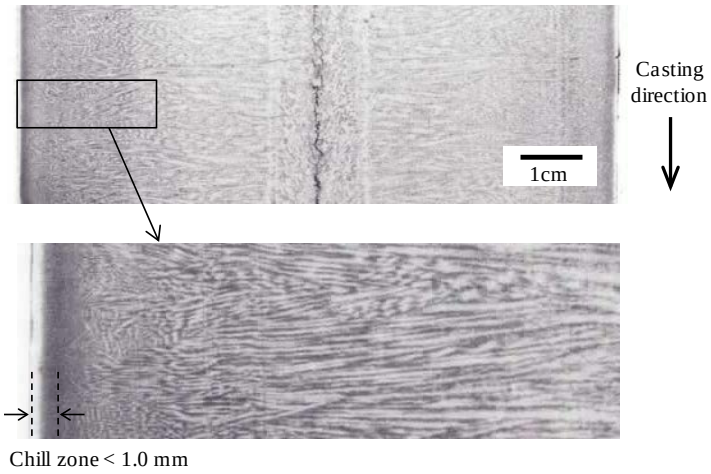

Fig.2.37 Solidification microstructure of a low-carbon steel from the 90mm thin-slab caster in Gwangyang Works, POSCO, South Korea (Specimen shows a cross-sectional area along the casting direction. Etched in a picric acid solution)

Hanao *et al.* [44] have shown for the first time, that shell growth in the region immediately below the meniscus in practical mould is significantly lower than further down the mould as shown in Fig.2.39, although they couldn't explain the reason of this delay. The solute elements build-up in the liquid ahead of the growing interface in the very early stages of solidification in the chill zone might be the root cause of this interesting finding.

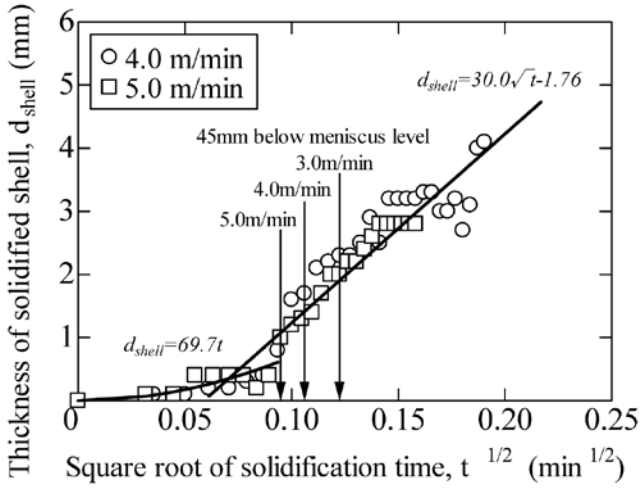

Fig.2.39 Shell thickness as a function of solidification time [44]

It is important in practice to predict the shell thickness just before the transformation of δ-ferrite to γ-austenite because the thickness of the shell at that stage determines in large measure the mechanical behaviour of the thin shell in the meniscus region of a continuous caster. This assessment was done by simulating industrial conditions in concentric solidification experiments within a high temperature laser-scanning confocal microscope by:

- observing experimentally the initial solidification rate
- determining experimentally the time interval between the start of solidification and the onset of the δ→γ phase transformation
- extrapolating these observations to estimate the likely cooling rate of 15000 °C/min [45] at the meniscus of an operational caster.

Using this value of the temperature gradient, the calculated shell thicknesses for the steels under investigation are shown in Tab.2.4.

Tab.2.4 Calculated shell thickness (The extrapolated values were obtained through radical root calculation)

Steel	Initial solidification rate (μm/sec)				Time to δ→γ transformation (min)				Shell thickness at tr. (μm) ①×②
	5 °C/min	20 °C/min	50 °C/min	Extrapolated ①	5 °C/min	20 °C/min	50 °C/min	Extrapolated ②	
A	4.5	11.4	14.8	326.4	24.33	7.15	2.15	6.26×10^{-3}	122.7
B	4.4	10.9	14.2	307.2	25.27	6.92	2.22	6.04×10^{-3}	111.4
C	4.0	9.8	12.6	256.5	22.65	5.95	2.38	9.12×10^{-3}	140.3
D	3.1	7.4	9.2	162.5	21.33	6.90	2.28	1.05×10^{-2}	102.7
E	3.0	7.1	8.8	153.3	19.65	4.77	-	5.49×10^{-3}	50.5
F	2.2	5.0	6.0	85.1	10.43	2.73	1.30	7.05×10^{-3}	36.0
G	3.0	7.2	8.9	153.3	28.97	5.78	2.28	3.98×10^{-3}	36.6

There is significant difference in the calculated shell thickness for the different steel grades and there is a clear tendency of the calculated shell thickness becoming smaller with an increased carbon equivalent. This index refers strictly to the initial solidification rate because the transformation will occur when the interface is still of planar morphology in the thin shell and hence the initial solidification rate, which is a function of the difference in solute concentration between the liquidus and solidus (as shown in Fig.2.22(b)) is the determining factor.

Although the index defined above plays an important role, it is necessary to also consider other variables such as the fraction of δ-ferrite transforming to γ, the kinetics of the transformation and the strength of the shell etc. Also it is critically important to understand and to taken into account the operational experience in terms of difficulties encountered in continuous casting practice, in order to fully evaluate and distinguish the behaviour of the different steels. An analysis of some of these variables will be the subject of discussion in subsequent chapters.

Chapter 3. Literature Review of Practical Issues Originating from Uneven Solidification in the Continuous Casting Process

It is generally accepted that the surface quality of continuously cast steel slabs is a strong function of events occurring during the early stages of solidification in the meniscus region of the mould. Surface cracking of continuously-cast steel slabs is a particularly serious problem and these surface cracks are still present after hot rolling. If the cracks are not too severe, it is possible to scarf the surface, but this is an expensive operation and if the cracks are too deep, the slab has to be scrapped.

It is well established that the peritectic phase transition occurs in the meniscus region of the mould and because many advanced steel grades are designed to be in peritectic composition range, it is important to consider the impact of this phase transition on the integrity of slabs. It is widely accepted that the volume contraction associated with the peritectic transition results in the detachment of the solidified shell from the mould and this incurs a decrease in heat flux leading to hot spots, which significantly increases the risk of surface cracking or breakouts. These risks are higher in the thin the slab casting process than in conventional casting process and the risks seem to increase as the casting speed increases. Fig.3.1 shows an example of a breakout that had occurred in an operational thin-slab caster due to uneven solidification in the mould.

Fig.3.1 A cross section of a breakout slab showing extremely uneven solidification. The breakout occurred just below the mould exit in the thin slab caster at Gwangyang Works, POSCO. The steel grade is same as Steel G (0.085C-2.8Mn-1.0Si-0.016Ti).

3.1 Brief Summary of the Likely Factors Contributing to Casting Problems in Steels of Near-Peritectic Composition

3.1.1 Transformation Shrinkage and the Effect of Carbon Content

Carbon content has been recognized as the strongest influencing factor on the frequency and severity of cracking during continuous casting of steels of near-peritectic composition. Steels in the hypo-peritectic carbon range (0.09 to 0.16 wt%) are particularly susceptible to crack formation, especially when cast at high speeds [46-49].

The unevenness of the solidified shell is related to the volume contraction that occurs during transformation of delta-ferrite to austenite. Body-centre-cubic (BCC) δ is 2.5 % to 3.0 % larger in molar volume than face-centre-cubic (FCC) γ and hence, a significant volume shrinkage accompanies the δ→γ transformation. Assuming isotropic behaviour, Konishi *et al.* [50] calculated the shrinkage of the steel in one dimension based on the density change with temperature by considering the change in lattice parameter. The calculated shrinkage for several steel grades, assuming equilibrium transformation, is shown in Fig.3.2.

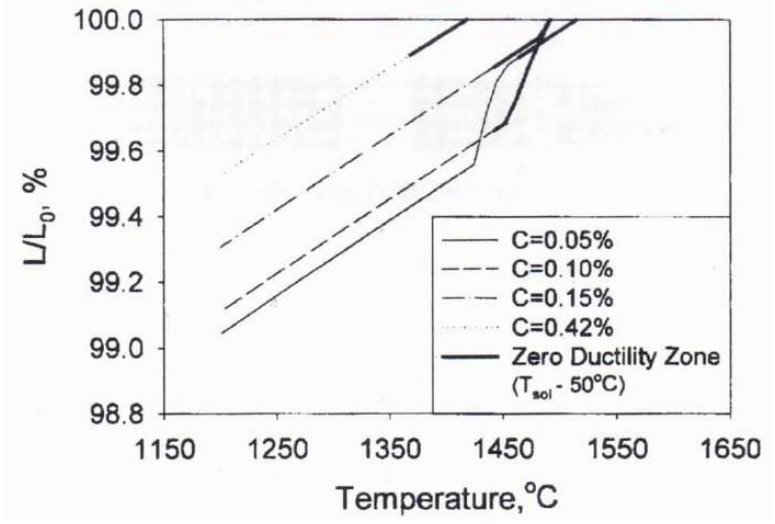

Fig.3.2 Linear shrinkage of steel following solidification under equilibrium conditions. The bold lines correspond to the 'zero ductility temperature (T_{sol}-50 °C) range' [50]

The following conclusions may be drawn from Konishi's calculations:

- Differences in the shrinkage behaviour of different steels are related to the δ→γ phase transformation. A 0.10 wt% carbon steel shrinks very rapidly due to the δ→γ phase transformation that occurs within 50 °C of the solidification temperature. This temperature

range corresponds with the so-called zero-ductility-temperature range. The total amount of linear shrinkage due to the δ→γ phase transformation is approximately 0.3 %. Since the ductility-to-fracture strain of steel just below the solidification temperature may be as low as 0.2 to 0.3 % [51], this shrinkage, due to the phase transformation, might very well lead to crack formation.

- The 0.05 wt% carbon steel is also subject to rapid shrinkage due to the phase transformation, but this transformation occurs at temperatures lower than 1450 °C, which is more than 50 °C below the solidus temperature. Since this temperature range is below the zero-ductility-temperature range, it is unlikely that cracks will form. In addition, a much thicker and stronger solidified shell has formed by the time the δ→γ transformation occurs and the thicker shell can better support the stresses imposed by the phase transformation.
- In the case of the 0.15 wt% carbon steel, the δ→γ transformation initiates at the same temperature (1493 °C) as in the 0.10 wt% carbon steel, but the transformation occurs in the presence of liquid and hence, transformation stresses can be better accommodated. Moreover, a much smaller fraction of δ phase will transform to γ and consequently, the total amount of shrinkage is much less.
- In the case of the 0.42 wt% carbon steel, the entire δ→γ transformation occurs with a co-existing liquid phase at the peritectic temperature. Under these conditions, liquid would accommodate the volume change due to shrinkage by flowing in between the dendrites. Hence, below the solidus temperature the steel would shrink by thermal contraction only.

The concept of zero-ductility is more clearly illustrated in Fig.3.3 where it is shown that steel has essentially no ductility in the temperature range between the solidus [52] and a temperature some 50 °C below the solidus.

Bernhard *et al.* [53] used a Submerged Split-Chill Contraction (SSCC) test to measure the contraction forces occurring during the solidification of steels with carbon content between 0.05 wt% and 0.2 wt% at constant manganese (1.55 %) and silicon (0.3 %) content. Fig.3.4(a) is an example of the reaction force that has been measured as a function of time for a 0.05 wt% C steel. The reaction force kicked in after about 3 seconds and reached a peak value of 1.0 kN after 16 seconds as denoted by arrows in the figure. Also shown in the figure is the calculated shell thickness for different fractions of solid formed (f_s=solid fraction). The dotted lines indicate the onset and end of the δ→γ transformation whereas the black squares represent the measured shell thickness and its standard deviation. The subsequent decrease in force cannot be attributed to crack formation, but is a result of creep because metallographic examination revealed only a relatively small number of cracks. In the case of the 0.128 wt% C steel, the contraction force kicks in at about 2 seconds and

reaches a peak of 1.5 kN after 7 seconds as shown in Fig.3.4(b). This behaviour is typical for all the steels tested with carbon content between 0.1 and 0.13 wt%, and is the result of the δ→γ transformation occurring following the onset of solidification. The steels with 0.2 wt% C show a similar behaviour to the 0.05 wt%C steels. After reaching a relatively low maximum, the force decreases.

Bernhard *et al.* [53] also showed that the maximum reactive force was obtained in steel with equivalent carbon content (C_p=[%C]+0.04[%Mn]+0.1[%Ni]-0.14[%Si]) between 0.09 wt% C and 0.16 wt% C as shown in Fig.3.5. This behaviour is attributed to to the δ→γ occurring following the onset of solidification.

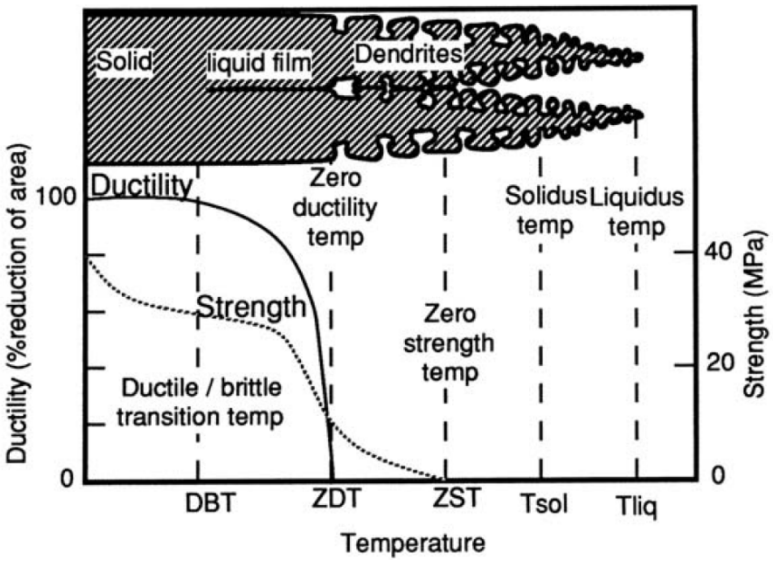

Fig.3.3 Ductility as a function of temperature, emphasizing the zero-ductility temperature [52]

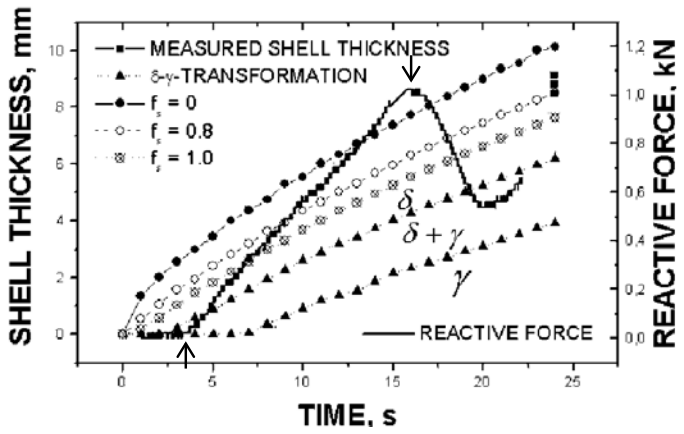

(a) 0.05 wt% carbon steel

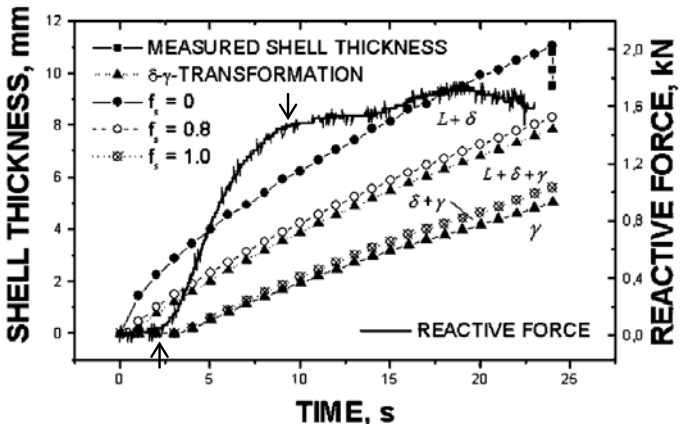

(b) 0.128 wt% carbon steel

Fig.3.4 Reactive force vs. time with isotherms for solid fractions of 0, 0.8 and 1 and isotherms for the δ→γ transformation [53]

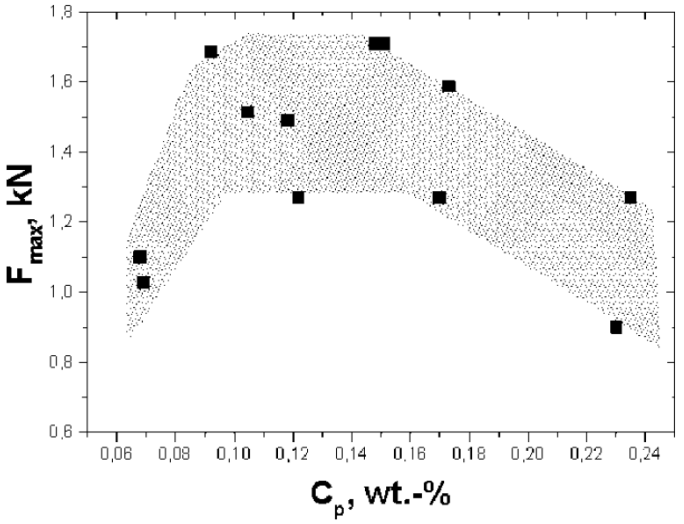

Fig.3.5 Maximum reactive force as a function of equivalent carbon content C_p. Fe-C-1.55%Mn-0.3%Si alloys were used. [53]

3.1.2 Uneven Solidification Resulting from Deformation of the Thin Shell due to the Occurrence of the δ→γ Transformation

Sengupta and Thomas [7] emphasized that steel composition plays a major role in the resulting surface shape following solidification in a continuous caster and they attributed uneven solidification to shrinkage occurring as a result of the peritectic phase transition. Suzuki *et al.* [54] argued that the dependence of uneven shell growth on carbon content is a result of different values of stress that develop in steels of different composition as a result of differences in solidification shrinkage and the δ→γ transformation. They introduced a method of estimating the unevenness of shell thickness: by using the standard deviation of the solidification constant, which is obtained through dipping tests using a copper plate. Anomalous rough surfaces and uneven shell growth were found in an ultra-low carbon steel (0.005 wt%C) and a hypo-peritectic carbon steel (0.116 wt%C), while a low-carbon steel (0.044 wt%C) and a hyper-peritectic carbon steel (0.304 wt%C), had flat surfaces. Mizukami *et al.* [55] argued that the surface quality dependence on carbon content is not related to the initial stages of solidification. They obtained cooling curves during the initial stages of solidification of ultra-low, low- and medium-carbon steel samples and explained the deformation behaviour of the initially solidified shell with respect to these cooling curves. They established that nucleation at the initial solidification is not dependent of carbon content, but that subsequent growth of the solidifying shell is.

Murakami *et al.* [56] conducted dip tests in order to evaluate the unevenness of a solidified shell and the appearance of such shells is shown in Fig.3.6. The outer surface (in contact with a water-cooled plate) of the shells in steel containing 0.054 wt%C and 0.276 wt%C were flat, whereas those containing 0.146 wt%C had a tortoise-shell depression pattern. Also the inner surface (metal side) of the shell containing 0.146 wt%C was clearly uneven.

They developed the concept of an unevenness parameter $\Delta d/l$, where Δd is the difference between neighbouring areas of maximum and minimum thickness, and l is the distance between these two points. Fig.3.7 shows the relation between carbon content and $\Delta d/l$. These results are in good agreement with previous findings and confirm the conclusion that surface cracks are most serious in the carbon range 0.1 - 0.2 wt% C.

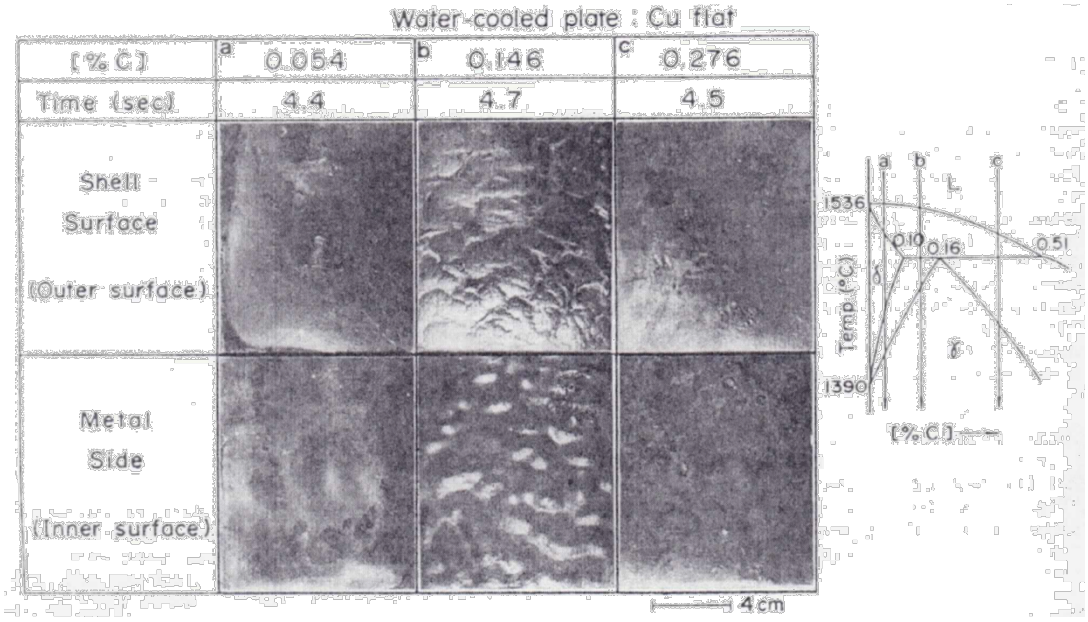

Fig.3.6 Appearance of shells containing 0.054, 0.146, 0.276 wt% carbon from dip tests. The composition of the specimens are shown on the Fe-C diagram [56]

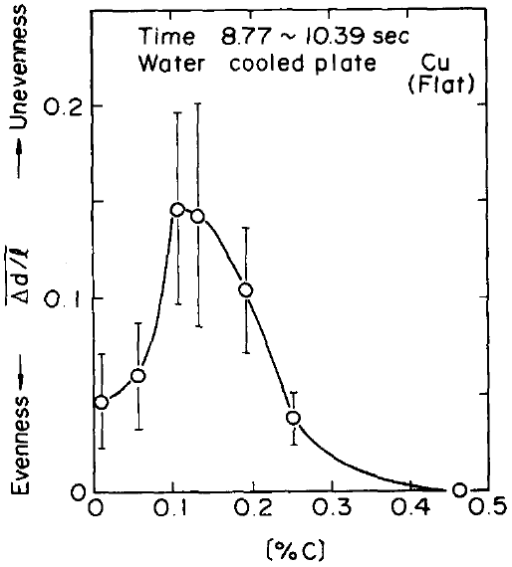

Fig.3.7 Effect of carbon content on the unevenness parameter Δd/*l* [56]

Suzuki *et al.* [5] calculated the amount of deflection of a solidifying shell based on their experimental observations and a comparison between low-carbon steel and hypo-peritectic steel is shown in Fig.3.8. Their calculations show that the maximum deflection decreased with increasing shell thickness and that the maximum deflection of a 0.126 mass%C (hypo-peritectic) steel is much larger than that of a 0.030 mass%C (low-carbon) steel. Since hypo-peritectic steels are stronger and shrinks more than low-carbon steels just below the solidus temperatures, the shell deflection of

hypo-peritectic steels is not straightened by the ferro-static pressure and hence remains larger, causing the anomalous decrease in heat transfer in the mould.

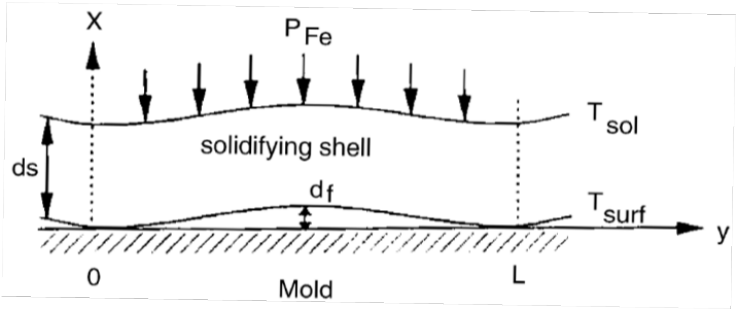

(a) Schematic diagram of the deflection of the solidifying shell in the mould

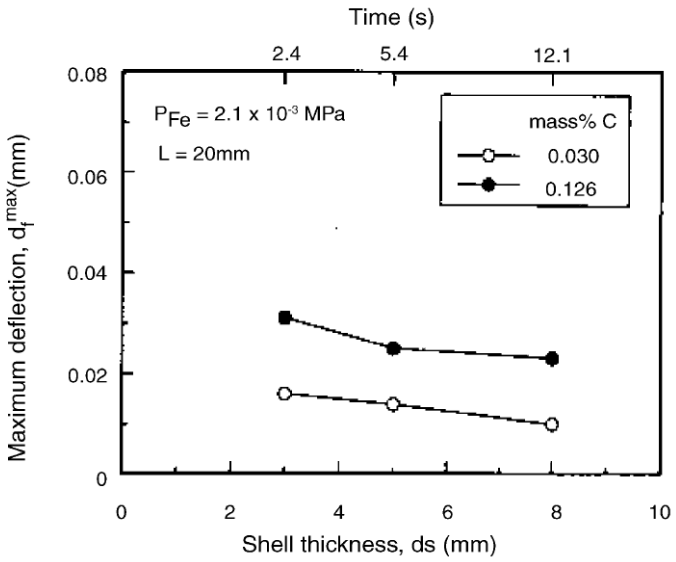

(b) Calculated deflection of solidifying shell

Fig.3.8 Air gap formation at the shell/mould interface caused by deflection due to thermal stress and counteracting ferro-static pressure during the solidification of steel shell in mould [5]

The air gap formed between shell and mould as a result of shell deflection particularly in peritectic steels, results in decreased heat extraction. This situation is summarized in Fig.3.9 [5, 56]. It follows that the mould temperature is lowest when casting carbon steel of near-peritectic composition, clearly an indication of a reduced heat transfer rate.

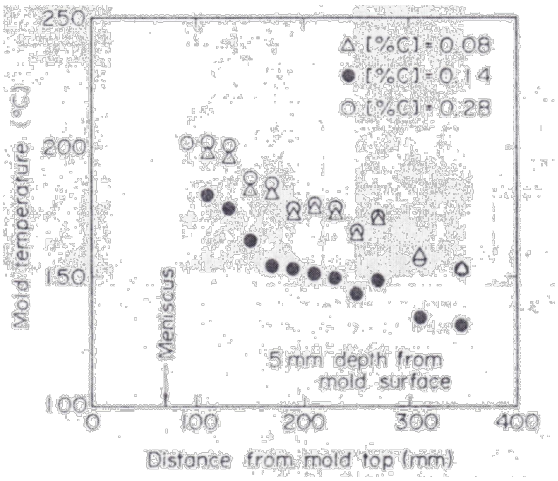

(a) Measured temperature in a pilot caster at the centre of the mould face, 5 mm below the meniscus [56]

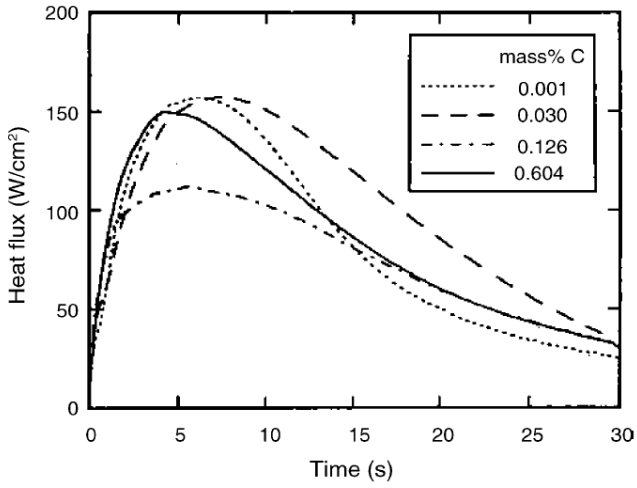

(b) Heat flux calculated from temperature measurements in a laboratory scale mould [5]

Fig.3.9 Reduced heat transfer rate due to air gap formation between shell and mould when casting steels of near-peritectic composition. (a) Measured mould temperature. (b) Calcualted hea transfer rate

In summary, stresses are generated as a result of solidification shrinkage and the δ→γ transformation during solidification of steel in a continuous casting mould. Because the shell is very thin in the initial stages of solidification, these stresses deform the shell and the shell detaches from the mould surface and the heat transfer rate is decreased. Apart from surface cracks that may form as a result of the development of these ‘hot spots’, breakouts can also occur when the thin solidifying shell cannot support the ferro-static pressure.

3.1.3 Surface Defects Attributed to the Peritectic Phase Transition

Longitudinal facial cracks and transverse cracks are the two main types of surface defect, which are most common and constitute serious problems during the production of steels of near-peritectic composition.

Konishi *et al.* [50] proposed a mechanism for the formation of longitudinal cracks. They argued that 'hot spots' are created on the shell surface in the meniscus region of the mould in addition to the stresses generated by the δ→γ transformation. In order to estimate the development of longitudinal cracks, a shrinkage model was used to determine the stresses in the transverse direction of the solid shell. A comparison of the tensile stress developed at the shell surface in the mould under the low, medium, and high heat-fluxes to the ultimate tensile strength of the steel under these heat-flux conditions, is shown in Fig.3.10.

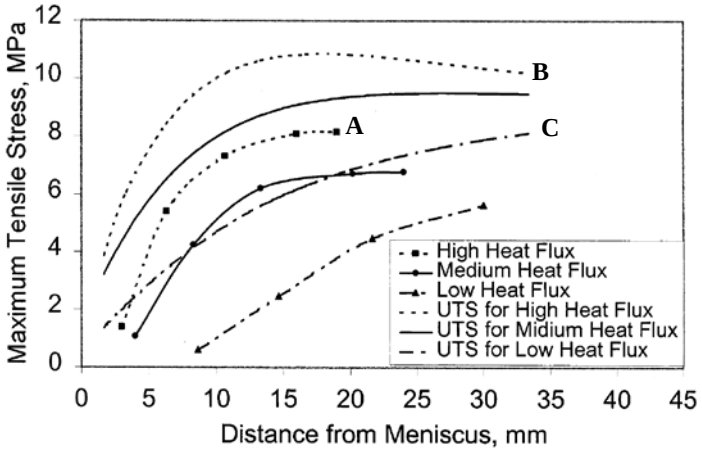

Fig.3.10 Comparison of UTS and computed maximum tensile stresses at shell surface under different heat-flux conditions [50]

This figure needs to be considered in more detail. In operational practice, a decrease in the meniscus heat flux is considered to be one of the most effective ways to prevent the generation of longitudinal cracks because stress generation is decreased. However, decreasing the meniscus heat flux also causes a decrease in the strength of the shell (assessed as the UTS), since the solid shell temperature will increase with decreasing heat flux. Consider now curves A and B in Fig.3.10. Curve A represents the maximum stress that develops at the solidifying shell under high heat flux conditions. Curve B is the UTS of the steel under the same heat flux conditions. The figure shows that even when the tensile stresses at the shell surface are increased, the maximum tensile stress is always below the UTS. Therefore, increasing the heat flux by itself would not cause longitudinal crack formation. However, if the heat flux is locally reduced, the local maximum tensile stress can exceed the UTS as shown in Fig.3.10 by comparing curves A and C. For example consider the

situation 10 mm below the meniscus under high heat flux conditions. The maximum tensile stress is 7 MPa while the UTS of the steel at this position in the mould is 10 MPa and no cracking will occur. However, if the heat flux is locally reduced, (curve C), the UTS is reduced from 10 MPa to 4.5 MPa and under these conditions it is most likely that cracks will initiate.

It follows from the arguments above that the formation of longitudinal cracks during continuous casting of peritectic steels is related to the stress generated by the δ→γ transformation and hot spots that form in the meniscus region of the mould. This implies that in order to eliminate longitudinal crack formation, uniform heat removal in the meniscus region is of the utmost importance. If the heat extraction is uniform, the tensile stress at the shell surface does not exceed the UTS of the shell surface even under high heat-flux conditions, and cracking is not a problem. However, the practical way to eliminate longitudinal cracks when casting at high speeds is to reduce the heat flux in the meniscus region, because as the heat flux increases (i.e. cooling rate increases), the maximum temperature fluctuation permissible before cracking occurs decreases [50].

Apart from a reduction in heat flux due to the formation of depressions, hot spots may also be generated by temperature fluctuations at the shell surface caused by other operational issues such as irregular heat transfer in the meniscus region due to metal level fluctuations or non-uniform infiltration of mould flux. As an example Fig.3.11 schematically depicts the situation of metal level fluctuations. The δ→γ transformation commences at the meniscus; i.e., at point A at the top of the wave and at point C at the bottom of the wave. Below the wave top the transformation is completed at point B, which is adjacent to point C, where the transformation has just commenced. The differential behaviour and resulting shrinkage may cause the bucking of the shell and the generation of a hot spot.

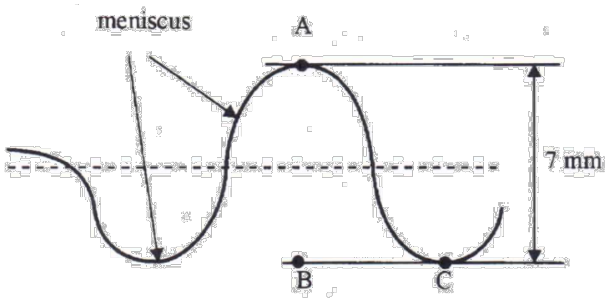

Fig.3.11 Schematic diagram of the meniscus shape resulting from a surface wave [50]

Emi *et al.* [57] summarized the sequence of events that leads to the occurrence of longitudinal facial crack in steel of peritectic composition as follows:

- When a peritectic steel melt is subject to initial solidification in the mould, a thin shell forms along the periphery of the mould near the meniscus. The contraction upon solidification and subsequent cooling of the shell impose hoop stresses on the shell. The contraction is greater for hypo-peritectic steels due to the peritectic transformation.
- Immediately after the thin shell is formed, a molten layer adjacent to the shell solidifies and then the shell buckles against the mould. This is because the contraction of a newly solidified shell onto the already solidified shell exceeds that of the original shell. This buckling should remain local due to the balance among the ferro-static pressure, the buckling force and the hoop stress. The lifted region due to buckling is reheated, forming the hot spots.
- The lifted region experience tension due to stretch-bending during the lifting according to beam-bending theory. Steep temperature gradients developing across the shell on further cooling in the mould impose additional thermal stress on the shell.
- When the sum of all the above stresses surpasses the fracture strength of the shell, tear at the hot spots, i.e. longitudinal facial cracks occur.

Fig.3.12 is a practical example of the occurrence of longitudinal facial cracks providing support to the arguments advanced above.

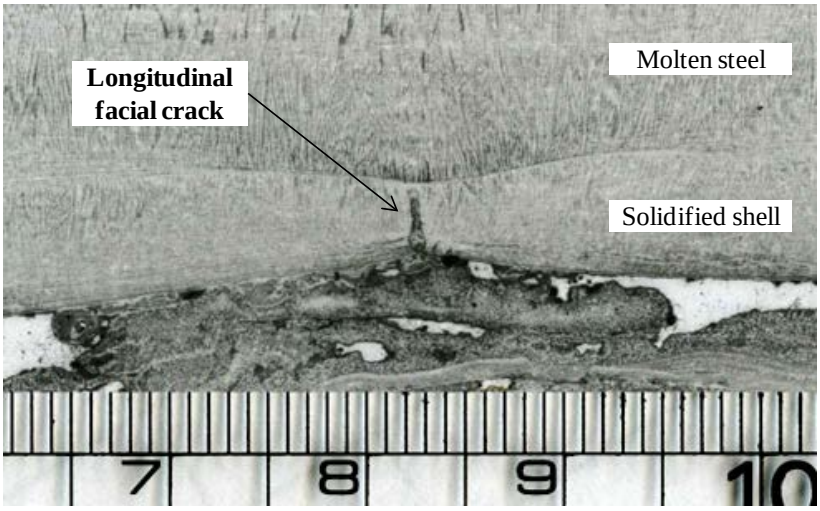

Fig.3.12 Cross section of a depressed area showing the occurrence of longitudinal facial cracks on the shell surface due to depression. Etched by picric acid for delineating liquid/solid interface (found near breakout point of slab in a thin slab caster, Gwangyang Works)

Another problem of producing peritectic steel in continuous casting practice is transverse cracking, which usually initiates at oscillation marks at the slab surface. Badri *et al.* [8] showed that ultra-low-carbon steel (C < 0.01 %) and peritectic steels (0.09 - 0.17 %C) have the deepest oscillation marks while low- and high-carbon steels have much flatter surfaces. Peritectic steel grades experience deeper oscillation marks and surface shape variation (wrinkling) ostensibly due to the extra shrinkage of the delta-ferrite to austenite phase transformation combined with the high strength of austenite that will withstand flattening. In addition, peritectic and ultra-low-carbon steels distort much more during level fluctuations, compared to low- or high-carbon steels. Molten steel level fluctuations in the mould give rise to deep transverse depressions and oscillation marks.

Wolf [58] suggested that such depressions provide the chance of large prior austenite grain growth because of locally reduced cooling rates as a result of lack of contact between the solidified shell and mould wall. Weisgerber *et al.* [59] showed a strong relationship between oscillation mark depth and austenite grain size as evidenced in Fig.3.13. Also Takeuchi *et al.* [60] confirmed that coarse austenite grains are frequently observed at the roots of oscillation marks. The air gap developing between the solidified shell and mould especially at an oscillation mark, increases the thermal resistance to heat extraction from the slab surface, with a concomitant decrease in heat extraction rate, which in turn causes the temperature to increase in the vicinity of the oscillation mark, causing the development of large austenite grains.

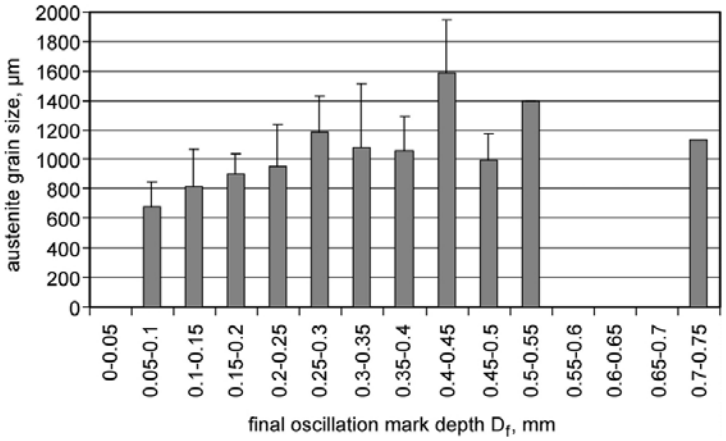

Fig.3.13 Austenite grain size as a function of final oscillation mark depth [59]

A coarse grained structure is detrimental to the ductility of steel, consequently leading to a higher cracking risk when the solidified shell is exposed to stress in the mould or in the strand [60-62]. Dippenaar *et al.* [63] established that transverse surface cracks are invariably inter-granular and follow along boundaries of exceptionally large prior-austenite grains which have a film of ferrite along the grain boundaries. Tsai *et al.* [4] have shown experimentally that transverse cracks followed the soft ferrite film outlining such large prior austenite grains. By microscopically

analysing specimens that have been subjected to hot-tensile testing, Carpenter [64] also found that the cracks develop along ferrite films. Plastic deformation is concentrated in the ferrite films because the yield stress in ferrite is considerably lower than that of austenite in the two-phase region. Hence, cracks initiate in the ferrite films, leading to crack propagation.

Schmidt and Josefsson [65] provided evidence that transverse surface cracks only occur in the presence of abnormally large austenite grains and Szekeres [66] provided an excellent example of transverse surface cracks in peritectic steel, seemingly initiated at the roots of oscillation marks as shown as Fig.3.14. It is quite clear that very large prior austenite grains and some transverse surface cracks are associated with the oscillation marks; that the cracks ostensibly developed along oscillation marks; but not every oscillation mark is associated with a crack.

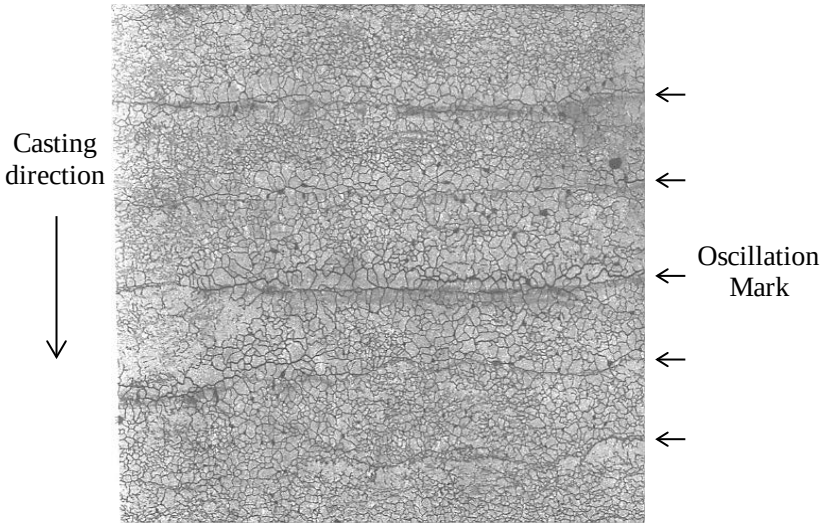

Fig.3.14 Large prior austenite grains along oscillation marks on the broad face of a continuously cast slab of peritectic composition. Also shown are transverse surface cracks that formed at the roots of oscillation marks [66]

3.1.4 Peritectic Transition and Prior Austenite Grain Growth

Maehara *et al.* [61] and Reiter *et al.* [67] have proven beyond reasonable doubt that the development of austenite grain following solidification of melt is determined by the dwelling time in the purely austenite phase region. They identified an equivalent carbon content of near the peritectic point as the composition related to the highest starting temperature for austenite grain growth and the largest austenite grains. The growth of austenite grains of a steel near the peritectic point occurred rapidly after the completion of either transformation to, or solidification into the γ

phase, for example the case of a 0.16 %C steel shown in Fig.3.15. Maehara *et al.* [68] summarized this grain coarsening effect on the hot ductility at the as-cast slab surface and on the surface cracking tendency as shown in Fig.3.16. Since the surface cracking occurs mostly with inter-granular fracture of austenite, the ductility should depend largely on the γ grain size. Thus, the grain growth behaviour of austenite during both solidification and cooling has been found that the γ grain size of as cast materials attains a maximum in the medium C range. Such a C dependence of austenite grain size corresponds to that of ductility loss and is in good agreement with the variation of austenite formation temperature in the Fe-C binary phase diagram.

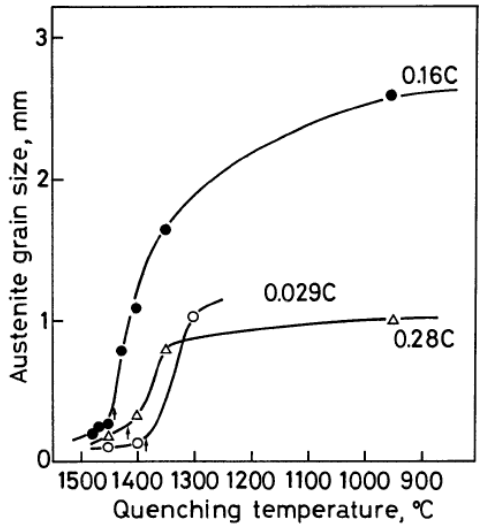

Fig.3.15 Grain growth of austenite during continuous cooling of 0.8 %Mn steels. The specimens were remelted at 1580 °C, cooled to a given temperature at a rate of 0.28 °C/s, and then quenched into water [61]

Uneven solidification due to the δ→γ transformation in steels with carbon content between 0.10 and 0.16 wt%C also results in coarsening of austenite grains as shown above. Maehara *et al.* [68] proposed a model to explain the impact of carbon content on the evolving γ grain structure in the mould by combining the effect of uneven solidification with the microstructural development of steels of different carbon content as shown in Fig.3.17. If the solidified shell is in close contact with the mould, the medium C steels will have a higher starting temperature for austenite grain growth and thus will develop larger austenite grains compared to the steels with higher or lower C content. Moreover the grains of the medium C steels will grow into columnar shapes. In addition to this effect, by the uneven surface solidification resulting from the peritectic reaction in the medium C steel, a local delay of cooling owing to lack of close contact with the mould will occur. This will enhance the coarsening of γ structure further, resulting in a very high surface cracking susceptibility.

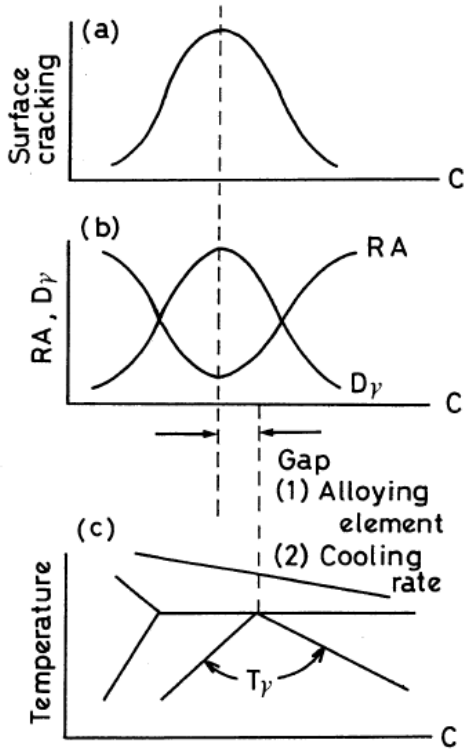

Fig.3.16 Dependence of (a) surface cracking frequency and (b) ductility (RA) and γ grain size D_γ of as-cast steels on carbon and (c) their relation to γ completion temperature T_γ (schematic). The 'gap' in C content between the peritectic point in (c) and peak or trough in (a) or (b) can be explained in terms of alloying elements and cooling rate through the segregation of impurity elements [68]

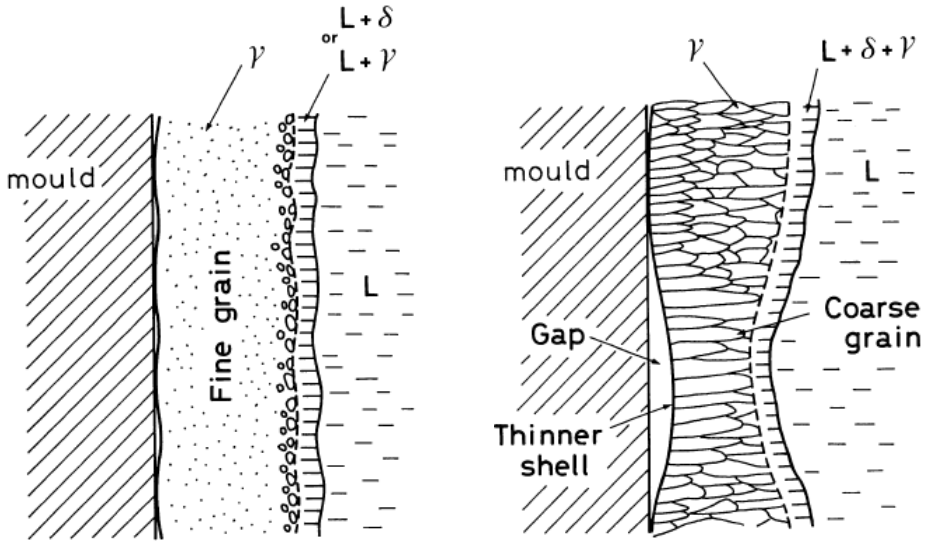

(a) Low- or high-carbon steel (b) Medium-carbon steel

Fig.3.17 Schematic austenite grain structure in a solidified shell [68]

3.2 Controlling Uneven Solidification

Many studies have been conducted in an attempt to reduce the risk of cracking or breakouts in producing peritectic steels by continuous casting techniques. The most common and practical approach in industry has been avoiding a composition design close to the peritectic range. This is generally done by the addition of suitable alloying elements, but this approach adds additional cost. In the section below, several other practical approaches aimed at controlling uneven solidification will be summarized.

3.2.1 Mild Cooling in the Mould

It is well established through our experiments in the high-temperature laser-scanning microscope that the rate of the $\delta \rightarrow \gamma$ transformation decreases at lower cooling rates, i.e. at lower rates of heat transfer accordingly less stress will be generated compared to stress development at higher cooling rates. When this fundamental information is translated to practical continuous casting practice, it implies that the design of a mild cooling strategy in the meniscus region of the mould will result in less thin-shell deformation. A lower propensity towards thin-shell deformation will in turn reduce the risk of hot-spots formation, thereby preventing longitudinal facial cracking. It will also lead to reduced austenite grain coarsening and hence, reduce the risk of the formation of transverse cracks especially at the roots of oscillation marks.

Murakami *et al.* [56] experimentally examined the effect of cooling intensity on the unevenness of shell of hypo-peritectic steels using a dip tester by varying the material, the thickness, and water the flow rate through a water-cooled mould plate in a dip tester. They used heat resistance R_t as a measure of cooling intensity as expressed by $R_t = D_c/\lambda + 1/h_w$ where D_c is the plate thickness, λ is the thermal conductivity and h_w is the heat transfer coefficient in the cooling slit of the mould. Fig.3.18 shows the relation between R_t and the un-evenness parameter $\triangle d/l$ as discussed in the previous section. $\triangle d/l$ decreased with an increase in higher heat resistance, i.e. as the water flow rate decreases and as the plate material has lower thermal conductivity. They confirmed that mild cooling is an effective means of reducing uneven shell growth in peritectic steels. However, it has to be borne in mind that because mild cooling leads to the formation of a thinner shell, there is an increased risk of breakouts below the mould, especially at higher casting speeds.

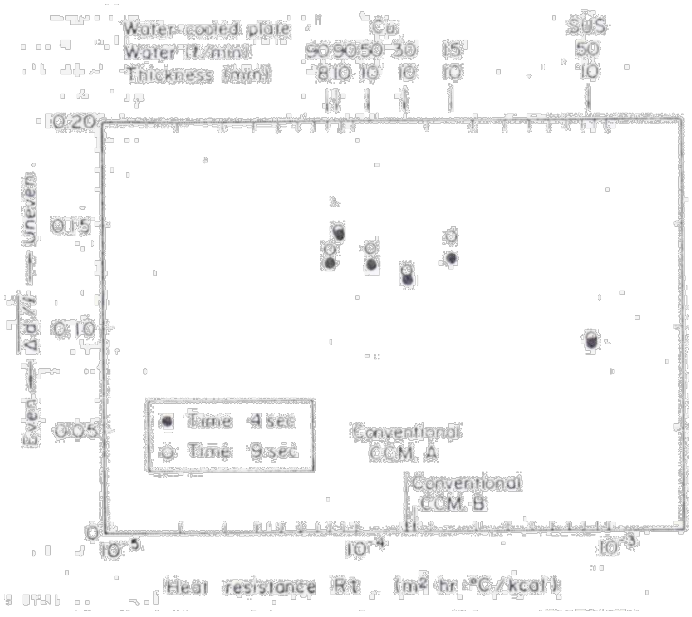

Fig.3.18 Effect of heat resistance R_t on the un-evenness parameter $\Delta d/l$ of the shell in a dip test [56]

3.2.2 Uniform Heat Transfer

Konoshi *et al.* [50] indicated that the formation of longitudinal cracks during continuous casting of peritectic steels is related to stress generation as a result of the $\delta \rightarrow \gamma$ transformation and the appearance of hot spots in the meniscus region as discussed above. They contended that in order to eliminate longitudinal cracks, uniform heat removal in the meniscus region is of utmost importance. If uniform heat extraction is achieved the tensile stress at the shell surface does not exceed the UTS of the shell surface, even under high heat-flux conditions and there is no cracking problem (see Fig.3.10). However, the practical approach taken in operational practice to eliminate longitudinal cracks when casting at high speeds, is to reduce the heat flux in the meniscus region, because as the heat flux increases (i.e. cooling rate increases), the maximum temperature fluctuations permissible before cracking occurs decreases. In operating continuous casting practice uniform heat transfer is approached by keeping a stable molten steel level in mould and ensuring that there is stable infiltration of mould flux into the gap between the solidifying shell and the mould, thereby maintaining a constant film thickness in the meniscus area and maintaining a constant crystalline/glass ratio in the film.

3.2.3 Mould Flux

It is well established in operational continuous casting practice that the most effective way to control cooling conditions in mould is to manipulate the properties of the mould flux.

Emi *et al.* [57] contended that the mould flux slag film controls the heat flux from the shell to mould by the following thermal resistances :

- Thermal resistance to conduction through the slag film
- Thermal resistance to radiation through the slag film
- Irregular contact between solidified slag film and mould

Cho *et al.* [69] introduced a schematic illustration of the resistances between the solidifying shell and the mould as shown in Fig.3.19. The film of mould flux in close proximity to the meniscus consists of three different layers: a molten slag layer; a solid crystalline layer and an air gap at the mould/mould flux film interface. They showed that the size of the air gap is a function of the specific mould flux used such as the ease and extent of crystallization of the molten slag. The resulting thermal resistance due to air gap plays an important role in the overall heat transfer in the mould as shown in Fig.3.20. An increase in thickness of the crystalline layer clearly leads to an increase in thermal resistance at the mould flux film/mould interface.

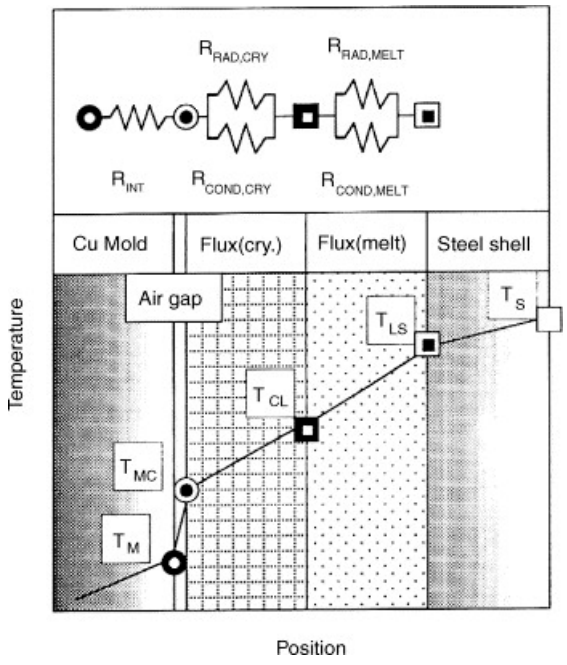

Fig.3.19 Modelling of heat transfer across the mould flux film to the continuous casting mould [69]

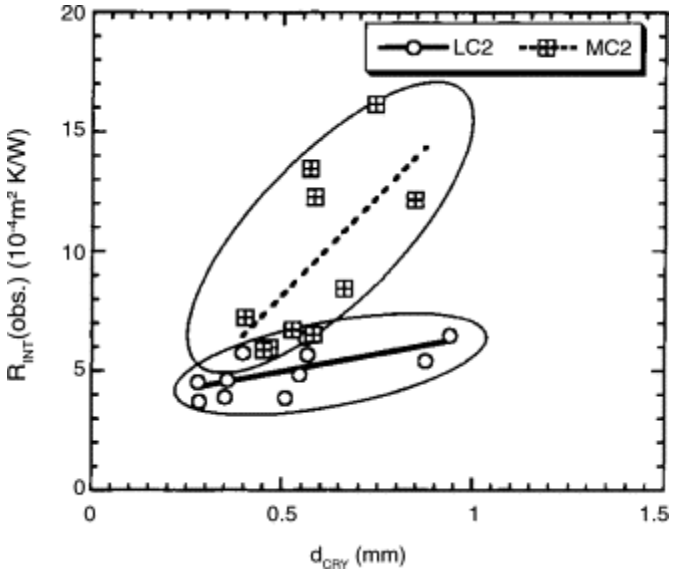

Fig.3.20 Increase in thermal resistance at the mould flux film/mould boundary as a function of the thickness of crystallized mould flux film in two different mould fluxes (Crystallizing temperature : LC2 - 1316 K, MC2 - 1436 K, Basicity CaO/SiO_2 : LC2 - 0.96, MC2 - 1.41) [69]

With regard to controlling uneven solidification, an increase in thermal resistance in the vicinity of the meniscus by using a mould flux with a larger fraction of crystallization, implies that the $\delta \rightarrow \gamma$ transformation will occur at a lower rate, which in turn results in the formation of a uniformly solidified shell. Kromhout *et al.* [70] provided convincing evidence obtained from in-plant trials that solidification within the first 200 mm under the steel meniscus is critical to the formation of a homogeneous steel shell and thus for the stability of the remaining part of the casting and slab quality. When using a mould flux with mild cooling properties, thanks to the outstanding effect of mild cooling near the meniscus, the redistribution of local mould heat transfer at the wide face of the mould occurs as shown in Fig.3.21. Reduced mould heat transfer in the upper part of the mould compared to a reference mould flux (where the reference resulted in uneven solidification) plays an important role in preventing uneven solidification during the early stages of solidification resulting in improved contact between shell and mould in the entire mould. As a result of maintaining more intimate contact between shell and mould in the upper region of the mould, the heat transfer rate in the lower part of the mould is increased (compared to the reference mould flux) leading to an increase in the shell thickness at the mould exit.

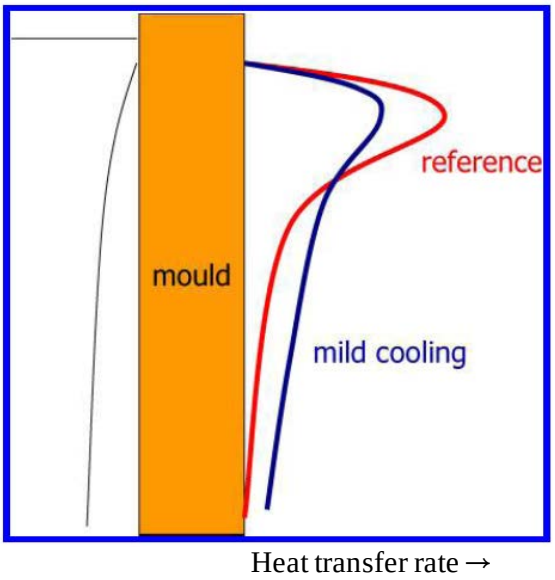

Fig.3.21 Redistribution of local mould heat transfer rate during casting as found during plant trials at a thin slab caster: a reduced mould heat transfer in the upper part of the mould, and an increased mould heat transfer in the lower part of the mould while maintaining a comparable average mould heat transfer rate [70]

A practical example of the schematic illustration in Fig.3.21 is shown in a mould flux trial shown in Fig.3.22. In this instance the mould flux was changed halfway through a casting sequence from a reference mould flux to a 'mild-cooling' mould flux. Following the change-over to 'mild-cooling', the contact between the thin solidifying shell and the mould is improved on the wide faces of the mould (BROADE = Broad face east and BROADW = Broad face west). This improved contact results in a higher heat extraction rate and as a consequence, a thicker shell in the lower part of the mould. The increased heat transfer rate will in turn lead to shrinkage of the shell on the broad faces and decreased contact on the narrow faces (narrow north and narrow south). The decreased contact on the narrow faces will cause the heat transfer rate to decrease hence, the observed decrease in heat transfer rate shown in Fig.3.22. This does not cause a problem in operational practice because the decreased heat transfer rate on the narrow faces can easily be compensated by adjustment of narrow face taper.

These conclusions have been verified by microscopic analysis, which showed that the use of a 'mild-cooling' mould flux provided a more homogeneous chill zone structure in the solidified shell.

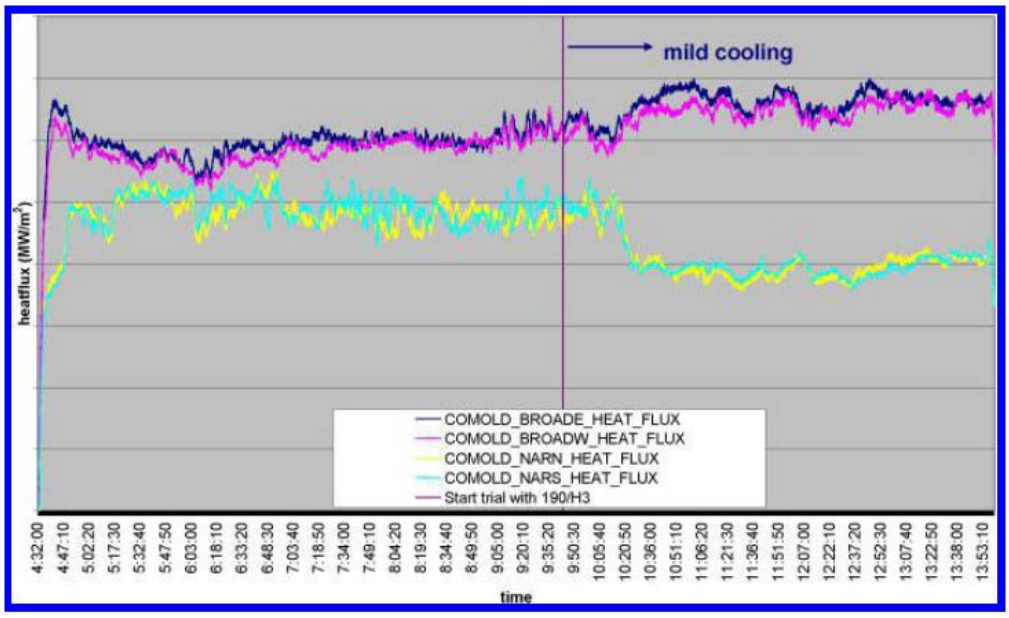

Fig.3.22 Average mould heat transfer (mould cooling water) during mould flux trial; DSP caster, V_c=5.4 m/min [70]

However, notwithstanding many efforts to develop ‘mild-cooling’ mould fluxes that are to be used for demanding steel grades many practical difficulties have been encountered. One way of achieving the ‘mild-cooling’ characteristics is increase the extent of crystallization in the mould flux. However, in doing so, the ability of the mould flux to provide effective lubrication is decreased. For example, by increasing the fraction of crystallization, the softening point and viscosity is increased thereby impeding smooth inflow of slag film into the gap in the meniscus region, which is likely to lead to sticking type breakouts, especially at high speeds in a thin slab caster [57, 71].

3.2.4 Mould Texturing

Another strategy to ensure even shell growth is to use a textured mould surface. There has been several trials of mechanical texturing such as shot blasting [72] or grooving [73] of the mould surface in an attempt to reduce mould heat transfer by locally increased the slag film thickness without decreasing effective mould lubrication. In principle, this is a similar approach to increasing the fraction of crystallization in a mould flux because texturing will also increase the thermal resistance in the immediate vicinity of the textured surface. It has also been argued that surface texturing improves surface roughness of slab by controlling nucleation and dispersing thermal and transformation strains [71]. A relatively fine surface roughness or small groove pitch are usually

used for even control of the heat transfer rate.

In contrast to the fine-grooving strategy, Murakami *et al.* [56] used mould textures having several millimeters of rough pitch. The rationale behind this approach is that the dispersion of deformation sites in the shell due to the δ→γ transformation occurs at every groove and thus diminishing the air gaps between the solidified shell and the mould. They employed dip tests using hypo-peritectic steels and a water cooled plate with longitudinal or lattice grooves with the groove interval 5.0 mm, depth 0.5 mm and width 0.5 mm. Fig.3.23(a) shows the appearance of shells on the flat plate, the plate with longitudinal grooves and lattice grooves. When using longitudinal grooves, the outer surface of the shell had depressions, and the shell became thinner at the depressions parts. When lattice grooves were used, there were no noticeable depression sites or uneven surface except for groove marks, and the shell was more even as shown in Fig. 3.23(b).

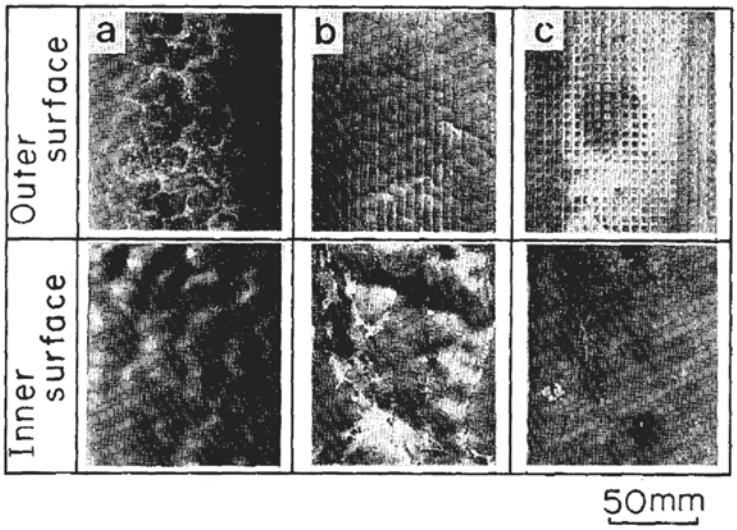

(a) Effect of surface conditions of water cooled plate on shell formation of hypo-peritectic carbon steel (Dipping time = 9.0 s)

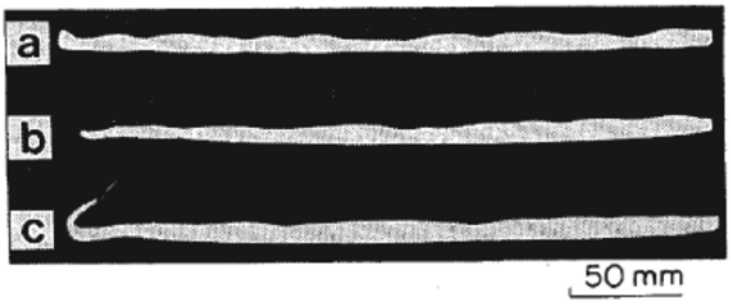

(b) Longitudinal cross section of the shell from dip tests

Fig.3.23 Effect of surface conditions of water-cooled plate on shell formation [56] (a：Flat Plate, b：Plate with longitudinal grooves (groove interval=5 mm, width=0.5 mm), c : Plate with lattice grooves (groove interval=5 mm, width=0.5 mm))

Murakami *et al.* [56] obtained the pertaining heat transfer rates by one-dimensional heat calculation on differential calculus as shown in Fig.3.24. The heat transfer rate for the water-cooled plate with lattice grooves was larger than that of the flat plate. The more even the shell, the larger the heat transfer rate, resulting in more growth of the shell on the plate with lattice grooves than on the flat plate for the same dipping time, as shown in Fig.3.23(b).

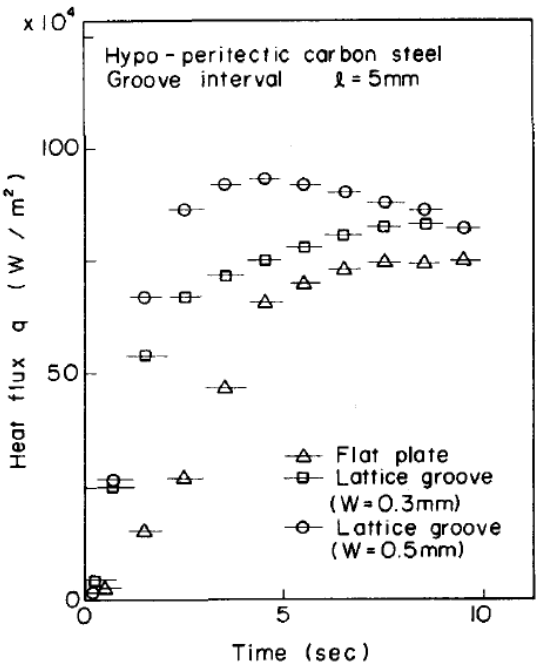

Fig.3.24 Effect of the surface condition of the water-cooled plate on heat transfer rate (W=groove width) [56]

They proposed the mechanism of shell growth in hypo-peritectic carbon steel, which is schematically shown in Fig.3.25 [56]. Solidification shrinkage and transformation shrinkage resulting from the $\delta \rightarrow \gamma$ phase transition bends the thin shell in the initial stages of solidification on a flat plate. The shell detaches from the mould surface at an average interval of 10mm under the pertaining heat transfer conditions in the dip test. The shell partially loses contact with the plate, heat transfer at these detached areas decreases and solidification is delayed as shown in Fig.3.25(a). On the other hand, on a plate with lattice grooves at smaller intervals than the depression interval, solidification is slightly delayed at the grooves. Since the groove interval fixes the deformation interval of the shell bending of the shell is decreased and the air gaps become smaller. Hence, contact between the shell and the plate is improved, and the shell forms evenly as shown in Fig.3.25(b).

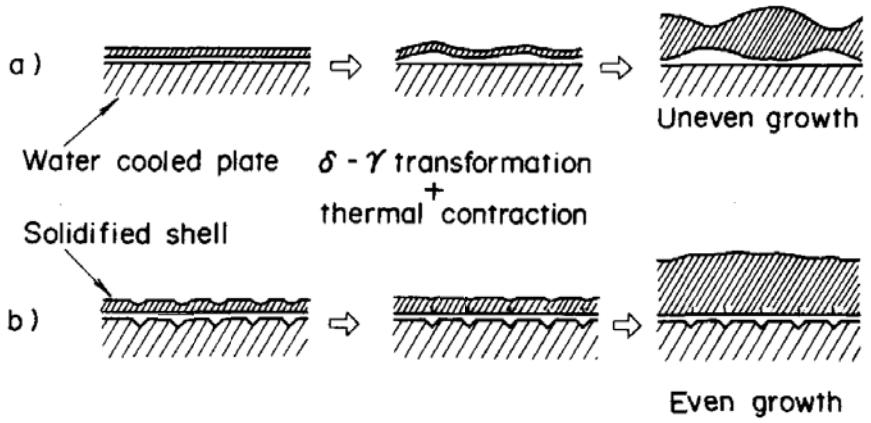

Fig.3.25 Mechanism of shell growth in hypo-peritectic carbon steel in the initial stages of solidification on a flat plate (a) and on a plate with lattice grooves (b) [56]

In another set of laboratory scale experiments, a mould flux was used in addition to using a nickel plated lattice grooved mould as shown in Fig.3.26. The thin Ni plating was applied on the mould surface in order to eliminate the friction between the groove and shell, which is likely to cause a sticking type breakout. They assessed groove spacing of 5, 10 and 20 mm and nickel plating of 0.1 and 0.5 mm and found the most effective lattice groove spacing to prevent surface unevenness in hypo-peritectic steel to be 10mm and the nickel plating thickness 0.1 mm. Using a mould flux with low heat resistance (lower crystallization temperature, thus fast-cooling) provided the best and most stable shell thickness profile as shown in Fig.3.27. This finding is contrary to many previous studies that have shown that mild-cooling is beneficial for producing peritectic steels. The reason was further explained by that in order to maximize the dispersion effect of deformation sites in the shell by groove, the difference in heat transfer rate between groove area and centre position between grooves should be maximized

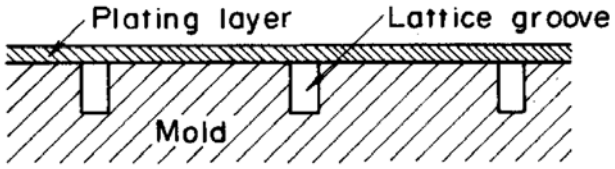

Fig.3.26 Schematic view of plating mould which includes lattice grooves cross section [56]

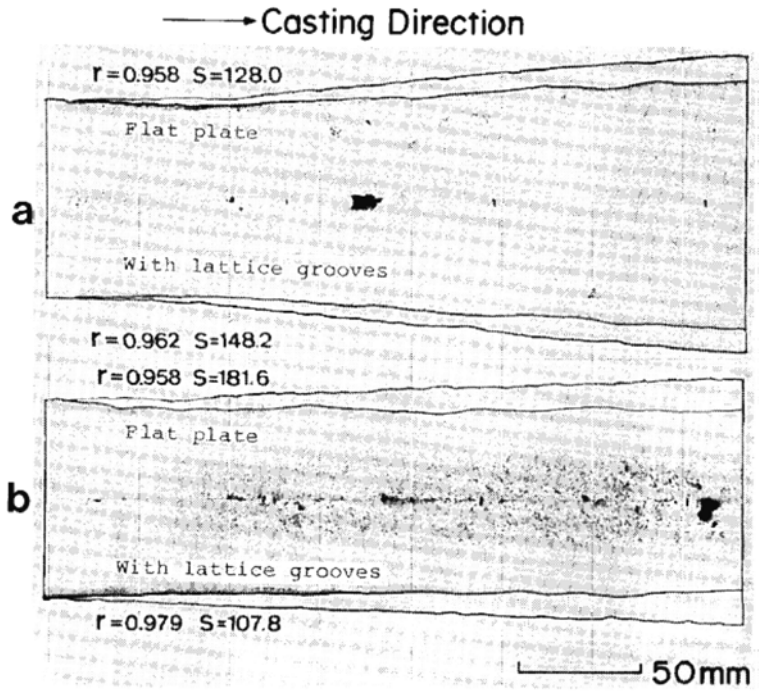

Fig.3.27 S-print images showing the effect of combination of a mould containing lattice grooves and mould flux on improvement of uneven shell formation [56] (Crystallization temperature of mould flux, a : 1145 °C, b : 1020 °C, unevenness parameter r and S from the shell thickness evaluation, the more even the shell, the closer r to 1.0 and the smaller S)

A ratio of partial heat transfer rate at the groove position (q_a) to that at the centre between grooves (q_{cu}) was calculated and the effects of plating thickness and groove width were estimated as shown in Fig.3.28.

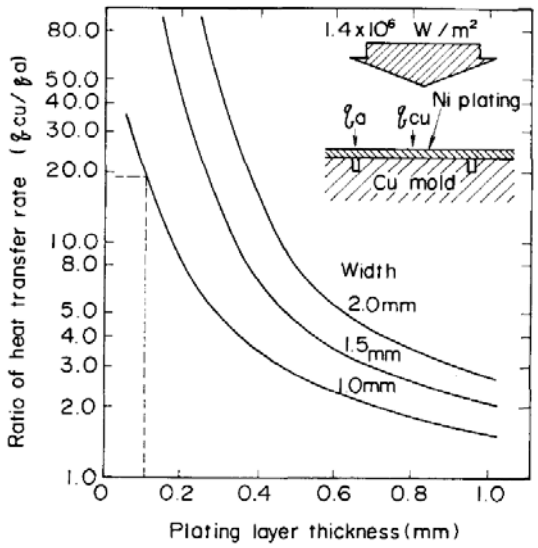

Fig.3.28 Effect of plating thickness and groove width on ratio of heat transfer rate (q_{cu}/q_a) in mould [56]

Under 1.0 mm groove width same as the test condition, with 0.5 mm plating thickness, q_{cu}/q_a was equal to 2.7 and was not enough for even dispersion of shell deformation resulting in uneven shell formation. But with 0.1 mm plating thickness the calculated q_{cu}/q_a was about 20 and the shell was most even. Therefore, q_{cu}/q_a may need as high as possible to prevent uneven shell growth. The plating thickness must be as thin as possible to increase q_{cu}/q_a. In a similar vein, it becomes more preferable to use lower heat resistance mould flux.

Chapter 4. In-Plant Analysis of Off-Corner Cracking of Titanium Bearing Steels close to the Peritectic Composition in a Thin Slab Caster

4.1 Background of Study

POSCO recently developed an in-line endless cast-rolling mill process, which has significant benefits over and above conventional continuous casting and rolling processes. The schematic layout is shown in Fig.4.1. The benefits of this process include reduced capital investment, reduced running cost, variety of steel grades that can be produced and homogeneous product quality.

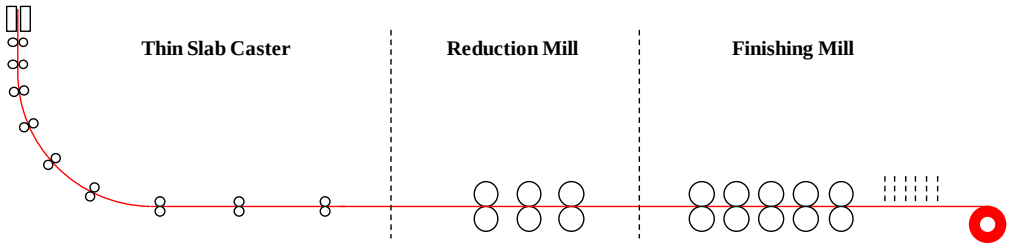

Fig.4.1 Schematic layout of in-line endless cast-rolling mill plant in Gwangyang, POSCO

The uniform and flexible temperature control that can be maintained throughout the process is especially beneficial for the production of high strength steels of minimum thickness which has been a bottleneck in finishing rolling mill operations in the conventional process due to the very high rolling forces required when producing these products. Because much lower rolling forces required in endless rolling operations, it is easier to produce high-strength products at much reduced thickness, normally containing micro-alloying elements for enhancing mechanical properties.

Titanium added steels where the titanium additions are typically more than 400 ppm have been produced in this process using the above benefit, however off-corner cracking in these steels has been a problem in the high-speed thin-slab casting operation of this process. It is not clear as to whether precipitation or the peritectic phase transition is the root cause of the problem. Fig.4.2 shows the image of off-corner cracks in hot-strip and Tab.4.1 shows the chemical composition of one of the main Ti-added steels.

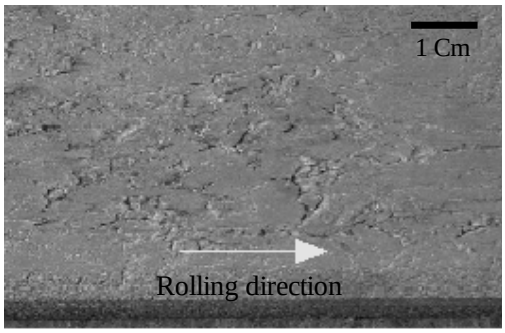

Fig.4.2 Image of off-corner cracks on hot strip

Tab.4.1 An example of composition of Ti-addition steel

Unit	C	Mn	Si	P	S	Al	Ti	N
wt%	0.061	1.434	0.021	0.0074	0.0011	0.02	0.115	0.009

4.2 Plant Data Analysis

The effect of carbon content on the formation of several surface defects in the thin-slab continuous casting mill has been studied by assessing inspection reports of the surface quality of some 68,802 of coils. The carbon equivalent is determined by the following equation, developed by Wolf [74].

$$C_{eq} = C+0.04\times Mn+0.1\times Ni+0.7\times N-0.14\times Si-0.04\times Cr-0.1\times Mo-0.24\times Ti \text{ (in weight \%)}$$

Fig.4.3 shows the longitudinal facial crack index (LFC) as a function of carbon content. The average LFC index increased in the order LC (low carbon), HC (high carbon), Hyper-peritectic, Hypo-peritectic grade showing well-known carbon dependency that is poor at peritectic carbon range. It shows peak value especially in the range 0.15 - 0.17 $\%C_{eq}$.

Traditionally, the occurrence of off-corner cracks in titanium containing steel was attributed to the decreased ductility in these steels as a result of grain boundary precipitation in austenite. When the slab is subjected to cooling in the secondary cooling zone in the caster, significant stresses are imposed on the solidifying slab and off-corner cracks can develop. However, more recently, titanium additions have been utilized in the steels near peritectic composition to adjust the properties of steel product considering mechanical strength and weldability and hence, the possibility that uneven solidification can be caused by the peritectic phase transition has to be considered. When the off-corner crack index is represented as a function of carbon content as shown in Fig.4.4, a peak in the index is found in the composition range 0.08 - 0.13 $\%C_{eq}$. However, most of steels in this carbon range are steels to which titanium additions have been made. Tab.4.2

shows that the average titanium content of this group of steels (in the carbon equivalent range 0.08 - 0.13 $\%C_{eq}$) is the highest. Accordingly, the fact that the tendency towards off-corner cracking showed peak value in the range of 0.08 - 0.13 $\%C_{eq}$ (Fig.4.4) can be interpreted that the root cause of the off-corner cracking problem might be related to the peritectic phase transformation.

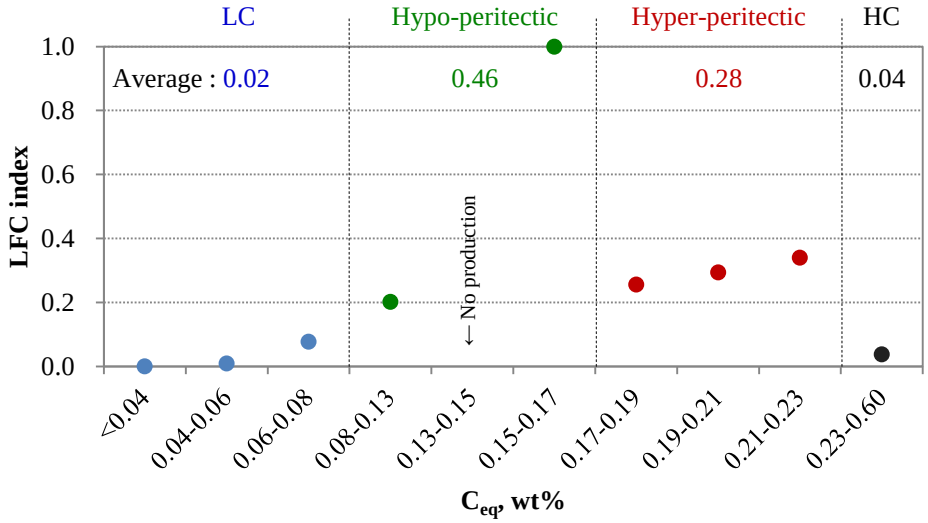

Fig.4.3 Relationship between the carbon content of a steel and the propensity towards longitudinal facial crack (LFC) formation in the thin-slab continuous casting mill at the Gwangyang Works

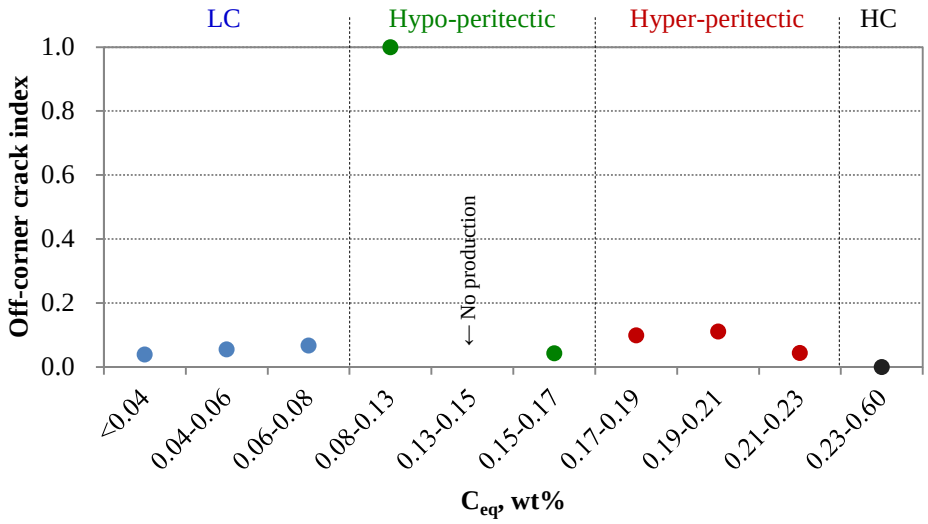

Fig.4.4 Relationship between the carbon equivalent content of steel and the occurrence of off-corner cracks in the thin-slab continuous casting mill at the Gwangyang Works

Tab.4.2 Average titanium content in each carbon group of the steels shown in Fig.4.4

C_{eq}, wt%	<0.04	0.04-0.06	0.06-0.08	**0.08-0.13**	0.13-0.15	0.15-0.17	0.17-0.19	0.19-0.21	0.21-0.23	0.23-0.60
Ti, ppm	24.3	3.8	12.1	**425.2**	-	3.9	3.0	19.4	6.0	16.5

4.3 Metallographic Examination

Fig.4.5 shows an off-corner crack on the surface of a transfer bar 20 mm thick that was reduced in thickness a 90 mm thick slab. The chemical composition of this steel is shown in Tab.4.1. Cracking occurred within 12 mm from the corner of the transfer bar.

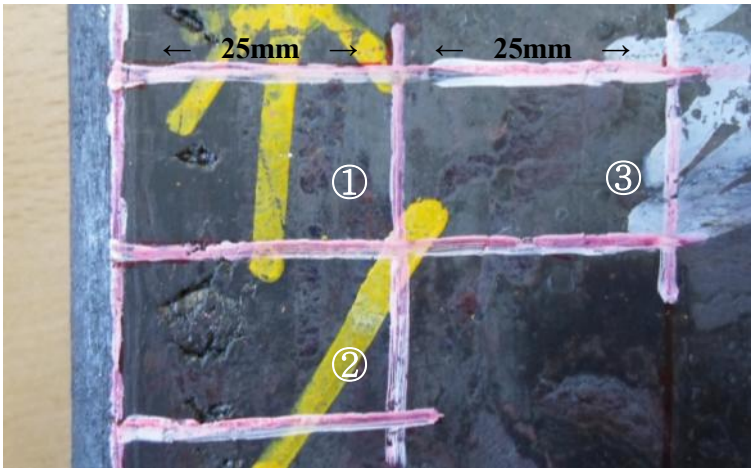

Fig.4.5 Image of an off-corner crack on the upper side of a transfer bar 20 mm thick, following reduction from a 90 mm thick slab in the roughing mill

For the purposes of exploring the possible origin of this defect, a series of metallographic analyses was conducted.

The sample was cut into pieces along the lines indicated in the figure and marked as ① and ② for samples containing cracking sites and ③ for a sample without a crack. 1 mm thickness of skin of all samples was removed and then the polished surfaces were etched in Nital. Fig.4.6 shows the images obtained from the optical microscope investigation.

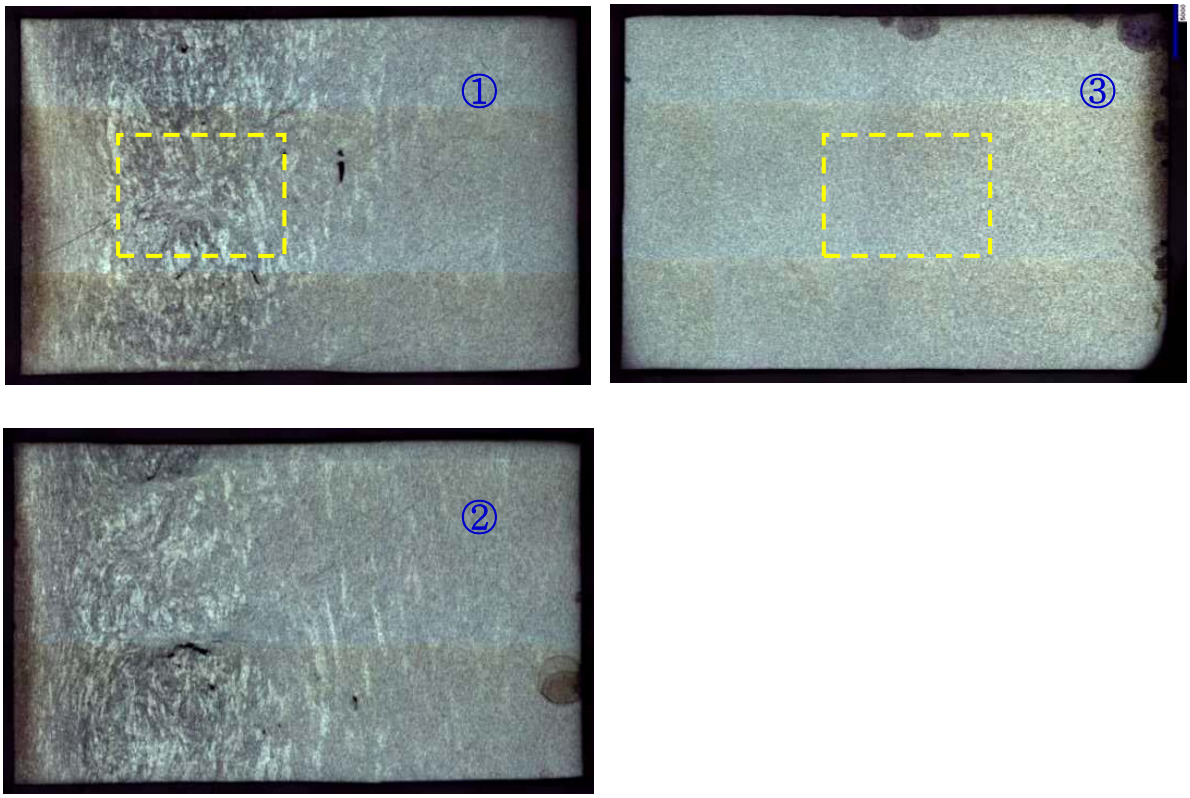

Fig.4.6 Images of samples etched with Nital (width of each sample is 25 mm - see Fig.4.5)

The examined area can be classified into two distinct regions: unevenly mottled region (left side of ① and ②) and a uniform region (right side of ①, ② and the total area of ③).

It is interesting to note that there is a distinct difference in structure between the areas where cracking occurred (mottled) and those in which cracks were absent. In order to explore these observations in more detail, the structures were examined at high magnification. The mottled region in sample ① and the uniform region in sample ③ (the broken-line rectangles in Fig.4.6) are shown in Fig.4.7 and Fig.4.8 respectively. In Fig.4.7, area ⓐ and area ⓑ marked as the broken-line rectangles shows the bright area and the dark area in the mottled region respectively. It is interesting to compare the grain sizes. From the observation at a magnification of a 1000 times, it follows that the base structure of the bright area in the mottled region is coarse-grained ferrite. Also, the grains in this region are larger than those in the uniform region as shown in Fig.4.8 and also much larger than the ferrite grains in the dark area of the mottled region (Fig.4.7ⓑ).

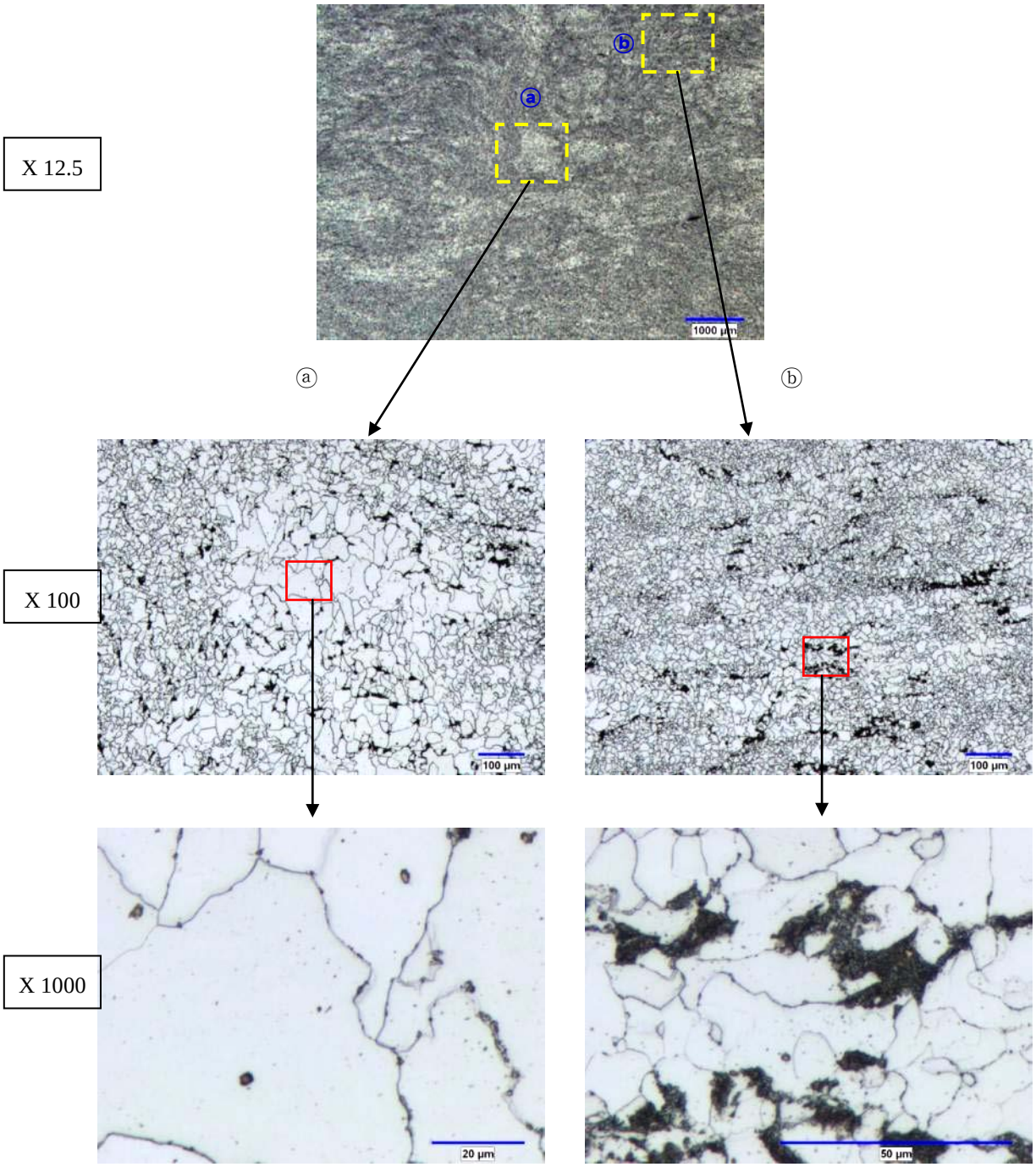

Fig.4.7 Optical microscopic observations of the mottled region in sample ① (the broken-line rectangle in Fig.4.6). Images ⓐ refers to the bright area and images ⓑ to the dark area

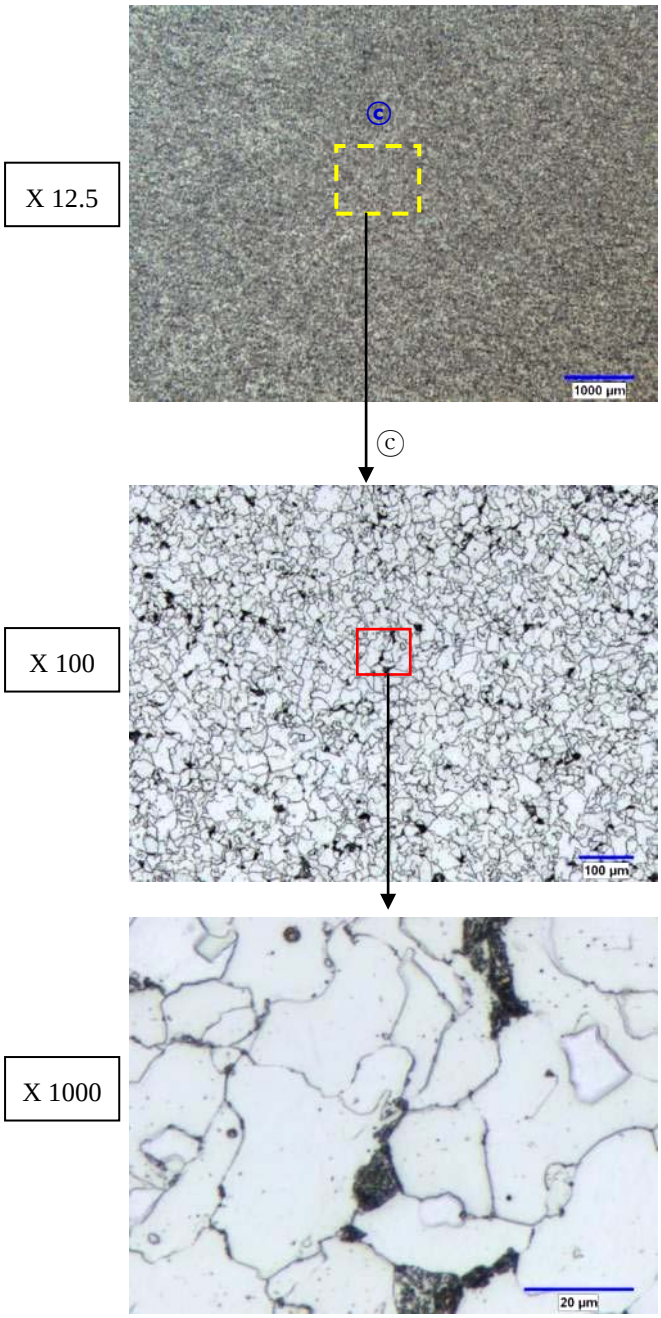

Fig.4.8 Optical microscopic observations of the uniform region in sample ③ (the broken-line rectangle in Fig.4.6)

On the other hand, irregularly shaped dark particles have been observed over all the area in the sample as shown in image ⓑ in Fig.4.7 and image ⓒ in Fig.4.8. In order to identify the structure within this dark area of the mottled region, SEM-analysis was conducted and Fig.4.9 shows compositional mapping of this area. It is clear that no alloying element segregation occurred in this irregularly shaped particle area.

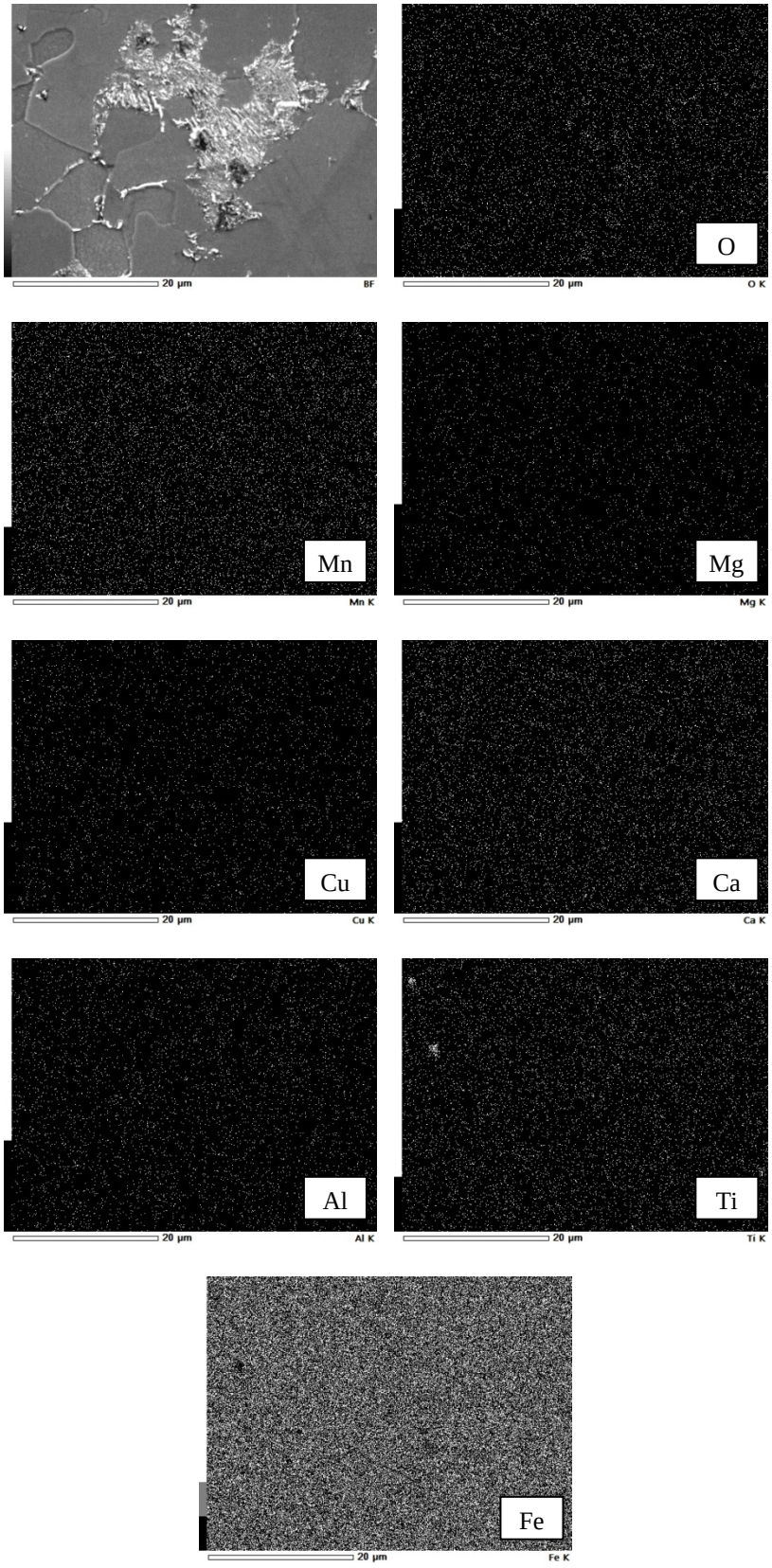

Fig.4.9 Composition mapping of an irregularly shaped dark particle observed in the dark area of the mottled region (shown as image ⓑ in Fig.4.7) using SEM-analysis

For further clarification of the irregularly shaped dark particles, the sample was polished in order to remove the etched layer and analyzed using FEG-SEM. Fig.4.10 shows one of electron beam images taken at many points across the sample. Irregularly shaped dark particles were not found in all examined areas. Thus, the irregularly shaped dark particles are thought to be artifact spots due to effect of preferential etching.

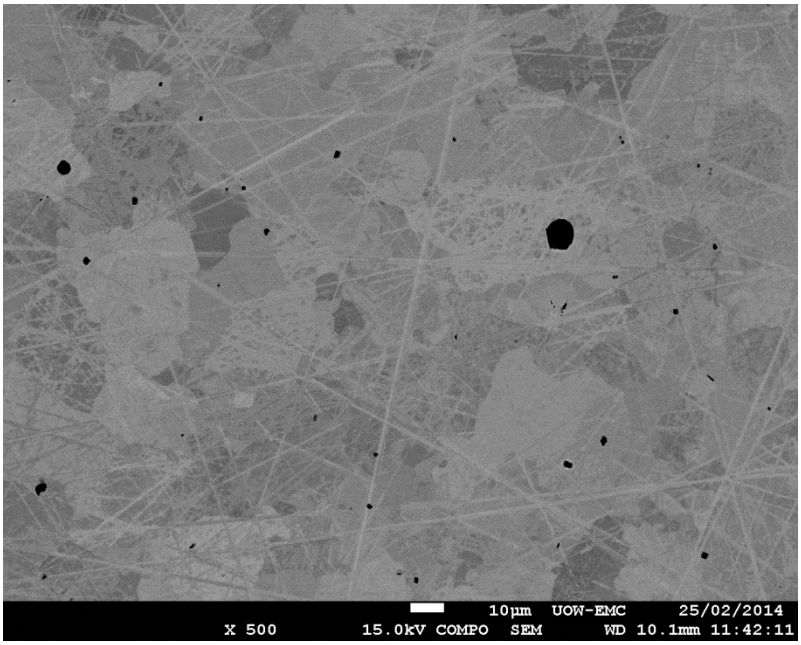

Fig.4.10 One of FEG-SEM electron beam images taken at many points across the sample

4.4 Grain Coarsening

The coarse grain structure in the bright area in Fig.4.7 might have originated from a large austenite grain structure. The background to this possibility is the following: in the endless rolling process, the 90 mm thick slab is reduced to a thickness of 20 mm in three consecutive rolling stands following very high continuous casting speeds as outlined in Fig.4.1 and hence, there is little opportunity to develop a fully recrystallized structure and remnants of the coarse grain structure could be retained. In contrast, during conventional continuous casting/rolling mill operations, the slab is cooled down and reheated before roughing is done in a reversing mill where large reductions in thickness are imposed in each rolling step. During soaking, the cast structure is homogenized to some extent and importantly, large reductions are applied during reversible roughing and in addition, sufficient time elapses between roughing steps to allow the development of a fully recrystallized structure. In the case of the endless rolling process, roughing is done in small reduction steps, at a high rate on a slab that has been slowly cooled from the delta-to-austenite transformation temperature and hence, there is sufficient time for the austenite grains to grow, but insufficient deformation to break down the coarse austenite structure and to allow for full recrystallization to occur.

In addition to general austenite grain growth, excessive grain coarsening at the roots of depressions and/or oscillation marks on the surface of the solidifying slab surface need to be taken into account. A coarse grain structure that can develop near the slab surface plays a role in the deterioration of ductility during continuous casting. These large austenite grains develop as a result of the much higher temperature at the roots of depressions and/or oscillation marks and when ferrite forms on further cooling, the stress is concentrated in the softer ferrite and as a result cracks grow in the thin ferrite layers. Szekeres [75] has schematically outlined this sequence of events as shown in Fig.4.11.

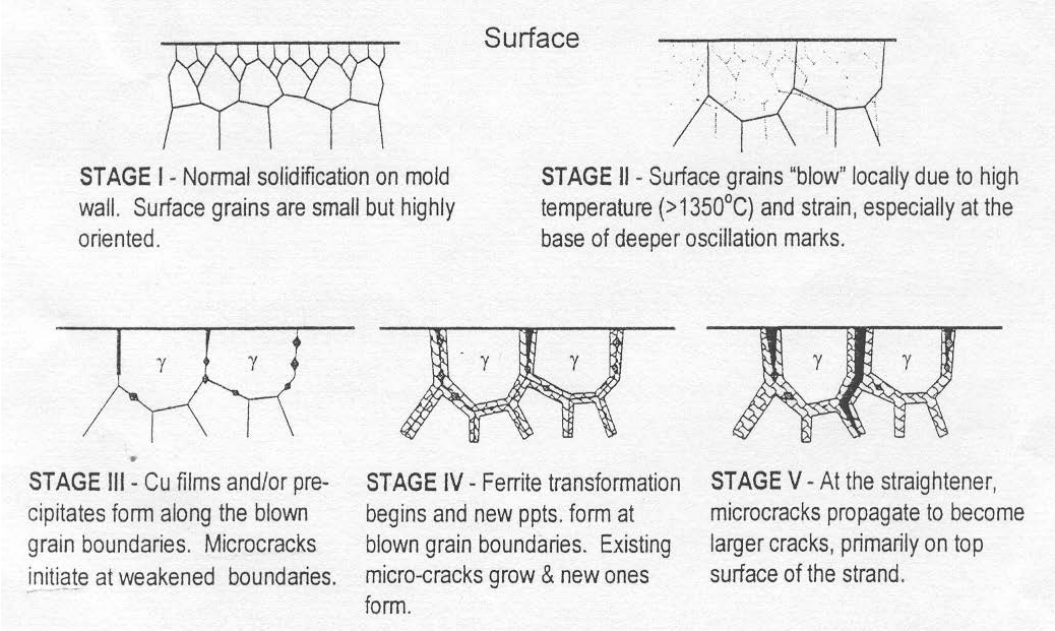

Fig.4.11 Formation of surface cracks due to the presence of 'blown grains' during casting as illustrated by Szekeres [75]

With respect to the present discussion, it is clear that the presence of an 'air gap' will render the same outcomes and hence, the formation of air gaps, especially in the meniscus region of the mould increases the propensity of crack formation. Wolf [58] suggested that large prior austenite grains form in such depressions (air gaps) because of locally reduced cooling rates as a result of lack of contact between the solidified shell and mould wall. Unstable continuous casting operation such as molten steel level fluctuations in the mould can give rise to the formation of 'air gap' such as deep transverse depressions or deep oscillation marks.

The formation of depressions (air gaps) in the off-corner area of a continuously cast thin-slab, leading to grain coarsening, is clearly illustrated in Fig.4.12(a). This figure shows a part of a breakout shell from a low-carbon steel close to peritectic composition from thin-slab caster having several depressions at the inner shell surface in close proximity of the corner region. These depressions must have formed as a result of a locally reduced cooling rate as a result of an air gap between the solidifying shell and mould. (No depressions were found on the outer shell of the breakout shell - the reason being that the embossed area between depressions on the outer shell was flattened by the reduction of the slab thickness by 10mm between the guide rolls just below the mould exit, while at the same time deepening the inner depressions. These macroscopic observations were augmented by further analysis at microscopic level. Samples were prepared to compare grain sizes between depressions and 'normal areas' as shown in Fig.4.12(b). It was possible to reveal the presence of prior austenite grains just before breakout because the hollow shell was quenched by spray cooling water just after breakout due to drainage of molten steel

through the breakout hole. Fig.4.13 shows the average grain size at the respective positions outlined in Fig.4.12(b). The average grain in the depression areas is significantly larger than that in the 'normal areas' as shown in Fig.4.13. These observations provide convincing experimental evidence of the existence of air gaps in the mould, which decrease the cooling rate and hence, the rate of heat transfer leading to higher temperatures at the roots of these depressions (hot spots) thereby creating favorable conditions for excessive austenite grain growth.

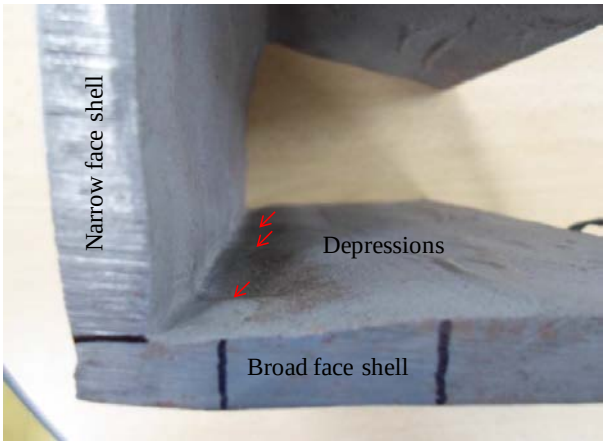

(a) Breakout shell having several depressions at off-corner area of inner shell

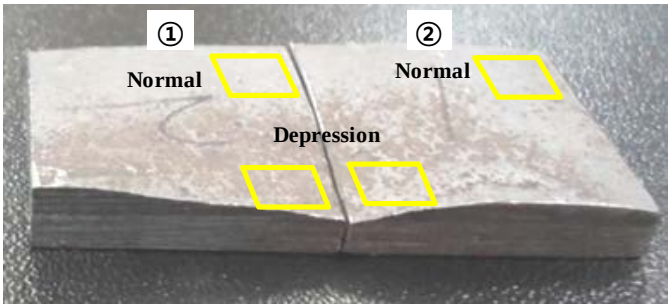

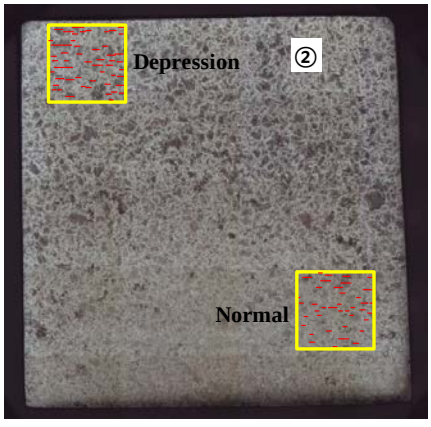

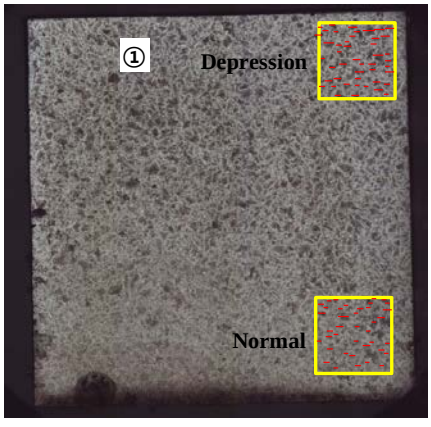

(b) Cutting - Milling 4 mm from outer shell surface - Polishing – Nital Etching

Fig.4.12 Breakout shell of low-carbon steel cast in a thin slab caster, displaying several depressions at off-corner positions and samples selected for the determination of prior-austenite grain size (Gwangyang Works)

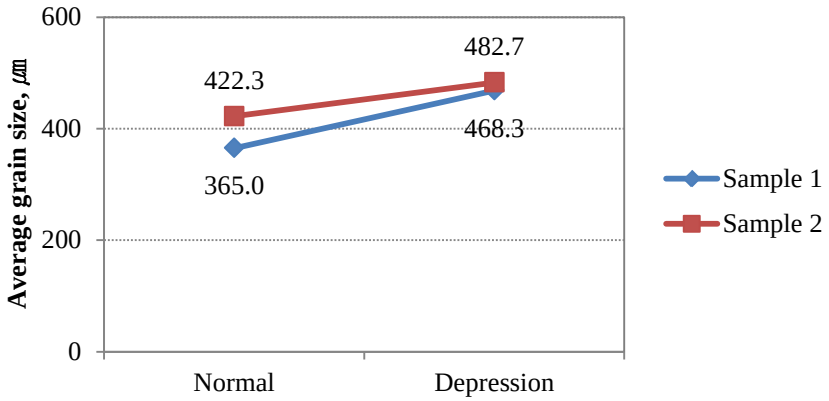

Fig.4.13 Average austenite grain size at the positions of the breakout shell shown in Fig.4.12

Having established that the deformation of the solidifying shell during continuous casting plays a significant role in the formation of air gaps (depression or deep oscillation marks), it is instructive to operational variable and/or practice that might lead to the formation of air gaps in the off-corner areas on the broad face of a slab. It is also pertinent to note that the potential causes of air gap formation in the off-corner areas outlined below are most relevant to the casting of steels of composition close to the peritectic.

- Corner rotation due to a lack of narrow side mould taper in the meniscus area of the mould relevant to the early stages of solidification. Insufficient mould taper, especially in upper part of mould, will fail to compensate for the contraction that occurs upon solidification. This mechanism, proposed by Thomas *et al.* [76], is schematically shown in Fig.4.14.

- Distortion of thin shell due to stresses originating from the massive-type δ-to-γ phase transformation. Due to two-dimensional heat transfer in the corner of the mould, this area is cooled at a much higher rate than the rest of the mould and hence, the massive-type of δ-to-γ phase transformation is more likely to occur. Also, sluggish molten steel flow at corner region compared to the centre of broad face which will lower diffusion of solutes in the liquid, thereby leading to partitioning and thus increase the possibility that the massive-type of transformation can occur. (See the detailed discussion in Section 2.4.3).

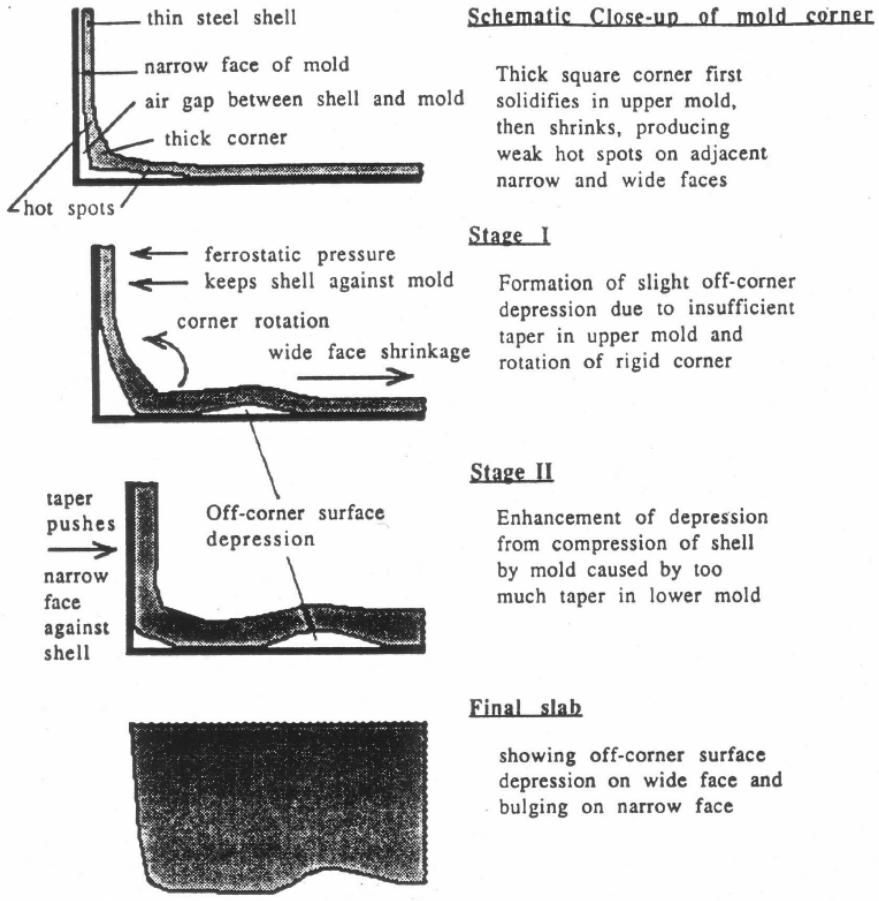

Fig.4.14 The mechanism of corner rotation, illustrated by Thomas *et al.* [76]

4.5 TiN Precipitation

Returning now to the observations shown in Fig.4.10, many black particles were found in this specimen and they can be classified into two types: big round shapes and small rectangular shapes. The big round shaped particles are of the order of 10^0-10^1μm size and are CaO-Al_2O_3 inclusions as shown in Fig.4.15(a). The ratio Ca/Al of all scanned particles was about 1 as shown in Fig.4.15(b) and the inclusions are likely to be $12CaO \cdot 7Al_2O_3$ which has a lower melting temperature and is typically found in calcium-treated steels in secondary refining process for avoiding clogging problem of submerged entry nozzle in thin slab casting process. The distribution of the inclusions along the width of the specimen in the indicated area was analyzed by FEG-SEM and shown in Fig.4.16. It is clear that the CaO-Al_2O_3 inclusions are distributed evenly over the width.

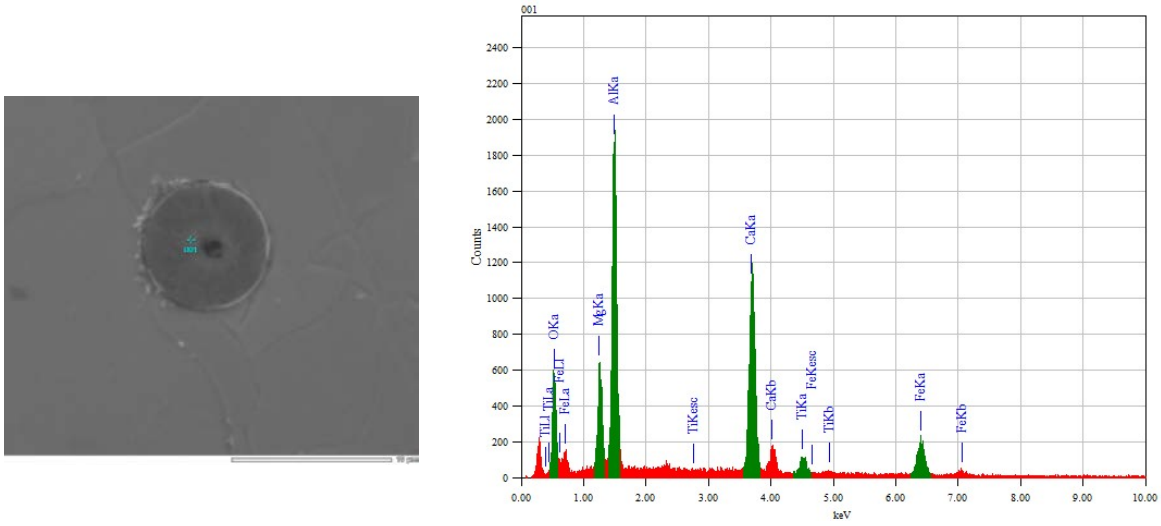

(a) Spectrum analysis on a round shaped particle

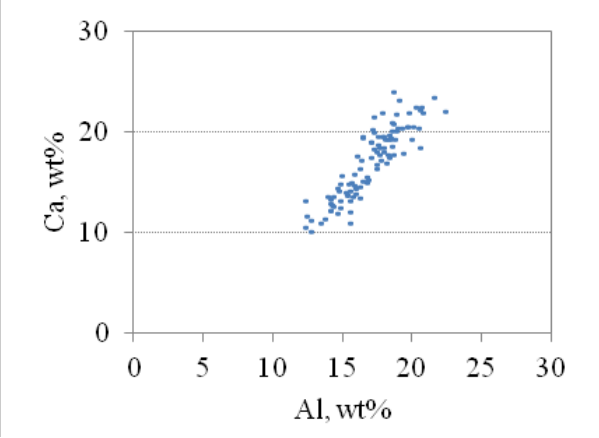

(b) Dot plot of composition of Ca and Al

Fig.4.15 Composition analysis of round shaped particles using FEG-SEM

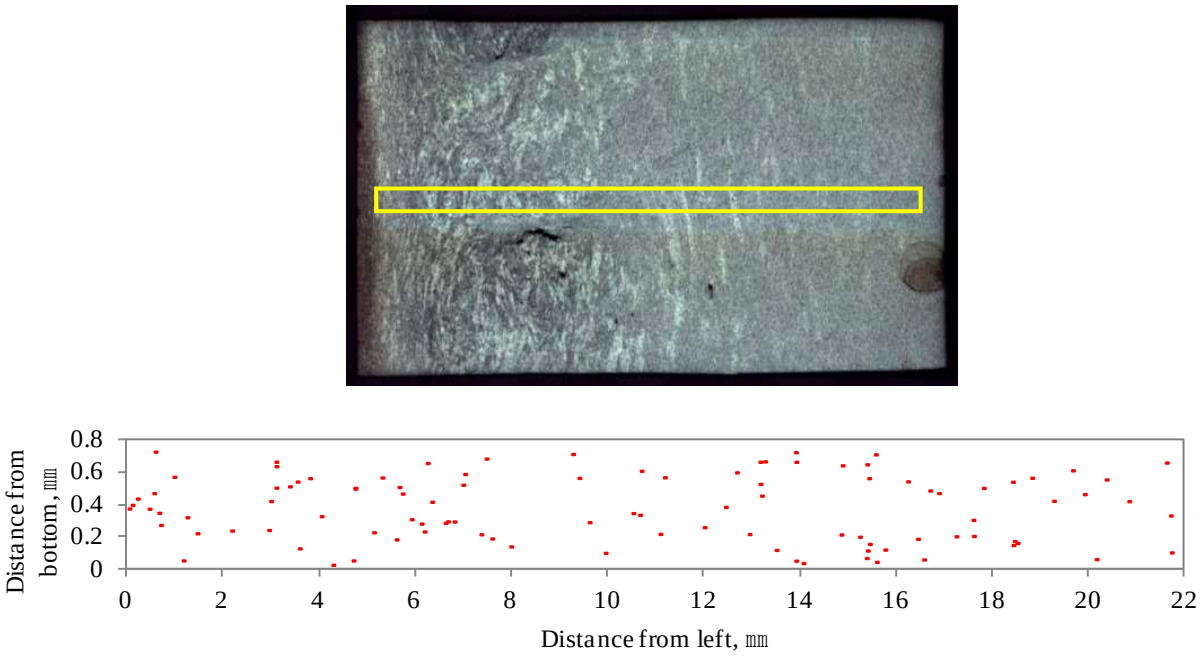

Fig.4.16 Distribution of $CaO\text{-}Al_2O_3$ inclusions in the indicated area (selection criteria ; particle size ≥ 4 μm, $Ca_{wt\%}$ ≥ 10%)

On the other hand, the small rectangular particles are of the order of 10^{-1}-10^{0} μm in size and they are TiN precipitates as shown in Fig.4.17. The distribution of TiN particles was examined, but due to limitations of the instrument, particles smaller than 0.7 μm could not be detected. It is interesting to note that TiN precipitations between 0.7 - 0.8 μm were mainly scattered around cracking area (Fig.4.18(a)), while TiN precipitations over 2.5 μm were mainly found on the area where no cracking occurred as shown in Fig.4.18(b).

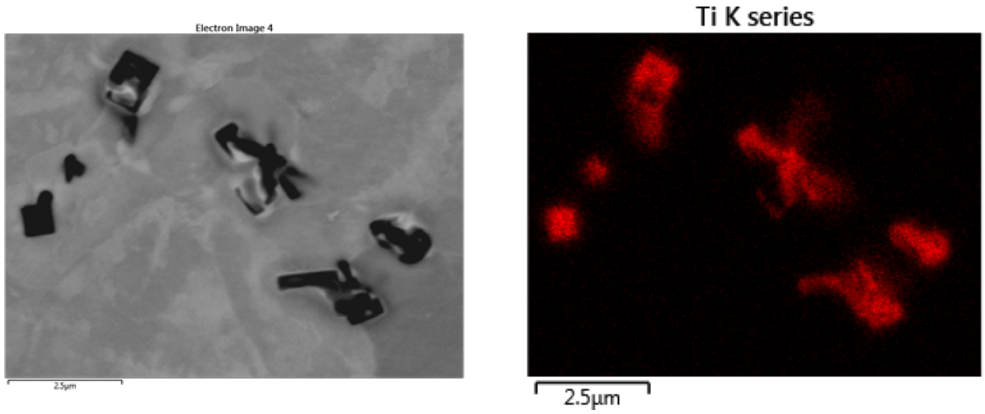

(a) Ti mapping on small rectangular particles

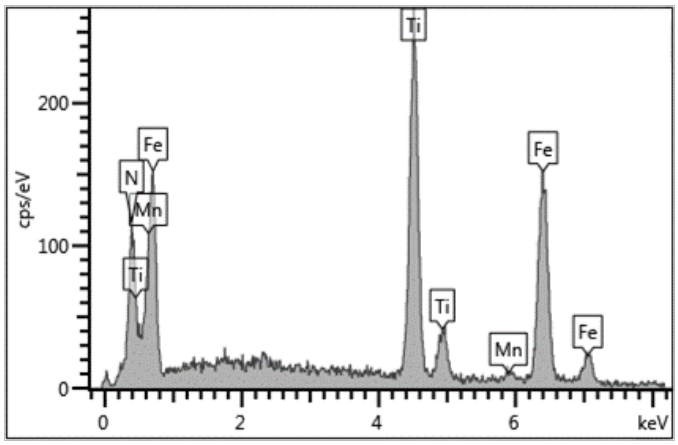

(b) Composition spectrum analysis of a particle

Fig.4.17 Analysis of rectangular shape particles

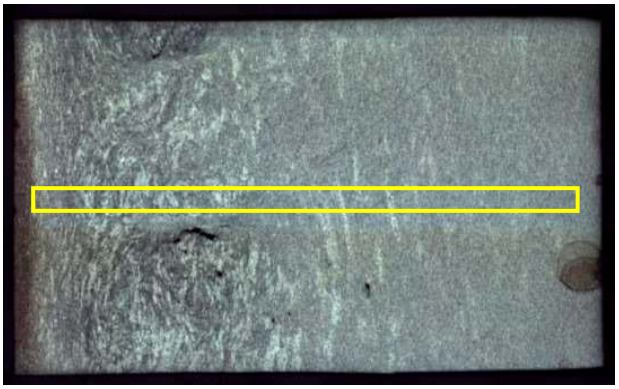

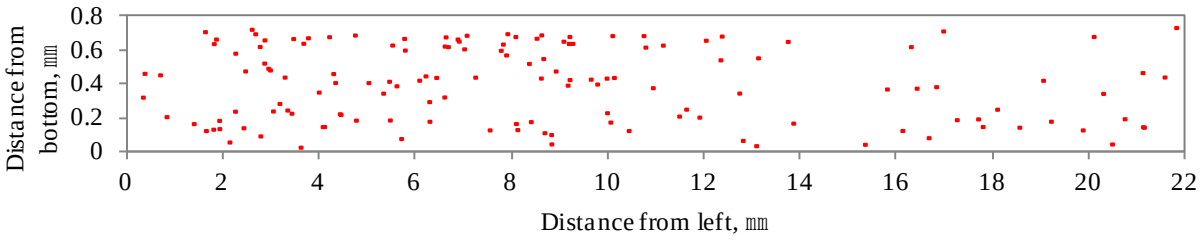

(a) Distribution of fine TiN particles (selection criteria: particle size 0.7 ~ 0.8 μm, $Ti_{wt\%} \geq 10$ %)

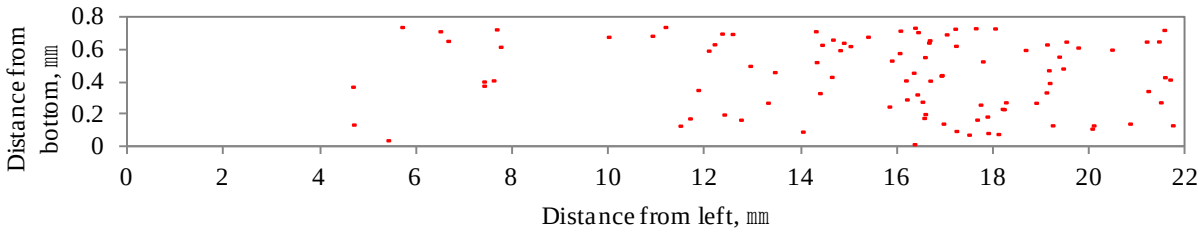

(b) Distribution of coarse TiN particles (selection criteria: particle size ≥ 2.5 μm, $Ti_{wt\%} \geq 15\%$)

Fig.4.18 Distribution of TiN precipitates in the indicated area

Although the TiN particles size in the area where cracking occurred is finer than in areas where no cracks were found (the 'normal' area), they are still much larger than the critical precipitate particle size (10^1-10^2 nm) that is known to induce cracking [52, 77, 78]. It is therefore pertinent to explore the reasons for this apparent discrepancy. Fig.4.19 shows a schematic layout of thin slab caster followed by reduction mill as well as the typical slab surface temperature of the sample studied. Also, a schematic TTP (Time Temperature Precipitation) diagram of TiN precipitation is overlaid except that a linear, rather than the usual logarithmic time scale is used. The sample in the present study was taken from the transfer bar stack, which was cooled in air following hot reduction and hence, the sample remained at high temperature for a long time in the stack. TiN precipitates that nucleated when the slab passed through the secondary cooling zone and especially

at straightener, grew to the sizes observed at the high temperature in the transfer bar stack and it is important to re-iterate that the TiN particle size is much smaller in the area where cracks were observed than in those areas where cracks were absent. There is therefore a distinct possibility that TiN precipitates contribute to the propensity to crack formation.

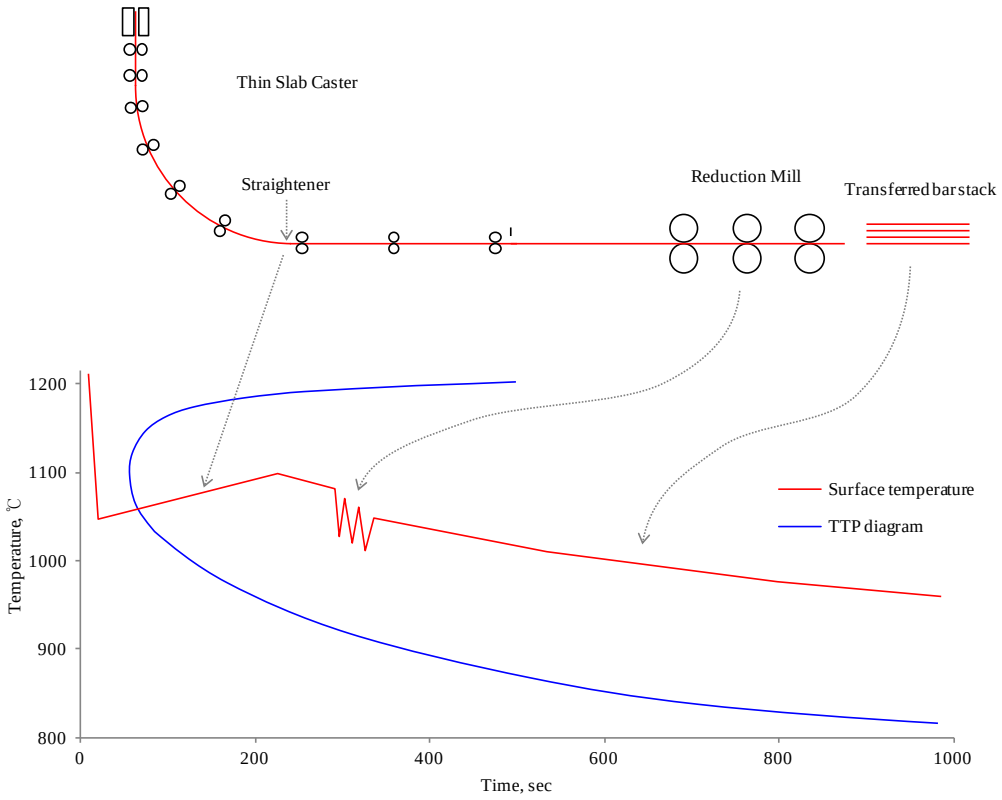

Fig.4.19 Schematic surface temperature profile of the transfer bar stack and schematic TTP diagram in thin slab casting process in Gwangyang Works

The question remains as to why finer TiN precipitates are formed in the off-corner area of the slab than in areas further away from the corner. It is well established that the corner area of slab is subjected to a much higher cooling rate due to two-dimensional heat extraction in the secondary cooling zone. With reference to the TTP-diagram shown in Fig.4.19, this means that the off-corner area might cut through the nose while the middle of broad face, which is cooled at a lower rate will pass through the nose such that larger TiN particles with increased inter-particle spacing will from.

4.6 Evaluation of each Individual Factor

The present study has shown that crack formation in the off-corner region of a continuously cast thin-slab can result because of excessive austenite grain growth or the precipitation of fine TiN particles. It is therefore instructive to assess the respective contributions of austenite grain growth and TiN precipitation to the propensity to off-corner crack initiation and growth. Mintz *et al.* [78] proposed that a minimum ductility expressed as the minimum reduction in area in a hot-tensile test (Min. RA (%)), is required to prevent crack formation, this critical ductility being given by the following equation:

$$\text{Min. RA (\%)} = 700\, d^{-1/2}\,(1 - 4.3s^{-1/2}) + 20(\log \dot{\varepsilon} + 2.5)$$

where : grain size (30 - 500 μm), s : the sum of the mean size of the particle and the inter-particle spacing (70 - 320 nm), $\dot{\varepsilon}$: strain rate (3×10^{-4} - 3×10^{-2} /s). Min. RA increases, i.e., ductility improves, with decreasing grain size, with increasing particle size and inter particle spacing and with increasing strain rate. However, it is not possible to determine quantitatively, the respective contribution of each of these factors in the present study, nor was it the purpose of the present study to do so. However, an estimate of the respective contribution of the peritectic phase transition and titanium additions to off-crack formation can be made with the little information at our disposal. Fig.4.4 showed that the crack index peaked in steels with carbon equivalent, C_{eq}, between 0.08 wt%C and 0.13 wt%C. However, most of the steels in this composition range contained titanium. When the steels that contain titanium are omitted from this analysis, the crack index is significantly reduced as shown in Fig.4.20, but it is still much higher than that of carbon steels that fall outside this carbon equivalent range.

It is therefore clear that there are at least two contributing factors to off-corner crack formation: The peritectic phase transition causes shell distortions due to transformation stress, which in turn cause excessive growth of austenite grains, titanium additions to steel results in the formation of fine TiN precipitates. In both cases the propensity to off-corner crack formation is increased.

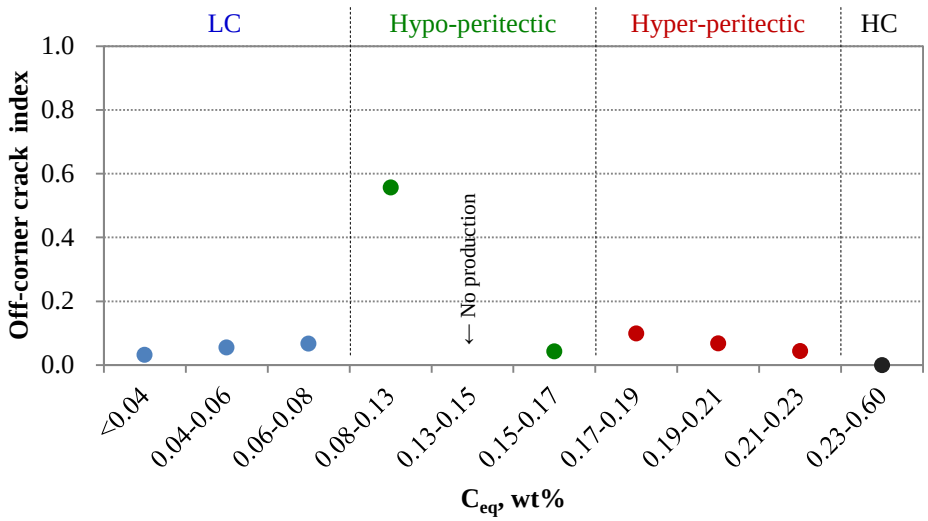

Fig.4.20 Off-corner crack index of steels which no deliberate titanium additions were made (Ti < 50ppm). The same off-corner crack index was used as that shown in Fig.4.4.

The relative crack index in the carbon equivalent range 0.08 wt%C to 0.13 wt%C is 0.56 for titanium-free steel, while it is 1.00 for whole steels. It may therefore be argued that the peritectic phase transition contributes 56 % and titanium nitrides 44 % to the cracking index respectively and therefore that these two factors contribute roughly equally to off-corner crack formation.

In conclusion, ductility in the off-corner area of a thin continuously-cast slab deteriorates significantly in steels in the carbon equivalent range 0.08 wt%C to 0.13 wt%C as a result of the occurrence of the peritectic phase transformation and is further deteriorated by titanium additions due to TiN precipitation at austenite grain boundaries.

Chapter 5. Evaluation of the Influence of Mould Texturing on the Solidification of Steel

It is well-established, as was shown in the literature review, that a finely profiled texture of the mould surface such as sandblasting or fine grooves (normally less than 1mm groove interval) provides 'mild cooling' of the solidifying strand. A textured mould surface increases the heat resistance, while at the same time diminishes air gaps between the solidified shell and the mould. In addition, when the thin solidifying shell deforms as a result of the peritectic phase transition, the grooved mould surface contributes to an even dispersion of these deformation sites

In an attempt to evaluate the effect of different mould surface textures on reducing the unevenness of a solidified shell in selected steels, a simple dip-test and mould simulator tests were conducted.

5.1 Dip Test

5.1.1 Test Procedures and Test Conditions

The dip tests were performed in collaboration with the Institute of Ferrous Metallurgy, University of Leoben, Austria.

Liquid steels were prepared in an induction melting furnace. Differently textured dummy cylinders were dipped into a liquid steel bath of a given composition and following the formation of a thin shell, withdrawn from the bath, cooled in air, sectioned and examined metallographically. Cylindrical, 20 mm diameter and 100 mm long low-carbon steel dummies were surface textured as shown in Fig.5.1.

Three steel grades were selected from the steels studied in the experiments outlined in Chapter 2. The compositional analysis of Steel B (low carbon), Steel E (hypo-peritectic) and Steel G (hyper-peritectic) are shown in Tab.5.1. Also included in the table are the compositions of steels studied in the HTLSCM experiments outlined in Chapter 2, shown as 'previous' in the table. In-plant observations of the behaviour of Steel G have been especially interesting because it is ostensibly a hyper-peritectic steel and far away from the peritectic composition as determined by the thermodynamic calculation shown in Fig.2.1(c). However, in practice it exhibits extremely uneven solidification during continuous casting as shown in Fig.3.1. In addition, *in-situ* observation in the HTLSCM showed that the $\delta \rightarrow \gamma$ phase transformation in this steel occurs by a massive-type of transformation at a very high rate as shown in Fig.2.18 and Fig.2.19. It is therefore important to

further investigate the solidification behaviour of this type of steel.

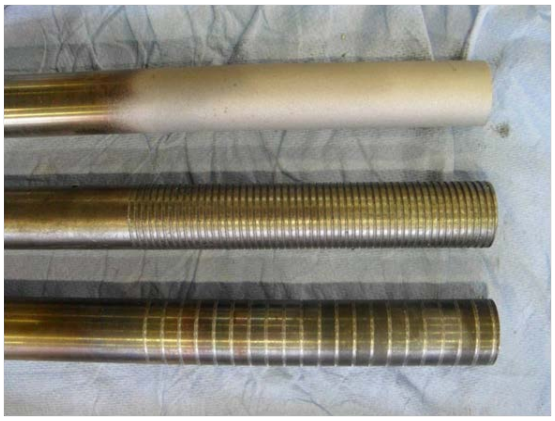

Fig.5.1 Different types of dummy with surface textures. From the top: Sandblasted with 30 μm roughness, 2 mm interval grooved and 5 mm interval grooved (Dummy diameter = 20 mm, the length of textured area = 100 mm)

Tab.5.1 Composition analysis of steels used in dip test (in wt%)

Steel		C	Mn	Si	Al	Ti	Nb
B	This study	0.050	0.31	0.15	0.028	0.001	0.014
	Previous	0.051	0.305	0.016	0.029	0	0
E	This study	0.085	1.63	0.34	0.025	0.013	0.024
	Previous	0.08	1.599	0.278	0.025	0.012	0.018
G	This study	0.100	2.75	1.11	0.097	0.014	0.020
	Previous	0.085	2.82	1.013	0.027	0.0158	0.02

5.1.2 Results and Discussions

The dummies were submerged for periods of 2, 4 or 8 seconds respectively in the liquid bath. The most discernible differences between the different dipping tests were on the dummies dipped for 2 seconds. The appearances of the shells formed on the dummies dipped for 2 seconds are shown in Fig.5.2. Cross sections of the shell along the cylinder length are shown in Fig.5.3 to Fig5.6 for each type of texture.

-	Steel B	Steel E	Steel G
No texturing			
30 μm sand			
2 mm interval groove			
5 mm interval groove			

Fig.5.2 Appearances of the shell surface at the molten steel side. Dipping time 2 seconds.

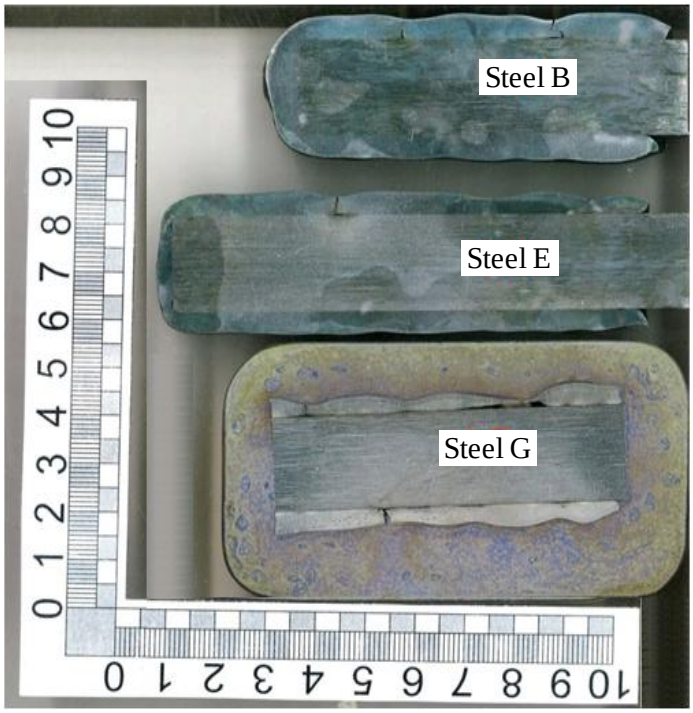

Fig.5.3 Cross section of shells formed on flat surfaced dummies. Dipping time 2 seconds.

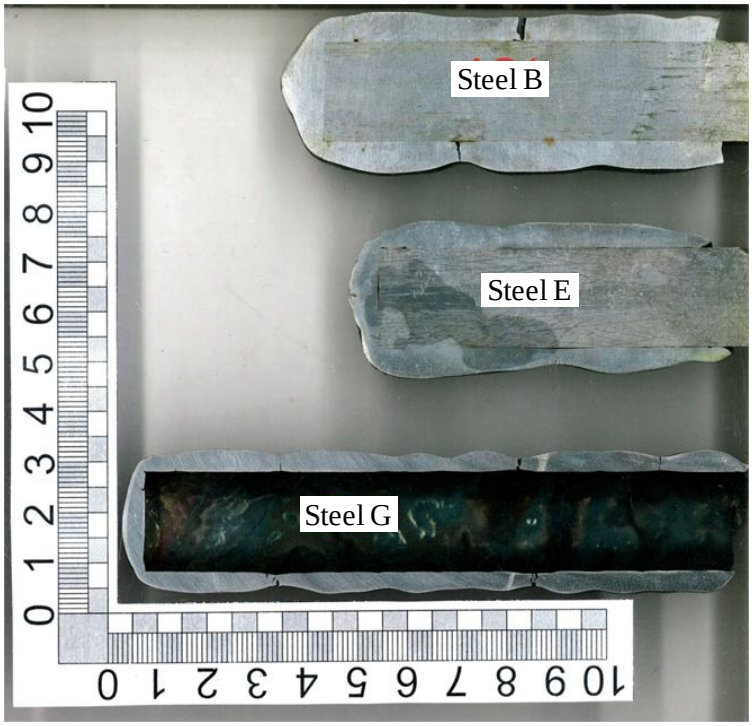

Fig.5.4 Cross section of shells formed on 30 µm sandblasted dummies. Dipping time 2 seconds.

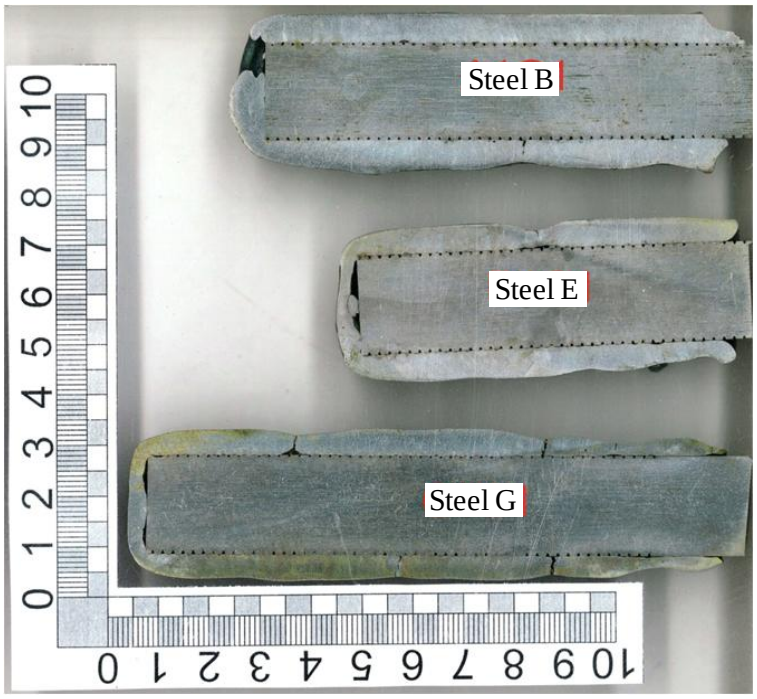

Fig.5.5 Cross section of shells formed on 2 mm interval grooved dummies. Dipping time 2 seconds.

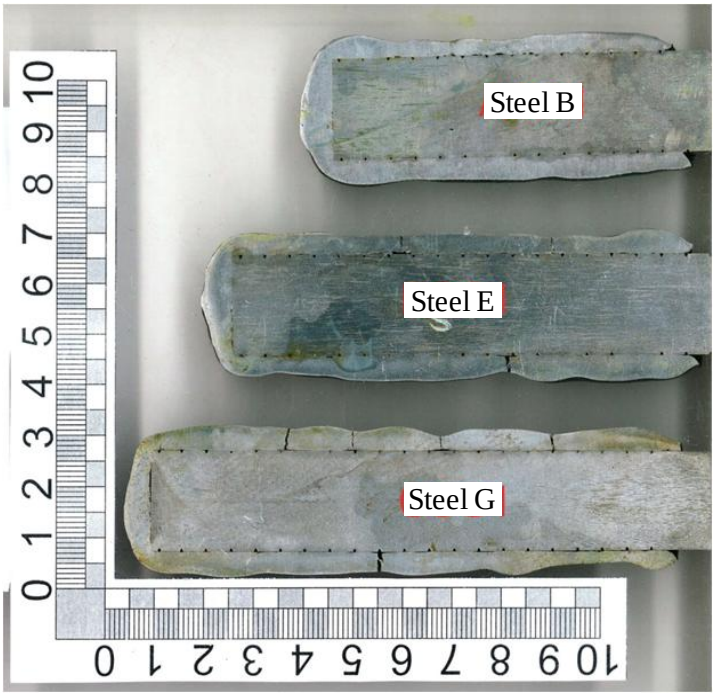

Fig.5.6 Cross section of shells formed on 5 mm interval grooved dummies. Dipping time 2 seconds.

From the appearance of shell surface on the molten steel side, it follows that Steel E and Steel G have many depressions on the shell surface and therefore they look more uneven than Steel B. The solidification in the case of the 2 mm interval grooved dummy seems to be much more even than the others. Many shrinkage cracks were found following withdrawal from the liquid steel bath and cooling to room temperature. It is evident that these are shrinkage cracks since there is no sign of penetration of liquid steel at molten steel side. Most of cracks are found in the thinnest area of the shells where the stress concentrated and thus the cracks are observed mainly under conditions that exhibited more uneven solidification. The dummies with 2 mm interval grooves have fewer cracks than the other textures.

No significant depressions (air gaps) are found on the substrate side even in the thinnest areas shown in Fig.5.3 to 5.6 while clear depressions were found at the dip-plate side in Murakami's dipping experiment [56] as shown in the case of a 0.146 wt%C steel in Fig.3.6. These ostensibly different findings can be reconciled by considering the geometry of the dummy used in the current dip tests. The perimeter of the shell around a cylinder will shrink during cooling to room temperature. This will diminish previously formed air gaps between shell and dummy. In the case of a dip-plate (the same as the in-plant condition), the shell can shrink without diminishing air gaps.

In order to evaluate the unevenness of the shell, the thicknesses of the shell at 3mm intervals along the length of cross section were measured. The differences in thickness between neighbouring points were averaged to get an unevenness index as shown in Fig.5.7. Although this result is from only a cross section of sample, it is clear that steel B (non-peritectic low carbon grade) is most even and Steel G (hyper-peritectic) is the worst in most dummy surface conditions. The 2 mm interval grooved dummies appear to have the most even shell of the three steel grades.

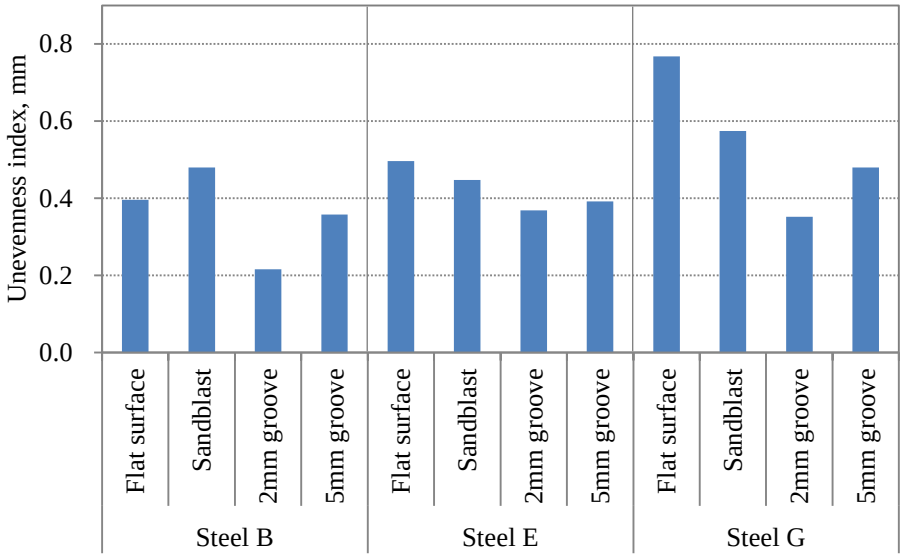

Fig.5.7 Unevenness index of shell for different test conditions

Average thickness of shell was obtained as an indicator of shell evenness because shell thickness is a function of the extent of contact between shell and dummy, i.e., less air gap results in overall increase of heat transfer thus rendering a thicker shell. As shown in Fig.5.8, Steel B has the thickest shell and Steel G has the thinnest shell (except in the case of the 5 mm groove). Also, the 2 mm interval grooved dummy had the thickest shell of the three steels.

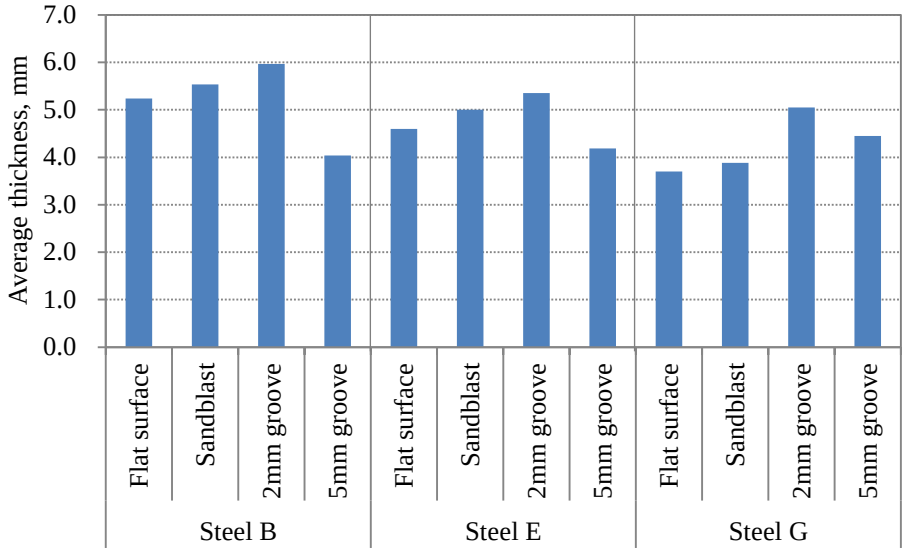

Fig.5.8 Average thicknesses of shell for different test conditions

The shell thickness achieved in the mould for a dipping time of 2 seconds is calculated as 4.4 mm when a solidification constant of 24 is assumed (this is the typical solidification constant in industrial continuous casting operations). A shell thickness of 4 - 5 mm is similar to the shell thickness obtained in practical in-plant operations. This means that the average cooling rate of the shell that has been dipped for 2 seconds in the dip-test is similar to that during initial solidification in an operational mould. The important conclusion to be drawn from this finding is that a laboratory study using the simple dip-test described above can be used to predict the solidification behaviour of steel in the mould of an operational continuous caster.

5.1.3 Conclusions from the Solidification Study using the Dip Test

- The dip test is a simple and inexpensive screening test to evaluate the evenness of shell formation in a continuous casting mould.
- The evenness of shell formation among steels is in the order Steel B (non-peritectic low carbon), Steel E (Hypo-peritectic) and Steel G (Hyper-peritectic). Steel G showed the most uneven solidification. Steel G is also the most sensitive to uneven shell formation in industrial continuous casting practice.
- Surface texturing of 2 mm interval grooves resulted in the most even solidification and it produced the thickest shell through the improved contact between shell and textured surface. The reason for this observation is most likely related to the effect of grooves on the dispersion of deformation sites in the thin shell as proposed by Murakami *et al.* [56] - see Fig.3.25.

5.2 Mould Simulator

5.2.1 Purpose of the Experiments

Mould flux plays an important role in controlling heat flux and lubrication between shell and mould through the formation of a thin mould flux film. Also, mould oscillation enables the stable infiltration of mould flux into the gap between shell and mould. For a detailed analysis of solidification occurring in a mould it is essential to approach as closely as possible the practical mould operating conditions in dip-test studies. Of critical importance is the way in which the mould flux is applied and the exact oscillation parameters used in the mould simulation tests.

Murakami *et al.* [56] have provided convincing experimental evidence that lattice-type texturing of a mould surface in the meniscus area could reduce uneven solidification of steel of near-peritectic composition. Also they found that nickel plating on the textured surface of a mould was effective in preventing shell-sticking type breakouts that originated from friction between shell and groove (although this is not a practical in industry in terms of cost and mould maintenance).

The main aims of present study are:

- to determine to what extent lattice grooving can prevent uneven solidification of steel of near-peritectic composition.
- to assess the possibility of developing a practical method to apply lattice type grooves on mould surface

For these reasons mould simulation studies were conducted on the mould simulator that is installed in the POSCO Research Laboratory in Pohang, South Korea.

5.2.2 Experimental Procedure

Fig.5.9 shows a picture of the mould simulator. It is equipped with three identical casting units so that three dipping experiments can be sequentially conducted using the same molten steel.

Fig.5.9 Mould simulator in the POSCO Research Laboratory

Fig.5.10 shows in brief the operational steps and the procedures followed to produce a solidified shell as have been outlined by Ko *et al* [79]. Once liquid steel of a given composition is prepared in the crucible, mould flux is added on top of the molten steel to provide a 20 mm thick molten slag layer. A mould set consists of a water-cooled copper mould and a steel cover plate as shown in Fig.5.10(a). First, the mould set descends towards the melt, while the mould oscillates. Once the mould set is submerged to an initial position in the molten steel, it is held for 3 seconds as shown in Fig.5.10(b). This step allows the formation of an initial shell, which grows on the cover plate. In the next step, the cover plate descends at a given speed (i.e. casting speed) while the mould keeps oscillating in the same position. During this step, a fresh shell grows on the mould as shown in Fig.5.10(c) (green colored shell). Theoretically, the shell can be formed under the exactly identical conditions pertaining in an operational mould during continuous casting. The cover plate keeps moving down further and once the desired length of shell is obtained the whole mould set is withdrawn from the liquid steel bath.

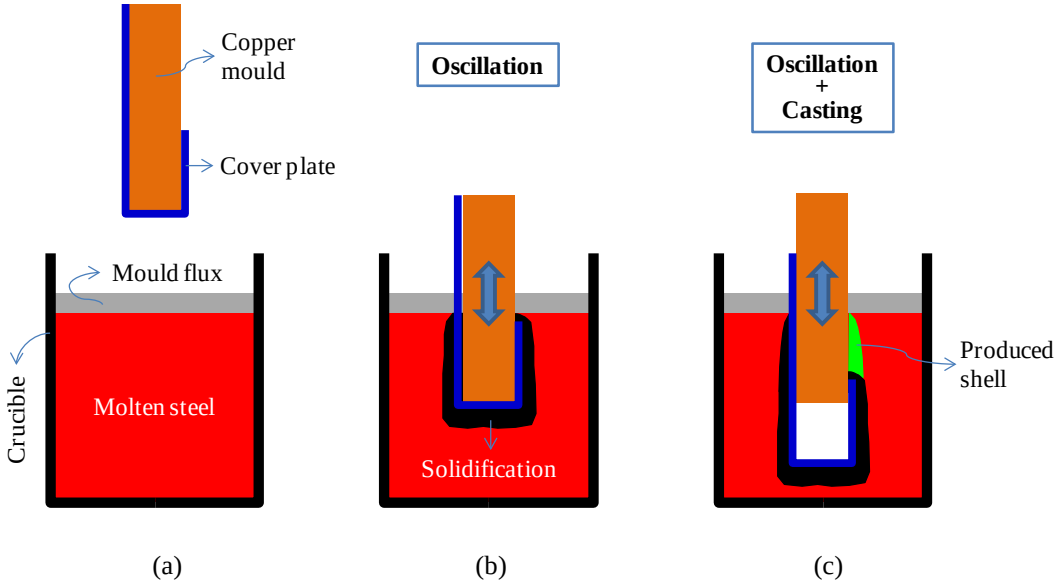

Fig.5.10 Sequence of experimental steps

Fig.5.11 shows the design of the mould, which is made of a copper-based chromium-zirconium alloy with water-cooling channels fabricated inside the mould for cooling. Different surface texture patterns can be prepared on one side of mould with an area of 135 mm × 300 mm where the meniscus level will be positioned and the shell will grow.

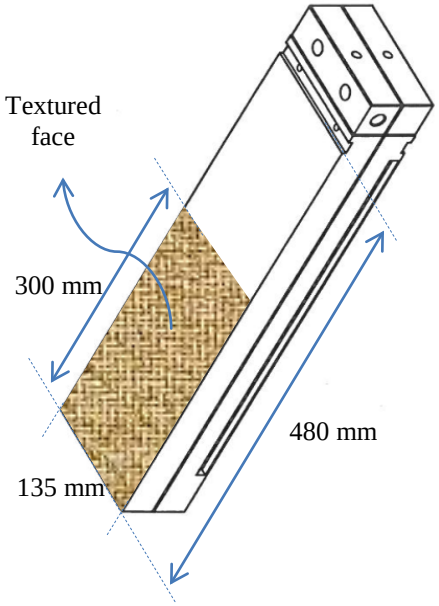

Fig.5.11 Schematic diagram of mould

5.2.3 Experimental Conditions

Steel E, as a typical hypo-peritectic grade was selected for this study and the chemical composition is shown in Tab.5.2. 280 kg of Al-killed steel was prepared in the induction melting furnace. The molten steel temperature was controlled at 1540 °C so as to have 20 °C of superheat from liquidus temperature.

Tab.5.2 Steel grade used in mould simulator test (in wt%)

Steel	Description	C	Mn	Si	Al	Ti	N	Nb
E	TMCP	0.08	1.599	0.278	0.025	0.012	0.0029	0.018

Four different texture patterns were prepared as shown in Fig.5.12. The sandblasted surface Fig.5.12(a) (hereafter SB) has 30 μm of roughness. Fig.5.12(b) shows the longitudinally grooved surface (hereafter GR). A detailed design of the longitudinally grooved surface is shown in Fig.5.13. Fig.5.12(c) and Fig.5.12(d) shows latticed surfaces having 14 mm intervals (hereafter L14) and 7 mm intervals (hereafter L7) respectively.

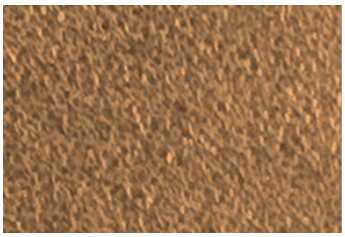

(a) 30 μm sandblast (SB)

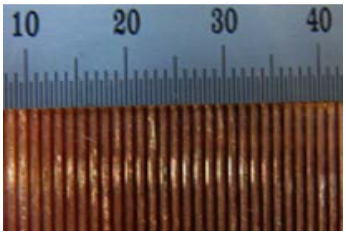

(b) Longitudinal groove (GR)

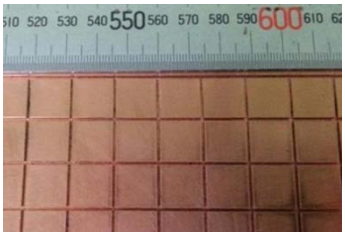

(c) 14 mm interval lattice (L14)

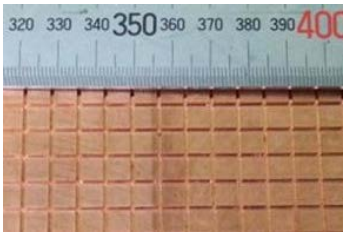

(d) 7 mm interval lattice (L7)

Fig.5.12 Four different type of textures on the mould surface

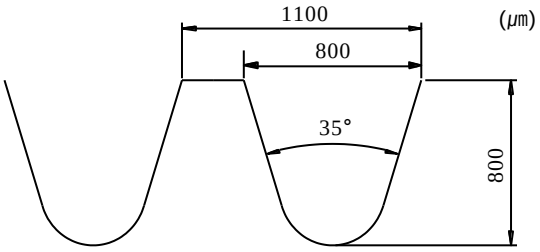

Fig.5.13 Design of the longitudinally grooved surface

Fig.5.14 indicates the detailed design of the lattice surface mould. Gel type alumina was filled into the gap and completely dried prior to a test. The rationale behind filling the groove with insulation material is to prevent shell sticking onto the mould wall as a result of the increased friction due to the grooves as indicated by Murakami *et al.* [56].

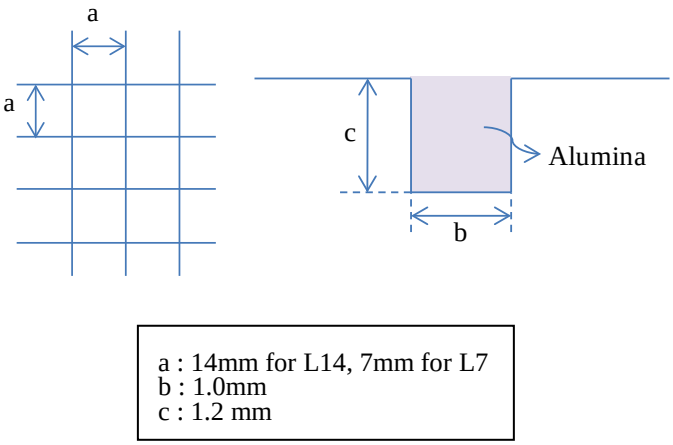

(a) Dimension of groove

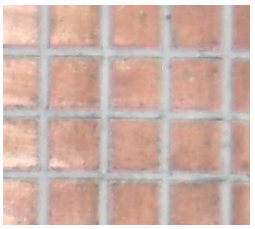

(b) Appearance of lattice after applying alumina

Fig.5.14 Detailed design of a lattice surface mould

The properties of the mould fluxes for the experiment are shown in Tab.5.3. The heat transfer coefficient of the mould flux that is normally used to cast hypo-peritectic steels is designed to be lower than those used for other steels, in order to avoid cracking. Hence, a mould flux with a low heat transfer coefficient (hereafter MfL) was selected for use with Flat, SB and GR textures. In the case of experiments with L14 and L7 textures a mould flux with a high heat transfer coefficient (hereafter MfH) was selected in order to maximize the effect of large pitched grooves on the dispersion of the contraction during the $\delta \rightarrow \gamma$ transformation. The reasoning behind this approach has been outlined by Murakami *et al.* [56] as discussed in Section 3.2.4.

Other casting parameters are summarized in Tab.5.4.

The cover plate was programmed to stop after casting 120mm length of shell. Each experiment was repeated twice. Fig.5.15 shows pictures taken during the experiments in addition to the shells formed on the mould.

Tab.5.3 Mould flux properties according to experiment mould type

Mould flux Type	Application Mould type	Mould flux properties					
		Basicity	CaO	SiO2	Viscosity 1300°C (poise)	Melting point (°C)	Crystalline Ratio (%)
MfL	Flat / SB / GR	1.19	39.0	33.0	2.58	1150	12.5
MfH	Flat / L14 / L7	0.90	25.7	28.5	0.54	820	3.0

Tab.5.4 Other parameters

Casting speed	Oscillation stroke	Oscillation frequency
1.5 m/min	8.8 mm	2.27 Hz

(a) Dipping

(b) The shells formed on the mould after completion of an experiment

Fig.5.15 Pictures of a mould simulator experiment

5.2.4 Results and Discussions

The solidified shells were separated from the mould by cutting along the edge. Fig.5.16 and Fig.5.17 show pictures of shell in case of experiments Flat/SB/GR with mould flux MfL and Flat/L14/L7 with mould flux MfH respectively (One of two repeated experiments is represented).

Mould	Inner shell (mould side)	Outer shell (molten steel side)
Flat		
SB		
GR		

Fig.5.16 Pictures of shells in case of Flat/SB/GR with mould flux MfL (width 140 mm)

Mould	Inner shell (mould side)	Outer shell (molten steel side)
Flat		
L14	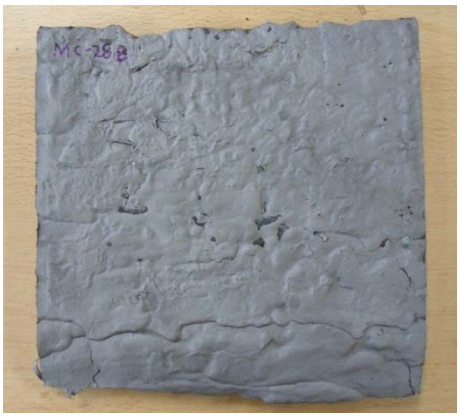	
L7		

Fig.5.17 Pictures of shells in case of Flat/L14/L7 with mould flux MfH (width 140 mm)

The oscillation marks on the inner shell surfaces (mould side surfaces) are not clear in most cases and in some cases quite irregular and hence, it is difficult to locate normal oscillation marks. It is therefore assumed that the conditions in the meniscus region of the mould were quite abnormal.

The reason is thought to be the variation of molten steel level during the experiment. The molten steel level rises as the cover plate descends because an additional volume is created in the melt in the space between the bottom of the mould and the base of the cover plate (see Fig.5.10(c)). The elevation of molten steel level is about 20 mm for 5 seconds of the casting period. This variation also provides a chance for the fresh lining of the melting furnace to react with risen molten steel and molten mould flux, which might result in convulsive molten steel levels. As the molten steel level is rising and fluctuating, the infiltration of mould flux becomes unstable and the oscillation marks become irregular.

In order to compare and quantify the unevenness of the shell, the thickness profile was measured using a laser line-scanner. Surface profiles were measured along the three lines with 40 mm intervals parallel to the casting direction as shown in Fig.5.18 and the measurements were repeated on the other side of the shell along the same positions as on the opposite side. By measuring the thicknesses at the start and end point in each line and processing each pair of surface profile data, shell thickness profile could be obtained.

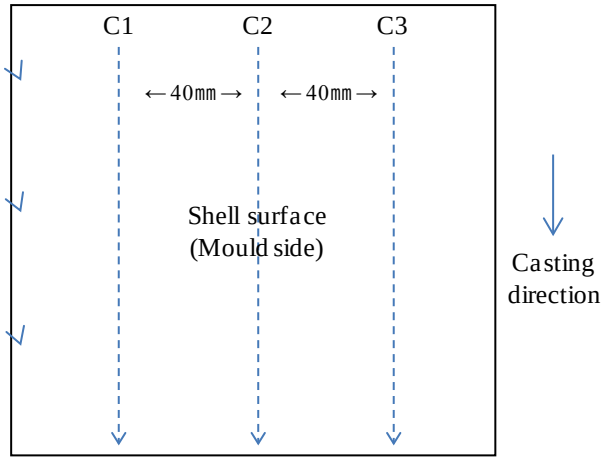

Fig.5.18 Measuring surface profiles

Fig.5.19 is an example of such a thickness profile of a solidified shell. The scanning start point was set at 10 mm from the top of the shell (meniscus). A length of only 80 mm from the scanning start point was taken although the length of cut samples were 140 mm or more, because the remaining length of the solidified shell was formed during the holding period prior to casting or alternatively likely to have been affected by holding the sample.

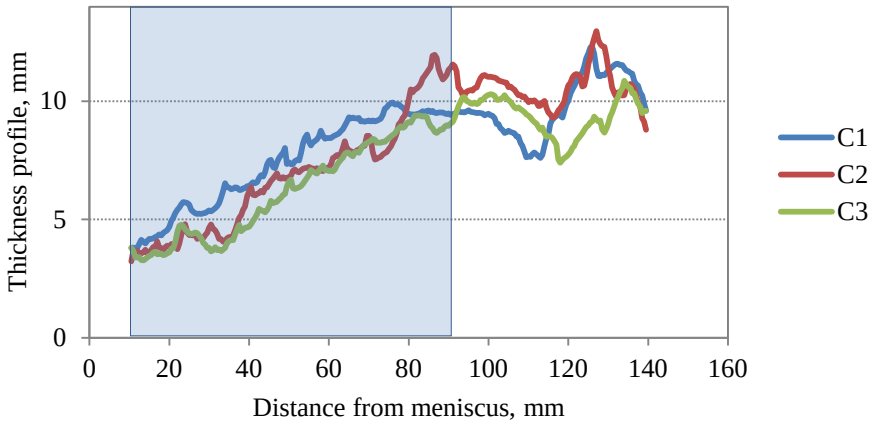

Fig.5.19 An example of measured thickness profiles of a solidified shell

Fig.5.20 and Fig.5.21 show the thickness profiles of experiment Flat/SB/GR with the use of mould flux MfL and experiment Flat/L14/L7 with the use of mould flux MfH respectively. Due to the similarity, only one set from the repeated experiments is presented.

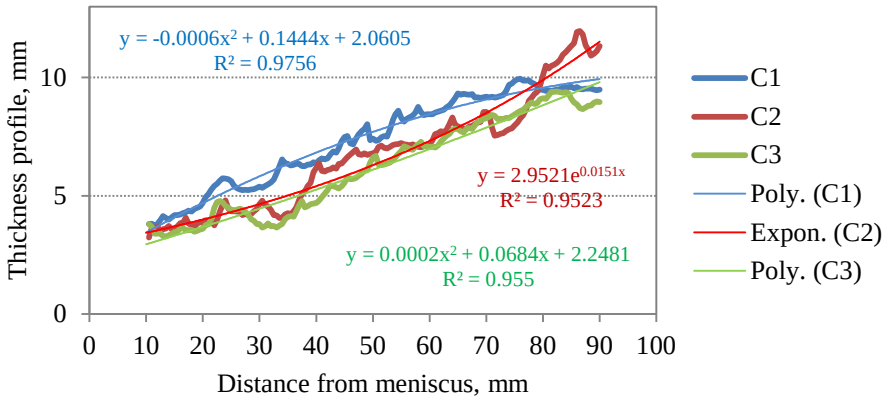

(a) Flat

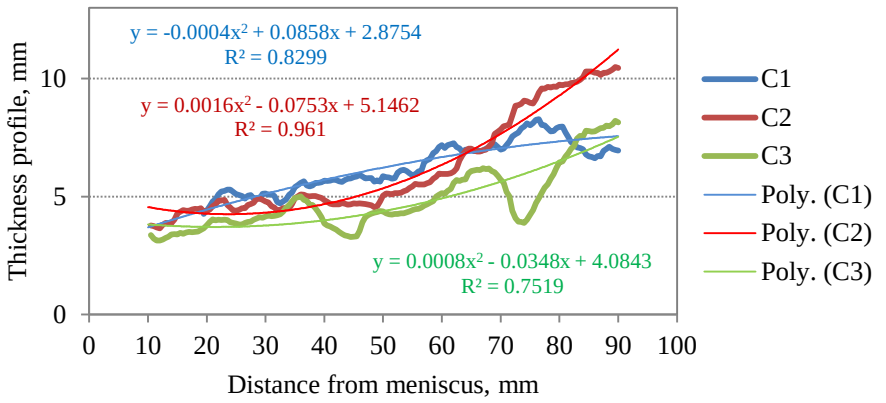

(b) SB

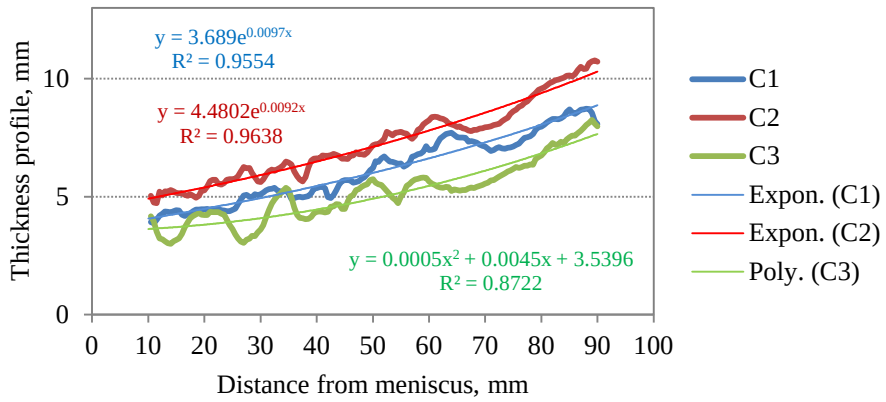

(c) GR

Fig.5.20 Thickness profiles of experiment Flat/SB/GR using mould flux MfL

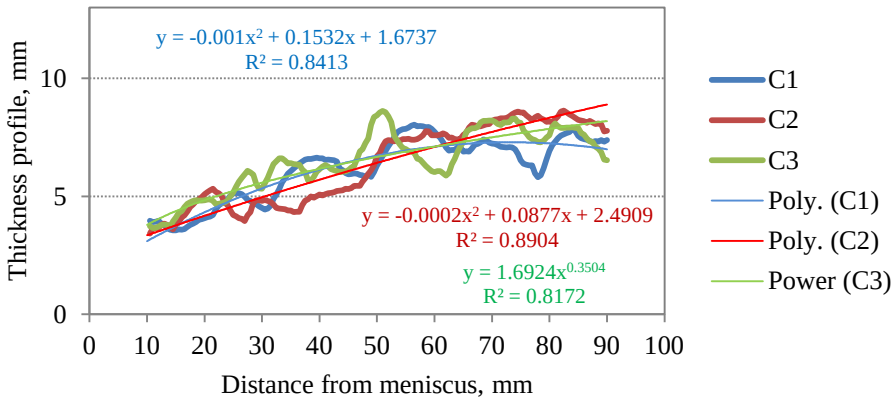

(a) Flat

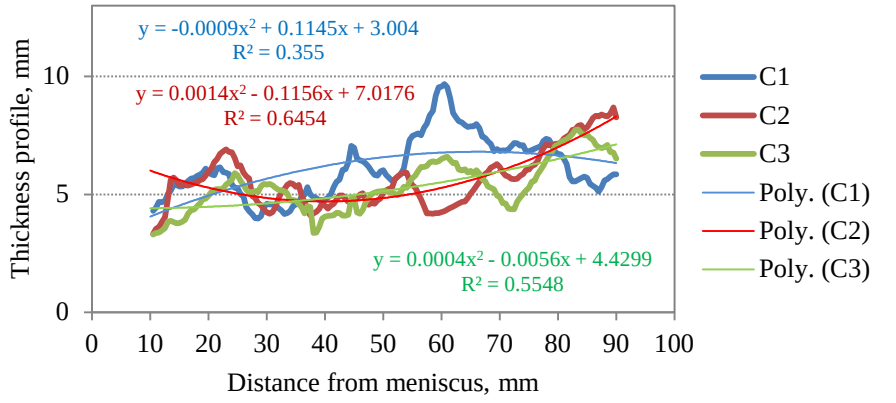

(b) L14

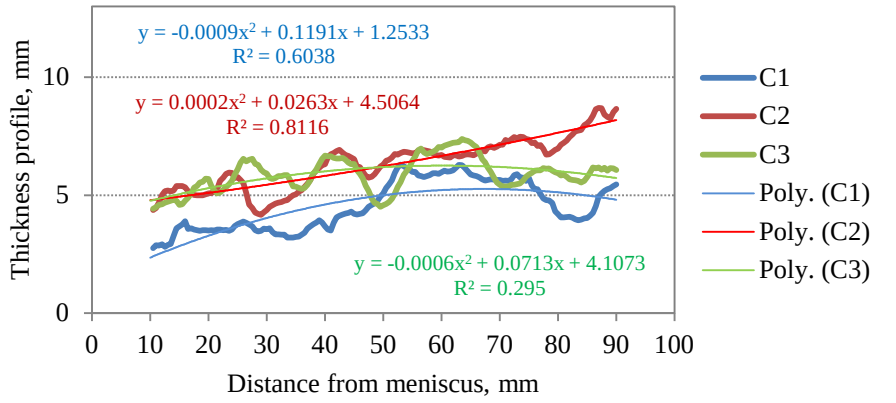

(c) L7

Fig.5.21 Thickness profiles of experiment Flat/L14/L7 using mould flux MfH

Suzuki *et al.* [54] used the standard deviation of the differences between measured thickness and theoretical thickness calculated by using a given solidification constant as an indicator of the unevenness of a shell for the purposes of evaluating continuously cast shells. However, two main problems were encountered in the present study when an attempt was made to apply this method. The first problem relates to the additionally grown shell during the withdrawal period because the bottom part of the shell grows more due to the longer dwelling time in the molten steel compared to the upper part of the shell. The second problem relates to the elevation of the molten steel level during the test as argued above, which also prevents the thickness profile from converging to stable growth under normal casting conditions.

Considering the difficulties encountered with Suzuki's technique, a new approach was taken. In order to evaluate the evenness of the shell, a trend line for each thickness profile was introduced by selecting linear, polynomial, logarithmic, power and exponential best fitting algorithms as shown in Fig.5.20 and Fig.5.21. R-squared values (correlation coefficients between thickness profile and trend line) are also included in the figures. They were taken as an indicator of evenness of the shell. An R-squared value closest to 1.0 is interpreted as the most even shell thickness profile.

Fig.5.22 summarizes the comparison of evenness with respect to the mould flux used when using a flat mould. It is clear that mould flux MfL produce a more even shell than mould flux MfH.

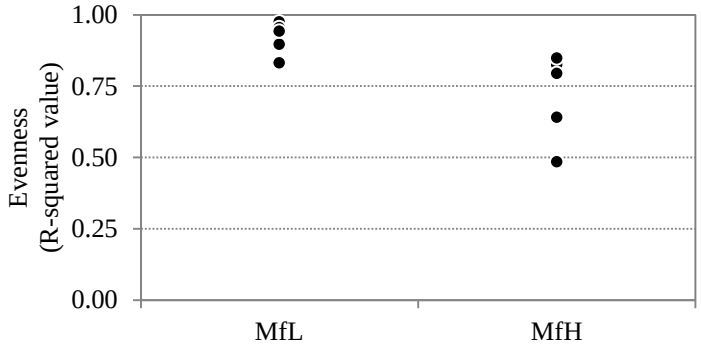

Fig.5.22 Comparison of evenness with respect to the mould flux used when using a flat mould. All data are from the repeated experiments, i.e. from the 3 points measurement at each of 2 solidified shells.

Fig.5.23 shows a comparison of the evenness in moulds Flat/SB/GR with mould flux MfL and Fig.5.24 shows a comparison of evenness in moulds Flat/L14/L7 with mould flux MfH. No discernible difference is found with respect to mould types in either comparison.

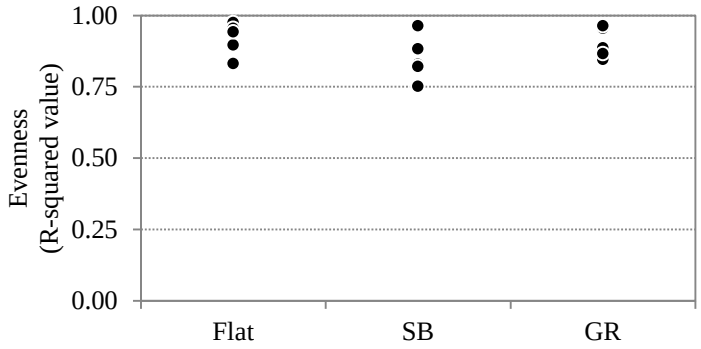

Fig.5.23 Comparison of evenness between moulds Flat/SB/GR with mould flux MfL

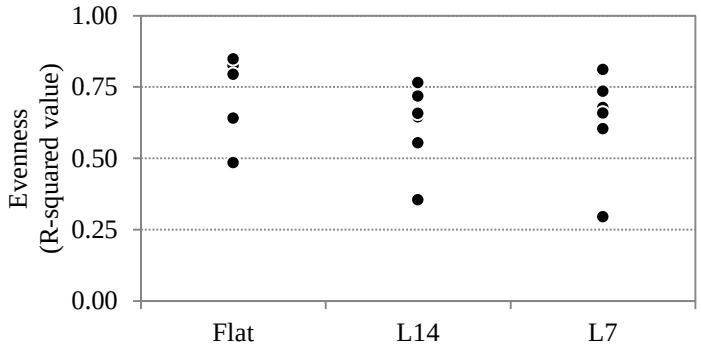

Fig.5.24 Comparison of evenness between moulds Flat/L14/L7 with mould flux MfH

In order to estimate the effect of the evenness of a shell on the growth thereof, it is necessary to compare the shell thickness because the thickness of a shell is determined by the heat transfer rate with a given size of air gap between shell and mould. Fig.5.25 shows a comparison of shell thickness with respect to the mould flux used with a flat mould. At 10mm below the meniscus the respective thicknesses were not much different although mould flux MfH might be marginally better. However, the situation is decidedly different at a distance 90mm from the meniscus. The use of mould flux MfL resulted in a much increased shell thickness compared to mould flux MfH. It is interesting to note that the application of a mould flux with a low heat transfer coefficient resulted in much more shell growth. Reduced mould heat transfer in the meniscus area plays an important role in preventing thin shell distortion by the volume change accompanying the $\delta \rightarrow \gamma$ transformation, resulting in improved contact between shell and mould over the entire length of the mould. As a result, the heat transfer rate in the mould is increased leading to an increase in the shell thickness at the bottom of mould. This observation is in good agreement with the observations in other studies conducted by Marakami *et al.* [56] and Kromhout *et al.* [70] as reviewed in Chapter 3.

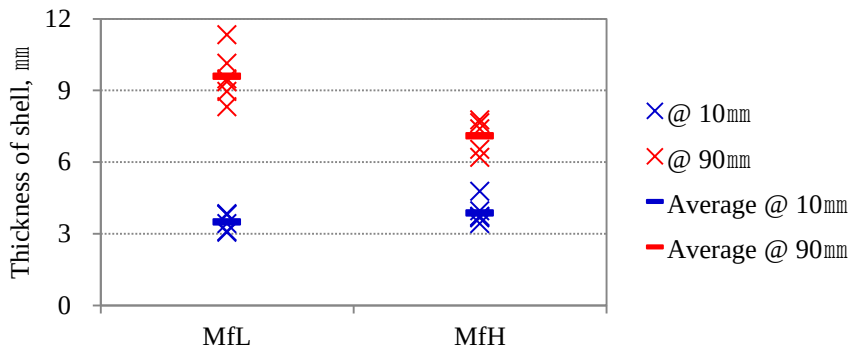

Fig.5.25 Comparison of shell thickness at 10 mm and 90 mm from meniscus according to mould flux with the application of flat mould

Comparisons of shell thickness for Flat, SB and GR moulds with MfL, and for Flat, L17 and L7 moulds with MfH are shown in Fig.5.26 and Fig.5.27 respectively. There is no discernible difference between the mould types with respect to shell thickness. It will be recalled that evenness was not much influenced by different mould type either (Fig.5.23 and Fig.5.24). In other words, the mould textures are unlikely to control the evenness of the shell.

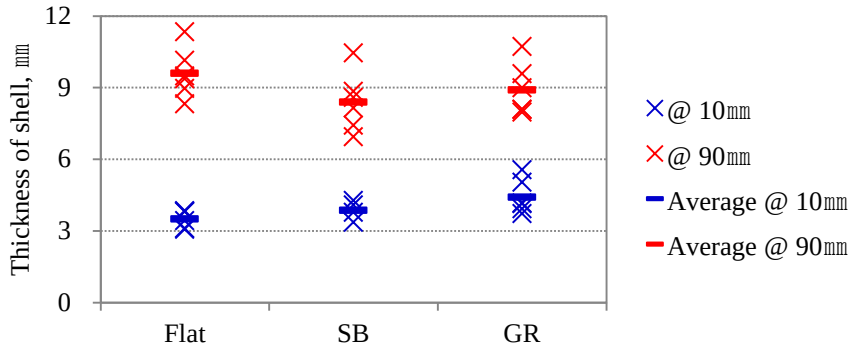

Fig.5.26 Comparison of shell thickness at 10 mm and 90 mm from meniscus according to mould type with the application of MfL

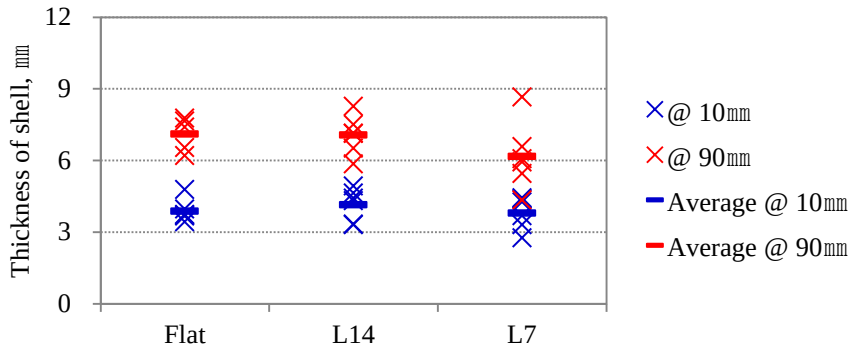

Fig.5.27 Comparison of shell thickness at 10 mm and 90 mm from meniscus according to mould type with the application of MfH

Observation of mould flux films taken from the gap between the solidified shell and the mould revealed that they vary in thickness between 3 to 5 mm. This is much thicker than mould flux films extracted from in-plant operations where the thickness varies only between 0.5 and 2.0 mm. Thick mould flux films play a role by providing greater barriers to heat transfer, which is likely to render mould texture ineffective. Recalling that Murakami *et al.* [56] (reviewed in Section 3.2.4) have shown that in order to prevent uneven shell growth the plating thickness on a mould surface must be as thin as possible to increase q_{cu}/q_a (a ratio of partial heat transfer rate at the groove position to that at the centre between grooves as was shown in Fig.3.28). However, in the present study the thicker mould flux film is likely to decrease q_{cu}/q_a, therefore rendering the mould texture ineffective with respect to controlling solidification.

5.2.5 Conclusions from the Solidification Studies in the Mould Simulator

- The growth of the solidifying shell in hypo-peritectic steel becomes much more even when a mould flux with a low heat transfer coefficient is used (mild cooling).
- The even shell resulting from using a ‘mild cooling’ mould flux provides more intimate contact between shell and mould and this intimate contact renders a much thicker shell at the bottom of the mould, essentially as a result of an increased heat transfer rate.
- The influence of mould texture on the evenness of shell could not be clearly discerned in this study. The inability to have found a direct correlation between mould texture and uneven shell growth seems to reside in the formation of an abnormally thick mould flux film, which masks the effect of mould texture.

Chapter 6. Characterization of Peritectic Steel Grades

In order to operate a continuous casting process with satisfactory quality of the slabs, it is important to identify if a steel grade is within the peritectic range. There have been numerous studies to develop practical methods to identify steel grades, for example, calculating carbon equivalent [74, 80, 81] or calculating carbon concentrations at the start/end point of the hypo-peritectic range at a given composition [82]. More recently several thermodynamic computer codes such as Thermo-Calc and FactSage have been employed to determine whether or not a given steel composition will undergo the peritectic reaction. These software packages rely on data experimentally measured for different alloy systems and therefore if a steel composition is complex or having higher concentrations of particular alloying elements than experimentally measured, the calculations by these software packages can lead to erroneous results. An example of such a discrepancy is provided in Fig.6.1 where the predicted phase diagram of the relatively simple Fe-C-1.0wt%Al system, using two different thermodynamic software packages renders decidedly different results [40].

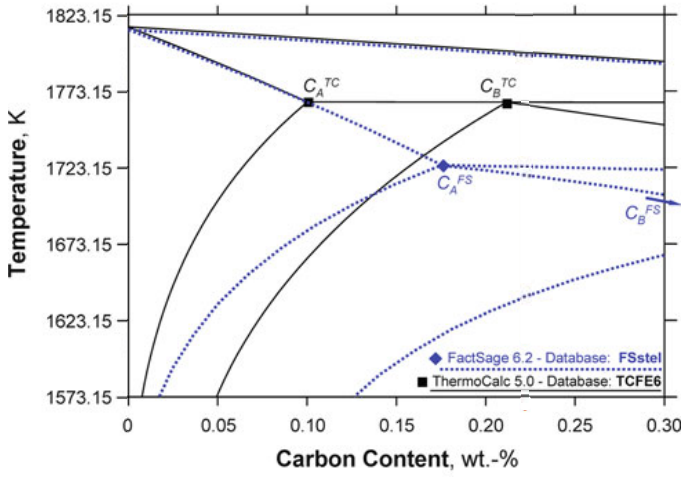

Fig.6.1 Thermo-Calc and FactSage calculation of the binary Fe-C phase diagram of the system Fe-C-1.0wt%Al [40]

Presoly *et al.* [40] developed a comprehensive experimental technique to precisely predict if a given steel falls within the peritectic range by using differential scanning calorimetric (DSC) technique. The use of high-temperature laser scanning confocal microscope confirmed that this method is also suitable for predicting the peritectic range of higher alloyed steels.

It is well established that steels of near-peritectic composition with an equivalent carbon

content of between 0.10 and 0.12 wt% show the highest contraction of all carbon steels and are subject to the worst surface quality of the cast product [50, 53, 83]. Bernhard *et al.* [53] measured the contraction forces occurring during the solidification of steels using submerged split-chill contraction (SSCC) test and confirmed that the contraction forces encountered during the initial stages of solidification is maximum in steels of hypo-peritectic composition carbon content. These contraction forces have often been attributed to the occurrence of the $\delta \rightarrow \gamma$ transformation during and immediately following solidification in the thin shell in the meniscus region of the continuous casting mould as discussed in section 3.1.1. Therefore, it is fundamentally important to develop a better understanding of the thermal contraction of the solidifying shell in the meniscus region of a continuous casting mould.

In the present study, Differential Scanning Calorimetry (DSC) measurement and Submerged Split-Chill Contraction (SSCC) tests were conducted with the aim of characterization selected steel grades that were used in earlier studies as part of the present investigation in order to support the previous observations and the conclusions derived therefrom as will be explained in more detail below.

This study was performed in the collaboration with Institute of Ferrous Metallurgy, University of Leoben, Austria.

6.1 DSC (Differential Scanning Calorimetry) Measurement

6.1.1 Description of Experiment

DSC tests comprise a thermo-analytical method by which the difference of heat required to increase the temperature of a sample relative to a standard is measured over time, making it possible to identify the occurrence of phase transformations, melting or solidification by a change in enthalpy.

Detailed descriptions of the DSC measurement employed in this study can be found in Presoly *et al.'*[40]. The DSC equipment used in this study is a NETZSCH DSC404F1 with a platinum DSC sensor and type-S thermocouples as shown in Fig.6.2. It consists of a sample and reference crucibles, which are connected by a heat flow plate both exposed, ideally, to the same heating power input by convection and radiation from a cylindrical heating furnace. The measurement signal is derived from the temperature difference between the sample and reference crucible

expressed in terms of a heat flow. The measurements were carried out under protective gas atmosphere (argon, quality 6.0) with a flow of 50 cm^3min^{-1} and two type of getters (Zr, Ti) are used to remove any remaining oxygen from the furnace atmosphere.

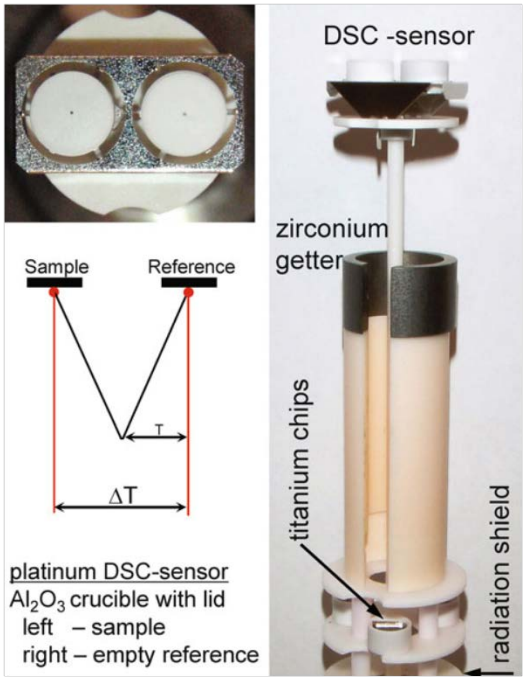

Fig.6.2 Layout of a high-temperature DSC sensor with Zr and Ti getters [40]

In order to achieve optimal equilibrium conditions, grounded samples with a mass of 50 mg were used. In order to obtain accurate results, measurements were made during heating rather than during cooling because on cooling undercooling plays a significant role and masks equilibrium conditions. The heating rate was controlled at 10 K/min for obtaining near-equilibrium conditions. Phase transformations accompanying a change in enthalpy results in a deviation from the horizontal baseline in the DSC-signal. The DSC-signals (the measured heat flows) were adjusted using software, which took into account the influence of heating rate, sample mass, configuration of crucible and the DSC-sensor in approaching equilibrium temperatures. A large number of DSC measurements of steels showed that the standard deviation of the temperature measurements of solid-solid transitions (low enthalpy change) is +/- 3 K and of solid-liquid transitions (high enthalpy change) is +/- 1.5 K.

6.1.2 Accuracy and Interpretation of Experimental Data

Presoly *et al.* [40] demonstrated that their interpretation of the DSC measurements of three different, but well characterized carbon steels (1.0wt%Si) are in good agreement with the respective phase diagrams derived from Thermo-Calc and FactSage. Because significant differences were found between the ThermoCalc and FactSage predictions of the phase relationships and the DSC measurements of some steels conducted in this study, it is important to refer in more detail to Presoly's study of steels of known composition. His study not only provided convincing evidence of the reliability of his technique, but also of the validity of his analysis and interpretation of the results.

Fig.6.3 shows DSC measurements and Fe-C phase diagram of Fe-0.08wt%C-1.0wt%Si alloy which is non-peritectic low-carbon steel. The first deviation from the baseline of DSC-signal was observed between 1679.6 K and 1733.7 K showing a slight increase of the heat flow, which indicates a transformation with only very small enthalpy changes, typical of the γ→δ transformation. DSC-signal increased again at 1754.2 K representing the onset of melting and showed a peak at 1792.4 K representing the liquidus temperature. Further heating resulted in complete melting, there was no change in enthalpy and hence, it represents a stable baseline in DSC-signal. All the observed temperatures are in excellent agreement with the phase diagram calculated by either Thermo-Calc or FactSage software.

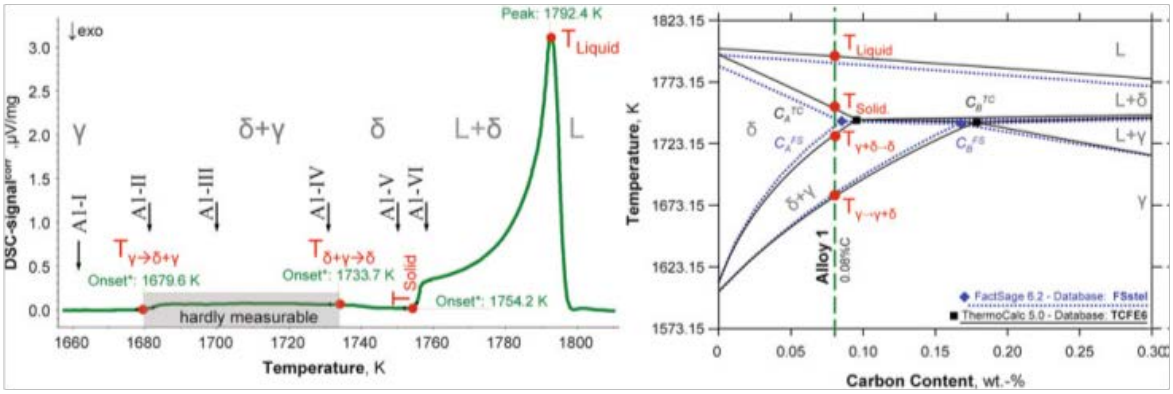

Fig.6.3 DSC measurement of a Fe-0.08wt%C-1.0wt%Si alloy [40]

Fig.6.4 shows DSC measurements of a Fe-0.14wt%C-1.0wt%Si alloy which is ostensibly a hypo-peritectic steel. In the beginning, the behaviour of DSC-signal is very similar to that of Fe-0.08wt%C-1.0wt%Si alloy. The temperature range of the γ→δ transformation in those two alloys is well presented. At 1746.2 K, a very sharp peak appears, reaching a maximum at 1747.9 K. This

peak is associated with the peritectic phase transformation and shows a maximum with the end of the transformation δ+γ→L+δ. Upon further heating, the residual δ phase melts and DSC-signal shows maximum peak at 1786.3 K corresponding to the liquidus temperature.

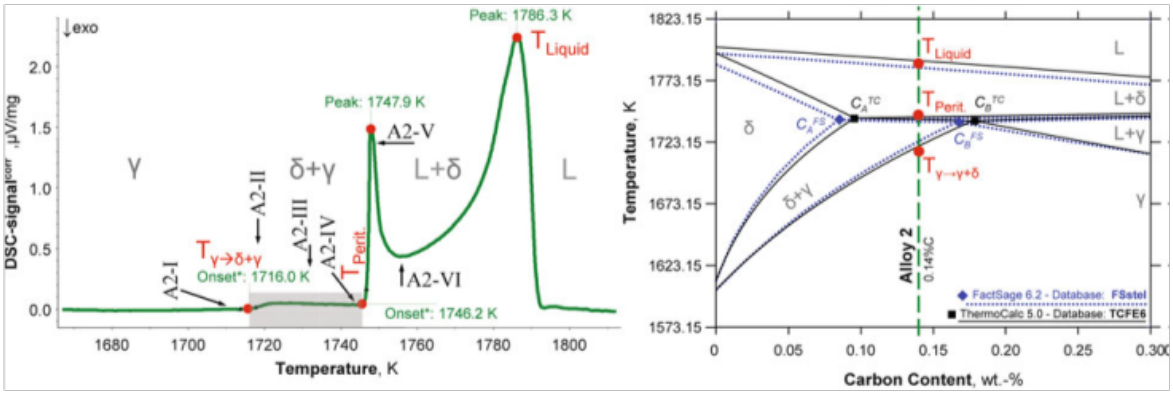

Fig.6.4 DSC measurement of a Fe-0.14wt%C-1.0wt%Si alloy [40]

Fig.6.5 shows DSC measurements of Fe-0.26wt%C-1.0wt%Si alloy, which is ostensibly a hyper-peritectic steel. There is no γ→δ transformation, resulting in a flat DSC signal baseline until the onset of the γ→L transformation. A sharp peak appears at 1746.3 K because of the L+γ→L+δ and showed a maximum at 1749.6 K at completion of the transition. The remaining δ-ferrite transforms into liquid, and the DSC-signal reaches the peak maximum at 1779.2 K, which corresponds to the liquidus temperature. Another typical feature of this hyper-peritectic steel is that the peritectic peak is higher than the following melting peak while it is opposite in the case of hypo-peritectic steel.

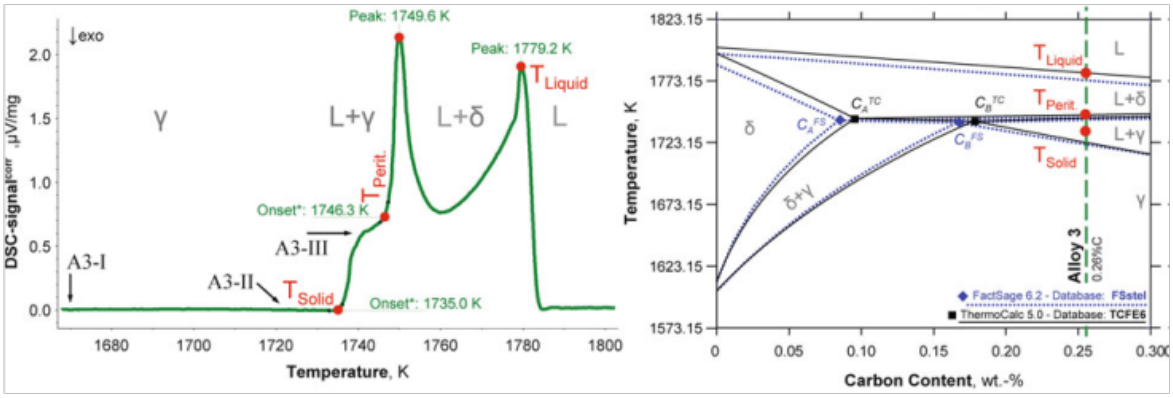

Fig.6.5 DSC measurement of Fe-0.26wt%C-1.0wt%Si alloy [40]

6.1.3 Results and Discussions

In the present study DSC analyses were conducted on the same steel grades, which were studied in the dipping experiments described in Chapter 5, i.e., Steel B (non-peritectic low carbon), Steel E (hypo-peritectic) and Steel G (hyper-peritectic). The samples for the DSC tests were taken from the shell of the dipping-test samples and therefore the composition analysis of the DSC samples are the same as those presented in Tab.5.1.

Fig.6.6 to 6.8 show the results of the DSC experiments. In the graphs of DSC-signal as a function of temperature, the axes have been interchanged in order to provide a more illustrative comparison with the respective phase diagrams. In order to identify the γ→δ transformation more clearly, the scale of the DSC-signal axis in the second graph was expanded to -0.01 to 0.03 μV/mg. A phase diagram calculated from Thermo-Calc is presented at the right hand side. The observed events deduced from the DSC-signal are indicated with dashed lines, which are linked to the corresponding steel in the phase diagram.

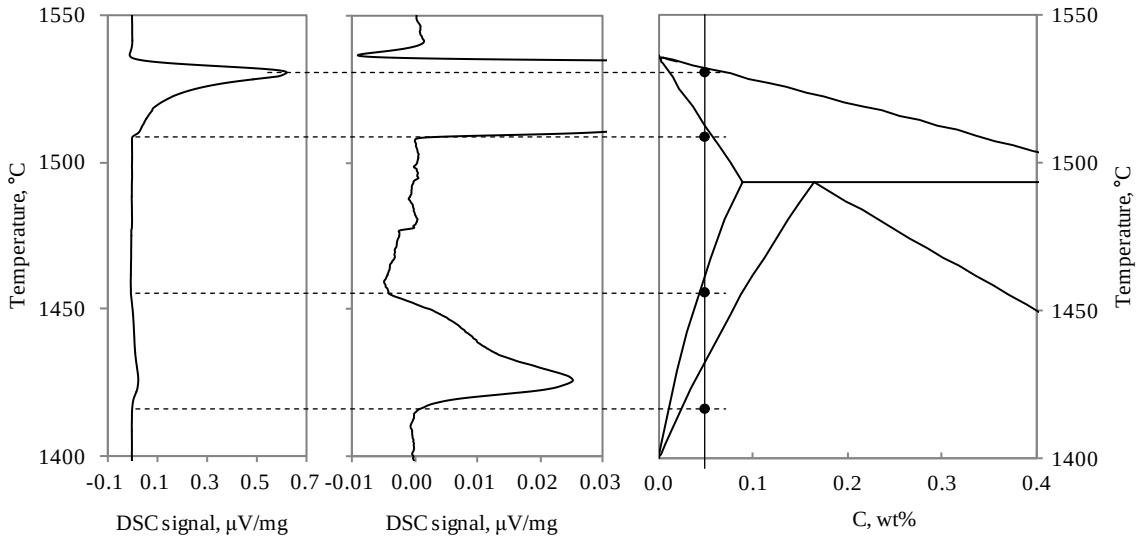

Fig.6.6 DSC measurements of Steel B

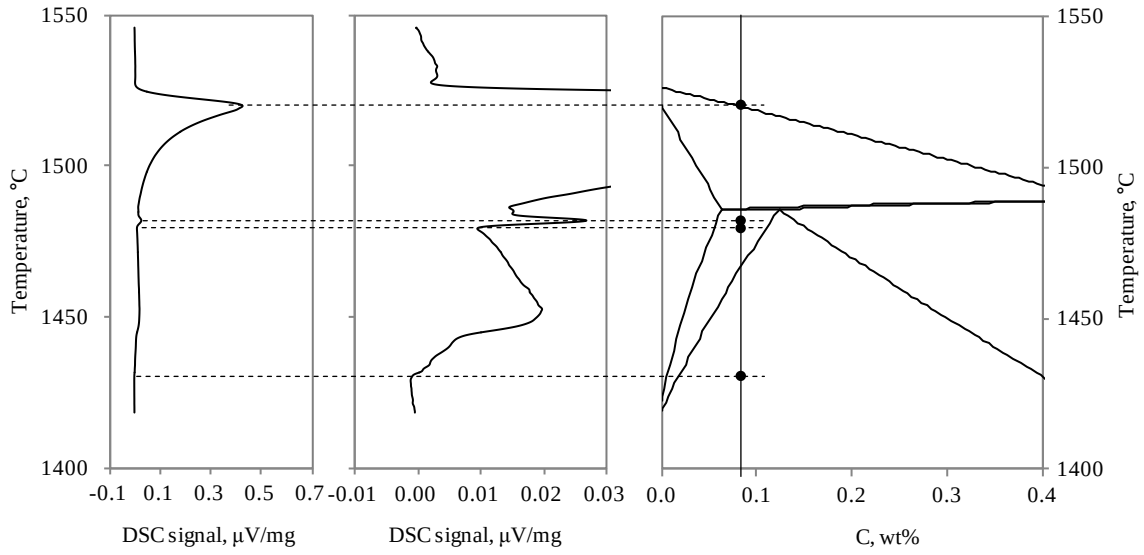

Fig.6.7 DSC measurements of Steel E

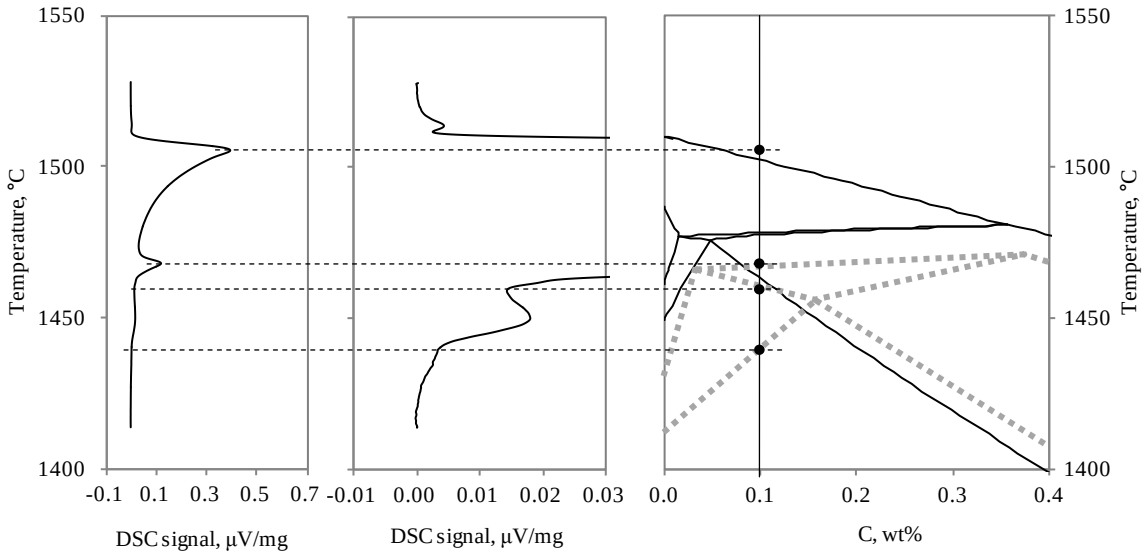

Fig.6.8 DSC measurements of Steel G

In the case of Steel B, the DSC-signal profile shown in Fig.6.6 is very similar to that of Fe-0.08wt%C-1.0wt%Si alloy that was shown in Fig.6.3 and the experimental measurements agree well with phase diagram predicted by Thermo-Calc as shown in the figure. In the case of Steel E, a small peritectic peak appeared at near peritectic temperature in a half way of converging to the

baseline as can be seen in the second graph in Fig.6.7. Also the peritectic peak is much lower than the following melting peak. These observations tend to indicate that this steel is hypo-peritectic composition. In case of Steel G, the signal profile is quite similar to that of Steel E. The peritectic peak appeared in the way of converging to the baseline and the height of the peak is also smaller than that of melting peak and it doesn't fit with the phase diagram. However, an imaginary phase diagram, which can explain the experimental observations is overlaid on the phase diagram (thick and gray dashed-line). Therefore, the experimentally determined DSC suggests very strongly that Steel G is hypo-peritectic as opposed to the thermodynamic prediction of it being hyper-peritectic. This conclusion based on experimental evidence is strongly supported by the observed behaviour of this steel type in operational practice in that extremely uneven shell formation is present, presumably because of the very high rate of the $\delta \rightarrow \gamma$ phase phase transformation.

6.2 SSCC (Submerged Split-Chill Contraction) Test

6.2.1 Experimental Procedure

SSCC-test aims at measuring the forces building-up during the contraction of a solidifying shell. Detailed descriptions of SSCC test can be found in Bernhard *et al.*'s work [53]. A split chill test body is submerged in liquid steel inside an induction furnace as shown in Fig.6.9. A steel shell solidifies around the test body, with the main crystallographic orientation perpendicular to the interface, similar to the situation in a continuous casting mould. The upper part of the test body is fixed, whereas the position of the lower part is linked to a load cell through a small cylinder rod, which measures the reaction force. During solidification, the reaction force of the thermal contraction of the steel shell is transferred to the load cell through the rod. After 30seconds of solidification, the test body is withdrawn from the melt.

The surface of the test body can be spray-coated with a zirconium oxide layer up to 0.5 mm thickness in order to control the heat flux. The maximum heat flux during the initial solidification period is approximately 4 - 5 MW/m² for an uncoated steel test body, which can be reduced to 2.5 - 3.0 MW/m² depending on the thickness of zirconium-oxide layer.

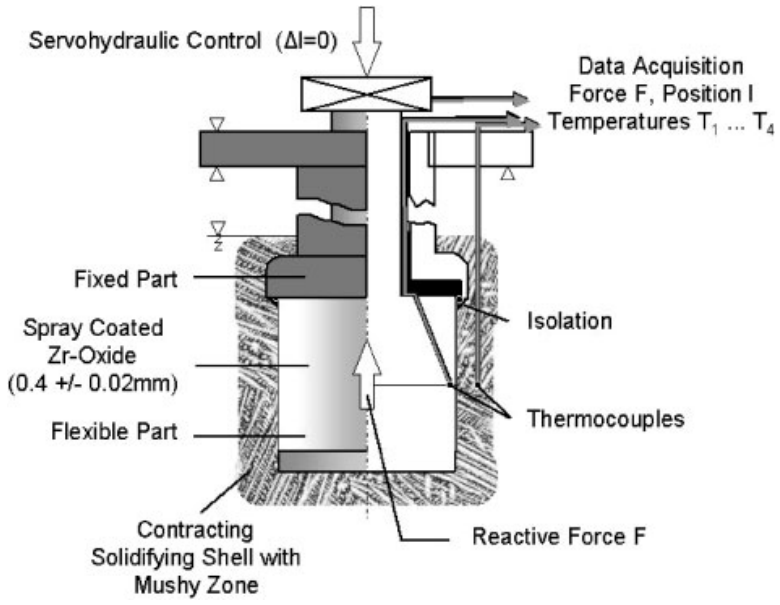

Fig.6.9 Schematic diagram of SSCC test [53]

6.2.2 Experimental Conditions

Steel B (non-peritectic low carbon), Steel E (hypo-peritectic) and Steel G (hypo-peritectic according to DSC analysis), were tested. Tab.6.1 shows the composition of the different steels. A reference steel (hyper-peritectic) has been included in the test series for the purposes of providing a better comparison of the results. Superheat was maintained between 25 and 35 °C. Two types of surface conditions were used in the test bodies - no coasting and a coating of 0.2 mm thick of a zirconium oxide layer as shown in Fig.6.10. The solidification time for all experiments was 30 seconds. Three experiments were conducted on each combination of steel grade and surface condition.

Tab.6.1 Compositions of steels used in SSCC test (in wt%)

Element [Tolerance]	C [±0.010]	Mn [±0.10]	Si [±0.05]	P [±0.002]	S [±0.002]	Al [±0.005]
Steel B	0.050	0.30	0.15	0.005	0.003	0.025
Steel E	0.080	1.50	0.30	0.005	0.003	0.025
Steel G	0.085	2.80	1.00	0.005	0.003	0.025
Reference	0.230	1.40	0.20	0.005	0.003	0.025

(a) Without coating (b) Zirconium oxide coating (0.2 mm) (c) Solidified shell

Fig.6.10 Pictures of split chill test bodies with different surface conditions and a solidified shell

6.2.3 Results and Discussions

The SSCC experiment is very delicate. The experiment is performed at temperatures close to the solidus and the measured forces are merely between 0.5 and 4.0 kN. Local differences, for example variations in superheat, effect the initial solidification resulting in a spread of the measured force. Hence, much experience is required to conduct the experiments and interpret the results. The experiments conducted in the present investigation were designed and overseen by the author, but conducted by a team of very experienced operators. The team has had many years of experience in conducting these experiments and had numerous feed-back loops to verify the validity of the experiments. Based on it, the controller of the experiment can immediately detect whether or not a measured value is reliable. However, successful experiments provide important and reliable information.

Fig.6.11 summarizes all the forces measured in the current set of experiments. The dash-lined curves indicate failed experiments. Steel B (low carbon) reaches a stable and constant contraction force of 2.0 - 2.3 kN. The reduction of heat withdrawal by the coating of 0.2 mm zirconium oxide layer causes a slower increase of the contraction force at the beginning. The subsequent decrease is thought to occur as a result of creep or by an unexpected incident caused by the penetration of liquid steel into the expansion joint between the upper and lower part of the test body. Even though the measured force was reduced, it didn't affect the actual contraction force.

In the case of Steel E (hypo-peritectic), the contraction force with no-coating on the dummy increases more rapidly compared to Steel B and it reaches a much higher maximum value of about 4 kN. It clearly followed the typical behaviour of hypo-peritectic steels assessed in previous SSCC test as described in more detail in section 3.1.1 [53]. These observations seem to be the result of a much faster $\delta \rightarrow \gamma$ transformation and a larger fraction of δ phase that transforms to the γ-phase (δ-ferrite is stronger than γ-austenite). Under the presence of higher contraction forces, distort of thin solidified shell is inevitable. The reduction of heat withdrawal of the coated dummy results in a lower rate of increase of the contraction force after 7 seconds. The final part of the curve is again characterized by a decrease of the measured force and this is thought to be for same reason as explained above.

For Steel G, the behaviour of the contraction force is quite similar to Steel E. The contraction force increases constantly and achieves a maximum of 3.5 kN. On the coated dummy with its lowered heat flux a maximum contraction force of between 2 and 3 kN is achieved. This observation confirms once again that this steel is of hypo-peritectic composition as observed in the DSC measurements. The decrease of the contraction force in the later part of the experiment is not well understood.

In the case of the reference steel (hyper-peritectic) with a dummy without a coating, the maximum measured force amounts to only 1.0 - 1.5 kN. Although the much lower maximum force compared to hypo-peritectic steels was anticipated as a result of an earlier study [53], the measured value is much lower than that of Steel B (low carbon). The reason for this observation is most likely that the higher carbon content, compared to other steels, results in a decreased shell thickness due to the lower solidification rate as previously observed in the HTLSCM experiments and described in section 2.4.1. The result is also likely to be affected by a lower critical strain for hot-tearing [84] and weakened shell strength due to the increased size of the mushy zone.

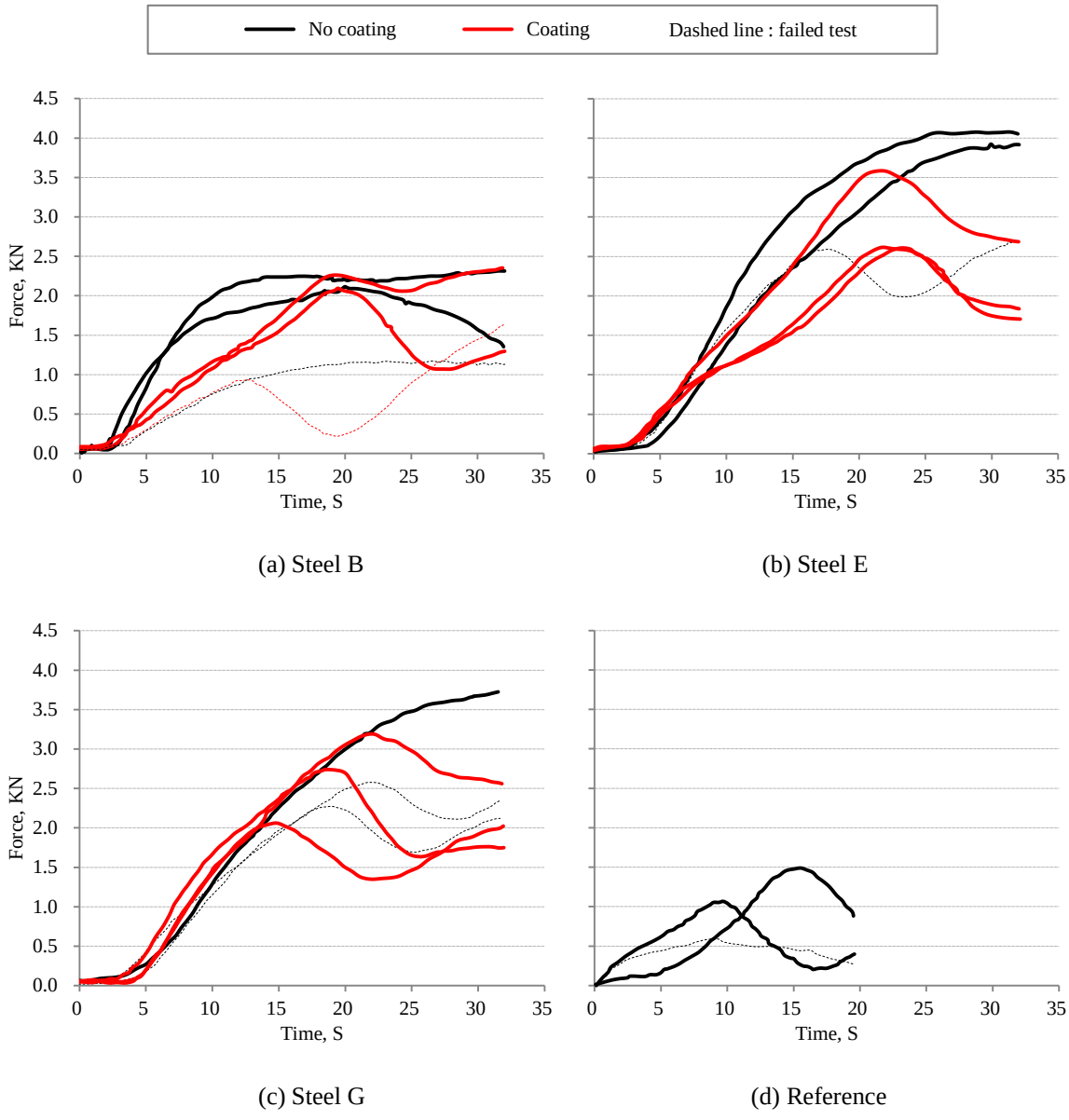

Fig.6.11 Measured contraction forces with different steels as a function of time

The maximum forces taken from each valid curve in Fig.6.10 are summarized as a function of equivalent carbon content in Fig.6.12. For the sake of comparison, the maximum force determined in the work of Berhard *et al.* [53] which was done under 0.4 mm thick zirconium oxide coating condition are included. Hypo-peritectic steels (Steel E and Steel G) are obviously showing the higher maximum force among steels. Also, for the hypo-peritectic steels the influence of heat withdrawal by coating on the maximum contractive force is extremely remarkable as they resulted in much lowered maximum contractive force with increased coating thickness. For the low-carbon steel and the 0.2 - 0.3 wt% carbon steels, this effect is less pronounced. This finding in hypo-peritectic steel further emphasizes that mild cooling in mould is essential in order to relieve uneven solidification.

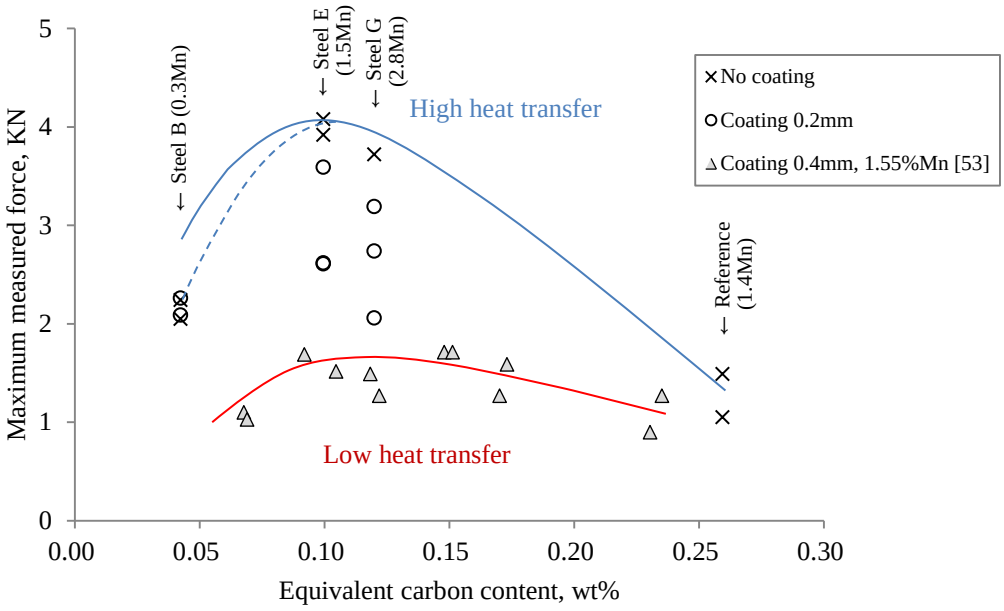

Fig.6.12 Maximum force in SSCC tests presenting the values determined in the present study and the values from the work of Bernhard *et al.* [53]. Equivalent carbon content, wt% = [%C]+0.04[%Mn]+0.1[%Ni]-0.14[%Si] for all steels except Steel G which refers to the phase transformation behavior in DSC measurements (see Fig.6.8)

A higher manganese content seems to account at least in part, to the attainment of a higher maximum contraction force because of increased strength of the thin solidified shell. Steel E, Steel G and reference steel contain higher manganese contents 1.4 - 2.8 wt% while Steel B has 0.3 wt% of manganese. Therefore, if steel B contained 1.4 - 2.8 wt% manganese, the expected contraction force with no-coating condition would be as shown by the solid blue line in the figure.

6.3 Conclusions from DSC Measurements and SSCC Tests

- Three different steel grades (Steel B, Steel E and Steel G) have been analysed by DSC measurements. The DSC results clearly showed that Steel B is a low-carbon steel while Steel E and Steel G are hypo-peritectic steels. It is important to emphasize that Thermo-Calc calculations indicated that Steel G is of hyper-peritectic composition.
- This observation emphasized the fact that steels of complex composition cannot simply be classified as hypo- or hyper-peritectic on the basis of existing thermodynamic data. There is therefore an urgent need to obtain reliable thermodynamic data, for example by DSC analysis, for such complex steels.
- In the SSCC test, the contraction force for Steel E is the highest and Steel G, which on the basis of Thermo-Calc calculations is hyper-peritectic behaves as if it is a hypo-peritectic steel.
- The effect of a reduction in heat transfer on the decreasing contraction force is more pronounced in hypo-peritectic steels than in steel of other compositions. This is an important implication in that mild cooling in the mould can be the most effective means of producing hypo-peritectic steels with minimum quality problems.
- Both DSC measurement and SSCC test were proved to be useful tools for the characterization of steels with respect to the peritectic reaction and the subsequent $\delta \rightarrow \gamma$ transformation.

Chapter 7. Summaries and Conclusions

7.1 Solidification Studies in the High-Temperature Laser-Scanning Confocal Microscope

A. In an attempt to contribute to an improved understanding of the root cause of surface defects, which occur as a result of uneven solidification in steel of near-peritectic composition, a dedicated study was conducted by using a concentric solidification technique within a high-temperature laser-scanning confocal microscope. The main advantage of the concentric solidification technique is that the early stages of solidification in the mould of a continuous caster can be modelled experimentally. Such a simulation is possible since there is great similarity between a concentric solidification experiment and the conditions pertaining to solidification in the meniscus region of the mould in terms of the direction of heat flow and the development of thermal gradients, although the magnitude of the respective values are quite different.

B. Significant enrichment of solute elements can occur ahead of the growing liquid/solid interface and the extent of segregation increases with increased cooling rate. As a result of alloying element segregation, non-peritectic steels, of composition less than 0.1 wt%C, can display the peritectic transition as predicted by calculation using the Scheil model. For example, peritectic transitions were observed at the liquid/solid interface in Fe-0.05wt%C alloys at a cooling rate of 50 °C/min, while at lower cooling rates only the solid state phase transformation of delta-ferrite to gamma-austenite occurred. From an industrial continuous casting practice point of view, it is usually assumed that the actual cooling rate in the meniscus region of the mould will render solidification behaviour somewhere between equilibrium and the Scheil model, but possibly closer to the Scheil model. In the result, low-carbon steels with an equivalent carbon content close to the lower peritectic limit, will frequently display peritectic behaviour.

C. The initial velocity of the liquid/δ interface decreases with the extent of segregation, i.e., with higher alloying elements and/or with higher cooling rate, because the migration of the interface requires the diffusion of large amounts of solute across the interface. The observation that the liquid/solid interface velocity decreases with an increase in the difference in solute concentration between the liquidus and solidus ($C_{Liquidus}$-$C_{Solidus}$) at the liquidus temperature supports this premise. The delay of shell growth due to the enrichment of solute elements (segregation) can be enhanced in the very early stage of solidification in the chill zone where planar liquid/solid interface morphology is maintained.

D. At a cooling rate of 20 °C/min and higher in all steels, the rate of δ→γ transformation was very high, typically that of a massive-type of phase transformation. Even at a cooling rate of 5 °C/min, the hypo-peritectic steel D (0.10C-0.48Mn-0.01Si) and E (0.08C-1.6Mn-0.28Si-0.012Ti), which are hypo-peritectic steels, showed a very high δ/γ interface velocity of more than 7.5 mm/s. The higher the fraction of primary solidified δ, the higher the solute concentration gradients in δ due to partitioning and insufficient back-diffusion of solute elements into the solid during solidification. These concentration gradients resulted in the diffusion of carbon from the liquid, through the liquid/δ interface (the γ nucleation site) into δ. The higher the magnitude of this flux, the higher the undercooling before nucleation initiates, which in turn leads to an increased rate of the subsequent δ→γ transformation due to the higher thermodynamic driving force for the formation of γ.

E. The δ→γ transformation that occurs in the presence of a liquid pool usually initiated at the liquid/δ interface in most of steels and the occurrence of the δ→γ transformation at the liquid/solid interface triggers the transformation of the remaining solid. In this way a massive transformation can occur on a large scale. In some cases the δ→γ transformation initiated in the solid behind growing solid/liquid interface even in the presence of a liquid pool. Although the liquid/solid interface is undercooled below the equilibrium peritectic temperature, the difference between the liquid/solid interface temperature and T_0 is not very high. In this case, if the driving force for the growth of the γ-phase in the solid is higher than that at the liquid/solid interface, nucleation can occur within the solid behind growing solid/liquid interface, preferably at grain boundaries.

F. Steel G (0.085C-2.8Mn-1.0Si-0.016Ti), notwithstanding the fact that thermodynamic calculations show that it falls well outside the hypo-peritectic range, displayed a much higher rate of the δ→γ transformation than Steel F (0.18C-0.35Mn-0.03Si) (which is supposedly a steel of peritectic composition) and behaved as if it were a hypo-peritectic steel. This is a most interesting observation because Steel G behaved as if it were a hypo-peritectic steel during plant trials in commercial production at the Gwangyang Works of POSCO (See Fig.3.1).

G. The shell thickness just before the occurrence of the δ→γ transformation in the meniscus region of a continuous caster was calculated using the experimentally determined initial solidification rate and the time required until the onset of the transformation. This index refers strictly to the initial solidification rate because the transformation will occur when the interface is still of planar morphology in the thin shell and hence the initial solidification rate, which is a function of the difference in solute concentration between the liquidus and solidus is the determining factor. The significance of this calculation is that it is the thickness of the solidified shell in the meniscus region of a continuous casting mould that determines in large measure, the mechanical behaviour of the thin shell.

7.2 Off-Corner Crack Formation in Titanium Bearing Steels That Have a Composition close to the Peritectic Composition

A. Relevant literature and analysis of in-plant data obtained from a commercially operating continuous caster have shown that the ductility in the off-corner region of a thin continuously-cast slab deteriorates significantly if the steel has a carbon equivalent in the range 0.08 wt%C to 0.13 wt%C and when it contains more than 400 ppm of titanium. Metallographic examination of surface cracks in transfer bar samples obtained from industrial operations following un-bending, revealed that the cracks propagated along thin ferrite films along coarse-grained austenite grain boundaries. These large austenite grains develop ostensibly as a result of an increased rate of austenite grain growth at the roots of oscillation marks or depressions because of the much higher temperature pertaining at the roots of oscillation marks and depressions as a result of unstable continuous casting operating conditions, such as molten steel level fluctuations in the mould. For steel of near peritectic composition, the most likely root cause of air gap formation in the off-corner areas is corner rotation due to a lack of mould taper in the meniscus area of the mould relevant to the early stages of solidification and the distortion of thin shell near corner area in mould due to stresses originating from the massive-type of $\delta \rightarrow \gamma$ phase transformation due to two-dimensional heat transfer in this area.

B. FEG-SEM analysis of the distribution of TiN particles in the transfer bar revealed that fine precipitates were scattered around cracks in the off-corner region of the slab. The corner region of a slab is subject to much higher cooling rates due to two-dimensional heat extraction in the secondary cooling zone of the continuous caster and hence, finer precipitates will form in this area relative to other regions in the slab.

C. Detailed analysis of in-plant data confirmed the metallographic observations shown above and provided convincing evidence that there are at least two dominating factors that affect off-corner crack formation, arguably contributing roughly equally: the peritectic phase transition, which causes shell distortions as a result of transformation stress, which in turn cause excessive growth of austenite grains and titanium additions to steel that result in the formation of fine TiN precipitates. In both cases the propensity to off-corner crack formation is increased.

7.3 Mould Texturing

A. In an attempt to evaluate the effectiveness of mould surface texturing on reducing the unevenness of solidified shells in selected steels, a simple dip-test in addition to the more sophisticated mould simulator tests were conducted.

B. In the dip-test, 20 mm diameter cylindrical dummies with different surface textures - flat, 30 μm sandblast, 2 mm interval horizontal groove and 5 mm interval horizontal groove - were assessed using Steel B (0.05C-0.3Mn-0.02Si), Steel E (0.08C-1.6Mn-0.28Si-0.012Ti) and Steel G (0.085C-2.8Mn-1.0Si-0.016Ti). The surface evenness deceased in the order Steel B, Steel E and Steel G. Steel G showed the most uneven surface upon solidification. This finding is in excellent agreement with observations made in an industrial operational continuous caster. The surface treatment of 2 mm interval grooves exhibited the most even solidification, resulting in the thickest shell through the improved contact between shell and mould-treated surface. The most likely reason for this improved surface evenness is the effect of grooves on the dispersion of deformation sites in the thin solidifying shell.

C. In the more sophisticated mould simulator tests, different texture patterns on mould surface were evaluated: flat, 30 μm sandblast, 1.1mm interval longitudinal grooves, 14 mm interval lattice type grooves and 7 mm interval lattice type grooves. Two different mould fluxes were evaluated by using of the hypo-peritectic Steel E since it has been found to be very sensitive (susceptible) to unevenness of the surface. The growth of the solidifying shell in hypo-peritectic steel becomes much more even when a so-called ‘mild cooling mould flux’ is used. This essentially means that a more even shell is produced when the heat-transfer rate in the meniscus region of the mould id reduced. Also, the reduced heat-flux in this region of the mould results in more intimate contact between the solidifying shell and mould, which in turn interesting enough, leads to an increased rate of shell growth towards the lower part of the mould as a result of increased heat transfer rate due to the intimate contact between mould and strand. It is important to note that the mould simulator tests are still in their infancy, the present study was one of the first investigations with this facility and the experimental techniques are still under development. It was found that an abnormally thick mould flux film formed, which masked the effect of mould texture and for this reason, quantitative information about the influence of mould texture on the evenness of shell formation could not be obtained. Further development of this experimental technique is in progress, but fall outside the scope of the present investigation.

7.4 Characterization of Peritectic Steel Grades

A. There is a running argument in the literature, but more importantly in industry, as to the criteria that should be applied to determine if a steel of a certain composition will be susceptible to the ill-effects of the peritectic phase transition in the course of continuous casting. Traditionally, the equivalent carbon content has been used as a criterion to determine if a steel falls within the peritectic composition range. However, in industrial practice, huge anomalies have been encountered when this criterion is used. In an attempt to determine whether or not the selected steel grades used in the present study fall within the peritectic composition range, differential-scanning calorimetry (DSC) measurements and submerged split-chill contraction (SSCC) test were employed. The steels Steel B, Steel E and Steel G used in the dip-tests were assessed. Without pre-empting the following discussion, it is worth mentioning that both the DSC measurements and the SSCC test proved to be very useful tools for determining whether a steel of a given composition could be classified as a steel which will undergo the peritectic phase transition.

B. The DSC measurements have proven beyond reasonable doubt that Steel B is a low-carbon steel and that both Steels E and G are hypo-peritectic steels. This finding is in stark contrast to the prediction by Thermo-Calc that Steel G is a hyper-peritectic steel.

C. The SSCC tests revealed that the contraction forces upon solidification of Steels E and G are considerably higher than those of steels of lower and higher carbon content. Steel G behaves as if it were a hypo-peritectic steel in concert with the DSC findings, but in contrast to Thermo-Calc predictions. A very important finding was that the reduction in heat transfer rate as a result of a zirconium oxide coating on the dummy in the SSCC-test decreased the contraction forces quite significantly. This reduction in contraction forces was more pronounced in the case of hypo-peritectic steels. This finding provides significant scientific evidence in support of the industrially accepted notion that ‘mild cooling’ in the mould (through the use of an appropriate mould flux) is an effective technique to reduce the incidence of quality problems in the continuous casting of hypo-peritectic steel.

7.5 Conclusions

A. From a critical assessment of the relevant literature and the outcomes of the present study, two distinct occurrences or conditions in close proximity to the liquid/solid interface in a solidifying steel shell within a continuous casting mould have been identified. These findings are schematically presented in Fig.7.

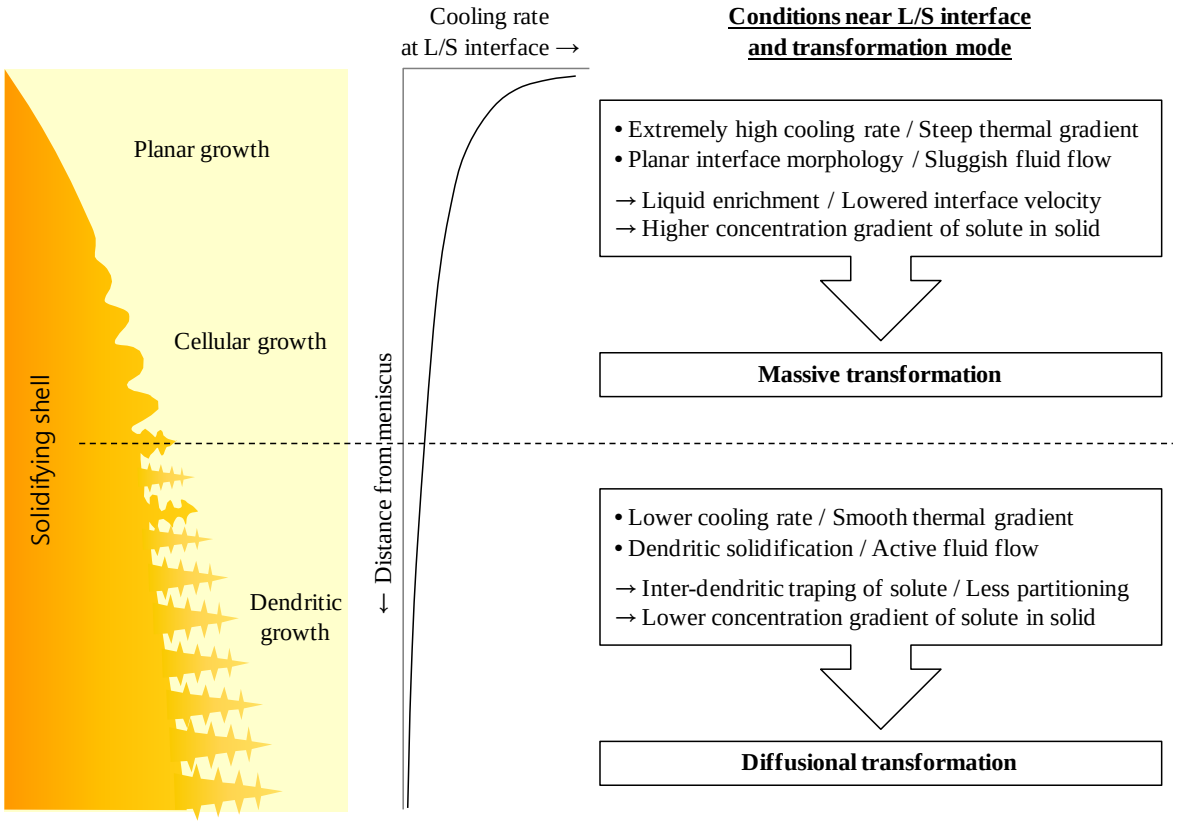

Fig.7 **S**chematic diagram of two distinct conditions in proximity to the liquid/solid interface in a solidifying steel shell within a continuous casting mould and the resulting transformation modes

B. An extremely high cooling rate and a very steep thermal gradient at the liquid/solid interface in proximity to the meniscus result in planar interface growth and solute elements build-up in the liquid ahead of the growing interface. The relatively sluggish macroscopic fluid flow due to the large distance from the submerged entry nozzle compared to other areas, prevents the solute-enriched liquid layer from mixing with fresh molten steel, which leads to significant partitioning. As a consequence, a higher concentration gradient of solute is established in the solid resulting in higher undercooling before the γ-phase can nucleate. These conditions favour the occurrence of a massive-type of δ→γ transformation as argued above. To make matters worse, solidification will be delayed due to the presence of a solute-enriched liquid layer at the

solidification front. This delay in solidification will increase the distance to which planar growth will occur, which in turn leads to an increased risk of distortion of the thin solidifying shell due to the high stresses developing as a result of the occurrence of the massive-type of phase transformation.

With continued solidification, the cooling rate at the liquid/solid interface is lowered and the thermal gradient reduced in the vicinity of interface, resulting in the formation of a dendritic structure. Moreover, an increased rate of fluid flow and the concomitant supply of fresh molten steel close to the submerged entry nozzle, play an important role in increasing the diffusivity of the solute in the liquid. In addition, solute-enriched liquid is trapped between dendrite arms, thereby reducing the concentration gradient in the vicinity of the solidification front and hence, the concentration difference between solid and liquid is reduced. Under these circumstances nucleation of austenite is not constrained and the phase transformation $\delta \rightarrow \gamma$ approximates equilibrium conditions. Although the picture painted above might be somewhat oversimplified, it does provide a theoretical framework for the interpretation of the very complex sequence of events occurring in the meniscus region in the mould of an industrial continuous caster.

C. An attempt was made to explore practical measures (or the directions towards improvement) aimed at minimizing defects resulting from solidification events in high-speed continuous casting processes such as uneven shell formation, depressions, cracks and even breakouts. Specific attention was paid to the high stresses that result from the massive-type of phase transformation occurring in the meniscus region. The major findings of these studies and the application thereof in industrial practice can be summarized as follows.

Composition adjustment of steel

The most common and practical approach in industry has been avoiding a composition design close to the peritectic composition range. This is generally done by the addition of suitable alloying elements, but this approach adds additional processing cost. Elements which promote the stiffness of thin shell at high temperature such as manganese, are not desirable if the adjusted equivalent-carbon content is close to the peritectic range because such steels produce higher contractive forces resulting in the enhancement of shell distortion.

Mild cooling and uniform heat removal in the near-meniscus region of the mould

Experimental simulations in the high-temperature laser-scanning confocal microscope, the submerged split-chill contraction test and the mould simulator confirmed that the rate of the $\delta \rightarrow \gamma$ transformation decreases at lower cooling rates. This lowered transformation rate in turn, leads to the development of lower contraction forces and eventually to the formation of a more even and thicker shell as a result of the more intimate contact between shell and mould. In addition, the lowered cooling rate leads to less pronounced concentration gradients in the solid

at the liquid/solid interface and possibly to the prevention of a massive-type of δ→γ transformation. Mild cooling can be obtained by the judicious design of mould flux properties. More importantly, uniform heat removal in the mould is most desirable because when uniform heat transfer in mould is obtained, steel level fluctuation caused by the bulging shell between support rolls have less of an adverse effect on stable operating conditions.

Maintaining adequate molten steel flow in the meniscus region of the mould

An increased rate of fluid flow into the liquid/solid interface prevents the build-up of solute-enrichment in the liquid, thereby preventing the occurrence of a massive-type of δ→γ transformation. However, a rate of high fluid flow can cause fluctuations in the molten steel level, which will hamper stable infiltration of mould flux into the gap between shell and mould. It is worth mentioning that electro-magnetic stirring of the molten steel in mould, which is being used in industry to homogenize the temperature distribution in the liquid, will at the same time increase the flow rate of liquid close to liquid/solid interfaces.

Stable control of the molten steel level

High-speed continuous casting operations increase the risk of unstable molten steel levels in mould due to the reduced shell thickness and thus increased interaction between bulged shell and supporting rolls. Unstable molten steel levels is a major cause of the formation of longitudinal facial cracks in industrial continuous casting practice because fluctuating steel levels disturbs stable infiltration of molten mould flux between strand and mould and therefore leads to the formation of ‘hot spots’. At higher casting speeds, the amount of heat that has to be extracted for the growth of a given shell thickness remains the same even though the heat transfer per unit area of mould increases. Therefore, the reason for the increased incidence of longitudinal cracking at high casting speeds cannot be explained by the increase in heat transfer rate in mould, but has to be linked to fluctuations in molten steel level. It is therefore very important in industrial practice to maintain stable molten steel levels in mould during casting.

Mould texturing

Finely profiled textured profiles on the mould surface such as sandblasting or fine grooves (normally with less than 1 mm groove intervals) play the role of increasing the heat resistance in similar vein to using a mould flux with a high heat resistance. On the other hand, mould surface textures varying over intervals of several millimeters, contribute to the even dispersion of deformation sites since the volume contraction upon solidification occurs at every groove. This even dispersion or distribution of nucleation sites and hence, distortion sites, diminishes the extent of air gaps formation between the solidified shell and the mould and leads to shell formation with an even thickness. Both methods are evidently effective in minimizing uneven solidification of peritectic steels, however, texturing is cost-intensive and the effectiveness of

texturing from an economic point of view has still to be assessed.

Measure for off-corner cracks

The large volume shrinkage associated with the solidification of steel of near-peritectic composition (compared to other steels) during the initial stages of solidification leads to the lack of narrow side mould taper in the upper area of the mould. This results in the formation of air gaps as a result of corner rotation and hence, the use of a multi step tapered mould which adapts the shape of narrow side solidification might reduce the incidence of off-corner cracks.

7.6 Future Work

- Investigation of the mechanism of the high rate of solid delta-ferrite to solid austenite transformation
- Investigation of whether the peritectic transition occurs when the liquid/solid interface is of planar morphology or not
- Proving if improved molten steel flow near the meniscus can reduce the risk of the peritectic transition by reducing the transformation rate
- Further investigation of the root cause of the delay of the initial solidification in the meniscus region of mould
- Improvements in the mould simulator technique to study interaction between mould, strand and mould flux

7.7 Concluding Remarks

As a metallurgical engineer working in the steel industry, I have had many occasions where I was unable to comprehend or understand the intricate interplay between cause and effect. I was particularly concerned about the mechanisms of solidification and the subsequent solid-state phase transformations occurring in the course of the continuous casting of steel. As an example, I have observed that when certain steels were processed, unexpected, very unstable operational conditions were encountered during continuous casting at high speed with a concomitant increase in slab surface defects, thereby hampering the production of quality product. A classic example was the unstable operational conditions experienced with Steel G. This steel displayed hypo-peritectic-like behavior such as abnormal molten steel level fluctuation and an increased incidence of surface undulations, notwithstanding the fact that thermodynamic calculations classified this steel as well outside the peritectic composition range. I was led to believe that there were some mystical, hidden properties of steels that were beyond our current understanding. It seems that notwithstanding many fundamental research studies as well as industrial trials and experimentation, we are still at a loss to fully comprehend the behavior of certain steel types in the course of the continuous casting of steel. It also seemed to me that there is an urgent need to make a greater effort to relate fundamental (academic) research to industrial practice.

In an attempt to make a contribution to making academic research more industry-relevant, I have attempted in the present study, to link findings of fundamental nature and importance to in-plant observations and analyses. More specifically, I attempted to extract from information in the literature and experimental observations, the key issues that bear relevance to industrial continuous casting operations. For example, I studied fundamental aspects of solidification by making *in-situ* observations in a high-temperature laser-scanning confocal microscope and then I introduced a simple dipping test followed by mould simulator studies to simulate thin shell growth in an operating continuous caster. By this approach, I was able to resolve a number of key questions, much like putting the pieces of a puzzle together. For example, Hanao *et al.* [44] have shown that shell growth in the region immediately below the meniscus in an operational mould is significantly lower than further down the mould. This is a most significant finding since if it were true, it can explain many of the difficulties encountered during continuous casting operations, especially problems encountered by casting steel close to peritectic composition at high casting speeds. However, the underpinning reasons for this observation could not be fully explained by the researchers. My study has shown that the most likely cause of this delayed rate of solidification is enrichment in alloying elements in the liquid layer immediately ahead of the growing interface as a result of a planar growth morphology of the solid/liquid interface in the very early stages of solidification.

I believe that another worthwhile outcome of this study has been the ability I developed to rationalize in simple terms, the complex solidification and phase transformation events during the early stages of solidification in a continuous casting mould: There are two distinctly different occurrences of the delta-ferrite to gamma-austenite transformation close to the liquid/solid interface: a massive type of transformation with a planar liquid/solid interface morphology and a diffusionally driven transformation upon further solidification in the region of dendritic growth.

In conclusion and on a philosophical note, I strongly believe in meaningful, mutual interaction between academia and industry; technology developments will be significantly enhanced if fundamental studies are driven by industrially-based investigations and conversely if fundamental studies can be converted to industrial applications. I have made an attempt to contribute to this approach and I trust that this thesis, which was aimed at integrating fundamental research with industrial practice achieved its goal. I hope that my contribution albeit small, will provide not only enhanced insights into the intriguing peritectic phase transition, but will also contribute to the enhancement of problem-solving skills in the workplace.

Bibliography

1. H. Shibata, Y. Arai, M. Suzuki, and T. Emi, *Kinetics of Peritectic Reaction and Transformation in Fe-C Alloys.* Metallurgical and Materials Transactions B, 2000. **31B**: p. 981-991.
2. N.A. McPherson and A. McLean, Continuous Casting, ISS, Warrendale, PA, 1997. **8**.
3. M. Wolf, *Continuous Casting: Initial Solidification and Strand Surface Quality of Peritectic Steels.* ISS, Warrendale, PA, 1997. **9**.
4. H.T. Tsai, H. Yin, M. Morales, and S. Morales, AISTech 05, May 9–11, Charlotte, NC, 2005.
5. M. Suzuki, C.H. Yu, H. Sato, Y. Tsui, H. Shibata, and T. Emi, *Origin of heat transfer anomaly and solidifying shell deformation of peritectic steels in continuous casting.* ISIJ Int., 1996. **36**(Suppl.): p. S171-S141.
6. V. Ludlow, A.W.A. Smith, A.S. Normanton, S. Landa, J. Wans, A. Gotti, and M. Thiemann, 4th European Continuously Casting Conference, Birmingham, UK, 2002: p. 206-214.
7. J. Sengupta, C. Ojeda, and B.G. Thomas, Second Int. Conf. on Advances in Solidification Processes, Graz, Austria, June 17-20, 2008. **in press**.
8. A. Badri, T.T. Natarajan, C.C. Snyder, K D. Powers, F.J. Mannion, M. Byrne, and A.W. Cramb, *A Mold Simulator for Continous Casting of Steel: Part2. The Formation of Oscillation Marks during the Continuous Casting of Low Carbon Steel.* Metallugical And Materials Transaction B, 2005. **36B**: p. 373-383.
9. Hiebler and C. Bernhard, Steel Research, 1999. **70**: p. 349-355.
10. C. Bernhard and G. Xia, 4th. European Continuous Casting Conference, Birmingham, UK, Oct. 14–16, 2002: p. 131-138.
11. B. Dhindaw, T. Antonsson, J. Tinoco, and H. Fredriksson, *Characterization of the peritectic reaction in medium-alloy steel through microsegregation and heat-of-transformation studies.* Mat.& Met. Trans. A, 2004. **25A**: p. 2869-2879.
12. H.W. Kerr, J. Cisse, and C.F. Bolling, Acta Metall., 1974. **22**: p. 677-686.
13. R. Dippenaar, H. Shibata, and T. Emi, Proceedings Materials '98 Conference, Wollongong, 6-8 July, 1998: p. 445-450.
14. D. Phelan, M. Reid, and R. Dippenaar, *Kinetics of the Peritectic Phase Transformation : In-Situ Measurements and Phase Field Modeling.* Metallurgical and Materials Transactions A, 2006. **37A**: p. 985-994.
15. D.M. Stefanescu, *Microstructure Evolution during the Solidification of Steel.* ISIJ International, 2006. **46**(No. 6): p. 786-794.
16. W.P. Bosze and R. Trivedi, Metall. Trans. B, 1974. **5**: p. 511-512.
17. H. Nassar and H. Fredriksson, *Peritectic Reactions and Transformations in Low-Alloy Steels.* Metallurgical and Materials Transactions A, 2009.

18. S. Griesser, *PhD Thesis "In-Situ Study of the Infuence of Alloying Elements on the Kinetics and Mechanism of the Peritectic Phase Transition in Steel"*. University of Wollongong, 2013.
19. D. Phelan, M. Reid, and R. Dippenaar, *Kinetics of the peritectic reaction in an Fe–C alloy.* Materials Science and Engineering, 2008. **A 477**: p. 226-232.
20. M. Hillert, *Solidification and Casting of Metals.* The Metals Society, London, 1979.
21. B. Chalmers, *Principles of Solidification.* John Wiley & Sons Ltd., Sydney, 1964.
22. Y. Arai, T. Emi, H. Fredriksson, and H. Shibata, *In-Situ observed dynamics of peritectic solidification and δ/γ transformation of Fe-3 to 5 at. pct Ni alloys.* Metall. Mater. Trans. A, 2005. **36**: p. 3065-3074.
23. H. Fredriksson and T. Nylén, Met. Sci., 1982. **16**: p. 283-294.
24. J.S. Lee, S.G. Kim, W.T. Kim, and T. Suzuki, *Numerical Simulation of Peritectic Reaction Using a Multi-phase field Model.* ISIJ International, 1999. **39**: p. 730-736.
25. D.A. Porter and K.E. Easterling, *5.9 Massive Transformation, Phase Transformations in Metals and Alloys.* Chapman & Hall, 1992: p. 349-357.
26. M. Hillert, *Communications: Nature of Massive Transformation.* Metallurgical and Materials Transactions A, 2004. **35A**: p. 351-352.
27. H. I. Aaronson, Metall. Mater. Trans. A, 2002. **33A**: p. 2285.
28. H. Yasuda, T. Nagira, and M. Yoshiya, *Massive transformation from δ phase to γ phase in Fe-C alloys and strain induced in solidifying shell.* Mat. Sci. and Eng., 2012. **33**: p. doi: 10.1088/1757-899X/33/1/012036.
29. S. Griesser, M. Reid, C. Bernhard, and R. Dippenaar, *Diffusional constrained crystal nucleation during peritectic phase transitions.* Acta mater., 2014. **67**: p. 335-341.
30. R. Dippenaar, C. Bernhard, S. Schider, and G. Wieser, *Austenite grain growth and the surface quality of continuously cast steel.* Metall. Mater. Trans. B, 2013: p. DOI: 10.1007/s11663-013-9844-6.
31. H. Yasuda, T. Nagira, M. Yoshiya, and M. Uesugi, *In-situ observation of peritectic solidification in Sn-Cd and Fe-C alloys.* Mat. Sci. and Eng., 2011. **27**: p. doi: 10.1088/1757-889X/27/1/012084.
32. J. Brimacombe and K. Sorimachi, Metall. Trans. B, 1977. **8B**: p. 489-505.
33. M. Reid, D. Phelan, and R. Dippenaar, ISIJ Int., 2003. **44**: p. 565.
34. *Thermo-Calc Version 4*, in *Foundation of Computational Thermodynamics*. 2006, Thermo-Calc Software AB: Stockholm.
35. *TCFE4, Steels/Fe-alloys databases*. 2006, Thermo-Calc Software AB
36. H. Chikama, H. Shibata, T. Emi, and M. Suzuki, *"In-situ" Real Time Observation of Planar to Cellular and Cellular to Dendritic Transition of Crystals Growing in Fe-C Alloy Melts.* Materials Transactions, JIM, 1996. **37**(No. 4): p. 620-626.
37. H. Yin, T. Emi, and H. Shibata, *Determination of Free Energy of δ-Ferrite/γ-Austenite Interphase Boundary of Low Carbon Steels by In-situ Observation.* ISIJ International, 1998. **38**(No. 8): p. 794-

801.

38. H. Yin, T. Emi, and H. Shibata, *Morphological Instability of δ-Ferrite/γ-Austenite Interphase Boundary in Low Carbon Steels.* Acta mater., 1999. **47**(No. 5): p. 1523-1535.
39. D.A. Porter and K.E. Easterling, *4.3 Alloy Solidification, Phase Transformations in Metals and Alloys.* Chapman & Hall, 1992.
40. P. Presoly, R. Pierer, and C. Bernhard, *Identification of Defect Prone Peritectic Steel Grades by Analyzing High-Temperature Phase Transformations.* Metallurgical and Materials Transactions A, 2013. **44**(12): p. 5377-5388.
41. *DICTRA 24 Users' guide*, in *Diffusion Controlled TRAnsformations in multicomponent systems*. 2006, Thermo-Calc Software AB: Stockholm.
42. *MOB2, Mobility databases, foundation of computational thermodynamics*. 2006, Thermo-Calc Software AB.
43. S. Niknafs, *ME(Res) Thesis.* University of Wollongong, 2007.
44. M. HANAO, M. KAWAMOTO, and A. YAMANAKA, *Growth of Solidified Shell Just below the Meniscus in Continuous Casting Mold.* ISIJ Int., 2009. **49**(No.3): p. 365-374.
45. M. Hanao, M. Kawamoto, and A. Yamanaka, *Influence of mold flux on initial solidification of hypo-peritectic steel in a continuous casting mold.* ISIJ Int., 2012. **52**(No.7): p. 1310-1319.
46. T. Saeki, S. Ooguchi, S. Mizoguchi, T. Yamamoto, H. Misumi, and A. Tsuneoka, Tetsu-to-Hagane, 1982. **68**: p. 1773-1781.
47. Y. Ueshima, S. Mizoguchi, T. Matsumiya, and H. Kajioka, *Analysis of Solute Distribution in Dendrites of Carbon Steel with δ/γ Transformation during Solidification.* Metallugical Transaction B, 1986. **17B**: p. 845-859.
48. M. Vereecke, W. Vermeirsch, and U. Meers, 4th Int. Conf. Continuous Casting, Verlag Stahleisen mbH, Dusseldorf, 1988. **1**: p. 128-141.
49. W.R. Irving and A. Perkins, IRSID Conf. on Continuous Casting, Biarritz, 1976.
50. J. Konishi, M. Militzer, J.K. Brimacombe, and I.V. Samarasekera, *Modeling the Formation of Longtitudinal Facial Cracks during continuous Casting of Hypoperitectic Steel.* Metallugical And Materials Transaction B, 2002. **33B**: p. 413-423.
51. H.V. Ende and G. Vogt, Iron Steel Inst., 1972. **210**: p. 889-894.
52. B.G Thomas, J.K. Brimacombe, and I.V. Samarasekera, *The Formation of Panel Cracks in Steel Ingots: A State-of-the-Art Review (1. Hot Ductility of Steel).* ISS Transactions, 1986. **7**: p. 7-20.
53. C. Bernhard and G. Xia, *Influeince of alloying elements on the thermal contraction of peritectic steels during initial solidification.* Ironmaking and Steelmaking, 2006. **33**(1): p. 52.
54. M. Suzuki and Y. Yamaoka, *Influence of carbon content on solidifying shell growth of cargon steels at the initial stage of solidification.* Materials Transactions, 2003. **44**(No. 5): p. 836-844.
55. H. Mizukami, S. Hiraki, M. Kawamoto, and T. Watanabe, *Initial solidification behavior of ultra low, low and middle carbon steel.* ISIJ International, 1999. **38**(No. 12): p. 1262-1269.
56. H. Murakami, M. Suzuki, and S. Miyahara, *Control of Uneven Solidified Shell Formation in Hypo-*

Peritectic Carbon Steel. Proceeding of The 6th International Iron and Steel Congress, Nagoya, ISIJ, 1990: p. 689-696.

57. T. Emi and H. Fredriksson, *High-speed continuous casting of peritectic carbon steels.* Mat. Sci. and Eng., 2005. **A413-414**: p. 2-9.
58. M. Wolf, *Intergranular surface craks in boom casting.* Trans. ISIJ, 1984. **24**.
59. B. Weisgerber, K. Harste, and W. Bleck, *Phenomenological Description of the Surface Morphology and Crack Formation of Continuously Cast Peritectic Steel Slabs.* Steel research int., 2004. **75**(No.10): p. 686-692.
60. E. Takeuchi and J.K. Brimacombe, Metall. Trans. B, 1985. **16B**: p. 605.
61. Y. Maehara, K. Yasumoto, and Y. Sugitani, *Effect of carbon on hot ductility of as-cast low alloy steels.* ISIJ Transactions, 1985. **25**: p. 1045-1092.
62. D.N. Crowther and B. Mintz, *Influence of grain size on hot ductility of plain C-Mn steels.* Materials Science and Technology, 1986. **2(9)**: p. 951-955.
63. R. Dippenaar, S-C. Moon, and E.S. Szekeres, AISTech, Cleveland OH, May 1-4, 2006: p. 833-843.
64. K.R. Carpenter, PhD Thesis, University of Wollongong, 2004.
65. L. Schmidt and A. Josefsson, Scand. J. Metallurgy, 1974(No. 5).
66. E. S. Szekeres, Proceedings of the Sixth International Conference on Clean Steel, Balatonfüred, Hungary, 10-12 June, OMBKE, Budapest, 2002: p. 324-338.
67. J. Reiter, C. Bernhard, and H. Presslinger, *Austenite grain size in the continuous casting process: Metallographic methods and evaluation.* Materials Characterization, 2008. **59**: p. 737-746.
68. Y. Maehara, K. Yasumoto, H. Tomono, T. Nagamichi, and Y. Ohmori, *Overview - Surface cracking mechanism of continuously cast low carbon low alloy steel slabs.* Mat. Sci. and Tech., 1990. **6**: p. 793-806.
69. Jungwook Cho, Toshihiko Emi, Hiroyuki Shibata, and Mikio Suzuki, *Heat transfer across mold flux film in mold during initial solidification in continuous casting of steel.* ISIJ International, 1998. **38**(8): p. 834-842.
70. J.A. Kromhout, E.R. Dekker, M. Kawamoto, and R. Boom, *Challenge to control mould heat transfer during thin slab casting.* Ironmaking & Steelmaking, 2013. **40**(3): p. 206-215.
71. J-W. Cho and H-T. Jeong, *Infiltration of Slag Film into the Grooves on a Continuous Casting Mold.* Metallurgical and Materials Transactions B, 2013. **44**: p. 146-153.
72. S. Tanaka, Y. Nuri, T. Egashira, R. Arima, and T. Ohashi, Tetsu-to-Hagane, 1982. **68**(4): p. 159.
73. K. Nakai, T. Sakashita, M. Hashio, M. Kawasaki, K. Nakajima, and Y. Sugitani, Tetsu-to-Hagane, 1987. **73**(3): p. 498-504.
74. M. Wolf, CAMP-ISIJ, 1992. **5**: p. 1303.
75. E.S. Szekeres, *A review of strand casting factors affecting transverse cracking.* Proceedings of the Sixth International Conference on Clean Steel, Hungary, 10-12 June, 2002: p. 324-338.
76. B.G. Thomas and W.R. Storkman, *Mathematical models of continous slab casting to optimize mold taper.* Medeling and control of casting and welding processes - IV, FL, USA, 1988: p. 287-297.

77. K.R. Carpenter, R. Dippenaar, and C.R. Killmore, *Hot ductility of Nb- and Ti bearing microalloyed steels and the influence of thermal history.* Metall. Mater. Trans. A, 2009. **40A**: p. 573-580.

78. B. Mintz, S. Yue, and J.J. Jonas, *Hot ductility of steels and its relationship to the problem of transverse cracking during continuous casting*. International Materials Reviews, 1991. **36**(No. 5): p. 187-220.

79. E-Y. Ko, J. Choi, J-Y. Park, and I. Sohn, *Simulation of Low Carbon Steel Solidification and Mold Flux Crystallization in Continuous Casting Using a Multi-Mold Simulator.* Met. Mater. Int., 2014. **20**: p. 141-151.

80. G. Xia, H.P. Narzt, C. Fürst, K. Mörwald, J. Moertl, P. Reisinger, and L. Lindenberger, *Investigation of mould thermal behaviour by means of mould instrumentation.* Ironmaking & Steelmaking, 2004. **31**(5): p. 364-370.

81. A.A. Howe, *Development of a computer model of dendritic microsegregation for use with multicomponent steels.* Applied Scientific Research, 1987. **44**(1-2): p. 51-59.

82. K. Blazek, O. Lanzi, P. Gano, and D. Kellogg, *Calculation of the Peritectic Range for Steel Alloys.* 2007 AISTech Conference Proceedings, Indianapolis, 2007.

83. A. Jablonka, K. Harste, and K. Schwerdtfeger, *Thermomechanical properties of iron and iron-carbon alloys: Density and thermal contraction.* Steel Research, 1991. **62**: p. 24-33.

84. R. Pierer and C. Bernhard, *The nature of internal defects in continuously cast steel and their impact on final product quality.* AIST Proceedings, Pittsburg, 2010: p. 193-203.